UNIVERSITY OF SOUTHAMPTON

Faculty of Engineering and the Environment

Theoretical Methods to Predict Near-field Fuselage Installation Effects due to Inlet Fan Tones

by

James Gaffney

Doctor of Philosophy

November 2016

UNIVERSITY OF SOUTHAMPTON

ABSTRACT

FACULTY OF ENGINEERING AND THE ENVIRONMENT
Institute of Sound and Vibration Research

Doctor of Philosophy

THEORETICAL METHODS TO PREDICT NEAR-FIELD FUSELAGE INSTALLATION EFFECTS DUE TO INLET FAN TONES

by James Gaffney

There are many analytical models to predict turbofan noise radiation in a free field. However, these models explicitly ignore the effect of the aeroplane components on the engine noise. The effects of the aeroplane on the radiated noise must be included because it is the installed engine that affects people in the cabin and community. The original contribution of this thesis is to present a theoretical model for the near-field fuselage installation effects on tonal noise radiating from a turbofan engine inlet.

Historically, the fuselage installation effects have been modelled using theoretical methods for open-rotor type sources. Installation effects include the scattering effect from the fuselage, and the refraction effect of the boundary layer running down the fuselage. In this thesis the established techniques are extended to include a new sophisticated analytical source for spinning modes radiating from a circular duct. The source model includes the diffraction effect of the duct lip. The model applies Fourier methods and implements the Wiener–Hopf method for diffraction. Owing to the physics of the problem, simplifications in geometry and flow do not curtail the validity of the predictions.

The refraction effect was quantified by evaluating the difference between sound pressure levels with and without the boundary layer. Upstream of the source the refraction leads to a paucity of surface acoustic pressure, yet downstream the boundary-layer effect was minimal. Further investigations led to an alternative method of simulating refraction by altering wavenumbers in Fourier space. The installation method was optimised for a turbulent boundary-layer profile by replacing a power-law with a scaled step-change boundary-layer profile.

The model developed in this thesis combines the most sophisticated analytic radiation models with current installation models. Due to the speed of the method, the intended purpose for industry is to refine variables via parametric studies. Once these are established, a numerical method could include more complex geometry and flow to the model. By calculating the noise on the outside of the fuselage, the quantity and distribution of acoustic lagging can be optimised. This, over the lifetime of an aeroplane, could lead to appropriate noise levels in the cabin whilst achieving potential reductions in fuel consumption, emissions and costs.

Contents

List of Figures

List of Tables

Nomenclature

$\square$	Used to denote any variable
$\widetilde{\square}$	Fourier transformed variable
$\square^{\pm}$	For $+/-$ axial values
$\square'$	Derivative
$\square_0$	Mean value
$\square^{\mathrm{o}}$	Degrees
$\square_F$	A Frobenius solution
$\square_L$	Linear profile
$\square_{PL}$	Power-law profile
$\square_{QS}$	Quarter-sine profile
$\square^{\mathrm{c}}$	Radians
$\square_c$	Pertaining to the critical layer
$\square_i$	Incident field
$\square_s$	Scattered field
$\square_t$	Total field
A	Acoustic admittance
BL	The installation function in Fourier space
F	Transform of particle velocity on the rigid source duct
G	Transform of pressure jump in the diffracted field in the Wiener–Hopf incident field
$\mathrm{H}_{\ell}^{(2)}$	Hankel function of the second kind of order ℓ

I	An integral (italic)
I_ℓ	Modified Bessel function of the first kind of order ℓ (roman)
J_ℓ	Bessel function of the first kind of order ℓ
K	Wiener–Hopf kernel (italic)
K_ℓ	Modified Bessel function of the second kind of order ℓ (roman)
M	Boundary layer profile (italic)
M	Mach number u_z/c_0 (Roman)
$\mathrm{M}^\sharp$	Total number of points over the domain (Roman)
M_∞	Free-field fluid velocity
P_{lq}	Amplitude of mode (l, q)
Q	Volume velocity
R	Radius in spherical polar coordinates
S	Shielding coefficient
Y_ℓ	Modified Bessel function of the first kind
$k_{z,lq}$	Axial wavenumber in the duct
a	Radius of the duct
a_0	Radius of the fuselage cylinder
b	Distance from the center of the source coordinates to the cylinder coordinates
c_0	Speed of sound
f	Solution of the ODE solver.
k_0	Source wavenumber
k_r	Radial wavenumber
k_z	Axial wavenumber
$k_z^\pm$	Doppler shifted frequency
l	Azimuthal order in duct

m	Azimuthal harmonic mode in the source coordinates
n	Azimuthal harmonic mode in the cylinder coordinates
p	Acoustic pressure
q	Radial mode
t	Time
$\mathbf{u}$	Acoustic velocity
Δ	A difference in decibels
Λ	Temporary variable used as an empirical constant
Ψ	Radial integral over the disc
α	The integrand of the full solution
α_c	Fuller's coefficient
β	Angle of the source
δ	Thickness of the boundary layer
δ^*	Displacement thickness of the boundary layer
ϵ	Error
ε	Width of the Frobenius solution
η_i	Incident field complex amplitude
ι	Small value
κ_{lq}	Duct radial wavenumber
λ	Acoustic wavelength
ω	Angular frequency
ρ_0	Mean density
σ	Relating to a monopole
ς	Centered location of critical layer
ξ_{lq}	Amplitude thing

ζ Cut-off ratio

$\bar{r}, \bar{\phi}$, and $\bar{z}$ Cylinder cylindrical coordinates

r, ϕ and z Source cylindrical coordinates

(l, q) Source azimuthal and radial mode

$\mathcal{B}$ Any Bessel function or linear combination of them

$\mathbb{Z}$ Any integer

ℓ Order of Bessel function

Authorship Declaration

I, James Gaffney, declare that the thesis entitled 'Theoretical Methods to Predict Near-field Fuselage Installation Effects due to Inlet Fan Tones' and the work presented in the thesis are both my own, and have been generated by me as the result of my own original research. I confirm that:

- this work was done wholly or mainly while in candidature for a research degree at this University;
- where any part of this thesis has previously been submitted for a degree or any other qualification at this University or any other institution, this has been clearly stated;
- where I have consulted the published work of others, this is always clearly attributed;
- where I have quoted from the work of others, the source is always given. With the exception of such quotations, this thesis is entirely my own work;
- I have acknowledged all main sources of help;
- where the thesis is based on work done by myself jointly with others, I have made clear exactly what was done by others and what I have contributed myself;
- parts of this work have been published as:
    1. Near-field sound radiation of fan tones from an installed turbofan aero-engine (McAlpine *et al.*, 2015),
    2. Sound radiation of fan tones from an installed turbofan aero-engine: fuselage boundary-layer refraction effects (Gaffney *et al.*, 2016).

Signed:.....

Date:.....

Acknowledgements

My ~~principle~~ principal thanks go to Alan McAlpine and Mike Kingan. Both of whom have graciously, patiently, and indeed eruditely, supported me far beyond what could be expected – I am truly grateful for your help and advice.

I am also grateful for the insightful comments and recommendations given by the internal examiners at the upgrade review. Also, thanks to Gwenael for allowing GXMunt be open.

I would like to thank Team Typo: Alan, Dad, Thinos, Tony and Jon T. Cheers guys – I owe you one. Also, thanks to Anderson, Victor and Tony for allowing their computers be part of the cluster.

Also I'd like to extend my appreciation to the people in Soton outside of the office; members of Sam Crabb's Jazz Disorder, The Sam Crabb Memorial Ska/Reggae/Jazz Disaster, The Sam Crabb Jnr Memorial Ska/Reggae/Jazz Disaster, the other band which can't be named in polite circles (or print) and Rally Ally B Team.

This project was funded by EPSRC and Rolls–Royce; thanks to both, especially Dr Christoph Richter at Rolls–Royce for his prompt assistance.

To my Grandparents.

Chapter 1

Introduction

As organisations such as the International Civil Aviation Organisation (ICAO, 2008) and the American Federal Aviation Administration (FAA) demand quieter aircraft, accurate noise radiation predictions from aeroplanes has become essential. At take-off and cruise the engines are a dominant source of noise from an aircraft. Turbofan engines are extremely complicated and, as such, the noise generation and radiation mechanisms are difficult to model accurately. The complexity is compounded by the presence of the airframe. Consequently, turbofan noise radiation predictions are usually modelled in the far and free field. However, the noise imposed on communities and those on the aeroplane are from the aircraft as a whole: fuselage, wings, landing gear in ensemble. The way in which the airframe and its components change the free-field predictions of noise sources are referred to as aircraft installation effects. This thesis will focus on tonal noise radiating from a turbofan engine and the fuselage installation effects.

This work will use theoretical methods to obtain noise predictions. In this context, theoretical methods refers to the use of predominantly analytical mathematics as far as possible. The benefit of this is that the solutions are exact and methods are relatively quick to compute so trends can be identified quickly. The limitations of using analytical methods are that simplifications to geometry and flow characteristics must be made. Other methods such as finite element methods would be able to include nuances in geometry and flow but require vast computational resources. The simplifications to the analytical model do not curtail the validity of the model, this will be discussed in due course.

This thesis details the developments of new methods to predict the fuselage installation effects from fan tones radiating from the inlet of an engine. The methods are different to previous work which focuses on propeller type noise sources. The new work in this thesis is all formulated based on fan tone sources from a turbofan jet engine. The method is very quick, and the intended use in industry is to obtain a prediction for shielding in the early design phase for either the turbofan design or fuselage acoustic lagging optimisation. A more detailed computational aeroacoustics (CAA) method

could then be used.

1.1 Aeroacoustics

However, before the bulk of the thesis a brief overview of aeroacoustics is given. Initially the aircraft noise limits are detailed before a short review of aircraft noise sources and their implications.

1.1.1 Aircraft Noise Regulations

Over the last half a century, increasing numbers of people are choosing to fly, so to meet demand the number of flights has increased. As the number of flights increases, so does the power and size of the aircrafts. In addition, the size and number of airports has increased. To limit the impact on communities, legislation has been introduced (for example ICAO (2011)).

Each aircraft has a unique Effective Perceived Noise Level (EPNL) measured in EPNLdB. The EPNL scale has been refined to include exposure duration and harmonic content. The longer and the more tonal (or rough) a noise, the more annoying it is the human observer and thus has a larger associated EPNL value.

Figure 1.1: Conversation in The Butcher's Hook (Southampton) is interrupted by landing gear noise.

In ACARE (2001) an aim to reduce 2000 EPNL values by 10 EPNLdB by 2020 was set. As 2020 approaches, this ambitious target was modified by the European Commission (2011) to reduce perceived 2000 noise levels by 65% (Astley, 2014). ICAO (2008)

suggests reducing EPNL values by reducing noise at source, effective land management, operational procedures (cut-back and flight path variation) and operating restrictions.

As Figure (1.1) demonstrates, in populated areas such as the south of England, noise imposed on the community is very significant due to flight path proximity. Therefore, to placate community pressure groups, airports in populated areas often impose more restrictive flight restrictions than the law requires (Smith, 1989). Heathrow voluntarily schedules no aircraft departures between 11 pm and 6 am (heathrow.com/noise/heathrow-operations/night-flights). Such strong restrictions are not required at airports with no immediate surrounding communities.

1.1.2 Aircraft Noise Sources

Aircraft noise can be split into three broad categories: engine, jet and airframe. Engine noise is covered in the literature review so jet and airframe noise is briefly discussed here.

Airframe noise can be categorised as: landing gear, flap and trailing edge noise (Lilley, 2001). On approach landing gear is dominant (Lockard *et al.*, 2004) but Smith (1989) reports that noise due to protruding flaps can be responsible for an increase of around 10 dB on a clean wing.

Landing gear is created by aeolian tones. The fast flow causes vortices to be shed and as the vortices separate from the solid they generate noise. For a single protrusion, the directivity in the far-field is similar to a dipole. Landing gear is an ensemble of many different geometries, the net effect is broadband noise. One way to reduce this noise is to install a splitter plate which interrupts the trailing vortex streets (Dobrzynski *et al.*, 2002).

Flow over cavities causes noise to be radiated in a more subtle way. Lockard and Lilley (2004) propose that noise from the leading edge of the cavity causes a vortex to shed and when the vortex hits the trailing edge noise is radiated. The acoustic wave then propagates to the leading edge and affects the rate of vortex shedding and thus has a feedback loop/quasi-resonance.

Vortices are shed from high–lift and flap edges. These in turn lead to noise generation. Theoretical models provide accurate predictions, for example, Stoker *et al.* (2003) published the sources of noise on the wing of a Boeing 777.

When the landing gear is stowed, the dominant source for airframe noise is generated by trailing edges of the wings and tail Campos *et al.* (1999). Crighton and Leppington (1970) modelled trailing edge noise analytically; they predicted that far-field intensity scales with fifth power of velocity. However, most solid/fluid interaction noise is modelled computationally. Such methods implement acoustic analogies such as the Ffowcs William-Hawking approximation, Ffowcs Williams and Hawkings (1969).

In addition to airframe noise, the jet makes a significant contribution to the EPNL value. The fast flow of the core mixes with the slower flow in the bypass or ambient fluid. When the fluid mixes a proportion of the pressure fluctuations radiate as noise. For subsonic flow the noise is broadband in nature, supersonic flows gain screech tones.

In the 1950s Lighthill, after some jiggery-pokery, assembled an inhomogeneous linear acoustic wave equation in quiescent flow from the Navier–Stokes equations. Balancing the wave equation were a collection of monopoles, dipoles and quadrupoles (Lighthill (1952) and Lighthill (1954)). These nonlinear source terms are referred to as Lighthill's tensor. He inferred these source terms are due to the turbulence. As such, Lighthill's source term is an analogy – albeit a good one.

To reduce the loudness of a jet, a non-specialist could recommend turning the jet off, or reducing the velocity. Lighthill's theory quantified the linear relationship between jet noise and eighth power of flow velocity. This has driven the reduction in flow velocity over the past half century.

This much lauded theory is flawed. At least some of the turbulence is due to the sheared flow. This and the propagation in the shear is not included in the model.

The convected wave equation in shear flow was derived by Lilley (1958) and Phillips (1960). Controversy surrounding the non-quadrupole sources in Lilley's model were clarified and cleared up by Goldstein (2001). Goldstein showed that, if the dependent variable is scaled, the source terms were quadrupoles after all (Stone, 2015).

The main drawback with the acoustic analogy is that the characteristics of the flow, including the turbulence, are required before you begin. Accurately predicting the exact nature of turbulence is impossible (Davisdson, 2004) and so for as long as this remains true, jet noise will never be precisely predicted without corrections factors. Alternatively, solutions may be found exclusively in the far-field for idealised flow. Ray theory is also a viable alternative for high frequency predictions.

It is worth noting that, like Lilley, in 1958, sound propagation in shear flow was also modelled by Pridmore-Brown (1958). His analysis was for flow inside a duct, therefore an incident field was already specified. This leads to a homogeneous form of Lilley's equation. The noise in the far-field is pertinent for jet noise, therefore to simplify the analysis Lilley's solution, valid in the far-field, is found by making a Green's function integral approximation. In the near field, Pridmore-Brown makes no such approximations and a numerical integral over axial wavenumbers is required. Pridmore-Brown suggests the method of Frobenius to bridge the singularity that corresponds to the critical layer. It is perhaps this more rigorous treatment that led to the acoustic wave equation in shear flow operator to be referred to as the Pridmore-Brown equation.

Either by reducing the jet velocity or by introducing chevrons on the trailing edge of the nacelle (Lee *et al.*, 2014), reductions in jet noise are responsible for large drops in noise levels (Smith (1989) and Casalino *et al.* (2008)). In fact, it has been suppressed

to such an extent that other noise sources are now becoming dominant.

1.1.3 Significance of Noise Sources

At the three measurement positions for EPNL evaluation, the levels of various aircraft noise sources are shown in Figure (1.2). It shows that the dominant noise source at take-off is the engines. However, on approach to land, the landing gear is as loud as the engine. It is very important to reduce all sources of noise, if not, tonal noise which may have been masked previously will dominate the noise signature. Although quieter, the aircraft would be more annoying and thus have a larger EPNL value – not ideal.

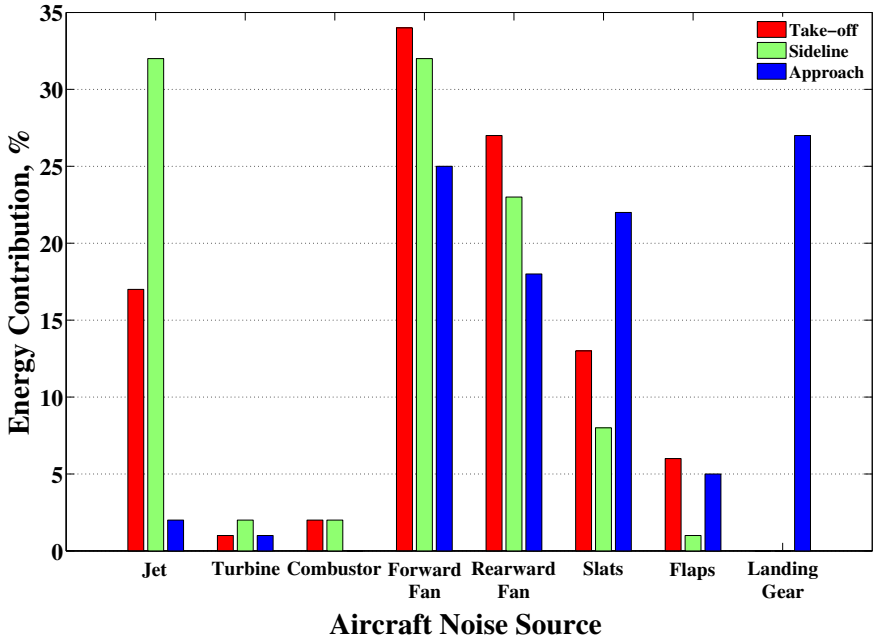

Figure 1.2: Typical relative noise levels at take-off, side line and approach for a mid-haul aircraft. Reproduced with permission from Lawrence (2014).

1.1.4 Installation Effects

All sources of noise are extremely complex to accurately model. Aeroacoustic noise sources are no different. As such, noise predictions tend to be modelled in isolation, i.e. in the free (and often far) field.

However, the noise that affects those on the aeroplane, and in the community, are exposed to noise by the whole aircraft. Therefore, models that accurately predict the noise once the source is installed in situ is expedient.

For example, many researches are investigating installed jet noise, one example (of hundreds) is Pastouchenko and Tam (2007). In this paper the authors compare the noise from the jet to the noise due to the jet impinging on the wing.

However, this thesis is concerned with radiating engine fan tones and how these are affected by the fuselage.

The physical presence of the solid, rigid fuselage will cause scattering. Some ambiguity surrounds this term; throughout this thesis scattering is defined as reflections and diffraction of sound due to a solid object. In addition, running down the fuselage is a boundary layer. For accurate predictions this must also be included in the model.

The importance of noise on the community is self evident. However, the pressure on the surface of the fuselage is also important. To reduce noise in the cabin, acoustic lagging and extra struts to damp panel resonances are installed in the fuselage walls, Wilby and Scharton (1973). The SPL from the engine has a direct affect on the quantity and distribution of acoustic lagging. If this could be minimised and optimised, over the lifetime of the aircraft the reduced weight would lead to significant reductions in fuel burn. This, in turn, would lead to reduced emissions, smaller fuel costs and would benefit those in the cabin.

1.2 Aims and Objectives

The aim of the thesis is to model the fuselage installation effects for a radiating engine fan tone. To achieve this aim and provide enough new, significant work for a PhD the following objectives have been met:

1. Review installation effects literature to identify gaps in knowledge.
2. Derive a new disc source model representative of fan tones radiation in both the near and far field.
3. Investigate the near-field characteristics of the incident field.
4. Add the diffraction effect of the nacelle lip by implementation of the Wiener–Hopf method.
5. Investigate the near-field effect of the duct lip.
6. Introduce a cylinder with boundary layer adjacent to the source to simulate fuselage installation effects.
7. Quantify the installation effects on the SPL levels on the surface of the cylinder. This was achieved by conducting a parametric study in source characteristics
   - source frequency,
   - azimuthal order,

   and flow effects

- ambient flow velocity,
- boundary layer profile,
- boundary layer thickness.

Each numbered objective will be referred to in the text when completed.

1.3 Layout of the Thesis and Original Contributions

The thesis is split into chapters; each chapter aims to fulfil an objective. They are listed below together with the original contributions.

Chapter 2: Literature Review

By reviewing the literature, it is identified that research into installation effects have prioritised propeller type sources and neglected turbofan sources. This chapter provides the motivation for the thesis.
Original contribution: Identifying this gap in knowledge.
Objective: 1

Chapter 3: Disc Source Incident Field Formulation and Validation

The derivation of a new formulation of spinning modes representative of fan tones from an inlet of a turbofan in the near- and free-field is presented. This derivation follows the Tyler and Sofrin (1962) method but makes no far-field assumptions – critical once the source is installed. Following is a discussion on the near- and far-field for the new disc source.
Original contributions: Formulating a distributed source and quantifying the near-field for the new disc source.
Objective: 2 and 3

Chapter 4: Duct Source Incident Field Theory

The Wiener–Hopf method is used to include the diffraction effect of the duct lip on the radiated near and far field.
Original contributions: By comparing the disc source to the Wiener–Hopf source, the near-field effect of the duct lip is quantified. The results show that differences in the diffracted field is most significant at maxima in the directivity pattern.
Objective: 4 and 5

Chapter 5: Installation Theory and Method

The main point/purpose/contribution of the thesis is in this chapter. The sources (derived in the thesis) are installed next to a infinitely long, rigid cylinder with a constant thickness shear layer running down its length. This cylinder and shear layer represents a fuselage and boundary layer.
Original contributions: The model for a turbofan fan tone source adjacent to a cylinder with boundary layer is new.
Objective: 6

Chapter 6: Near-Field Installed Results

The model is used to generate predictions of sound pressure on the surface of the cylinder. Via a parametric study, the effects of the various parameters on cylinder scattering and boundary–layer shielding are quantified.
Original contributions: All the results in this chapter are new. The main conclusions are that fan tones are significantly shielded upstream and moderately affected downstream. This chapter also introduces a new metric that considers the effect over the whole cylinder, not at discrete points or contours.
Objective: 7

Chapter 7: Near-Field Discussion

The near-field model and results are discussed in detail.
Original contributions: It is found that an axisymmetric source leads to an asymmetric results on the cylinder. A phase change was mathematically proven and observed in the instantaneous pressure for odd modes with opposite spin direction. The refraction effects of the flow can be simulated with a wavenumber filter in Fourier space. Additionally refraction characteristics for in-duct flow was confirmed on the exterior of the cylinder and a scaled step-change boundary layer profile gave equivalent shielding as a power-law profile. This leads to an extremely quick method for only a small decrease in accuracy.
Objective: 7

Chapter 8: Conclusion and Future Work

The material in the thesis is summarised and some future work is recommended.

1.4 Publications

So far, the PhD project has led to two published papers

1. McAlpine, A., Gaffney, J. and Kingan, M. (2015). Near-field sound radiation of fan tones from an installed turbofan aero–engine. *Journal of the Acoustical Society of America*. **131**, 1313 – 1324.

    - Corresponds to Chapters 3 and 5.

2. Gaffney, J., McAlpine, A. and Kingan, M. (2016). Sound radiation of fan tones from an installed turbofan aero-engine: fuselage boundary–layer refraction effects. In *22nd AIAA/CEAS Aeroacoustics Conference, Lyon, France*. AIAA-2016-2878.

    - Corresponds to Chapters 3, 5 and 6.

and one journal paper currently under review

3. Gaffney, J., McAlpine, A. and Kingan, M. Fuselage boundary-layer refraction of fan tones radiated from an installed turbofan aero–engine. *Journal of the Acoustical Society of America*. Submitted September 2016.

    - Corresponds to Chapters 5 and 6.

Note that Chapters 4, 5 and 6 will lead to another journal paper. This work corresponds to the installation effects for the source that includes the diffraction effect of the source duct lip. This model is also being used to generate evidence for the co-sponsor (RR) to file a patent.

Chapter 2

Literature Review

The previous chapter gave a broad introduction to the field of aeroacoustics. This chapter presents an in-depth critique of installation acoustics literature with particular attention paid to fuselage effects. Broad trends in the theoretical models and numerical methods are identified over the history of the subject. Significantly, it is shown that the installed sources are either propeller type or fundamental sources. In anticipation of installing a turbofan, this leads to a discussion on turbofan noise in a free field. Sophisticated models for radiation from a circular duct are discussed in detail.

2.1 Models for fuselage scattering and boundary layer refraction

Both theoretical and computational methods are reviewed in detail. The theoretical models are presented chronologically which also corresponds to an increase in model complexity. CAA methods are discussed after.

2.1.1 Installation Theoretical Models

Analytical models that predict the effect of the fuselage boundary layer on noise propagation have steadily improved over the last 30 years. As the analytical models have become more comprehensive and accurate the complexity has also increased. This section documents the model developments.

A brief letter to the editor of JSV by McAninch (1983) suggested to use a Pohlhausen profile to predict refraction due to a boundary layer running down an aeroplane fuselage. This publication was the first mention of the Frobenius[1] series as a solution to the singularity.

[1]The Froebenius solution was used in Pridmore-Brown (1958) so perhaps this set a precedent for the treatment at the critical layer.

Hanson (1984) was one of the first published papers to attempt to model the fuselage boundary layer effects. The model was based upon a two dimensional model in laminar flow by Brand and Nagel (1982). The motivation for the model was based on measurements taken on an aeroplane fuselage upstream of a prototype scale model of an open-rotor engine whilst in flight.

The metal fuselage can be expected to behave like a rigid boundary. On this type of boundary the pressure field would double the free-field predictions. However, the experimental data showed that the measured values were more than 20 dB lower than the expected 6 dB increase. Analysis of the measured data showed that the discrepancy was Mach number, angle and frequency dependent. These errors showed that the prior models were inadequate at accurately predicting the sound field on the fuselage whilst in flight.

When flow is near a solid surface a boundary layer develops. It was the absence of the boundary layer in the model that caused the large discrepancies. This initial Hanson paper developed a simple model for the boundary layer and its effect on acoustic propagation.

Many of the subsequent papers are based upon this model, and because of the relative simplicity, but generality to all subsequent models, the physics is described here. The solid, rigid body was a flat plate in two dimensions. The boundary layer was a simple step change from zero to the ambient flow velocity. Harmonic waves were assumed to have a general function in the perpendicular direction. The pressure field outside of the boundary layer is a sum of the incident and the reflected waves. The reflected wave takes the shape of the scattering object, in this case a plane wave. The fuselage boundary is rigid so the derivative of pressure is zero. In this case, the solution to the wave equation can be simple trigonometric functions. The waves in the boundary layer and outside are matched on the surface of the boundary layer by continuity of pressure and particle displacement. All unknowns can be solved by the set of equations.

Hanson (1984) predicted significant reductions in free-field pressure levels upstream of the noise source. For some boundary layer thicknesses the refraction effect caused a decrease in SPL of up to 40 dB. When the boundary layer was reduced to zero the 6 dB increase was predicted, which corresponds to pressure doubling. Although this model was in two dimensions and had a very simple boundary layer the predictions were reasonably consistent with measured results and was an encouraging start to installation acoustics.

As this was one of the first analytical studies of boundary layer effects, naturally there were many simplifications: a step-change boundary layer profile, laminar flow with a boundary layer of constant thickness and a flat plate. This study was for noise generated by turboprops in the near field. The incident waves were plane in the model, however, noise generated by these processes at such proximity do not behave like plane

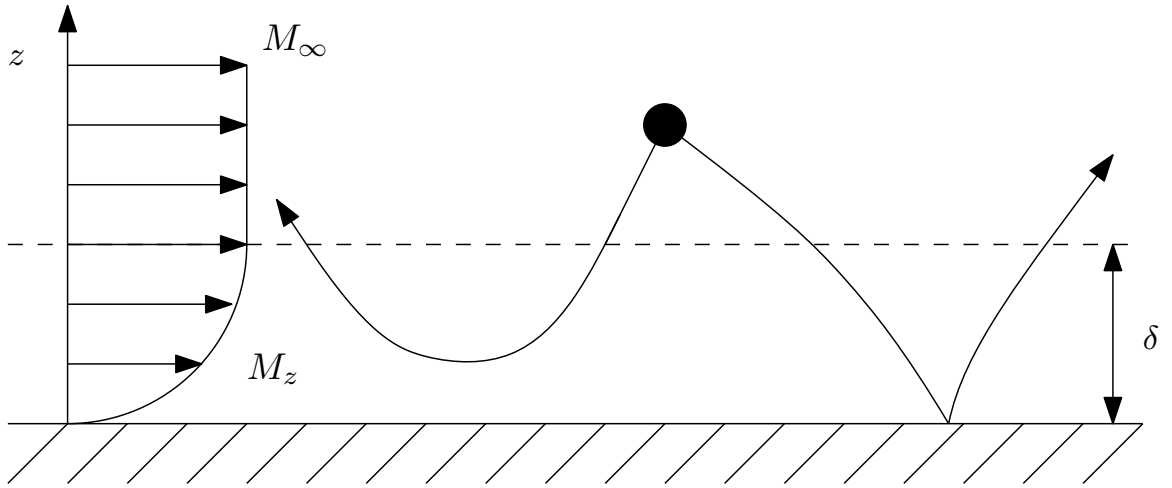

Figure 2.1: The ray leaving the source upstream is refracted out of the boundary layer layer whilst the downstream ray is refracted onto the fuselage.

waves.

McAninch and Rawls (1984) devotes significant time in demonstrating the derivation of the wave equation in shear flow from the mass, momentum and entropy equations (which can be found in Miles (1957), Ribner (1957) and Morse and Ingard (1968)). Solving the Pridmore-Brown equation is non-trivial due to a singularity at the critical layer.

Integrating over the singular point is discussed at length and the Frobenius method was favoured over a complex integration variable. The refraction effect on a plate was compared successfully against measured values for open-rotor measurements in flight on the fuselage surface. The plate assumption is reasonable in this case because the microphone array was axially in line with a scaled down open-rotor engine.

A year later Hanson teamed up with Magliozzi (Hanson and Magliozzi, 1985) to develop the earlier model of Hanson (1984). This model is significant because it included an infinitely long cylinder to represent the fuselage, a more realistic source (to model an open-rotor blade) and an arbitrary boundary-layer profile. Because this paper was attempting to match propeller experimental data, the source term was a rotating distribution of monopole and dipole sources, developed by Hanson (1985). The model was derived by matching the particle velocity at the boundary layer edge. The singularity is dealt with by the method presented by Tam and Morris (1980). The model was solved by 'unwrapping' the boundary layer so it can be solved in Cartesian coordinates. This is a valid method if the boundary layer thickness is thin compared to the radius of the cylinder.

Next, the theory was tested against measured values of a scale turboprop on a fuselage in flight. The measured values were to within an acceptable amount of error to the predicted values. Experimentally and analytically a strong dependency on the Mach

number was observed. Above 0.7 M in the forward direction saw a decrease of more than 20 dB compared to free-field predictions. The fuselage had an extreme shadowing effect beyond 50^o (measured from the engine axis). This effect is more severe for higher frequencies.

The effects of the nuances of the boundary layer was the subject of an in depth review by McAninch (1987). The pressure field was described by an incident and reflected plane wave impinging on a flat infinite plate in laminar flow. The continuous, vortex sheet and Poulhausen boundary layer profiles were compared. The main conclusions were that the only significant attenuation occurs upstream of the noise source, attenuation was strongly flow velocity dependent, incident angle was important and the effect was more significant for high frequencies. The attenuation was dependent on the number and placement of the notches in the Poulhausen boundaries. There was a strong dependence on the thickness of the boundary layer.

The model developed by Hanson and Magliozzi (1985) was further improved by Lu (1990). Whilst the 1985 model gave good predictions, Lu argues that the boundary layer should not be limited to being thin in comparison to the radius of the fuselage. Furthermore the boundary layer was not necessarily isothermal. The analysis is similar, again the Frobenius series was used to integrate over the singular point at the critical layer. The shielding effect of the boundary layer was shown to be strongly dependent on Mach numbers, with significant shielding for $M > 0.5$. The other variables only tend to affect the noise propagating in the forward direction and typically by 5 dB or less. The boundary layer profile, frequency and angles have little effect. The other aim of the paper was to include temperature changes. Temperature change was a non-result as it had no significant effect on the SPL. The model was tested against measured data for boundary layers on a smooth plate and tripped by two different rough surfaces. The values for the predicted and the measured SPL of the tone was to within 0.8 dB.

Recently[2] the solutions to installation effects have been researched with highly theoretical approaches. Belyaev (2012) studied the effect the fuselage boundary layer had on the reduction of open-rotor noise. Various parameters were changed including rotation speed of the source, flow velocity, boundary-layer velocity profile, boundary-layer thickness and observer incident angles. One surprising result was that, of the profiles tested, the boundary-layer profile did not affect the difference in SPL significantly.

The most recent study to include the boundary layer was Brouwer (2016) for open-rotor sources near a cylinder. Both surface pressure and far-field predictions were given. For the near-field predictions the turbulent profile boundary-layer refraction effect was, again, reasonably strong upstream of the source. The results were only shown on the

[2]Installation effects research is closely linked to open-rotor research. The amount of open-rotor research fluctuates with price of aviation fuel. In the 1990s and 2000s fuel was not particularly expensive. However, the price has increased recently, as has interest in efficient engines. This is the reason for the gap from 1990 to 2012.

near-side of the cylinder. In the far-field the boundary-layer was only moderately significant.

The scattering effect of a cylinder in quiescent flow was modelled by Fuller (1989). A schematic of scattering is shown in Figure (2.2). The fuselage was an infinite cylinder and the noise source were monopoles and dipoles near the fuselage. The total field is a summation of incident and scattered waves. The scattered field is derived by Bowman and Uslenghi (1969). A similar scattering paper by McAlpine and Kingan (2012) made significant effort to obtain analytical expressions for realistic open-rotor sources and the effect of an infinite cylinder with flow. Kingan and Self (2012) also concentrated on theoretical effects of scattering and derived tailored Green's functions for infinitely long and rigid cylinder, again this work was applied to open-rotors.

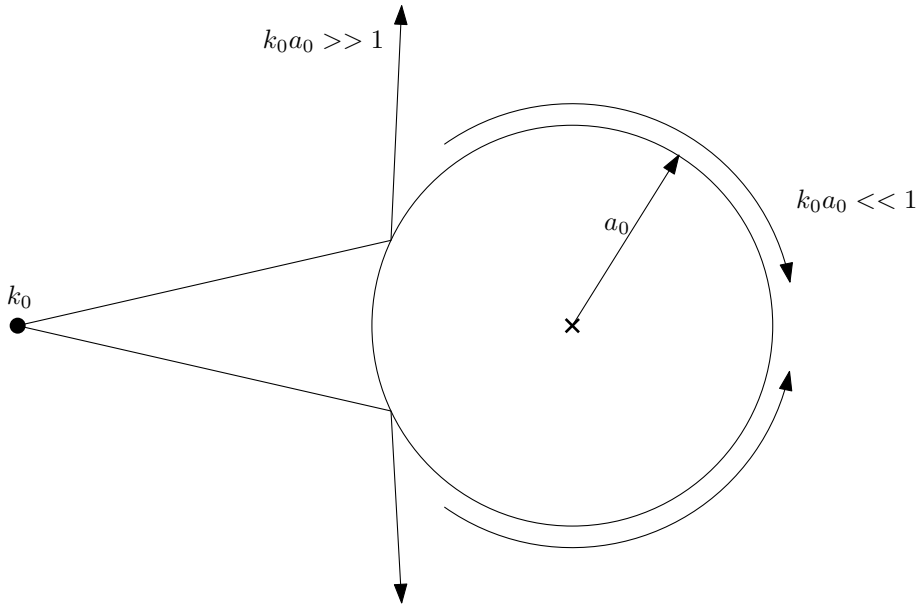

Figure 2.2: Scattering is dependent on frequency, for high k_0a_0 values significant shielding occurs, for low frequencies the waves diffract around the cylinder.

The models discussed so far have simplified the boundary layer to laminar flow or disregarded it completely. Salikuddin *et al.* (1988) included a more realistic turbulent boundary layer. Aircraft are sufficiently fast and irregular to trip the laminar flow in the boundary layer. Salikuddin *et al.* (1988) compared theoretical predictions to a wind tunnel experiment for a flat plate. Measurements in a square wind tunnel with a turbulent boundary layer and point source agreed with the theoretical model. The model included a term that modelled the eddy viscosity effects. Large argument asymptotic approximations were used so community noise was the motivation of this study. By including viscosity the critical layer singularity is damped out. The numerical integration used to solve the equation for pressure was stiff and takes more computational resources. The main conclusions of this study were that attenuation was position, frequency and flow velocity dependent. This is the same as the laminar cases. The authors do not

include a direct comparison between the effects of a laminar and turbulent boundary layer so the significance of the turbulence is unknown.

The models that were used in the previous papers represented the fuselage as an infinitely long cylinder. Due to weight considerations and other practical concerns, fuselages are usually of finite length, therefore a model of a finite cylinder would be more realistic. The scattering effect of finite cylinders for acoustic waves has been modelled analytically but not by aeroacousticians. Whales, sand banks and large groups of zooplankton can apparently be modelled as cylinders of finite length. The initial papers attempted to model the signal for SONAR signals. Stanton (1988) modelled the finite cylinder but neglected to include the effects of the cylinder ends. The targets were marine animals so the model was underwater based and boundary conditions were not rigid. Ye (1997) improved the model to include the end effects. Although the expressions may need some modifications to be used for aeroacoustic applications they have potential to be used in installation effects.

The installation effects of aircraft engines have been modelled to a reasonable degree of complexity. Focus has been placed on open-rotors because of the large amplitude noise generated by the blades and the proximity to the cabin. This has meant that the focus of some papers has been to apply and test open-rotor noise models. Furthermore, the pressure on the fuselage surface is often the goal. However, broad trends are consistent in all cases of installation effects. The main ones are; fuselage produces a shadow zone at large k_0a values and there is significant attenuation upstream of the source. Insignificant effects are the profile and temperature of the boundary layer. The impact of the effect of turbulence and realistic, finite fuselage geometries are at this point unknown. The installation effects due to noise generated from tonal fan noise have, to the author's knowledge, not been predicted using theoretical methods.

2.1.2 Installation Numerical Methods

Theoretical methods are a good way of understanding the physics and mechanics of engineering problems and trends can be quickly evaluated. However, for the model to be fully analytic, simplifications must be made. This usually involves approximating geometries to simple shaped and simplifying complex, extended noise generators to fundamental sources. To include the intricacies of geometry and realistic predictions of flow numerical methods can be employed. In this context numerical methods refers to ray theory, Finite Element (FE) and Boundary Element (BE) methods. The discussion in this section will focus on the results of the research into installation effects that have utilised numerical methods, not on the process itself.

One of the first published paper into the numerical method to predict scattering of installed aeroacoustic sources was by Atalla and Glegg (1991). Atalla and Glegg (1991)

implement the ray acoustic method to predict scattering effect. The code developed is based on a branch of ray acoustics called Geometric Acoustics (GA). The method developed allowed for a moving source, moving fuselage, variable flow and a scattering body of arbitrary shape. The GA method was applied to aeroacoustics for the first time in this paper, however some of the underlining theory was developed by Lighthill (1972), Candel (1972) and Whitham (1974). The GA code developed, which included a solver of 18 simultaneous ODEs, was validated against theoretical predictions for spheres and cylinders obtained from Morse and Ingard (1968). For large k_0a values the difference between the new ray theory and the analytic solutions was negligible.

The problem highlighted by Atalla and Glegg (1991) of the large amounts of memory required to model installation problems using numerical methods is tackled by Stanescu *et al.* (2003). Stanescu *et al.* (2003) calculate the solutions of inviscid flow equations by the discontinuous Galerkin spectral element method. The nacelle, fuselage and a reasonably realistic coaxial jet were included. This was made possible because of the recent developments in computing power and the efficient way in which the power is used.

A more recent application of ray acoustics was to demonstrate the significant reduction to community noise that installation effects can have on the 'silent' aircraft idea, shown in Figure (2.3). Agarwal *et al.* (2007) predicted through ray tracing calculations, that a reduction in the far-field of more than 10 dB can be achieved by placing the engines above the fuselage/wing. Although the application is slightly sensational, a good discussion on ray acoustics theory is presented. To solve the equations, various software was used including one that was developed for electromagnetic waves. Experiments on a scale model of the plane was compared against predicted values. They did not compare particularly well because the sharp corners and small size of the winglets cause diffraction that was below the apparent size to wavelength ratio limit.

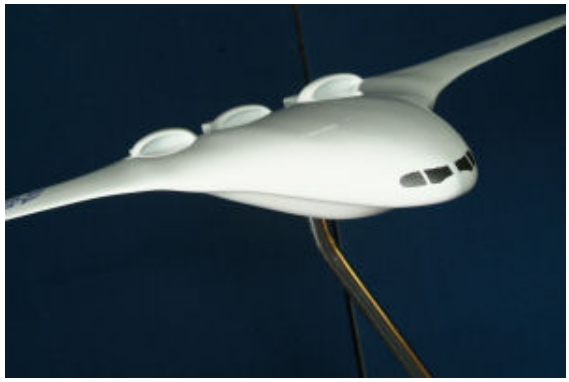

Figure 2.3: The silent aircraft concept that has been modelled using ray acoustics by Agarwal *et al.* (2007). From eng.cam.ac.uk

Spence (1992) implemented the analytical results derived by McAninch and Rawls (1984). To do this, Spence (1992) developed a optimised numerical method that im-

plemented the many infinite integrals and sums that are required in the solution. The results are consistent with those predicted by analytical results. The results were compared to measurements taken from an aircraft in flight and corresponded well.

BE methods have been utilised to investigate installation effects. One such example is Wang and Zhou (1998) which utilised the BE method to investigate the fuselage scattering effect due to propeller noise. Unlike the theoretical models of the previous section, the solution is calculated based on the Ffowcs Williams-Hawkings equation. Forward velocity of the fuselage is less than 0.3 M and the fuselage was rigid. They contentiously assumed that flow of less than 0.3 M leads to negligible refraction. The code was validated against analytical solutions.

The effect of the wing on the noise from a propeller was investigated by Marretta *et al.* (2001) by implementing the BE method. The method made use of increasingly accurate aerodynamic predictions and measurements of the flow around a wing. The method incorporated the aerodynamic results to predict the acoustic field via the Ffowcs Williams-Hawkings equation. The aim of the paper was to investigate the effect of the wing on the sound field at low Mach numbers. Boundary layer effects are negligible at low speeds (Hanson and Magliozzi (1985) and Lu (1990)). The fuselage was also neglected. Despite these simplifications, the method gave reasonably accurate predictions when compared to measured data by Sulc and Benda (1982). The predictions showed that the wing affects the field modestly and is space dependent.

Siefert and Delfs (2011) investigated the effect of refraction and spectral broadening due to fuselage boundary layers from a monopole source. They calculated the flow field along a cylinder by solving the Reynolds-averaged Navier-Stokes (RANS) equation at 0.75 M. Turbulence was added to the boundary by a Random-Particle-Mesh method (RPM). The noise source was a monopole and the field was calculated by CAA, in this case PIANO was used to solve the linearised Euler equations. As expected the high frequency waves were refracted strongly away from the fuselage surface upstream of the noise source. When turbulence was introduced to the boundary layer the sound was scattered. The scattered noise was scattered into shadow zones. The tone was also affected by haystacking effects of turbulence.

The computational model was made more realistic by Dierke *et al.* (2013). They used realistic airframe geometry and most significantly changed the noise source to a mode propagating from the turbofan. The change in source type was shown to be very significant to the predicted pressure on the fuselage. The same method was used as in Siefert and Delfs (2011) apart from additional code to calculate the propagating mode from the turbofan engine. The modes that propagated from the engine was the $(l, q) = (20, 1)$ and $(l, q) = (24, 1)$. Turbulence was included so haystacking and geometrical scattering was modelled. The relatively quick flight condition of 0.85 M ensured that the refraction effect of the boundary layer was significant. When the boundary layer was

included, it was shown that the fuselage pressure was very dependent on the incident angle of the incident wave. Although this is true for any source the effect is highlighted for the $(m, n) = (20, 1)$ because of the two lobed directivity pattern. The lode with less incident angle was refracted very strongly and a reduction of 15 dB can be expected. Contrary to a more modest, although still significant, reduction of 8 dB for the larger grazing angle. The turbulent boundary layer scatters pressure into a broader area but tends not to reduce the peak level significantly.

Although Dierke *et al.* (2013) showed some interesting results, they could only predict the pressure in a reasonably small volume at low free stream velocities. The results took one week to solve on 4 CPUs. The volume was created by extruding a two dimensional result.

By reviewing the literature from numerical approaches to installation effects have shown some extremely interesting results. Ray acoustics was employed by Agarwal *et al.* (2007) however the lower limit of the high frequency limit was breached and significant differences between predicted and measured values were observed. The established CAA software PIANO was used to investigate the refraction and scattering (both spectral and geometrical) effects due to the boundary layer by Siefert and Delfs (2011) for a monopole. Dierke *et al.* (2013) then improved the source to a realistic tone propagating from a turbofan. The differences between the two sources were extremely significant. All the papers discussed in this section broadly agreed with the analytical results of the previous section i.e. strong refraction upstream, angle of incidence and profile dependent. The installation effects of tonal noise from turbofan engines have only been studied using numerical methods and have been shown to be very significant.

2.2 Fan-tone Radiation

The previous sections have shown that analytic installation effects have been studied with either fundamentally basic or propeller type sources. A new source for the engine fan tone will be formulated to fill the gap in this knowledge. Fortunately there have been several papers that model an engine fan tone in a free field. In this section, an examination of engine fan tone radiation models is presented.

Turbofans are a type of aero-engine that generate thrust by compressing and setting fire to a gas. This gas then expands to generate thrust. In a turbofan engine the expansion drives a fan upstream of the combustion. This fan sucks more air into the engine, and the cycle repeats. Thanks to the fan and the nacelle (which surrounds the mechanisms) this type of engine is efficient and powerful and are installed on virtually all mid to long haul aeroplanes.

Noise is generated in various sections of the engine, shown in Figure (2.4). Jet and combustion noise tends to be broadband whereas the other types are tonal or a sum of

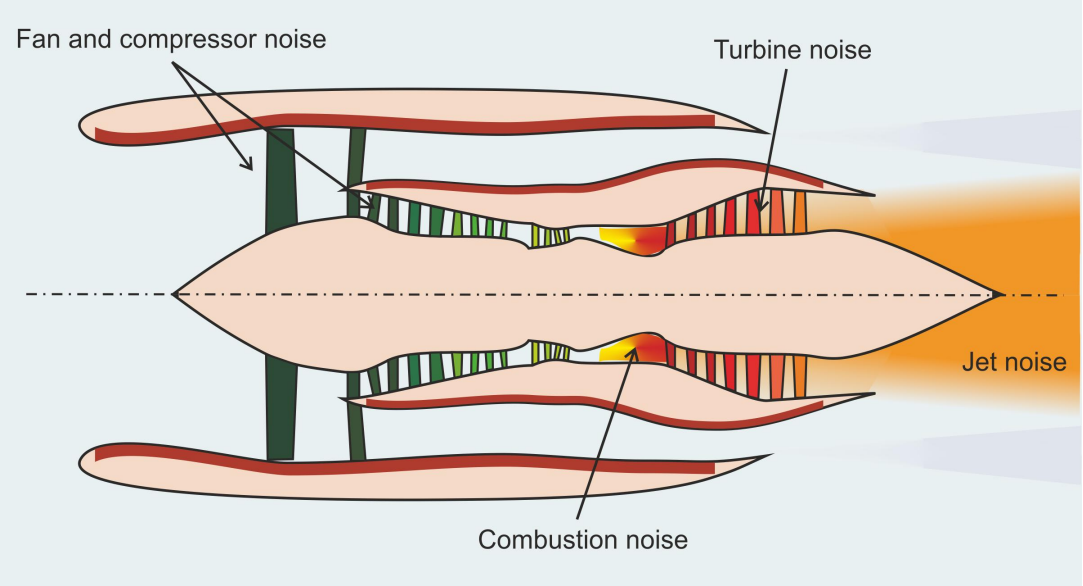

Figure 2.4: Turbofan schematic with noise sources. Used with permission from A. McAlpine: southampton.ac.uk/engineering/about/staff/amca.page.

tones.

As before, theoretical and numerical methods are examined for modelling fan-tone radiation.

2.2.1 Theoretical Models for Radiation

In this analysis of theoretical methods to predict free-field radiation, two papers are examined in detail; the blue ribbon paper for turbofan machinery noise Tyler and Sofrin (1962) and a recent theoretical model by Gabard and Astley (2007).

The first significant paper to analytically model turbofan noise was Tyler and Sofrin (1962). The authors start with the noise generating mechanisms for the rotor-locked mode. As the fan (rotor) spins, it generates a pressure field which spins at the angular velocity of the blades with a frequency equal to the blade passing frequency. This pressure wave propagates along the duct. For physical reasons the acoustic mode is of the same order as the number of blades. The nacelle was simplified to form a circular duct. Under this condition, the acoustic field can be described as a summation of simple mode shapes.

In a perfectly circular duct, via the method of separation of variables, the azimuthal mode function is an exponent. The radial solution is a Bessel function. These shapes propagate down the duct. This result can be gleaned from any number of methods, however the rotor-stator interaction tones analysis was new. This simple observation states that an azimuthal mode may be excited by the interaction between the fan and the stators (located behind the fan). The mode order is the difference between the number of blades and stators.

This observation was very significant because the number of rotors and stators is easily engineered such that the rotor-stator interaction mode may be optimised for purpose. The mode could be high such that the mode grazes the nacelle liner, or so that the mode radiates out the front of the fuselage.

For these generating mechanisms the forcing frequency is real. Therefore the modes propagate down the duct with no loss in amplitude. The amplitude of a propagating mode can be reduced with the addition of a liner. This thesis does not consider cut-off modes.

The radiation from the duct termination was also modelled. The pressure on the duct face can be described by simple modes mentioned above. An element of area on the face is then modelled small enough to be thought of as a monopole source. The strength of the source is proportional to the particle velocity normal to the duct plane. A distributed source can be formed by integrating over the area of monopoles with a volume velocity strength proportional to the analytic mode shape function.

Community noise was prioritised, therefore they moved to the far-field to integrate over the source. This has the added advantage of making the integral over the source simpler than the full, near-field solution.

Although the predictions give reasonably realistic values, at high polar angles the results are not good. The reason for this is that directivity forces the principle lobe to a large polar angle. At these large angles the diffraction due to the duct lip becomes significant. To model these effects the Wiener–Hopf method could be implemented.

The Wiener–Hopf method is an analytic method that allows differential equations with mixed boundary conditions to be solved. The important step is to split the relevant transform into two parts. For example, for a mode radiating from a duct, the axial transform is split from negative infinity to zero, and then from zero to positive infinity to account for the rigid to boundary of the semi-infinite duct. The next step is to allow the integrating variable to be complex. By doing these two steps, the full integral can be taken (Noble, 1958).

The full integral is from negative to positive infinity. So long as these limits are applied the path taken can stray from the real axis. An important part of the Wiener–Hoft method is choosing the correct contour of integration. Care must be taken to ensure that the integrand is regular whilst including the contributions of poles which may or may not be physically relevant. Full analysis is presented Noble (1958) and for concise treatment see; Mathematics for Acoustics (Wright, 2001) and Modern Methods in Analytical Acoustics (Crighton *et al.*, 1992).

The diffraction from a duct lip in the context of a turbofan engine was modelled by Gabard and Astley (2006). This paper builds on Munt (1977) and **?**. Munt (1977) modelled a radiating mode from an outlet of a turbofan engine. In this set-up, the model must incorporate the faster flow of the jet in the annulus. The original Munt predictions

were in the far field. Rienstra added a centre body to the model, again this cannot be ignored for radiation from the outlet of a turbofan. Thankfully, for the inlet problem considered in this thesis, these added complexities may be ignored.

A diffraction problem is set up like so; the incident field is prescribed, the diffracted field is formed such that the total field satisfies the boundary conditions (on the diffracting object) and the far-field radiation criteria are satisfied.

In this model, the incident field is the mode radiating along the duct. The duct boundary conditions are rigid and of infinitesimal thickness. The new part of the Gabard paper was to include the vortex sheet as a boundary condition. This was done by solving the convected wave equation for potential flow. The vortex sheet is described by the Kutta condition and modelled by continuity of particle velocity. By summing the two fields the total acoustic field is formed. No far-field approximations were made in formulating the problem. Importantly for installation effects, the resulting equation is an inverse Fourier transform. For a single tone and mode, the result show a strong effect of the various variables.

In an engine all the modes below the highest mode are cut-on. Therefore it is very important to model multimode sources. Very briefly, a recent example of multimode modelling can be found in Sinayoko *et al.* (2010). This paper adds flow to the model of Joseph and Morfey (1999). They use energy considerations to construct expressions for the multimode solution in the far field.

Lastly, the effect of the incline of a flanged duct with quiescent flow was analytically modelled in the far-field by McAlpine *et al.* (2012). The principle lobe is translated by the angle of the highlight.

To sum up, analytic methods for modelling a mode radiating from a circular duct has improved so that the analytical model includes; diffraction from duct lip, flow, a vortex sheet for outlet problems, different flow velocities in/out of the core and a center-body. The flow must be along the axis of the duct.

2.2.2 Numerical Methods for Radiation

Subtle changes in geometry and flow may be included in FE analysis. CAA modelling of turbofan noise is summarised in Astley *et al.* (2010). Although CAA can give very accurate predictions for realistic geometry and flow, they take too long to use in a parametric study.

2.3 Chapter Summary

Historically, installation effects have been studied in the context of open-rotors. Significant, general trends have been identified for fuselage scattering and boundary layer

refraction, important effects are; significant shielding occurs at large $k_0 a_0$ values on the far-side of the fuselage, fuselage boundary layer effects are small below about 0.5 M are stronger upstream. An insignificant effect is temperature change in the boundary layer. In all these studies the boundary layer thickness has been constant along the cylinder. The impact of the effect of turbulence and realistic, finite fuselage geometries have at this point not been theoretically modelled in the context of installation effects. Also, the installation effects due to noise generated from tonal fan noise are yet to be predicted using theoretical methods. By identifying this gap in knowledge, the first objective has been achieved.

Numerical methods have been successfully utilised to predict installation effects. Tonal noise from turbofan engines have been modelled and the results can be used to check future analytical work. The installation effects of tonal noise from turbofan engines have only been studied using numerical methods and have been shown to be very significant. The numerical methods are suitable for investigating complex geometries.

Noise radiating from a circular duct has been modelled in a free field. The models have become sophisticated such that they include the diffraction from the duct lip, regions of different flow speeds, an annular duct and vortex shedding. The latter three of these is essential for accurate predictions for an outlet of an engine. Numerical methods can be used for realistic turbofan geometries in three dimensions. However these calculations can take a very long time.

Chapter 3

Disc Source Incident Field Theory and Validation

The noise radiating from the inlet of a turbofan in a free-field is analytically modelled in this chapter. The sound field is obtained by solving the inhomogeneous convected wave equation. The source is formulated by approximating the turbofan as a semi-infinite circular duct. A distribution of monopoles are integrated over with no far-field approximations to form the source. The source strength of the monopoles are taken as the axial velocity of a mode of the circular duct. In doing this, the radiation due to a propagating spinning mode is modelling in the near field. The diffraction of the duct lip is explicitly neglected, therefore the model is only valid in the forward arc.

After the derivation of the incident field the directivities of the radiated field are discussed. Specific attention to the near- and far-field of the new source is investigated. Implementing the full solution is critical to accurate predictions in the near field.

3.1 Disc Source Theory

This section presents the derivation of the new source. The derivation of the source is similar to McAlpine, Gaffney and Kingan (2015) however all variables are non-dimensional in this derivation. The non-dimensional length scale is referenced to the radius of the cylinder, a_0 (the cylinder radius introduced in Chapter 5, it is used here for consistency and only scales the results), the reference velocity is equal to the speed of sound, c_0, and the reference density is equal to the ambient density, ρ_0. The pressure is scaled by $\rho_0 c_0^2$.

3.1.1 The Duct Approximation

Turbofan noise is generated through many mechanisms: fan gust interaction, rotor noise, rotor vane interaction, to name a few. Modelling these sources accurately is extremely

challenging. However, because the nacelle wraps the engine in a duct, the propagation of the sound is greatly simplified by modelling the problem with duct acoustics; any sound field in a duct can be expressed as a sum of incoherent modes. Furthermore, the mode shapes of circular ducts are analytical functions. Consequentially, turbofan are commonly simplified as circular ducts. The first step in the derivation is to approximate the inlet as an infinitely long, rigid circular duct. The modal superposition is valid for any source.

Solving the wave equation by separation of variables shows the mode shapes functions are Bessel's function (J_l) in the radial direction, viz

$$p\left(r,\phi,z,t\right)=\sum_{l=-\infty}^{\infty}\sum_{q=0}^{\infty}P_{lq}^{\pm}\mathrm{J}_l(\kappa_{lq}r)\,\mathrm{e}^{-j(l\phi+k_{z,lq}^{\pm}z)}\,\mathrm{e}^{j\omega_0 t}, \tag{3.1.1}$$

where mode (l,q) is the l^{th} azimuthal mode and the q^{th} radial mode. In this thesis, only a single mode propagating in the upstream (where the superscript + has been dropped) direction is examined

$$p_{lq}\left(r,\phi,z,t\right)=P_{lq}\mathrm{J}_l(\kappa_{lq}r)\mathrm{e}^{-j(l\phi+k_{z,lq}z)}\,e^{j\omega_0 t}, \tag{3.1.2}$$

where ω_0 denotes the source frequency. See Figure (5.2) on page 69 for geometry.

Via the momentum equation, the non-dimensional axial particle velocity is

$$u_{z,lq}\left(r,\phi,z,t\right)=\xi_{lq}P_{lq}\mathrm{J}_l(\kappa_{lq}r)\mathrm{e}^{j(-l\phi-k_{z,lq}z)}\mathrm{e}^{j\omega_0 t}, \tag{3.1.3}$$

where the velocity mode amplitude coefficient is

$$\xi_{lq}=\frac{k_{z,lq}}{(k_0+M_\infty k_{z,lq})},\qquad k_0=\omega_0>0. \tag{3.1.4}$$

The flow in the uniform flow region, which includes the duct, is denoted by M_∞. The ambient flow is positive in the negative direction. This is done such that the fuselage would move in the positive axial direction.

The dispersion relationship for the mode is

$$\kappa_{lq}^2+k_{z,lq}^2=\left(k_0+k_{z,lq}\,M_\infty\right)^2, \tag{3.1.5}$$

and the radial wavenumber, κ_{lq}, is an eigenvalue determined by $\mathrm{J}_l'(\kappa_{lq}a)=0$. Therefore, κ_{lq} is determined by the azimuthal mode of order l and the radius of the duct, a.

The axial wavenumber propagating against the flow in the duct is obtained by solving

Equation (3.1.5) to give

$$k_{z,lq} = \frac{k_0 M_\infty + \sqrt{1 - (1 - M_\infty^2)\kappa_{lq}^2 / k_0^2}}{1 - M_\infty}. \tag{3.1.6}$$

The axial wavenumber for the upstream propagating wave is a smaller value than the downstream wave.

If the value under the square root in Equation (3.1.6) is less than zero, the wavenumber is complex. When this occurs the wave is evanescent and exponentially decays with distance. The frequency ratio at which this occurs is given by

$$\zeta_{lq} = \frac{k_0}{\kappa_{lq}\sqrt{1 - M_\infty^2}}, \tag{3.1.7}$$

referred to as the cut-off ratio. When ζ_{lq} is less than unity the wave is cut-off, above unity and the mode propagates. The cut-off ratio leads to the mode triangle; the salient fact is that high forcing frequencies have a higher number of propagating modes.

The group velocity of the mode is smaller than the phase velocity. This is because the wave travelling in the azimuthal direction travels around the duct and has further to travel. If one were to look at a constant phase the mode appears to spin. The speed at which the mode spins is dictated by the circumferential phase velocity. The circumferential phase velocity decreases with increasing azimuthal mode (l). A barely cut-on mode ($\zeta_{lq} \gtrsim 1$) spins slowly, in a lined duct such as a turbofan, thus has longest contact with a liner so attenuation is increased.

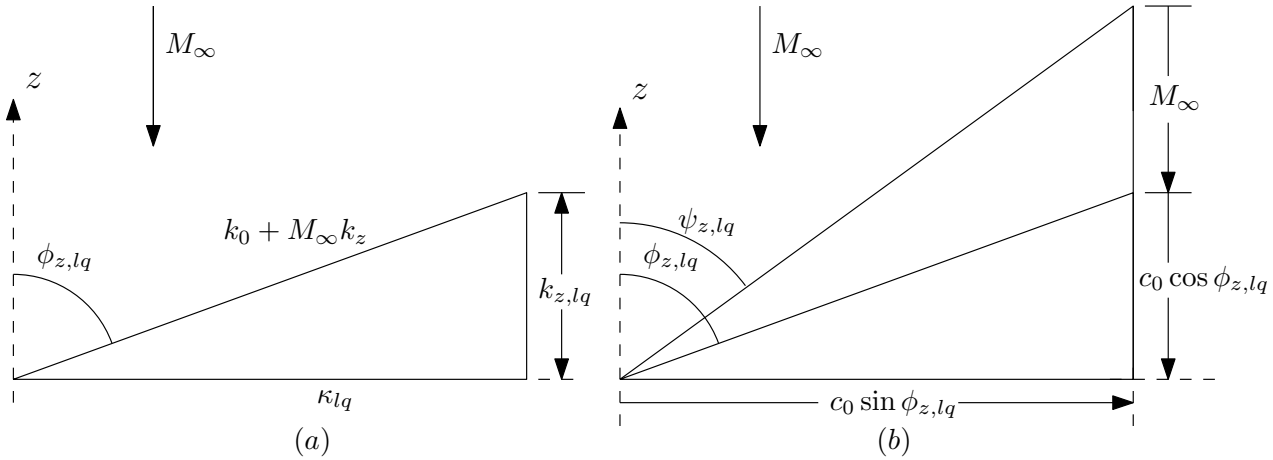

Figure 3.1: A diagram of the dispersion relationship (leads to $\phi_{z,lq}$), in (a) and is the inner triangle in (b), and the group velocity triangle (which leads to $\psi_{z,lq}$) in (b).

The angle at which the vector normal to the wave fronts of the mode is ϕ_{lq}, this angle is important for cut-on/off. The angle ψ_{lq} is the angle at which the group velocity vector makes with the duct axis, this angle will come up later in the thesis. These angles are

identical in quiescent flow. A diagram of these angles are shown in Figure (3.1).

The commonly referred to 'spinning' modes are a slight misnomer. In a rectangular duct the standing wave is formed by a superposition of two waves travelling in opposite directions. In a circular duct a standing wave can be simulated by superimposing a clockwise rotating mode ($-l$) and an anticlockwise rotating mode (l). The standing wave is not formed because in the azimuthal direction there are no boundaries.

In a turbofan operating with a supersonic tip speed, the amplitude of the rotor-locked mode is much greater than the other modes. The real valued modal amplitude P_{lq} can be chosen appropriately to replicate a source. In this thesis, single mode calculations are performed and without loss of generality the modal amplitude is always set equal to unity.

Furthermore, it can be shown that at $z = 0$ the pressure is

$$p_{lq}|_{z=0} \sim \mathrm{J}_l(\kappa_{lq} r)\, \mathrm{e}^{-jl\phi}, \tag{3.1.8}$$

the relationship between a clockwise and anticlockwise mode is

$$p_{l,q} = (-1)^l\, p^*_{-l,q}\,, \tag{3.1.9}$$

where $*$ is the complex conjugate. This result means that for even order modes the real pressure is identical whereas there is a phase change of π radians in the imaginary component. For the odd modes the imaginary component is identical for clockwise and anti-clockwise spinning modes, whereas the real component has the phase change of π.

Figure (3.2) shows the incident pressure for modes used later in the thesis. They show that the energy is more concentrated towards the radius outer wall as the azimuthal order increases. This is due to the property of the first kind of Bessel function.

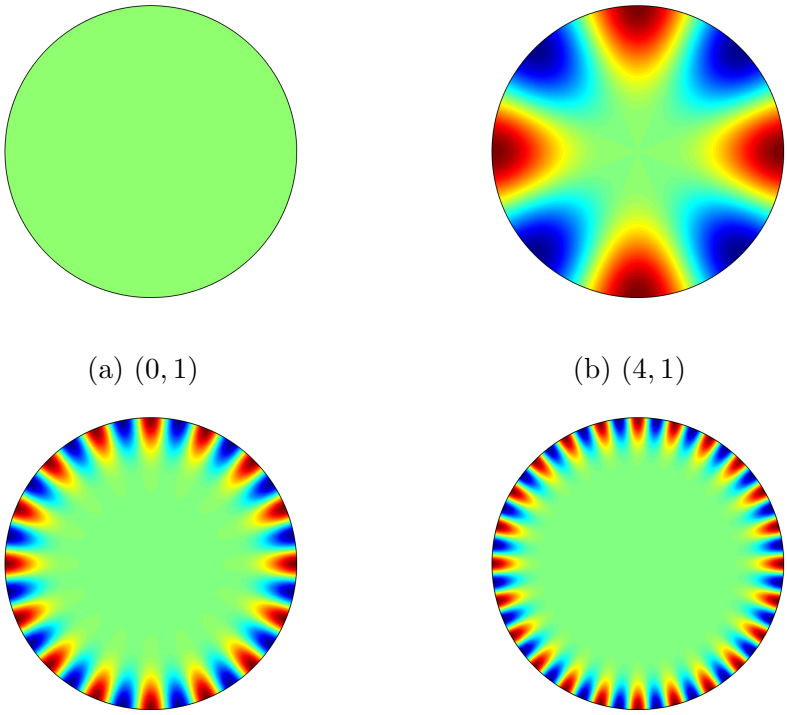

(a) $(0, 1)$ (b) $(4, 1)$

(c) $(16, 1)$ (d) $(24, 1)$

Figure 3.2: Normalised instantaneous pressure for spinning modes (l, q).

3.1.2 Derivation of Source

At this point the turbofan has been approximated as a cylindrical duct with a superposition of modes for an arbitrary source. In this section, the distributed source is formed by taking the conditions on the cross section of the duct at a location equivalent to the inlet's highlight. This is achieved by imposing the axial acoustic velocity from the duct on a distribution of monopoles. The solution is found by starting with the solution to the wave equation in cylindrical coordinates for a monopole. From this result a number of monopoles are manipulated so that the solution for a ring and then mode solution is derived.

Throughout this thesis the Fourier and inverse Fourier transform is defined as

$$\widetilde{p}_m\left(r, k_z, \omega\right) = \int_{-\infty}^{\infty}\int_{-\pi}^{\pi}\int_{-\infty}^{\infty} p\left(r, \phi, z, t\right) \mathrm{e}^{j(k_z z + m\phi - \omega t)}\, \mathrm{d}z\, \mathrm{d}\phi\, \mathrm{d}t, \tag{3.1.10}$$

and

$$p\left(r, \phi, z, t\right) = \frac{1}{(2\pi)^3} \sum_{m=-\infty}^{\infty} \left(\int_{-\infty}^{\infty}\int_{-\infty}^{\infty} \widetilde{p}_m\left(r, k_z, \omega\right) \mathrm{e}^{-j(k_z z - \omega t)}\, \mathrm{d}k_z \mathrm{d}t \right) \mathrm{e}^{-jm\phi}. \tag{3.1.11}$$

Note that all the solutions are time harmonic of the convention $e^{j\omega_0 t}$.

Point Source Model

The pressure due to a single monopole (σ) in cylindrical coordinates is given by the Fourier series of inverse transforms

$$p_i^\sigma(r,\phi,z,t) = \frac{1}{(2\pi)^2}\sum_{m=-\infty}^{\infty}\int_{-\infty}^{\infty}\widetilde{p}_{i,m,\sigma}\,\mathrm{e}^{-jk_z z}\mathrm{d}k_z\,\mathrm{e}^{-jm\phi}\,\mathrm{e}^{j\omega_0 t}, \tag{3.1.12}$$

where the transformed pressure is

$$\widetilde{p}_{i,m}^\sigma(r,k_z) = \frac{\pi}{2}Q^\sigma(k_0+k_zM_\infty)\;\mathrm{H}_m^{(2)}(k_r r_>)\mathrm{J}_m(k_r r_<), \tag{3.1.13}$$

and

$$r_> = \begin{cases} r & r>\tau \\ \tau & r<\tau, \end{cases} \tag{3.1.14a}$$

$$r_< = \begin{cases} \tau & r>\tau \\ r & r<\tau. \end{cases} \tag{3.1.14b}$$

The source is located at radial position τ is a temporary variable used in this integral only whereas r is the field position.

This result is derived in McAlpine and Kingan (2012) in dimensional form and need not be re-derived in full. Briefly, the solution was obtained by Fourier methods. In the Fourier domain the wave equation in cylindrical polar coordinates reduces to Bessel's equation, which is where the $\mathrm{H}_l^{(2)}$ and J_l come from. The second kind of Hankel function is chosen to ensure appropriately decaying outwardly propagating waves. The method of variation of parameters is used to solve the inhomogeneous Bessel's equation.

For a source at the centre of the origin the expression reduces to

$$p_i^\sigma(r,\phi,z) = \frac{1}{(2\pi)^2}\int_{-\infty}^{\infty}\widetilde{p}_{i,m}^\sigma\,\mathrm{e}^{-jk_z z}\mathrm{d}k_z, \tag{3.1.15}$$

and

$$\widetilde{p}_{i,m}^\sigma(r,k_z,t) = \frac{\pi}{2}Q^\sigma(k_0+k_zM_\infty)\;\mathrm{H}_0^{(2)}(k_r r). \tag{3.1.16}$$

Only the zero-th term is required because $\mathrm{J}_n(0)\equiv 0$ for $n\in\{\mathbb{Z}|n\neq 0\}$ and $\mathrm{J}_0(0)=1$.

The radial wavenumber of the radiated field, k_r, is given by the dispersion relationship

$$k_r^2 + k_z^2 = (k_0+k_zM_\infty)^2\ , \tag{3.1.17}$$

and equals zero at

$$k_z^- = -\frac{k_0}{1+M_\infty} \quad\text{and}\quad k_z^+ = \frac{k_0}{1-M_\infty}\,. \tag{3.1.18}$$

In the range $k_z^- < k_z < k_z^+$, the wavenumber k_r is real and positive, and corresponds

to wavenumbers which radiate to the far field. Outside of this range, $k_r = -j\gamma$ where $\gamma = \sqrt{k_z^2 - (k_0 + k_z M_z)^2} > 0$, this wavenumber range corresponds to an evanescent field. Accordingly, the integration of the inverse Fourier transform in Equation (3.1.2) is split into three parts as shown in Table 3.1.

Label	Limits		k_r
	lower	higher	
I_1	$-\infty$	k_z^-	$-j\gamma$
I_2	k_z^-	k_z^+	$\sqrt{(k_0 + M_z k_z)^2 - k_z^2}$
I_3	k_z^+	∞	$-j\gamma$

Table 3.1: Breakdown of the inverse Fourier transform integral. The full integral is given by $I_1 + I_2 + I_3$. The value of the wavenumber k_r in each region is specified.

The dispersion relationship leads to a removable singularity when the argument of the Hankel function is equal to zero. The branch cuts are chosen to go from $k_z^{\pm}$ to infinity, this becomes crucial later in Chapter 4. This is shown in Figure (3.3).

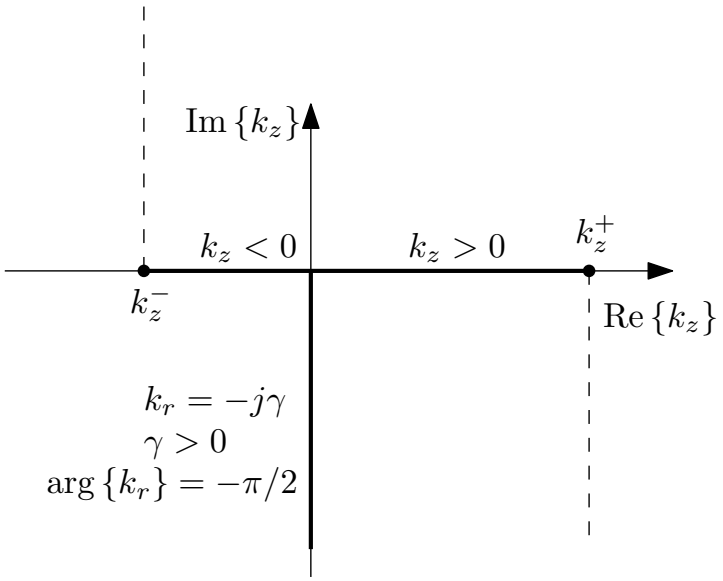

Figure 3.3: Argand diagram of radial wavenumber for real k_z. Branch points at $k_z^{\pm}$ are shown with dots. The branch cuts are shown as dashed lines.

Distributed Source Model

In this section the monopole solution is extended to a distribution to represent a ring and then a spinning mode source. The axial acoustic velocity in a plane of the duct is taken as a source strength for a distribution of monopoles. The method is similar to Tyler and Sofrin (1962) however we make no far-field approximations.

Let a single monopole, σ, be at angular displacement

$$\widehat{\phi} = \phi - \sigma\Delta\psi, \tag{3.1.19}$$

where $\Delta\psi$ is the angular displacement between the equally spaced monopoles, see Figure (3.4). This immediately substitutes into Equation (3.1.12) as

$$p_i^{\sigma}(r,\phi,z) = \frac{1}{(2\pi)^2}\sum_{m=-\infty}^{\infty}\int_{-\infty}^{\infty}\widetilde{p}_{i,m}^{\sigma}\,\mathrm{e}^{-jk_z z}\mathrm{d}k_z\,\mathrm{e}^{-jm(\phi-\sigma\Delta\psi)}. \tag{3.1.20}$$

The source strength Q^{σ} for each monopole is specified by taking the axial particle velocity of the mode (l,q) at the duct termination, so the position of the monopole is $(r,\phi,z) = (\tau,\sigma\Delta\psi,0)$;

$$Q^{\sigma}(\tau,\sigma\Delta\psi,0) = u_{z,lq}(\tau,\sigma\Delta\psi,0)\;\delta A = \xi_{lq}P_{lq}\mathrm{J}_l(\kappa_{lq}\tau)\mathrm{e}^{-jl\sigma\Delta\psi}\,\tau\delta\tau\,\delta\psi, \tag{3.1.21}$$

where $\delta A = \tau\delta\tau\delta\psi$.

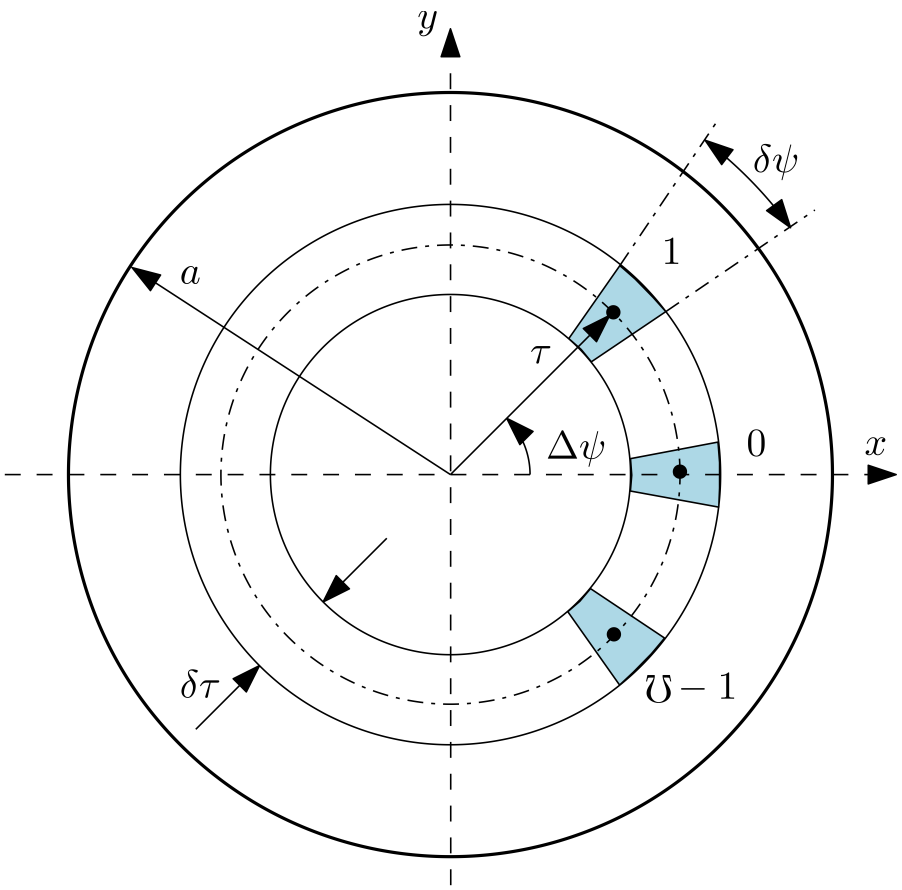

Figure 3.4: A sketch of the finite monopole arrangement. This shows a ring of monopole sources at $r = \tau$.

So for a single monopole (σ) at an angle ($\sigma\Delta\psi$) the transformed pressure is

$$\widetilde{p}_i^{\sigma} = \frac{\pi}{2}\xi_{lq}P_{lq}\mathrm{J}_l(\kappa_{lq}\tau)\mathrm{e}^{-jl\sigma\Delta\psi}(k_0 + k_z M_\infty)\ \mathrm{H}_m^{(2)}(k_r r_>)\mathrm{J}_m(k_r r_<)\,\tau\,\delta\tau\delta\psi. \tag{3.1.22}$$

Initially the solution for a ring source is formulated. The number of monopoles equally angularly spaced (at the same radius, τ) is increased and the space between them is reduced, see Figure (3.4). For $\mho - 1$ monopoles the coherent sum is

$$\widetilde{p}_i^{\mho} = \sum_{\sigma=0}^{\mho-1}\frac{\pi}{2}\xi_{lq}P_{lq}\ \mathrm{e}^{-jl\sigma\Delta\psi}(k_0 + k_z M_\infty)\ \mathrm{H}_m^{(2)}(k_r r_>)\mathrm{J}_m(k_r r_<)\mathrm{J}_l(\kappa_{lq}\tau)\,\tau\delta\tau\delta\psi, \tag{3.1.23}$$

which is evaluated by the standard sum formula

$$\sum_{\sigma=0}^{\mho-1}\mathrm{e}^{-j(l-m)\sigma\Delta\psi} = \frac{\mathrm{e}^{j(l-m)\Delta\psi}\left(1-\mathrm{e}^{-j(l-m)\mho\Delta\psi}\right)}{\mathrm{e}^{j(l-m)\Delta\psi}-1} = \begin{cases} 0 & m \neq l - n\mho \\ \mho & m = l - n\mho \end{cases}, \tag{3.1.24}$$

where n is any integer. This modifies the expression for pressure to

$$p_i^{\mho} = \mho\frac{\xi_{lq}P_{lq}}{8\pi}\sum_{n=-\infty}^{\infty}\int_{-\infty}^{\infty}(k_0 + k_z M_\infty)\mathrm{H}_{l-n\mho}^{(2)}(k_r r_>)\mathrm{J}_{l-n\mho}(k_r r_<)\,\mathrm{J}_l(\kappa_{lq}\tau)\mathrm{e}^{-jk_z z}\,\mathrm{d}k_z$$
$$\mathrm{e}^{-jl\phi}\,\tau\delta\tau\delta\psi. \tag{3.1.25}$$

A continuous ring of monopoles is formed by letting the number of monopoles tend to infinity as the area they occupy tends to zero

$$\lim_{\substack{\Delta\psi\to 0\\ \mho\to\infty}} \mho\,\delta\psi = 2\pi. \tag{3.1.26}$$

The n series represents duplicates in the azimuthal direction of the source. Furthermore, large order asymptotic approximations show that the value of the Bessel functions decrease to zero as the order increases to infinity for a finite argument. Therefore only $n = 0$ terms in the series are sufficient for the solution

$$p_{i,l} = \frac{\xi_{lq}P_{lq}}{4}\int_{-\infty}^{\infty}(k_0 + k_z M_\infty)\mathrm{H}_l^{(2)}(k_r r_>)\mathrm{J}_l(k_r r_<)\mathrm{J}_l(\kappa_{lq}\tau)\,\mathrm{e}^{-jk_z z}\,\mathrm{d}k_z\,\mathrm{e}^{-jl\phi}\,\tau\delta\tau. \tag{3.1.27}$$

This is the solution for a ring source of order l.

To obtain a disc source, for mode (l, q), the solution is integrated from $\tau = 0$ to a

$$p_{i,lq} = \frac{\xi_{lq}P_{lq}}{4}\int_{-\infty}^{\infty}\left((k_0 + k_z M_\infty)\int_{\tau=0}^{a}\mathrm{H}_l^{(2)}(k_r r_>)\mathrm{J}_l(k_r r_<)\mathrm{J}_l(\kappa_{lq}\tau)\tau\ \mathrm{d}\tau\right)\mathrm{e}^{-jk_z z}\,\mathrm{d}k_z\mathrm{e}^{-jl\phi}. \tag{3.1.28}$$

The integral over τ is renamed $\Psi_{lq}^{\flat}$

$$\Psi_{lq}^{\flat} = \int_{\tau=0}^{a} \mathrm{H}_l^{(2)}(k_r r_>)\mathrm{J}_l(k_r r_<)\mathrm{J}_l(\kappa_{lq}\tau)\tau \ \mathrm{d}\tau. \tag{3.1.29}$$

Other authors make far-field approximations, but we maintain the full, exact solution by evaluating the integral exactly

$$\Psi_{lq}^{\flat} = \begin{cases} \mathrm{H}_l^{(2)}(k_r r)\frac{k_r a}{\kappa_{lq}^2 - k_r^2}\mathrm{J}_l(\kappa_{lq}a)\mathrm{J}_l'(k_r a), & r > \tau, \\ \\ \mathrm{J}_l(k_r r)\frac{k_r \tau}{\kappa_{lq}^2 - k_r^2}\mathrm{J}_l(\kappa_{lq}\tau)\mathrm{H}_l^{(2)}(k_r\tau)\Big|_{\tau=0}^{r} + \mathrm{H}_l^{(2)}(k_r r)\frac{k_r a}{\kappa_{lq}^2 - k_r^2}\mathrm{J}_l(\kappa_{lq}\tau)\mathrm{J}_l(k_r\tau)\Big|_{\tau=r}^{a}, & r < \tau. \end{cases} \tag{3.1.30}$$

However, to find the pressure away from the source only requires the $r > \tau$ result[1]. The final solution is the inverse Fourier transform

$$p_{i,lq} = \frac{\xi_{lq} P_{lq}}{4} \int_{-\infty}^{\infty} (k_0 + k_z M_\infty)\mathrm{H}_l^{(2)}(k_r r)\Psi_{lq} \ \mathrm{e}^{-jk_z z} \ \mathrm{d}k_z \ \mathrm{e}^{-jl\phi}, \tag{3.1.31}$$

with

$$\Psi_{lq} = \begin{cases} \frac{k_r a}{\kappa_{lq}^2 - k_r^2}\mathrm{J}_l(\kappa_{lq}a)\mathrm{J}_l'(k_r a), & k_r \neq \kappa_{lq}, \\ \frac{1}{2}\left(a^2 - \frac{l^2}{\kappa_{lq}^2}\right)\mathrm{J}_l^2(\kappa_{lq}a), & k_r = \kappa_{lq}. \end{cases} \tag{3.1.32}$$

For plane waves the integral over the disc reduces to

$$\Psi_{01} = \begin{cases} -\frac{a}{k_r}\mathrm{J}_0'(k_r a), & k_r \neq 0, \\ \frac{1}{2}a^2, & k_r = 0. \end{cases} \tag{3.1.33}$$

To aid discussion and clarity we break the transformed pressure field into a distance component, in this case the Hankel function, and a complex amplitude η with the subscript lq to denote disc source mode

$$p_{i,lq}(\bar{r}, \bar{\phi}, \bar{z}, t) = \int_{-\infty}^{\infty} \widetilde{\eta}_{lq}\mathrm{H}_l^{(2)}(k_r r) \ \mathrm{e}^{-jk_z z} \ \mathrm{d}k_z \ \mathrm{e}^{j\omega_0 t}, \tag{3.1.34}$$

where for a spinning mode the complex amplitude is

$$\widetilde{\eta}_{lq} = \frac{\xi_{lq} P_{lq}}{4}(k_0 + k_z M_\infty)\Psi_{lq} \ \mathrm{e}^{-jl\phi}. \tag{3.1.35}$$

Since the duct itself, and thus the diffraction effect of the duct lip, has been omitted these new solutions are only valid at $\bar{z} > 0$.

[1]The $\tau < r$ solution is evaluated in this chapter only.

3.2 Disc Source Incident Field Method

This section introduces the method. After a discussion on how the theoretical equations are implemented the method is validated by comparing the predictions for a simple monopole case. Furthermore, the method is tested against simple far-field asymptotic predictions.

3.2.1 Description of Method

The method for evaluating Equations (3.1.34) and (3.1.35) is discussed. The expression for the incident field due to the spinning mode is not particularly complicated. However, the integral over the axial wavenumber domain has some quirks that are easiest discussed for this simple expression. For ease of reading, and foresight, only the expression for $r > a$ is discussed.

The inverse Fourier transform integral over the k_z domain is split as shown in Table (3.1). This corresponds to the integral

$$\int_{-\infty}^{\infty} \widetilde{p}_i \, \mathrm{e}^{-jk_z z} \, \mathrm{d}k_z = \underbrace{\int_{-\infty}^{k^-} \widetilde{p}_i \, e^{-jk_z z} \, \mathrm{d}k_z}_{I_1} + \underbrace{\int_{k^-}^{k^+} \widetilde{p}_i \, e^{-jk_z z} \, \mathrm{d}k_z}_{I_2} + \underbrace{\int_{k^+}^{\infty} \widetilde{p}_i \, \mathrm{e}^{-jk_z z} \, \mathrm{d}k_z}_{I_3} . \quad (3.2.1)$$

The integrals I_1 and I_3 are in the evanescent part of the spectrum, an example of the integrand is shown in Figure (3.5).

Large k_z values are in the evanescent part of the spectrum (I_1 and I_3). By replacing the relevant components with their large argument asymptotic approximations

$$\lim_{k_z \to \infty} \mathrm{H}_l^{(2)}(-j\gamma r)\mathrm{J}_l'(-j\gamma a) \propto \lim_{k_z \to \infty} \mathrm{K}_l(\gamma r)\mathrm{I}_l'(\gamma a) \approx \frac{1}{2\pi} \mathrm{e}^{k_r(a-r)} \left(\frac{1}{\sqrt{k_r a}} - \frac{1}{\sqrt{(k_r a)^3}} \right) \to 0. \quad (3.2.2)$$

Because it would be computationally inefficient to integrate from minus to positive infinity, the limits of the integral are appropriately chosen at finite values. As the large argument asymptotic expansion shows, at very large values of of k_z the contribution to the overall integral is negligible. Therefore, the integral is truncated at appropriately large values of k_z until the function becomes significant (larger than a felicitous tolerance). At this value of k_z (plus or minus a safety Δk_z to be extra sure) the limit of integration is set.

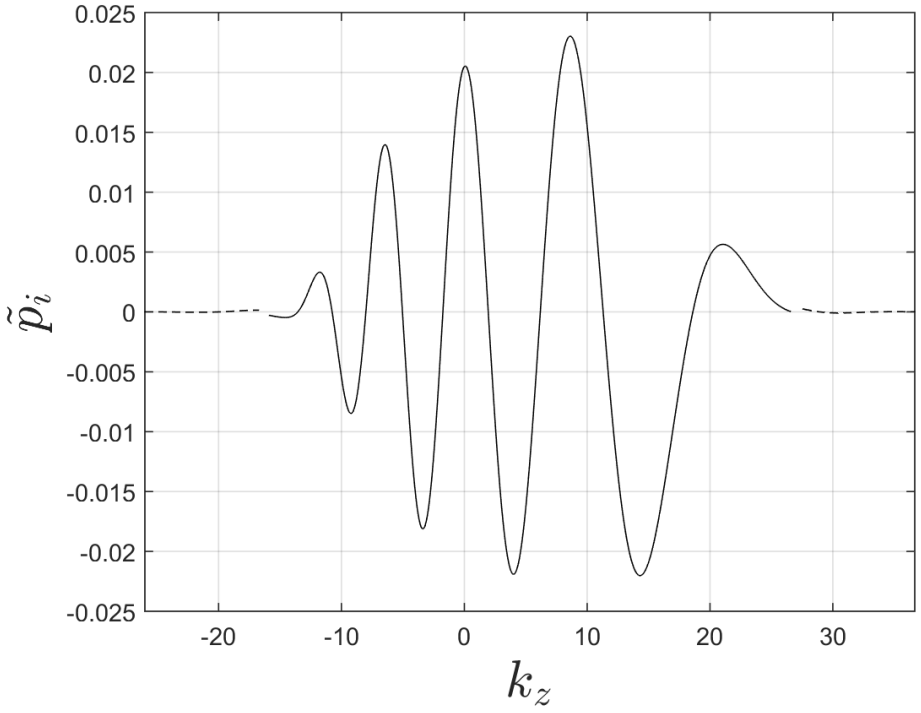

Figure 3.5: The integrand of Equation (3.1.34), I_1 and I_3 are shown in dashed lines. Relevant parameters are: $r = 0.707, z = 0.707$ ($R = 1$ and $\theta = \pi/4^{\text{c}}$) for $k_0 a = 10$, $(l, q) = (4, 1)$ and $M_\infty = 0.75$.

Bessel's function of the first kind is well behaved over the whole domain. However, the Hankel function is singular when the argument is zero, this occurs at $k_z^{\pm}$. However small asymptotic analysis shows that the singularities are removable for $l \neq 0$. The relevant components are

$$\Psi_{lq} \mathrm{H}_l^{(2)}(k_r r) \propto \frac{k_r a}{\kappa_{lq}^2 - k_r^2} \mathrm{J}_l'(k_r a) \mathrm{H}_l^{(2)}(k_r r), \tag{3.2.3}$$

for $l \neq 0$ the limit for small k_r is[2]

$$\lim_{k_r \to 0} \frac{k_r a}{\kappa_{lq}^2 - k_r^2} \frac{\frac{1}{2}\left(\frac{1}{2} k_r a\right)^{l-1}}{(l-1)!} j \frac{(l-1)! \left(\frac{1}{2} k_r r\right)^{-l}}{\pi} = \frac{j}{\pi \kappa_{lq} r^l}, \tag{3.2.4}$$

and for $l = 0$

$$\lim_{k_r \to 0} \mathrm{J}_0(k_r a) \mathrm{H}_0^{(2)}(k_r r) \to j\infty. \tag{3.2.5}$$

The integration is performed by the built-in MATLAB routine *quadgk* which is adaptive and designed to integrate oscillatory functions with singularities on the integration limits.

[2]Note this discussion is for $r > a$.

3.2.2 Validation of Method

In this section the method for computing the incident field is validated. To show that the new code is working correctly, it is benchmarked against simple, established results. Initially the plane wave mode is examined and it is shown to be comparable to a monopole under certain conditions. Secondly the incident field directivity is compared to simple directivity approximations at large observer positions.

Comparison with a monopole point source

In Cartesian coordinates and no flow, the solution to a single monopole at the origin is

$$p_\sigma(\mathbf{x},t) = P^\sigma j k_0 \frac{\mathrm{e}^{-j\mathbf{k}_0\mathbf{x}+j\omega_0 t}}{4\pi|\mathbf{x}|}. \tag{3.2.6}$$

where P^σ is a real amplitude coefficient.

The new disc model can be compared to this solution. To simulate a monopole the plane wave mode $(0,1)$ is chosen. If the radius of the disc is much smaller than the acoustic wavelength of the source then the directivity tends towards omnidirectivity. The complex amplitude of the plane wave mode is

$$\widetilde{\eta}_{01} = \frac{1}{4}(k_0 + k_z M_\infty)\Psi_{01}\ \ \mathrm{e}^{-jl\phi}, \tag{3.2.7}$$

where ξ_{01} has been omitted because it is equal to one. For the zeroth mode and no flow this simplifies to

$$\widetilde{\eta}_{01} = \frac{1}{4}k_0\Psi_{01}. \tag{3.2.8}$$

Figure (3.6) shows that the two normalised predictions are essentially identical. The solutions are plotted against multiples of the disc radius (of 0.01) to show that the radius is small compared to the wavelength, $\lambda/a \approx 126$.

It can be shown that if the radius of the disc is sufficiently small the solution for the distributed source is identical to that of the monopole solution in cylindrical coordinates. Using the small asymptotic arguments the integral over the disc radius is set to a small value

$$\lim_{a\to\iota}\Psi_{01} = \frac{1}{2}\iota^2 + O\left((k_r\iota)^3\right), \tag{3.2.9}$$

where $\iota << 1$.

For the value of Ψ_{01} in Equation (3.2.9) to remain accurate the product $k_r\iota$ also must be small. As ι is very small the maximum real value of $k_r\iota$ is also very small. However in the evanescent field, k_r approaches $j\infty$. As before the Hankel function decays at greater rate than $(k_r\iota)^3$ becomes large.

The plane wave mode solution for a small disc is

$$\widetilde{p}_{i,01} = \underbrace{\pi^2 \frac{1}{2} \iota^2}_{\text{Real amplitude}} \quad (k_0 + k_z M_\infty)\, \mathrm{H}_0^{(2)}(k_r r), \tag{3.2.10}$$

which is identical apart from real amplitude constant to the monopole solution at $r = 0$ given by

$$\widetilde{p}_{i,\sigma} = \underbrace{\frac{\pi}{2} Q_0}_{\text{Real amplitude}} \quad (k_0 + k_z M_\infty)\, \mathrm{H}_0^{(2)}(k_r r), \tag{3.2.11}$$

from Equation (3.1.12). At $r = 0$ the sum drops out because $\mathrm{J}_\ell(0) \equiv 0$ for integer $\ell \neq 0$.

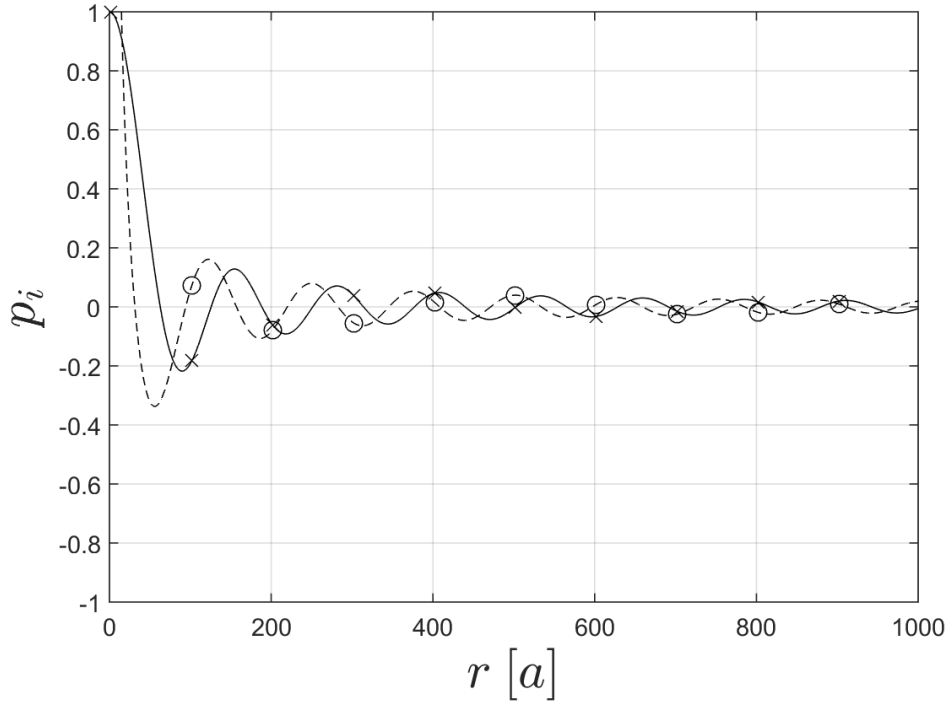

Figure 3.6: The disc source and monopole solutions for $k_0 = 5$ and disc radius of $a = 0.01$. The real part is solid line and the imaginary component is dashed line. The monopole solution is shown with added $\times$ for real and $\circ$ imaginary components. $R \in [0.02, 10]$ and $\phi = \pi/4^{\mathrm{c}}$. Both solutions have been normalised.

Far-Field Comparison

The new source formulation contains no far-field approximations. As such it is more complicated than far-field approximations. Such approximations are used because they are less complex. The new code can be validated against the far field approximations in the far field.

The far-field approximation for a mode radiating from a circular duct is

$$p_{i,ff}\left(R\right) = \frac{P_{lq}}{R} j^{l+1} \kappa_{lq} a \frac{k_0 a \sin\theta}{\left(\kappa_{lq} a\right)^2 - \left(k_0 a \sin\theta\right)^2} \, a \mathrm{J}_l'\left(k_0 a \sin\theta\right) \mathrm{J}_l(\kappa_{lq} a) \, \mathrm{e}^{-j(l\phi + kz)}, \quad (3.2.12)$$

from McAlpine *et al.* (2012). Tyler and Sofrin (1962) derived the far-field radiation for a spinning mode in a duct, and is surmised by McAlpine *et al.* (2012).

Figure (3.7)[3] shows that the near- and far-directivity give very similar results. The example result is for a high frequency of $k_0 a = 40$. As frequency increases the integrand becomes increasingly oscillatory and the numerical integration becomes less accurate. It is therefore encouraging that the results are practically the same.

The results are shown against polar angle at a constant radius of $20a$, equivalent to $127\lambda_0$ which is well away from the source. This value is in the far field, the discussion on this is presented in the next section.

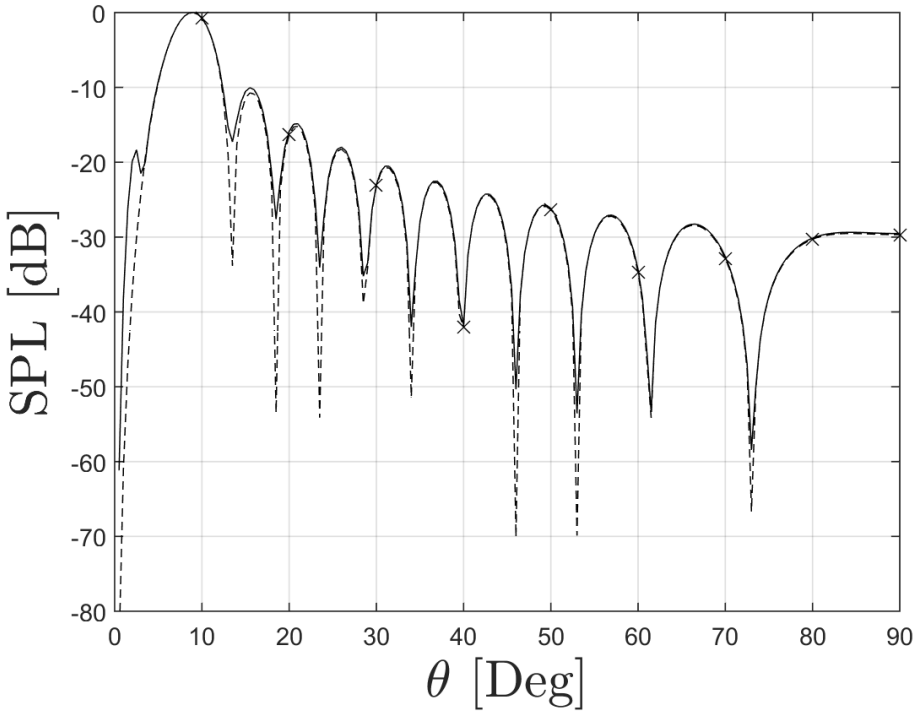

Figure 3.7: The disc source predictions at $R = 20$ (solid line) and the far-field directivity (dashed line, $\times$) are in almost exact agreement. The relevant parameters are: $k_0 a = 40$, $a = 0.5$, $(l, q) = (4, 1)$ and $M_\infty = 0$.

3.2.3 Comparison against Measured Results

In McAlpine *et al.* (2015) the incident field predictions were compared against measured data. The comparisons showed that an incoherent sum over all cut-on mode solutions

[3]All decibel predictions throughout the thesis are normalised, therefore the reference value is 1 Pa and does not need to be included.

compared well against the measurements.

3.3 Source Discussion

So far, the turbofan inlet has been simplified to a cylindrical duct, the pressure field inside is extracted from the duct to formulate the source. In this section the incident field is discussed. The results show that the new, full solution is critical to obtain accurate predictions in the near field. Following, is a discussion on where the far-field for the new source begins. Some of the incident fields of the new source are presented and related to the duct acoustics.

3.3.1 Location and Amplitudes of Principal and Side Lobes

The directivity of a mode radiating from a duct consists of the principal and side lobes. Several methods are available to calculate the angle of the principal lobe. This section shows that only full calculation of the near-field solution leads to accurate principal lobe angle.

For a hollow cylindrical duct, the principal lobe is the first lobe (measured from the duct axis) and always has the largest amplitude; the principle lobe is the global maximum. As the polar angle is increased, side lobes may appear when $k_0 a >> l$. The value of the relative amplitude of these lobes decreases with angle. The results are normalised to the amplitude of the principal lobe.

The far-field for the sound propagating from a duct is given in the previous section, Equation (3.2.12). The far-field directivity is Equation (3.2.12) without the $1/R$ term. The angle of the principal lobe may be found by taking the derivative of the far-field directivity with respect to polar angle and then solving for the angle at which the derivative is zero. The roots of this equation must be found numerically. The derivative of the near-field equation cannot be found analytically. Again the turning point may be found numerically.

Alternatively, in the far-field the angle of the principle lobe was predicted by Rice *et al.* (1979) as

$$\cos\left(\psi_{z,lq}\right) = \sqrt{1 - M_\infty^2} \left\{ \frac{1 - 1/\zeta_{lq}^2}{1 - M_\infty^2 \left(1 - 1/\zeta_{lq}^2\right)} \right\}^{1/2}, \tag{3.3.1}$$

where ζ_{lq} is the cut-off ratio of Equation (3.1.7). Rice collected work from Candel (1973), Homicz and Lordi (1975) and Lansing *et al.* (1970) to derive the above result. A diagram of this angle is shown in Figure (3.1).

The incident fields are shown in Figures (3.8) – (3.11) in the near- and far-field for parameters that will be used later in the thesis. The normalised directivity functions

are shown against polar angle at $R = 2a$ and $R = 100a$. The blue dot on the following figures denote the Rice prediction, the far-field prediction maximum is shown by the red dot and the near-field solution maximum is highlighted by the yellow dot.

Figure (3.8) shows the incident field for a reasonably low frequency of $k_0 a = 10$ and $(l, q) = (4, 1)$. For this mode and frequency the mode is reasonably cut-on. The principal angle predicted by Rice, Equation (3.3.1), is about 32°. The maximum of the near- and far-field directivities are close, as the lobe is wide. The $\psi_{z,lq}$ value under predicts the actual maximum in the near-field by ten degrees and the near-field maximum by 7°.

The near-field prediction differs significantly to the far-field directivity at angles above the principal angle. The maximum difference between the two predictions is around 30 dB. This occurs at the null in the directivity.

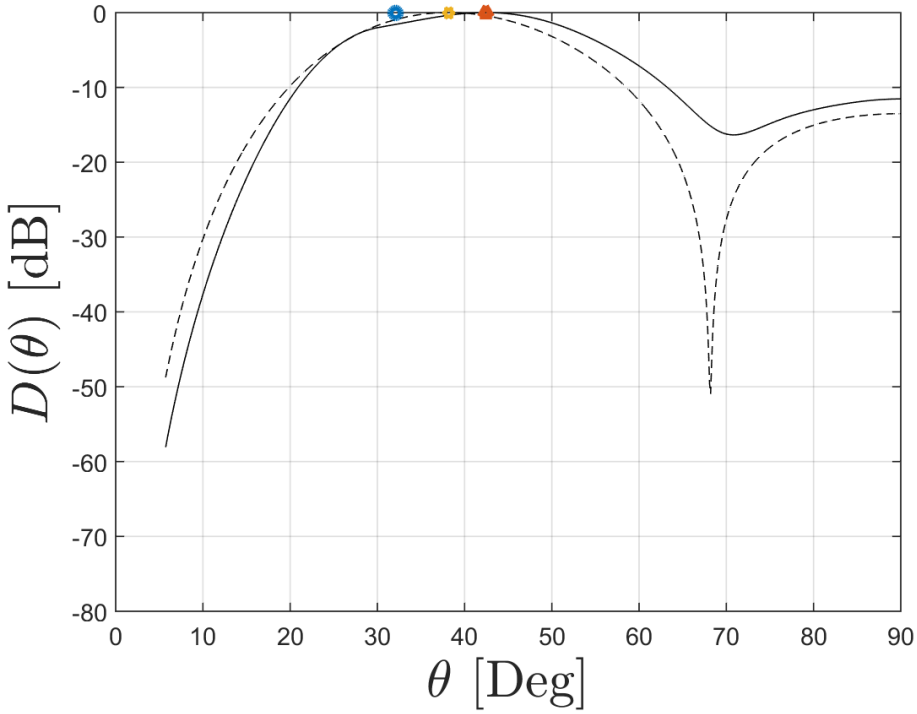

Figure 3.8: Disc source at $R = 2a$ (solid line) and the far-field directivity (dashed line) at a low frequency of $k_0 a = 10$, $a = 0.5$, $(l, q) = (4, 1)$ with $M_\infty = 0$.

The frequency has been increased in Figure (3.9) with all other variables kept constant. The mode is very cut-on, with a principal angle of roughly 18° for both predictions in the near and far field. Again the Rice formula under predicts by about 5° for these parameters. The principal lobe angle has decreased because the modal radial wavenumber, κ_{lq} has not changed as this is determined by the radius of the duct, but the axial and resultant wavenumber have increased.

At the higher frequency the number of side lobes has increased. This is because the $k_0 a$ value has increased to be much larger than l. At low values the source becomes

omnidirectional.

The difference between the near- and far-field directivities is more than 5 dB at angles greater than the principal lobe angle. Apart from the relative amplitude difference the angular location of the turning points of the side lobes are greater for the near-field predictions. The difference is 5° at the fourth lobe.

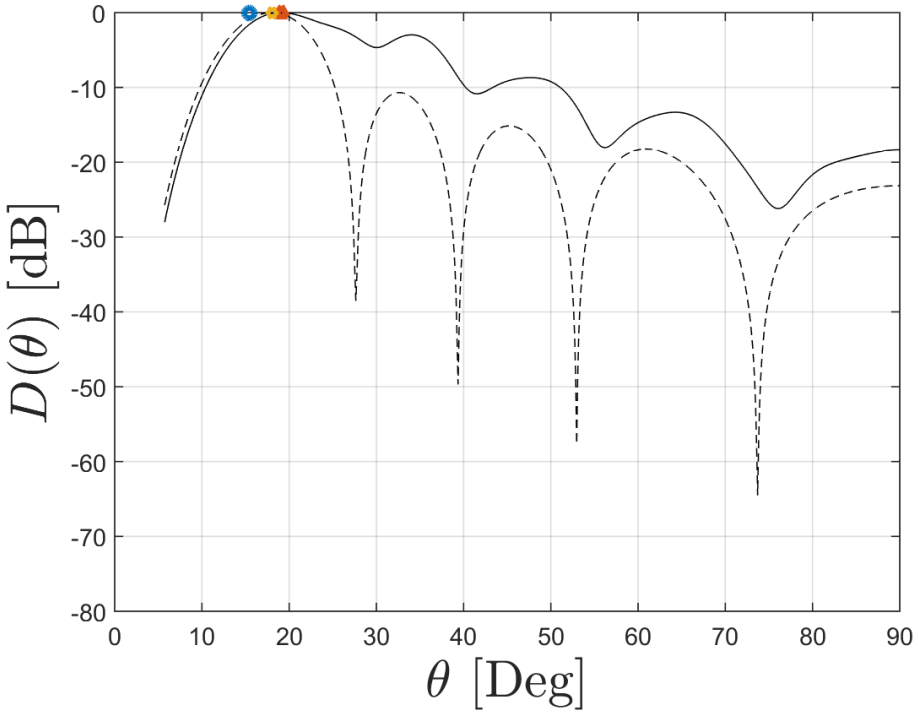

Figure 3.9: Disc source at $R = 2a$ (solid line) and the far-field directivity (dashed line) at a high frequency of $k_0 a = 20$, $a = 0.5$, $(l, q) = (4, 1)$ with $M_\infty = 0$.

The flow velocity has been increased in Figure (3.10) from quiescent flow to $M_\infty = 0.75$. The sound is propagating against the flow. The convective effect means that the axial wavenumber increases (wavelength decreases) and as such the $k_z^+ a$ value increases. This does not change the angle of the principal lobe significantly. However, for this mode the increase in $k_z^+ a$ has resulted in 4 extra side lobes. As before, the angular position and relative amplitudes are significantly different between directivities in the near and far field.

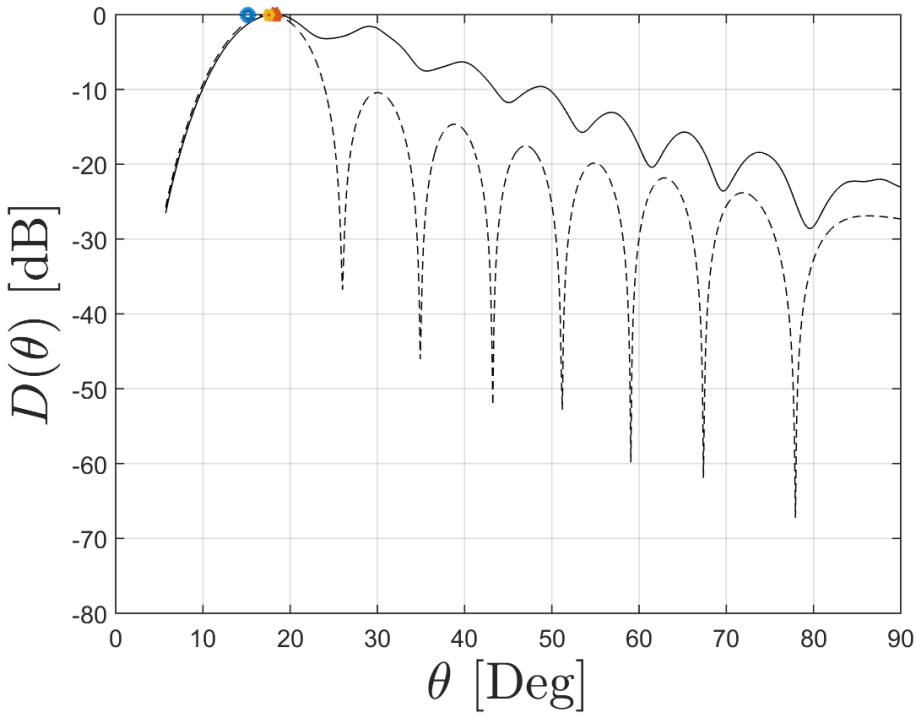

Figure 3.10: Disc source at $R = 2a$ (solid line) and the far-field directivity (dashed line) at a frequency of $k_0 a = 20$, $a = 0.5$, $(l, q) = (4, 1)$ with flow increased to $M_\infty = 0.75$.

The azimuthal mode has increased in Figure (3.11) from $(l, q) = (4, 1)$ to $(24, 1)$. At this high frequency the mode is only just cut-on. This means that the principal lobe has increased to 75°. Despite the high frequency no side lobes are present; although $k_0 a$ is larger, l is also large. The predictions are similar between the directivities in the near and far field.

At this high azimuthal value the radial wavenumber is high. The phase speed in the radial direction is low. Mathematically, in the far-field the directivity is proportional to the derivative of the Bessel's equation. The derivative stays zero with increasing argument for longer as order is increased.

This short section has introduced the incident field of the disc source. It has been demonstrated that the mode angle of Rice *et al.* (1979) and the far-field predictions are not sufficient for accurate predictions for the angle of the principal lobe.

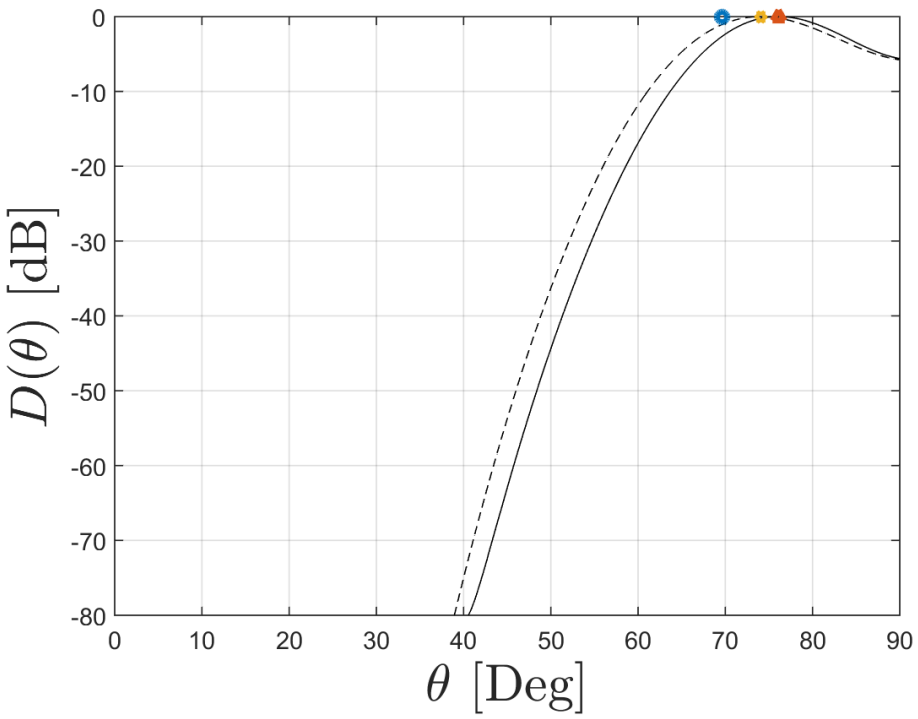

Figure 3.11: Disc source at $R = 2a$ (solid line) and the far-field directivity (dashed line) for the mode $(24, 1)$. The other parameters are: $k_0 a = 20$, $a = 0.5$ and $M_\infty = 0.75$.

3.3.2 Near/Far Field

In the following Chapters the source will be radiating with a cylinder in the near field. Therefore it is necessary to show that the more complicated source formulation is required for accurate pressure predictions on the cylinder. To define the difference between the near- and far-field directivities is defined

$$\Delta\,[\mathrm{dB}] = D_\infty - D\,(R). \tag{3.3.2}$$

There are two far fields; the acoustic far-field and a geometrical far field. The acoustic far-field is usually defined as several wavelengths away from a source. For the new disc source of $k_0 a = 20$, the associated wavelength is approximately 0.15. Over the diameter of the source there are approximately $6\lambda_0$. Therefore one side of the source is in the acoustic far-field from the other. The geometric far-field is where the dimensions of a distributed source are negligible.

Figure (3.12) shows the difference between the directivity at $R = 100$ and the directivities nearer the source. The different lines correspond to increasing R at different polar angles. The radiation pattern is shown in Figure (3.8). It shows that the difference between the directivities is negligible for $R > 5$. However nearer the source the differences increase to 4 dB.

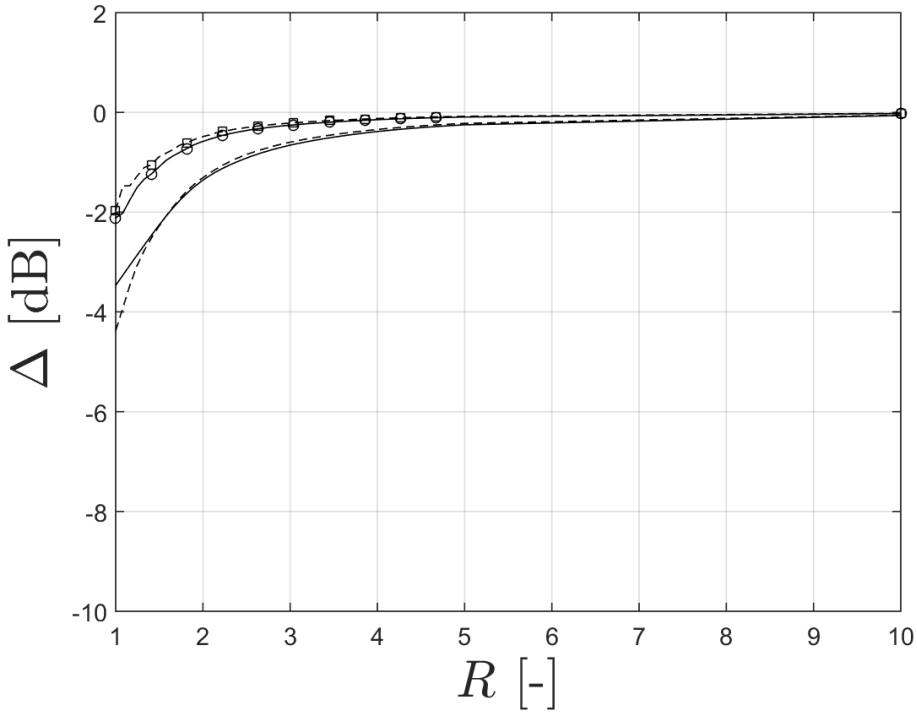

Figure 3.12: The difference (Δ) between near- and far-field values at 45° (solid line), 60° (dashed line), 75° (solid, $\circ$) and 90° (dashed, $\square$). The parameters are: $k_0 a = 10$, $a = 0.5$, $(l, q) = (4, 1)$ and $M_\infty = 0.75$.

Under the same conditions but at a higher frequency of $k_0 a = 20$ the difference Δ is shown in Figure (3.13). The difference is larger than the lower frequency in Figure (3.12) for small values of R. For $R > 6$ the difference is negligible.

The frequency effect is not large. This confirms that the geometric far-field is the relevant one. The far-field begins at $R > 6a_0$ or $12a$. This is true regardless of the source frequency because very low frequency modes cut-off and aeroacoustic applications are mostly concerned with frequencies similar to the blade passing frequencies. This frequency is relatively high.

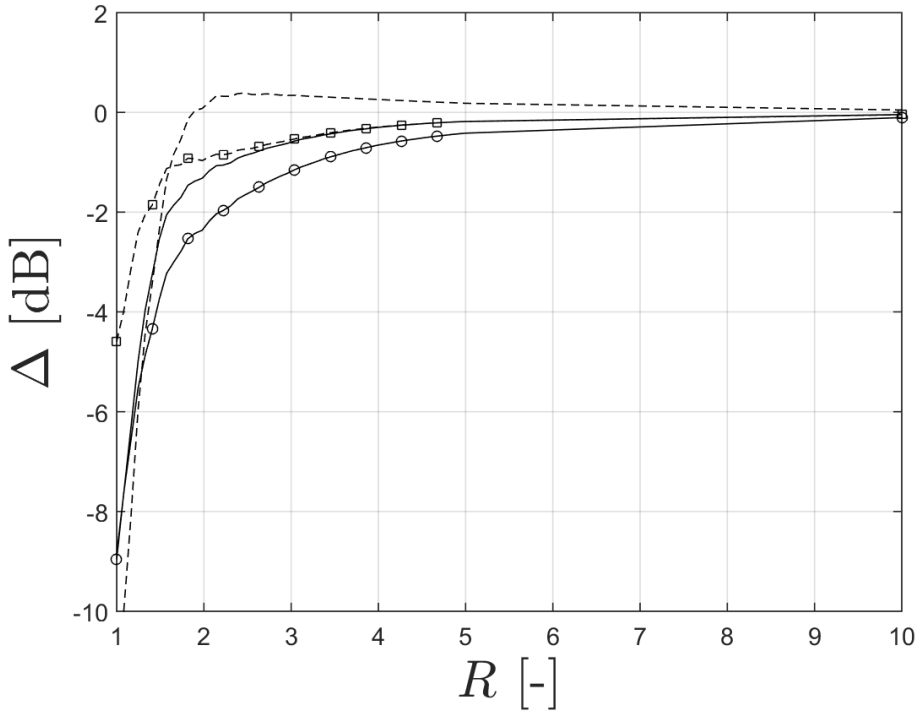

Figure 3.13: The difference (Δ) between near- and far-field values at 45° (solid line), 60° (dashed line), 75° (solid, $\circ$) and 90° (dashed, $\square$). The parameters are: $k_0 a = 20$, $a = 0.5$, $(l, q) = (4, 1)$ and $M_\infty = 0.75$.

However, as ascertained in the previous section, the difference in the directivities are greatest in the nulls of the directivity pattern. The difference between the first null and the second lobe are compared in Figure (3.14). The source is the same as Figure (3.13). For the lobe maximum, the difference is reasonably small over the range. The non-zero values of Δ arises from the change in angular displacement of the lobe discussed in the previous section. At the null the difference is significant over the whole range.

Mathematically, the reason that the near- and far-field predictions are different is due to the contributions of I_1 and I_2. For the near-field variables shown in Figure (3.13) at $\theta = 45°$, I_1 and I_3 contribute about 6% of the overall integral. At $R = 10$ these integrals only contribute 7×10^{-10}% of the total integral. Physically, these two integrals correspond to the evanescent field, so naturally do not propagate to the far field.

The results in this section show that the directivity of the source changes as a function of radial distance and that it is very important to use the new, full solution for installation effect predictions. If the far-field predictions were used, the position and the relative amplitude of the side lobes would be wrong. The side lobes and nulls need to be accurate. Once the source is installed adjacent to the cylinder the side lobes are nearest to the source and are thus most susceptible to the near-field affects. Additionally, if the far-field approximations were used then the nulls would be at a significantly lower amplitude than they actually are. As under predictions are potentially more damaging than over

predictions, it is therefore critical to use the near-field solutions in installation problems.

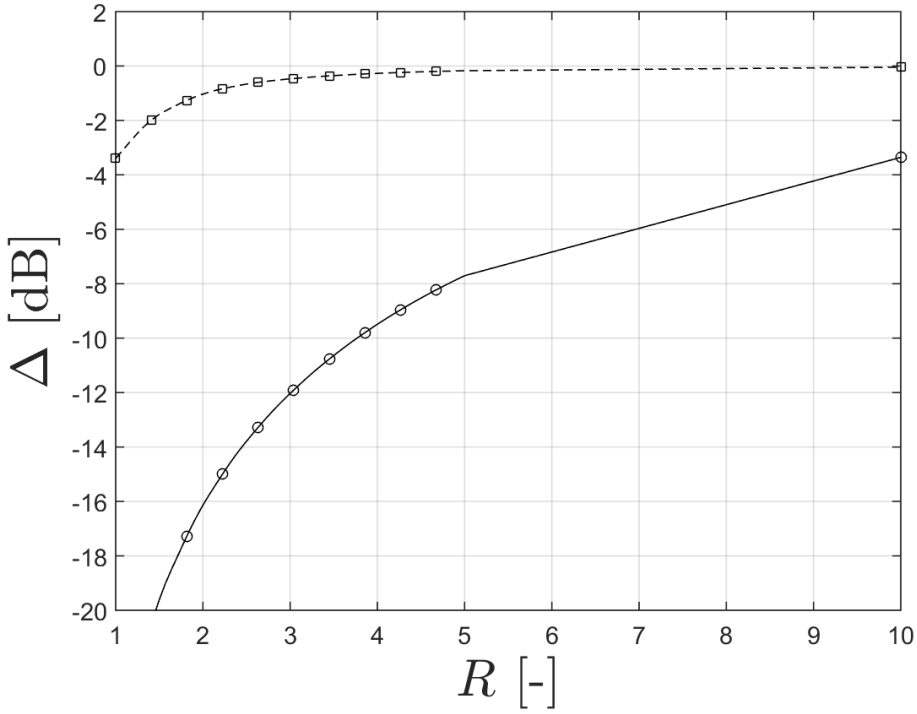

Figure 3.14: The difference between far- and near-field (Δ) values at the maximum of the far-field side lobe (dashed line) and the minimum of the first null (solid line). The parameters were: $k_0 a = 20$, $a = 0.5$, $(l, q) = (4, 1)$ and $M_\infty = 0.75$.

3.4 Chapter Summary

This chapter started by formulating the source representative of a turbofan. By approximating the turbofan inlet as a semi-infinitely long cylindrical duct the noise source can be represented as spinning duct mode. A new source was formed by

- truncating the duct to represent the inlet,
- taking the pressure field and using the associated axial velocity for a mode,
- imposing it on a distribution of monopoles,
- integrating over the disc without any far-field approximations.

In formulating the source Objective 2 has been met.

The expressions for the types of source at the origin are expressed in the inverse Fourier transform and the zero-th order of the series

$$p_i(r, \phi, z) = \frac{1}{(2\pi)^2} \int_{-\infty}^{\infty} \widetilde{p}_i \, \mathrm{e}^{-jk_z z} \, \mathrm{d}k_z, \tag{3.4.1}$$

where the transformed pressure is further split into a complex amplitude η and a propagation function

$$\widetilde{p}_i = \widetilde{\eta}_i \, f(r). \tag{3.4.2}$$

For the sources used in this thesis the complex amplitude and propagation are summarised in Table (3.2). Note that sum over m has not been included because all the sources are at the origin and $m \neq 0$ orders are identically zero.

Type of Source	Subscript, $i =$	Complex amplitude, $\widetilde{\eta}_i$	$f(r)$
Single monopole	σ	$(\pi/2)Q^{\sigma}\,(k_0 + k_z M_{\infty})$	$\mathrm{H}_0^{(2)}(k_r r)$
Ring (order l)	l	$\pi^2 \xi_l P_l \,(k_0 + k_z M_{\infty})\,\mathrm{J}_l(k_r \eta)\mathrm{J}_l(\kappa_l \eta)\mathrm{e}^{-jl\phi}$	$\mathrm{H}_l^{(2)}(k_r r)$
Mode (l, q)	lq	$\pi^2 \xi_{lq} P_{lq}\,(k_0 + k_z M_{\infty})\,\Psi_{lq}\mathrm{e}^{-jl\phi}$	$\mathrm{H}_l^{(2)}(k_r r)$

Table 3.2: The complex amplitude and propagation function for the sources used in the thesis for $\tau = 0$.

The implementation of the resulting equations was then discussed. The radiation of the incident field was discussed. It was shown that

- with a very small disc and plane wave mode, the solution converges to a monopole solution in quiescent flow,
- the new formulation matches the far-field approximations very well,
- in the geometric near-field the angular position and relative amplitudes values for side lobes are different depending on the distance from the source,
- the levels of the nulls in the directivities are extremely different depending on the distance from the source.

Far-field approximations for the frequencies and modes relevant to aeroacoustics are not accurate for values for $R < 6$ (or $12a$). This discussion fulfilled Objective 3.

Chapter 4

Duct Source Incident Field Theory

In the analysis up to this point, the diffraction at the duct termination has been neglected. As such, the disc source is only valid in the forward arc. The aim of this chapter is to include the diffraction effect of the duct lip on the radiated field and thus extend the solution to all polar angles. To achieve this aim, the Wiener–Hopf method is used to model a spinning mode exiting from a semi-infinite circular duct of infinitesimal wall thickness. Although this theory is not new, a concise derivation is presented for nomenclature continuity and to aid discussion in later chapters.

The resulting equations are implemented by the established in-house code GXMunt. This code is adapted later in the thesis, so the implementation of the method is discussed. The discussion focuses on sign convention and branch cut location. To quantify the effect of diffraction in the near-field the disc source (lq) and duct model (d, lq) are compared for the relevant parameters used throughout the thesis. Quantifying the duct effect in the near-field has not previously been investigated.

4.1 Brief Theory of Wiener–Hopf

The derivation presented here for a mode radiating from a duct is based on Gabard and Astley (2007), there are several differences between this derivation and the one presented here. This derivation uses pressure, not velocity potential, for nomenclature continuity. Velocity potential is required to model the vortex shedding, but the problem presented is an inlet problem vortex shedding is not relevant. Another difference is that the opposite time convention is used here, this means the final solution of one method is the complex conjugate of the other. Finally, uniform flow is assumed everywhere. Physically, this is a reasonable assumption for the inlet problem.

4.1.1 Problem Set-up

This section outlines the geometry and boundary conditions before the Wiener–Hopf technique is applied to solve the problem. The geometry is shown in Figure (4.1).

Initially, a mode propagating against the flow in a circular, rigid duct takes the form

$$p_{i,lq} = P_{lq}\mathrm{J}_l(\kappa_{lq}r)\,\mathrm{e}^{-j(l\phi+k_{z,lq}z)}\,\mathrm{e}^{j\omega_0 t}, \qquad \forall z \text{ and } 0<r<a, \tag{4.1.1}$$

where all the symbols have the same meaning as defined in Chapter 3. For brevity P_{lq} is unity and omitted from the analysis along with $\mathrm{e}^{j\omega_0 t}$. The problem is formulated such that the mode propagates on axis from negative to positive infinity.

The problem is axisymmetric, therefore the diffracted field $(diff, lq)$ will take the same azimuthal form as the incident mode

$$p_{diff,lq} = \Lambda_{lq}(r,z)\,\mathrm{e}^{-jl\phi}, \qquad \forall z \text{ and } r>0, \tag{4.1.2}$$

where Λ_{lq} is to be determined.

The total field is a superposition of the mode in the duct and the diffracted field, so takes the form

$$p_{d,lq} = \left[\Lambda_{lq}(r,z) + \mathrm{J}_l(\kappa_{lq}r)\,\mathrm{e}^{-jk_{z,lq}z}\right]\mathrm{e}^{-jl\phi}, \qquad r>0. \tag{4.1.3}$$

To find Λ_{lq} the boundary conditions are used. From the non-dimensional momentum equation, for all of z on $r=a$ the pressure radial derivative is equal

$$-\frac{\mathrm{D}_0}{\mathrm{D}t}u_r = \frac{\partial p_{d,lq}(a^-)}{\partial r} = \frac{\partial p_{d,lq}(a^+)}{\partial r}, \qquad \forall z, \tag{4.1.4}$$

where the superscript $-$ denotes approaching a from the inside of the duct, and $+$ the outside. The walls have infinitesimal thickness so $\lim_{r\to a^-} r = \lim_{r\to a^+} r = a$. Furthermore, on the rigid duct wall the derivative is zero

$$-\frac{\mathrm{D}_0}{\mathrm{D}t}u_r = \frac{\partial p_{d,lq}(a^-)}{\partial r} = \frac{\partial p_{d,lq}(a^+)}{\partial r} = 0, \qquad z\leqslant 0, \tag{4.1.5}$$

and in front of the duct is pressure continuity in the total field

$$p_{d,lq}(a^-) = p_{diff,lq}(a^-) + p_{i,lq}(a^-) = p_{diff,lq}(a^+) = p_{d,lq}(a^+), \qquad z>0. \tag{4.1.6}$$

This is not true for either side of the duct boundary. On the duct, the incident field is the sum of the propagating mode and the diffracted field

$$p_{diff,lq}(a^+) + p_{i,lq}(a^-) \neq p_{diff,lq}(a^+), \qquad z<0. \tag{4.1.7}$$

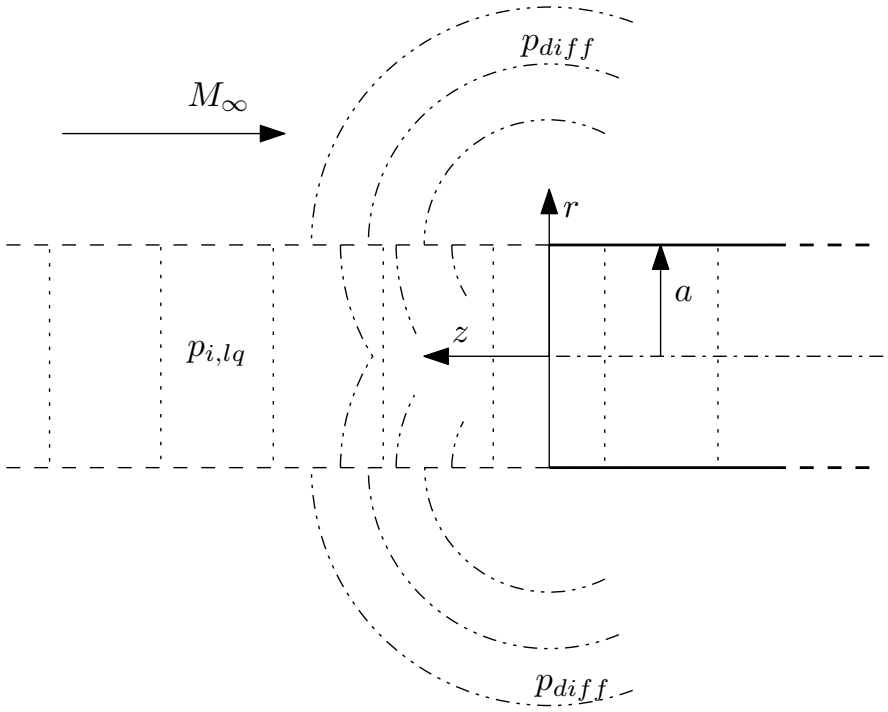

Figure 4.1: A schematic of the diffraction problem. The mode is represented by dots and the diffracted field is represented by dot-dot-dashes. Showing a discontinuity at a in the incident (i, lq) and diffracted field $(diff)$.

Therefore, to maintain continuous pressure the diffracted field must be discontinuous at a. This must lead to a pressure jump in the diffracted field

$$\Delta p_{diff,lq} = p_{diff,lq}(a^-) - p_{diff,lq}(a^+) = p_{i,lq}(a^-), \qquad z > 0. \tag{4.1.8}$$

This is especially prudent because the pressure on the inside of the incident field is known due to the prescribed, analytic mode shape and may be calculated.

Solving the Problem

As before, Fourier methods are used to reduce the wave equation to an ODE. In the work leading up to this chapter, the axial wavenumber was real, this leads to wholly real or imaginary radial wavenumbers. For the diffraction problem the wavenumber is now complex, i.e.

$$k_z = \Re\{k_z\} + j\Im\{k_z\} = |k_z|\, \mathrm{e}^{j\epsilon}, \tag{4.1.9}$$

where $-\pi/2 \leqslant \epsilon \leqslant 0$ which leads to complex radial wavenumbers.

To take account of the mixed boundary conditions on $r = a$ the axial Fourier transform is split at the duct termination

$$\widetilde{p}^-(k_z) = \int_{-\infty}^{0} p_{d,lq}(z)\, \mathrm{e}^{jk_z z}\, \mathrm{d}z \quad \text{and} \quad \widetilde{p}^+(k_z) = \int_{0}^{\infty} p_{d,lq}(z)\, \mathrm{e}^{jk_z z}\, \mathrm{d}z, \tag{4.1.10}$$

so the full transform is

$$\widetilde{p}_{d,lq} = \widetilde{p}^{-} + \widetilde{p}^{+}. \tag{4.1.11}$$

The other transforms are the same as before, Equations (3.1.10) on page 29.

Upon Fourier transformations the convected wave equation simplifies to Bessel's equation, the solutions are chosen, again, as

$$\widetilde{p}_{d,lq} = \begin{cases} A(k_z)\,\mathrm{H}_l^{(2)}(k_r r), & r > a, \\ B(k_z)\,\mathrm{J}_l(k_r r), & r < a. \end{cases} \tag{4.1.12}$$

The radial wavenumber is now factorised to

$$k_r = k_r^- k_r^+ = (k_0 - k_z(M_\infty - 1))^{1/2}(k_0 - k_z(M_\infty + 1))^{1/2}, \tag{4.1.13}$$

which are equal to zero, and thus lead to branch points, at $k_z^{\pm}$. The branch cuts are the same as shown in Figure (3.3) on page 31.

The transform of the acoustic velocity on a, labelled F, simplifies to the half transform

$$F_+(k_z) = \int_0^\infty u_r\,\mathrm{e}^{jk_z z}\,\mathrm{d}z, \tag{4.1.14}$$

because the particle velocity, and thus F_-, is zero on the rigid duct.

From Equation (4.1.12), on the outside of the duct wall (a^+) the pressure derivative and acoustic pressure is

$$-j(k_0 + k_z M_\infty)F_+(k_z) = A(k_z)\,k_r \mathrm{H}_l^{(2)\prime}(k_r a), \tag{4.1.15}$$

and on the inside (a^-)

$$-j(k_0 + k_z M_\infty)F_+(k_z) = B(k_z)\,k_r \mathrm{J}_l'(k_r a). \tag{4.1.16}$$

The task at hand is to obtain $A(k_z)$ and $B(k_z)$ by deriving an expression for F_+.

The transform of the pressure jump of the diffracted field (Equation (4.1.1)) is

$$G(k_z) = \widetilde{\Delta p}_{diff,lq} = \int_{-\infty}^{\infty} \left[p_{diff,lq}(a^+) - p_{diff,lq}(a^-)\right]\,\mathrm{e}^{jk_z z}\,\mathrm{d}z, \tag{4.1.17}$$

which is

$$G\,(k_z) = A(k_z)\,\mathrm{H}_l^{(2)}(k_r a) - B(k_z)\,\mathrm{J}_l(k_r a). \tag{4.1.18}$$

The pressure is continuous in front of the inlet and the positive component of G can be evaluated analytically

$$G_+(k_z) = \int_0^\infty \mathrm{J}_l(\kappa_{lq} r)\,\mathrm{e}^{-jk_{z,lq}z}\,\mathrm{e}^{jk_z z}\,\mathrm{d}z = j\frac{\mathrm{J}_l(k_r a)}{k_{z,lq} - k_z}. \tag{4.1.19}$$

Next, substituting for $A(k_z)$ and $B(k_z)$ from Equations (4.1.15) and (4.1.16)

$$G\left(k_z\right) = G_-(k_z) + G_+(k_z) = \frac{F_+}{k_r} K, \tag{4.1.20}$$

where the kernel K is

$$K\left(k_z\right) = j(k_0 + k_z M_\infty)\left(\frac{\mathrm{H}_l^{(2)}(k_r a)}{\mathrm{H}_l^{(2)\prime}(k_r a)} - \frac{\mathrm{J}_l(k_r a)}{\mathrm{J}_l'(k_r a)}\right). \tag{4.1.21}$$

The functions will be factorised into analytic and non-analytic functions in the upper and lower half planes. So factorise K to positive and negative functions

$$K = \frac{K_+}{K_-} \tag{4.1.22}$$

where K_+ is regular in the upper half plane and K_- is regular in in the lower half plane. When substituted into Equation (4.1.20) this gives

$$G_-(k_z) K_- k_r^- + G_+(k_z) K_- k_r^- = \frac{F_+}{k_r^+} K_+. \tag{4.1.23}$$

In order to ensure that G_+ term (and thus the L.H.S) is regular in the negative plane, Equation (4.1.23) is modified as follows

$$G_-(k_z) K_- k_r^- + G_+(k_z) K_- k_r^- - k_r^-(\kappa_{lq}) K_-(\kappa_{lq}) G_+(k_z) = \frac{F_+}{k_r^+} K_+ - k_r^-(\kappa_{lq}) K_-(\kappa_{lq}) G_+(k_z). \tag{4.1.24}$$

Using Liouville's theorem (see Noble (1958)) both sides of Equation (4.1.24) are equal to a constant, say E. Let $E(k_0) = -k_r^-(\kappa_{lq}) K_-(\kappa_{lq}) G_+(k_0)$ so that F_+ may be found as

$$F_+(k_z) = -k_r(\kappa_{lq}) \frac{K_-(\kappa_{lq})}{K_+(k_z)} \left[G_+(k_0) - G_+(k_z)\right]. \tag{4.1.25}$$

Using the method in Gabard and Astley (2006) shown in their Appendix A, $K_\pm$ can be evaluated. The constants for the Bessel's functions are now

$$A(k_z) = -j(k_0 + k_z M_\infty) \frac{F_+}{k_r \mathrm{H}_l^{(2)\prime}(k_r a)}, \tag{4.1.26}$$

$$B(k_z) = -j(k_0 + k_z M_\infty) \frac{F_+}{k_r \mathrm{J}_l'(k_r a)}, \tag{4.1.27}$$

so the transformed pressure is

$$\widetilde{p}_{d,lq}\left(k_z\right) = -j(k_0 + k_z M_\infty) \frac{F^+}{k_r} \begin{cases} \frac{\mathrm{H}_l^{(2)}(k_r r)}{\mathrm{H}_l^{(2)\prime}(k_r a)} & r > a, \\ \frac{\mathrm{J}_l(k_r r)}{\mathrm{J}_l'(k_r a)} & r < a. \end{cases} \tag{4.1.28}$$

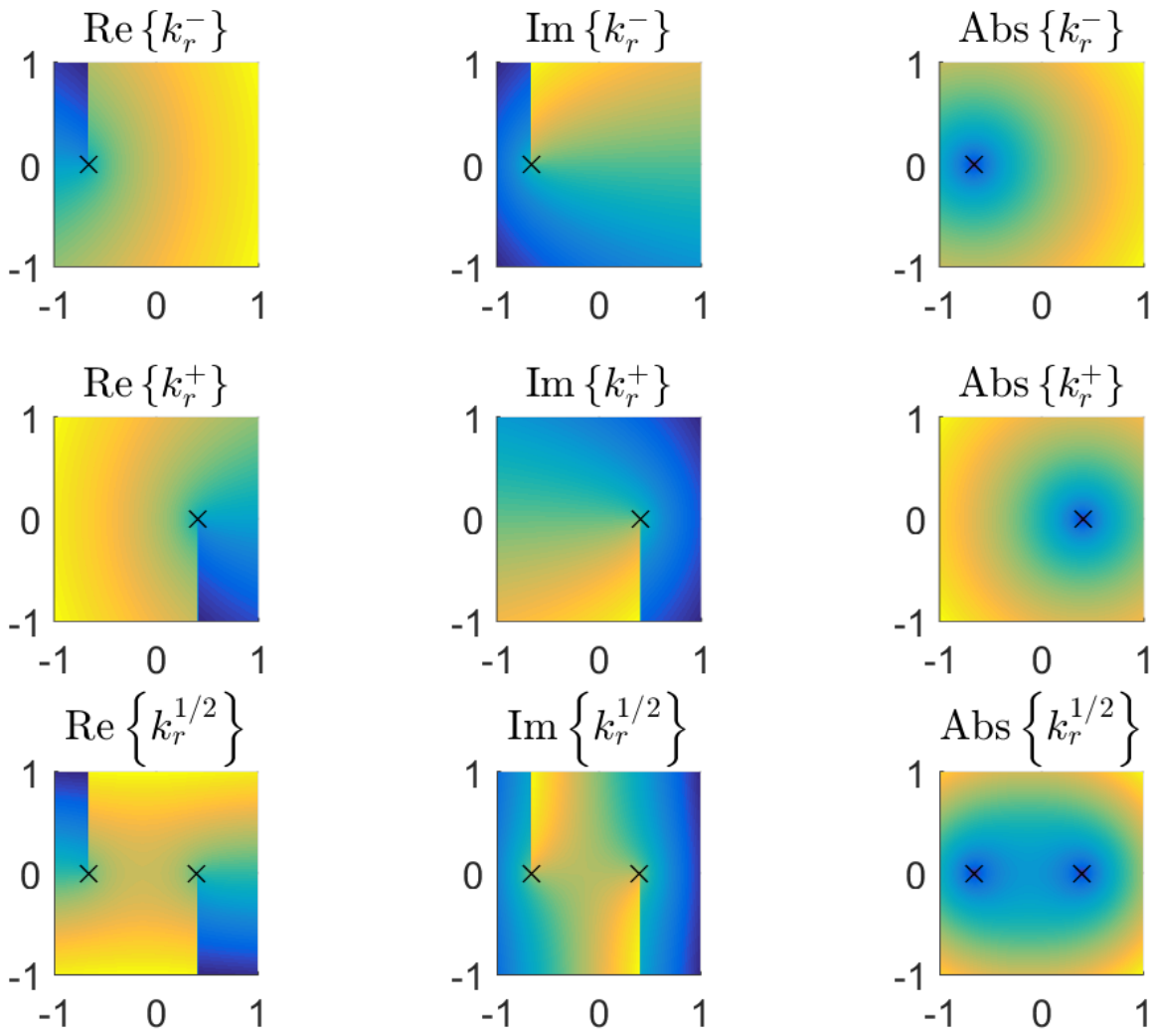

Figure 4.2: k_r in the complex plane. $k_0 = 0.5$ and $M_\infty = 0.25$.

The pressure is then the inverse Fourier transform of Equation (4.1.28) which is

$$p_{d,lq}(r,z,\phi) = -\frac{j}{2\pi}\begin{cases} \int_{-\infty}^{\infty} \frac{(k_0+k_zM_\infty)F_+}{k_r\mathrm{H}_l^{(2)\prime}(k_ra)}\,\mathrm{H}_l^{(2)}(k_rr)\,\mathrm{e}^{jk_zz}\,\mathrm{d}k_z\,\mathrm{e}^{-jl\phi}, & r>a, \\ \int_{-\infty}^{\infty} \frac{(k_0+k_zM_\infty)F_+}{k_r\mathrm{J}_l'(k_ra)}\,\mathrm{J}_l(k_rr)\,\mathrm{e}^{jk_zz}\,\mathrm{d}k_z\,\mathrm{e}^{-jl\phi}, & r<a. \end{cases} \tag{4.1.29}$$

Note the expressions preceding $\mathrm{e}^{-jl\phi}$ are equal to Λ_{lq} from Equation (4.1.1).

For the installed duct the expression required is

$$p_{d,lq}(r,z,\phi,t) = -j\frac{P_{lq}}{2\pi}\int_{-\infty}^{\infty} \frac{(k_0+k_zM_\infty)F_+}{k_r\mathrm{H}_l^{(2)\prime}(k_ra)}\,\mathrm{H}_l^{(2)}(k_rr)\,\mathrm{e}^{jk_zz}\,\mathrm{d}k_z\,\mathrm{e}^{-jl\phi}\,\mathrm{e}^{j\omega_0t}, \tag{4.1.30}$$

where the real valued modal amplitude constant P_{lq} has been reintroduced.

The integration contour is in a strip such that all the functions (including the + and − components) are analytic, in practice this is along the contour Γ as defined in Gabard and Astley (2006). In the Fourier domain, the directivity of the radiation is enveloped by all the functions preceding the Hankel function. The Hankel function is related to propagation.

This discussion has focused on a hollow duct with uniform flow. This simplification was done for readability and this thesis prioritises inlet applications. However it is trivial to adapt the theory to an annular duct. The form of the final solution does not change; the only change to the implemented expressions is in Equation (4.1.21). This would be modified to

$$K = (k_0 + k_z M_\infty) \left(\frac{\mathrm{Y}'_l(k_r h)\,\mathrm{J}_l(k_r a) - \mathrm{J}'_l(k_r h)\,\mathrm{Y}_l(k_r a)}{\mathrm{Y}'_l(k_r h)\,\mathrm{J}'_l(k_r a) - \mathrm{J}'_l(k_r h)\,\mathrm{Y}'_l(k_r a)} - \frac{\mathrm{H}^{(2)}_l(k_r a)}{\mathrm{H}^{(2)\prime}_l(k_r a)} \right), \qquad (4.1.31)$$

where $h = a/a_{inner}$. This is reproduced and adapted from Gabard and Astley (2006) and the analysis would continue as before.

4.1.2 Issues with Implementation

The incident field formulation is now complete. Now attention is focussed on the implementation of the expressions derived in the previous section. The implementation is done in GXMunt, an established in-house code. This code is adapted later in the thesis so a discussion of the simpler free-field case is prudent.

For a real frequency, branch points $k_z^{\pm}$ lie on the real axis. At these points k_r is zero so a singularity is caused by the Hankel function evaluating an argument of zero. The inverse Fourier transform integrates from negative to positive infinity, therefore this integral will cross over the branch point. At the branch point the function is not analytic. The singularities in the disc source were dealt with by the integration routine.

To avoid integrating over the non-analytic points the path of integration can be chosen such that it is slightly displaced from the real axis. Cauchy's integral theorem shows that deforming the contour is equivalent to integrating along the real axis, so long as the integration limits are the same.

Furthermore, the branch cut of a principle square root of a complex number is usually defined to run along the negative real axis. The radial wavenumber is now complex, the branch cut location is of practical importance. To ensure that the integral path is not affected by the branch cuts they can be defined to go to infinity at an angle of $\pm\pi/2$ radians.

Figure (4.2) shows that the branch cuts that were defined in Chapter 3 (Argand digram in Figure (3.3), page 31) but for complex axial wavenumbers. They show the branch cut from k_z^-, at an angle of $\pi/2$ radians which is analytic in the negative complex

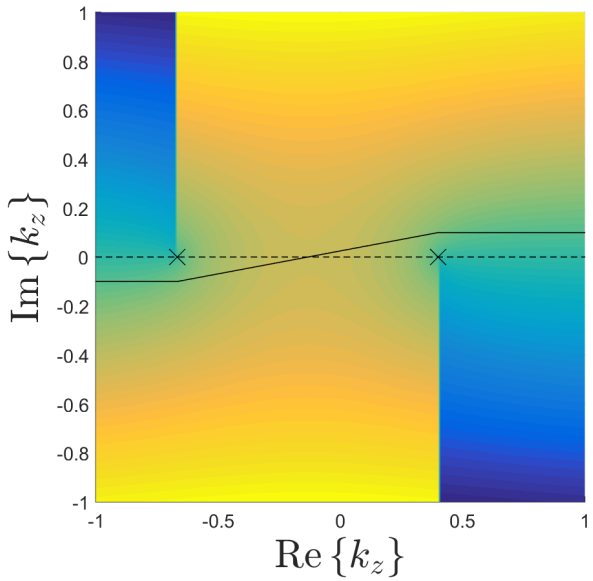

Figure 4.3: An example of deformation of path of integration with the chosen sign convention. $k_0 = 0.5$ and $M_\infty = 0.25$

plane. Contrastingly, the branch cut from k_z^+ at an angle of $-\pi/2$ radians. Hence the contour is deformed into the negative plane for negative k_z and positive plane for positive k_z. By doing this the functions are all analytic.

The $e^{j\omega_0 t}$ convention has been chosen. As such, the path must be deformed into the negative quadrant for negative k_z and is positive for the positive k_z. As well as avoiding the branch cut, the function is not analytic on the other side of the real line. This is shown in Figure (4.3). In practise, this leads to the complex conjugate of Gabard and Astley's (2006) solution to the one presented here.

4.2 Near-Field Effects of the Nacelle Lip

The far-field effects of the nacelle lip on sound radiation are well documented. Hocter (1999) and Homicz and Lordi (1975), for example, showed that the diffraction effect on radiation was negligible below approximately 80° measured from the source axis. However, the near-field effect is not well documented. This section quantifies the diffraction effect of the duct lip in the near field. This is possible using the disc source formulation. As the Wiener–Hopf method is more complicated, it is strange this has not been quantified in previous work. The coordinates system employed in this section is spherical polar coordinates.

Predictions between the two methods are shown in Figures (4.5) – (4.10). The variables are the same as some of the examples shown in the previous chapter. All predictions and differences are evaluated along a line or at a point shown in Figure (4.4). Initially the effect of frequency is analysed, followed by the radial distance and

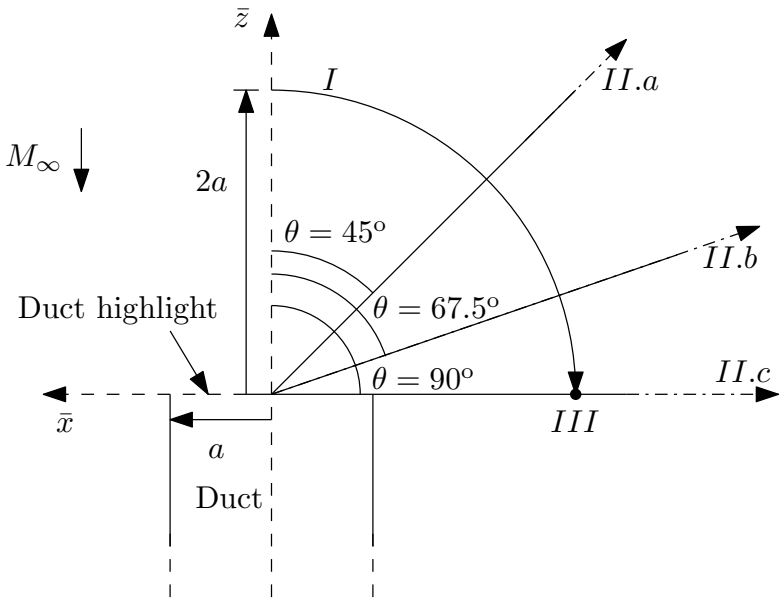

Figure 4.4: Schematic showing the duct and where the comparisons are made.

azimuthal mode order.

The predictions from the two models for $k_0a = 10$ and $(l, q) = (4, 1)$ on an arc of radius $2a$ $(= 1a_0)$ (contour I in Figure (4.4)) are shown in Figure (4.5). For this case the predictions are very similar from the source axis to approximately 75°. The slight differences at low polar angles is due to the difference in the methods and is negligible. At polar angles above 75° it is seen that there is an increasing difference between the models. The largest difference is at 90° and is about 4 dB.

For the same mode as before but with a higher frequency, of $k_0a = 20$, the predictions are shown in Figure (4.6.a). For the previous frequency the low mode of $(l, q) = (4, 1)$ means the mode is very cut-on. The two models give very similar predictions up to around 80°. The maximum difference is about 6 dB at 90°. Figures (4.5) and (4.6) show that the effect of the nacelle is insignificant for angles upto approximately 75°, and that for a given mode the frequency does not significantly alter the lobe and null structure of the directivity pattern.

Figure (4.6.b) shows the same variables as Figure (4.6.a) but with a very high azimuthal mode order of 24, this means the mode is only just cut-on. As before, the differences are negligible up to about 80°. Above this value the difference increases to a maximum of 5 dB.

By plotting predictions from the two models a modest difference is observed at high polar angles. A useful metric to quantify the effect of the nacelle lip is to compare the difference between the two models. Initially, the difference between the models as a function of polar angle is defined as

$$\Delta_\theta = \mathrm{SPL}_{d,lq}(\theta) - \mathrm{SPL}_{lq}(\theta), \tag{4.2.1}$$

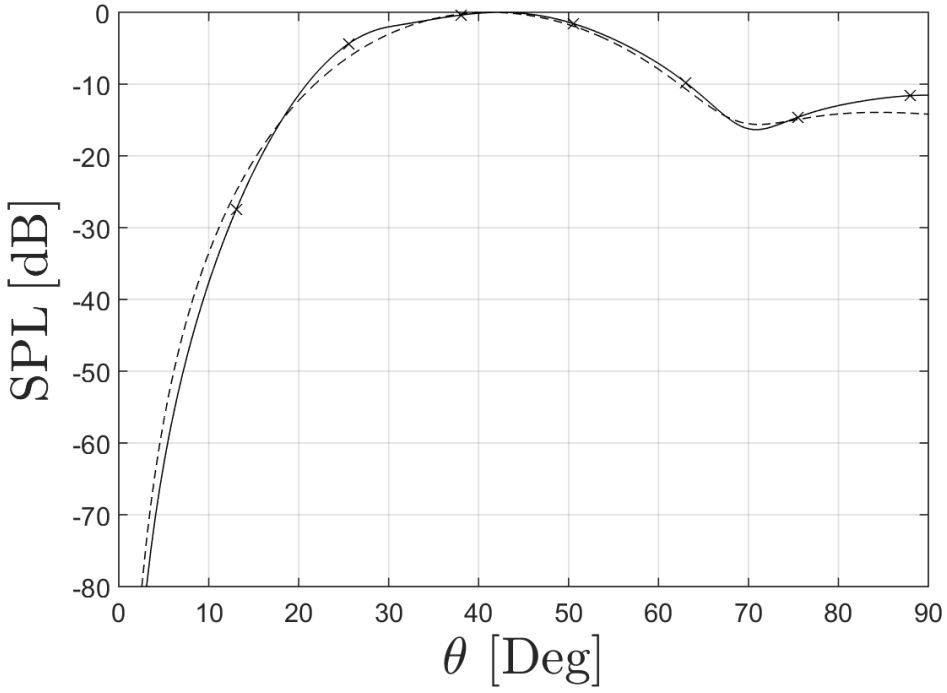

Figure 4.5: Predictions of the new source (solid line, ×) and Wiener–Hopf (dashed line) against polar angle at $R = 2a$ (on contour I). The parameters are the same as Figure (3.8): $k_0 a = 10$, $a = 0.5$, $(l, q) = (4, 1)$ and $M_\infty = 0$.

evaluated in the near-field at $R = 2a$. Negative values of Δ_θ indicate shielding due to the diffraction of the duct lip.

The difference is shown in Figure (4.7). It shows that for angles greater than 70° the difference for all the parameter variables increases with increasing polar angle. The maximum difference for all cases is at 90°. For all the variables the difference is no more than 5 dB. This is surprisingly small considering the rather large range in the variables.

Next, the effect of increasing radial distance on the diffracted field. For a given polar angle the difference is defined as

$$\Delta_r = \mathrm{SPL}_{d,lq}(r) - \mathrm{SPL}_{lq}(r), \tag{4.2.2}$$

again this means that negative values indicate shielding. This is shown on the schematic in Figure (4.4) as lines $II.a$, $II.b$ and $II.c$. This metric is useful because any large differences between the models would shown a dependency between the near/far field.

Figure (4.8) shows Δ_r for $k_0 a = 20$ and mode $(l, q) = (4, 1)$ along the radial lines. They show that the models are very similar at 45° and 62.5° ($\pi/4$ and $\pi/8$ radians).

At 90° the two models give significantly different predictions. For the well cut-on mode the difference is 6 dB and for the just cut-on mode it is slightly more at 7.5 dB. Predictions start at $1.5a$ and extends to $25a$, this corresponds to $0.75 - 12.5$ in the

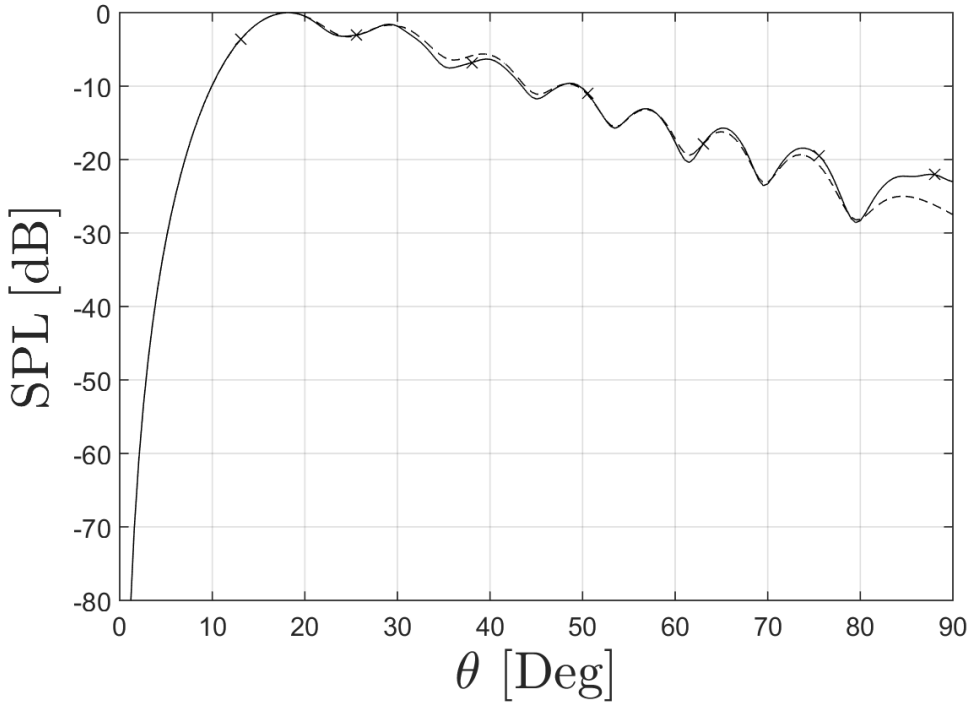

(a) $(l, q) = (4, 1)$

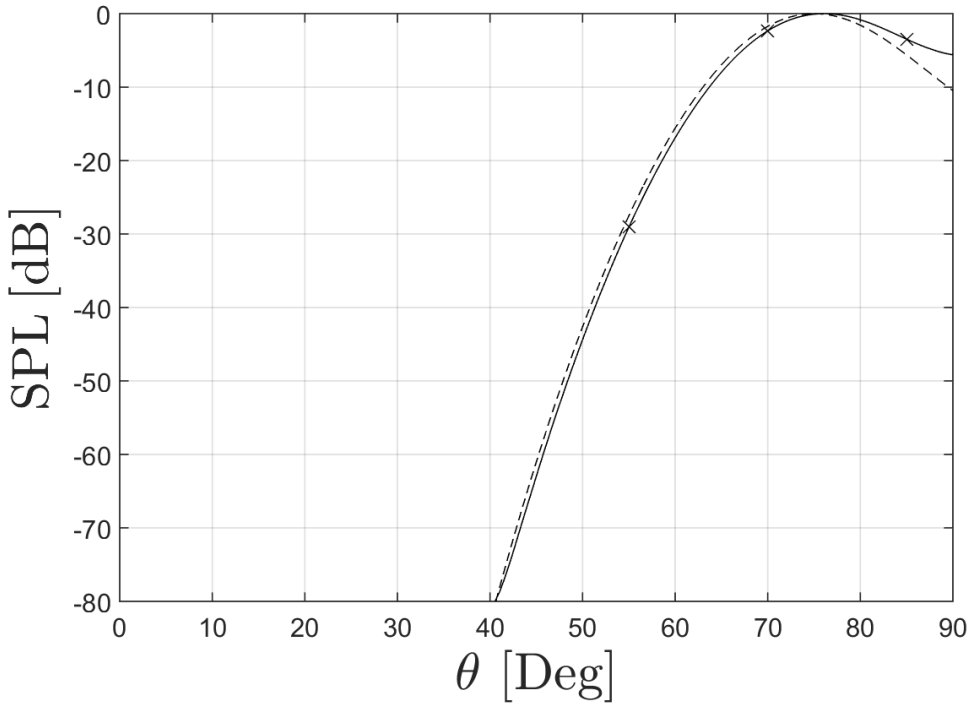

(b) $(l, q) = (24, 1)$

Figure 4.6: Predictions of the disc source (solid line, $\times$) and Wiener–Hopf (dashed line) against polar angle for two modes at $R = 2a$ (on contour I). The parameters are the same as Figure (3.10) and (3.11): $k_0 a = 20$, $a = 0.5$, $(l, q) = (4, 1)$ and $M_\infty = 0.75$.

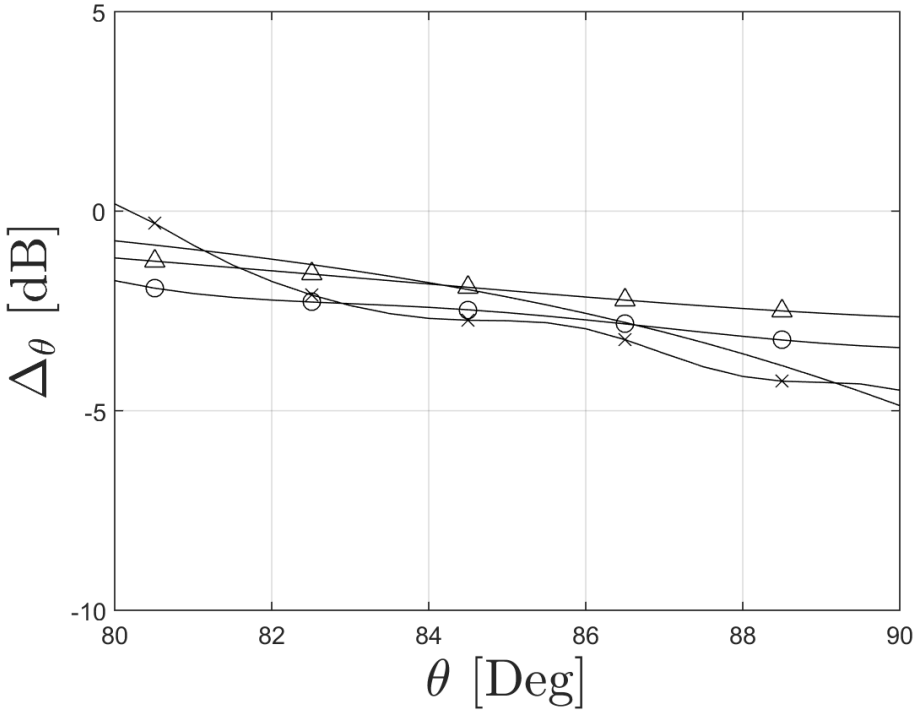

Figure 4.7: The difference between the predictions of the disc source and Wiener–Hopf along contour III for; $k_0a = 20$ and $(l, q) = (24, 1)$ (no symbols), $k_0a = 20$ and $(l, q) = (4, 1)$ ($\circ$), $k_0a = 10$ and $(l, q) = (4, 1)$ ($\triangle$) and $k_0a = 5$ and $(l, q) = (4, 1)$ ($\times$). The other parameters are: $R = 2a$, $a = 0.5$ and $M_\infty = 0.75$.

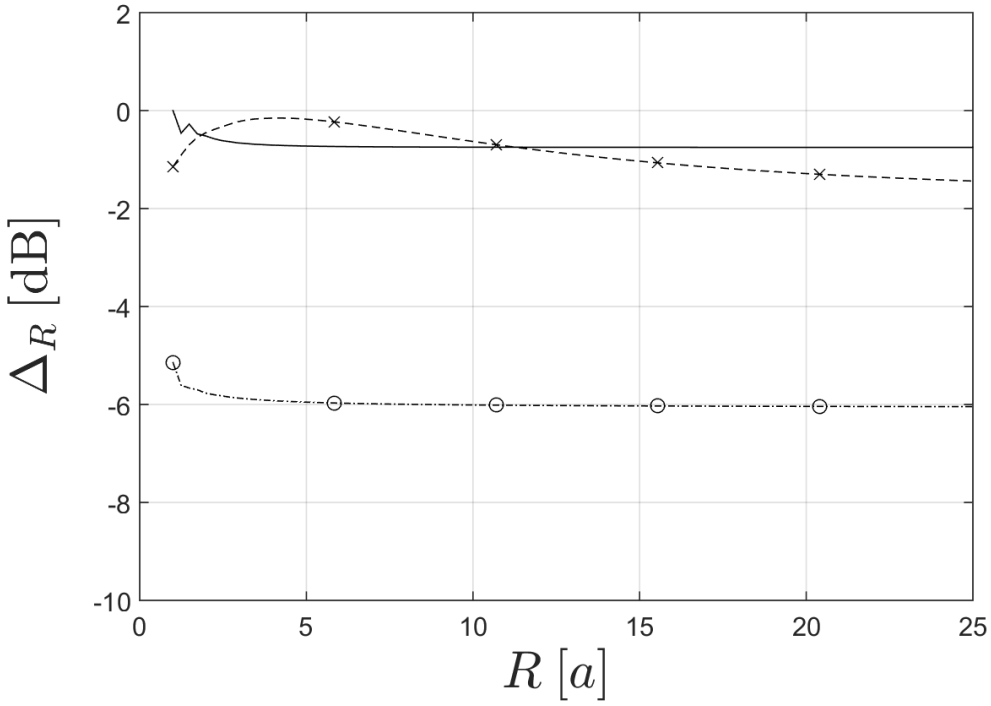

(a) $(4, 1)$

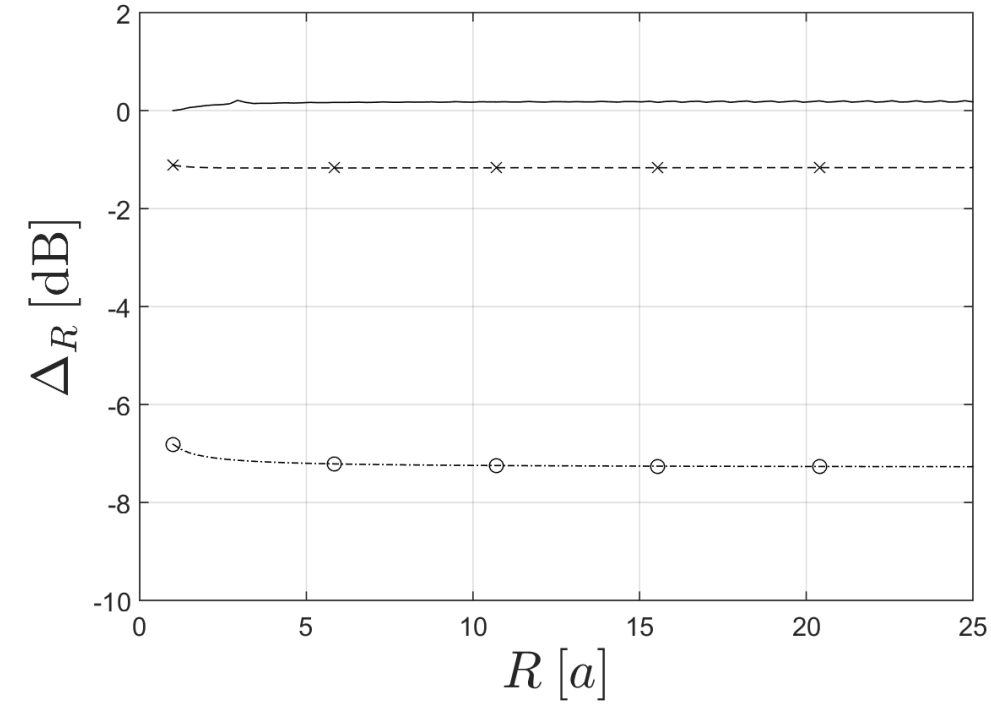

(b) $(24, 1)$

Figure 4.8: The difference between the two models as a function of radial distance for two modes $(l, q) = (4, 1)$ and $(24, 1)$ for angles; 45° (solid line, contour $II.a$), 62.5° (dashed, $\times$ for contour $II.b$) and 90° (dash-dot, $\circ$ for contour $II.c$). Note that the non-dimensional range for this example is 0.75 – 12.5. The parameters are the same as Figure (4.6): $k_0 a = 20$, $a = 0.5$ and $M_\infty = 0.75$.

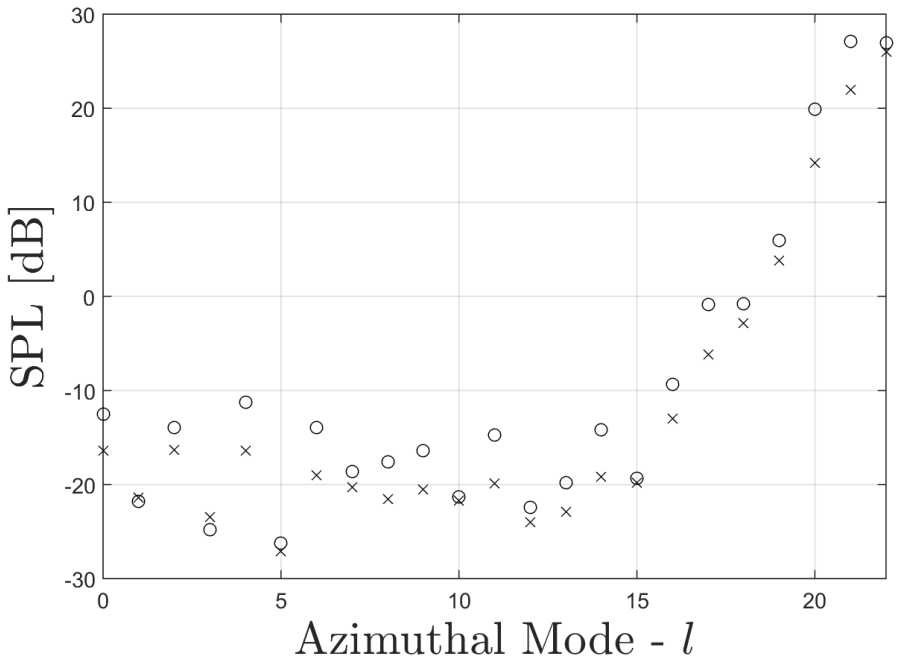

Figure 4.9: Predictions at 90° (point III) for the disc source (∘) and Wiener–Hopf (×) against azimuthal mode up to cut-off. The parameters are: $k_0a = 20$, $a = 0.5$, $R = 2a$ and $M_\infty = 0.75$

non-dimensional length units referenced to a_0. The lower limit is in the near-field and the upper in the far-field, as shown in the previous chapter. Importantly, because Δ_r is constant the near-field is affecting the diffracted field in the same way as the disc source. This shows no significant near-field effects on the diffracted field compared to the disc source.

The last two figures are predictions shown at point III. Figure (4.9) shows the predictions at 90° and $R = 2a$ for $k_0a = 20$, as the azimuthal mode is increased from 0 to 24. The graph shows that the Wiener–Hopf solution is always at a lower amplitude. However the difference between the two models is not constant.

Figure (4.10) shows a very similar trend as Figure (4.9), however the wavenumber is increased for the mode $(4, 1)$. The peaks correspond to a lobe and the minima are nulls in the directivity. This graph shows that the difference between the two models are greatest at the maxima and nulls, but the difference can be negligible between these. This is more clearly shown by plotting the SPL. The combination of variables such that a lobe occurs at 90° is the relevant factor.

The purpose of this section was to quantify the diffraction effects of the duct lip on a radiating mode in the near field. Therefore, the conclusion to be drawn is that the maximum destructive interference caused by the lip is a fairly moderate maximum of about 7 dB. Therefore, generally the diffraction effect can be neglected in the forward arc (as it was in McAlpine, Gaffney and Kingan (2015)). But is crucial in the rear arc. However, this difference is not constant, the effect is strongest at 90° to the duct and

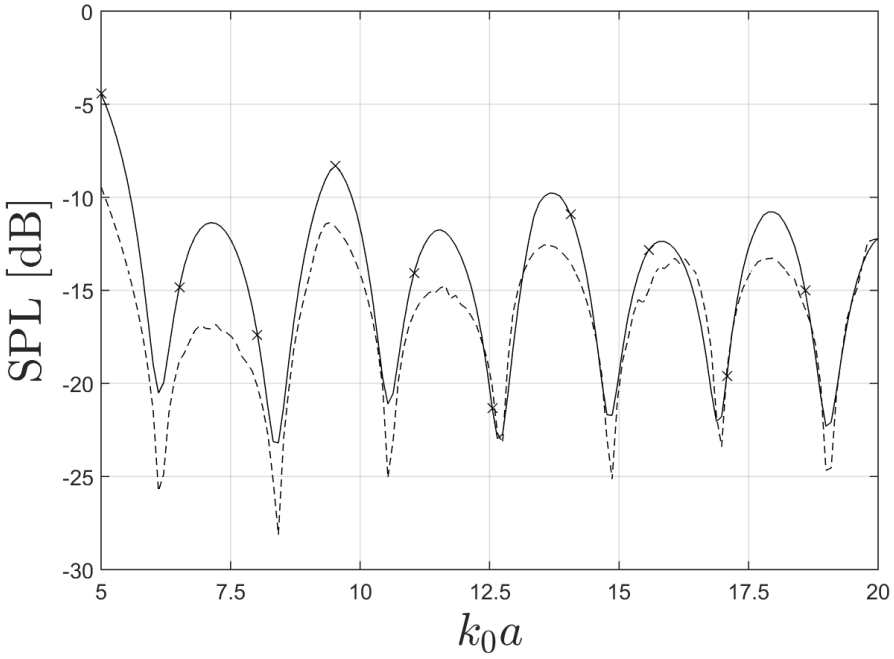

Figure 4.10: Predictions at 90° (point III) for the disc source (solid line, $\times$) and Wiener–Hopf (dashed line) against frequency. The parameters are: $(l, q) = (4, 1)$, $R = 2a$ and $M_\infty = 0.75$

when there is a lobe near this angle. Therefore the diffraction effect does not depend on mode or frequency – it depends on the the ratio of these variables. Also, the diffracted field is affected by the same amount as the disc source.

4.3 Chapter Summary

This chapter has presented a derivation of the sound field due to a mode radiating from a semi-infinite circular duct of infinitesimal wall thickness, Objective 4. With the adoption of complex axial wavenumbers, branch cut locations, caused by the square root in k_r, are of practical relevance. A comparison between the disc source and the Wiener–Hopf predictions showed that

- the effect of the duct in the forward arc moderately reduces amplitude at large polar angles (75° – 90°),
- for a given angle, no single parameter change causes a monotonic increase or decrease in the Δ's,
- the important factor is the ratio between the mode and frequency such that at a maxima in the radiation directivity is where most reduction occurs,
- the shielding due to the duct does not depend of radial distance for the distances examined.

This investigation has completed Objective 5. The disc source is not as complicated as the Wiener–Hopf model and is simpler to implement. It is therefore very important to quantify the diffraction of the duct if the disc source is to be used in predictions. The main reason to include the diffraction effect is to extend the range of predictions to the rear arc.

Chapter 5

The Installation Theory and Method

The engine tone radiation in the free-field has been modelled in the previous section. In this chapter a cylinder of infinite length is introduced to simulate the scattering effect of the fuselage. Running down the length of the cylinder is a boundary layer of constant thickness. The model includes the refraction effects of the boundary layer by solving the Pridmore–Brown equation. The Pridmore-Brown equation contains a singularity referred to as the critical layer. This singularity is discussed and a solution in its locality is derived as a Frobenious solution. The special case of a boundary layer of infinitesimal thickness leads to the scattered solution for uniform flow.

The disc source method is then validated against published results. In addition the Fourier sum, ODE solver, Frobenius series and the optimisation of the method are discussed in detail. The Wiener–Hopf method solution is discussed separately as the method is significantly different to the disc method.

5.1 Installed Theory

In this first part of the chapter, an infinitely long cylinder is placed adjacent to the new sources. As before, Fourier methods are used and the same normalisation is employed. The source is described using a coordinate system centred in the cylinder. The cylinder is introduced and the pressure in the boundary layer is evaluated.

5.1.1 Graf's Addition Theorem

The results derived in the previous chapter give the sound expressed in the coordinates of the source. With foresight, it is more convenient to express the total field in new coordinates centred on a cylinder. The inclusion of the cylinder in the model is in the next section; this section allows room for the cylinder.

The pressure due to an untranslated source is given by

$$p_i(r,\phi,z,t) = \int_{-\infty}^{\infty} \widetilde{p}_i\,(k_z)\,\mathrm{e}^{-jk_z z}\,\mathrm{d}k_z\,\mathrm{e}^{-jl\phi}\mathrm{e}^{j\omega_0 t}, \tag{5.1.1}$$

where

$$\widetilde{p}_i\,(k_z) = \widetilde{\eta}_i\,\mathrm{H}_l^{(2)}(k_r r), \tag{5.1.2}$$

as ascertained in Section 3.1.2 (page 34).

Graf's Addition theorem is used to transform from the source coordinates (r,ϕ,z) to the cylinder coordinates $(\bar{r},\bar{\phi},\bar{z})$. By doing this the incident field is expressed in the cylindrical polar coordinates centred on the cylinder. The theorem is

$$\mathcal{B}_\ell(w)\mathrm{e}^{j\ell\chi} = \sum_{n=-\infty}^{\infty} \mathcal{B}_{\ell+n}(u)\mathrm{J}_n(v)\mathrm{e}^{jn\alpha} \tag{5.1.3}$$

where $\mathcal{B}_\ell$ can be any Bessel function or any linear combination (Abramowitz and Stegun, 1964) of integer order ℓ. The arguments may be complex.

Figure (5.1.1) shows that $w = k_r r$, $u = k_r b$, $v = k_r \bar{r}$, $\chi = \pi - \phi + \beta$ and $\alpha = \bar{\phi} - \beta$. Note these are different for the far-field solution.

So, to shift coordinates from r and ϕ to $\bar{r}$ and $\bar{\phi}$, application of Graf's theorem gives

$$\mathrm{H}_l^{(2)}(k_r r)\,\mathrm{e}^{-jl\phi} = \sum_{n=-\infty}^{\infty} (-1)^{(l+n)}\mathrm{H}_{l-n}^{(2)}(k_r b)\mathrm{J}_n(k_r\bar{r})\mathrm{e}^{-jn\bar{\phi}}\mathrm{e}^{-j(l-n)\beta}. \tag{5.1.4}$$

Therefore the incident field expressed in the cylinder coordinates $(\bar{r},\bar{\phi},\bar{z})$ is

$$p_i(\bar{r},\bar{\phi},\bar{z}) = \frac{1}{(2\pi)^2}\sum_{n=-\infty}^{\infty}\int_{-\infty}^{\infty} \widetilde{p}_{i,n}\mathrm{e}^{-jk_z\bar{z}}\,\mathrm{d}k_z\,\mathrm{e}^{-jn\bar{\phi}}, \tag{5.1.5}$$

where the transformed pressure now takes the form

$$\widetilde{p}_{i,n} = \widetilde{\eta}_{i,n}\,\mathrm{J}_n(k_r\bar{r}). \tag{5.1.6}$$

For example, the disc source ($i = lq$) is now

$$\widetilde{p}_{i,n}(\bar{r},\bar{\phi},\bar{z}) = \underbrace{\pi^2\xi_{lq}P_{lq}(-1)^{(l+n)}\mathrm{e}^{-(l-n)\beta}\,(k_0 + k_z M_\infty)\,\Psi_{lq}\mathrm{H}_{l-n}^{(2)}(k_r b)}_{\widetilde{\eta}_{lq,n}}\,\mathrm{J}_n(k_r\bar{r}). \tag{5.1.7}$$

By translating the source, the radial distance function has changed from the second type of Hankel function to the first kind of Bessel function. The translation introduces azimuthal harmonics $e^{-jn\bar{\phi}}$ of order n. Therefore, the final solution is represented as a Fourier series with each term an inverse Fourier transform.

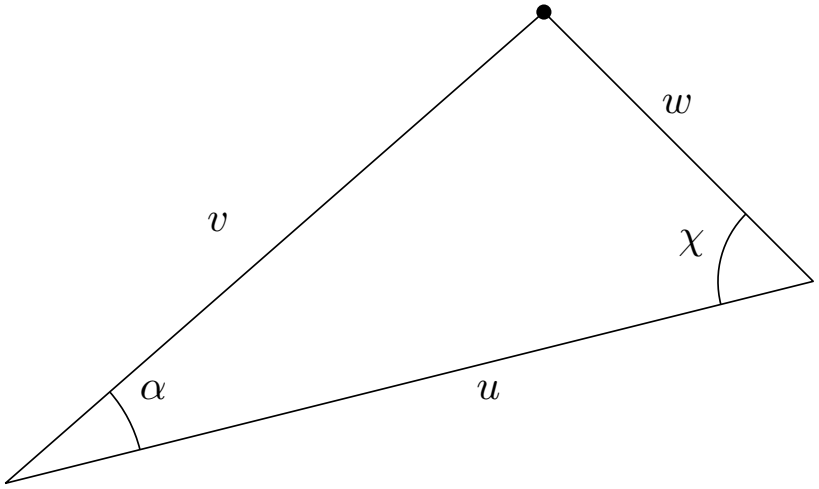

(a) The geometry used for Graf's Addition theorem.

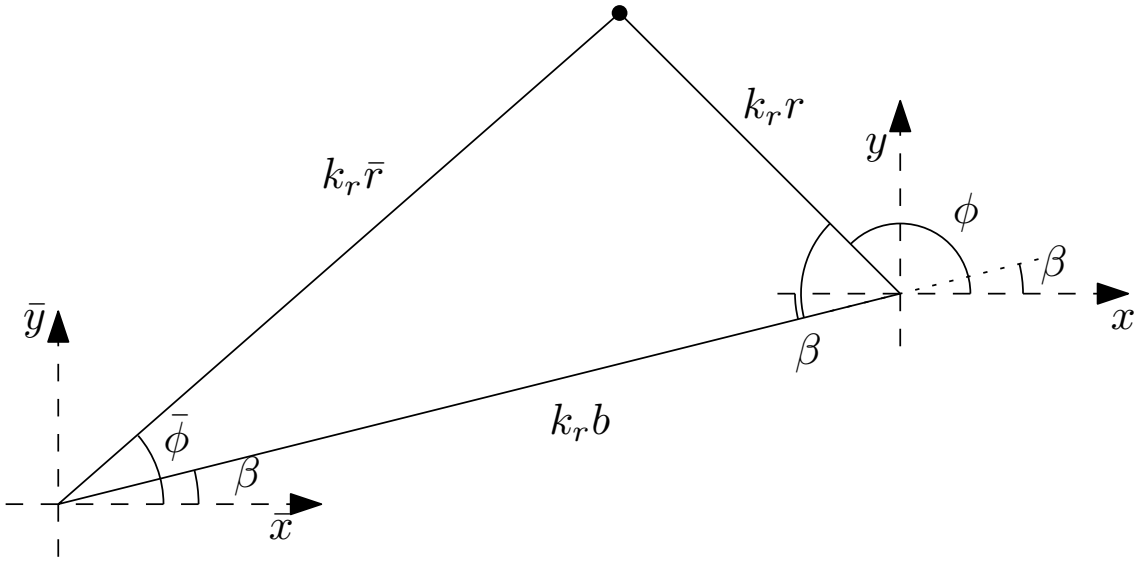

(b) The same triangle as (a) with the arguments of the Bessel functions included on the sides of the triangle and the angles measured from the relevant coordinate systems.

Figure 5.1: The two similar triangles used to apply the near-field application of Graf's Addition theorem. The observer is located at the black circle.

The translated incident field for the sources given in the previous chapter can all now be expressed in the cylinder's coordinates. The translated amplitude coefficients and distance function are given in Table (5.1).

Type of Source	Subscript, $i =$	Complex amplitude, $\widetilde{\eta}_i$	$f(\bar{r})$
Single monopole	σ	$(\pi/2)\,(k_0 + k_z M_\infty)\, Q^\sigma (-1)^n \mathrm{e}^{-jn\beta}$ $\mathrm{H}^{(2)}_{l-n}(k_r b)$	$\mathrm{J}_n(k_r \bar{r})$
Ring (order l)	l	$\pi^2 \xi_l (-1)^{l+n} \mathrm{e}^{j(l-n)\beta} P_l\,(k_0 + k_z M_\infty)$ $\mathrm{J}_l(k_r \eta)\mathrm{J}_l(\kappa_l \eta)\mathrm{H}^{(2)}_{l-n}(k_r b)$	$\mathrm{J}_n(k_r \bar{r})$
Mode (l, q)	lq	$\pi^2 \xi_{lq} (-1)^{l+n} \mathrm{e}^{j(l-n)\beta} P_{lq}\,(k_0 + k_z M_\infty)\, \Psi_{lq}$ $\mathrm{H}^{(2)}_{l-n}(k_r b)$	$\mathrm{J}_n(k_r \bar{r})$
Diffracted (l, q)	d, lq	$\xi_{lq} (-1)^{l+n} \mathrm{e}^{j(l-n)\beta} P_{lq}(k_0 + k_z M_\infty) \frac{F_+}{k_r \mathrm{H}^{(2)'}_l (k_r a)}$ $\mathrm{H}^{(2)}_{l-n}(k_r b)$	$\mathrm{J}_n(k_r \bar{r})$

Table 5.1: The complex amplitude and propagation function for the translated sources used in the thesis.

5.1.2 The Installed Field

The source has been translated to make room for the cylinder, this section inserts one. The fuselage is approximated as an infinitely long, rigid cylinder. This assumption is discussed in Chapter 7. Running down the fuselage is a boundary layer. A boundary layer of constant thickness is included in the model for a prescribed velocity profile. In one fell swoop we can put the cylinder (and scattering effects) and the boundary-layer refraction effects in the model. The solution outside the boundary layer will be matched, in Fourier space, to the solution inside the boundary layer, whilst ensuring that the appropriate boundary and radiation conditions are satisfied. The geometry for the problem is shown in Figure (5.2).

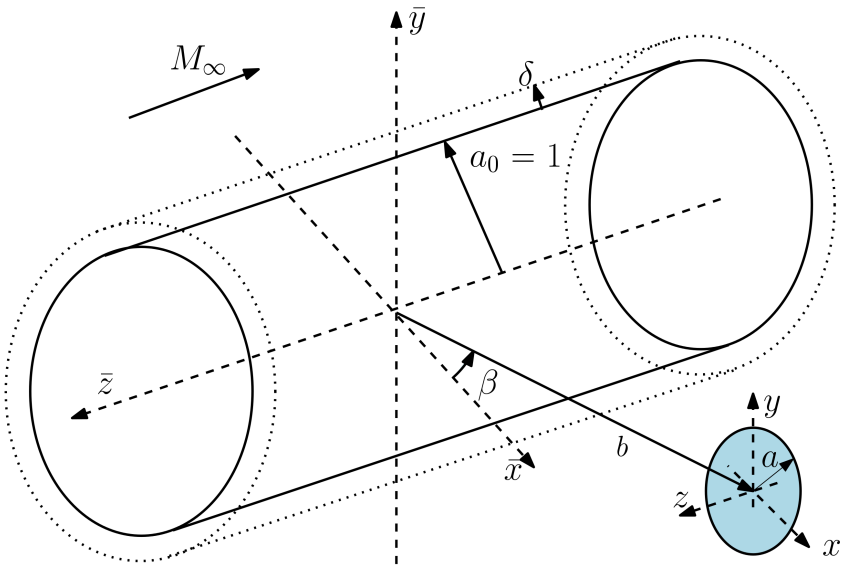

Figure 5.2: Sketch of the cylindrical fuselage, including a constant-thickness boundary layer.

A cylinder of infinite length is placed with its centre aligned with the $\bar{z}$ axis. The radius of the cylinder is a_0, however since this is the reference length the non-dimensional radius of the cylinder is unity.

The Mach velocity profile M_z is given by

$$M_z = \begin{cases} M(\bar{r}), & 1 < \bar{r} \leq 1 + \delta, \\ M_\infty, & 1 + \delta < \bar{r}, \end{cases} \tag{5.1.8}$$

where δ is the non-dimensional thickness of the boundary-layer, and M_∞ is the constant Mach number of the uniform flow outside the boundary-layer region.

Outside the boundary layer, where there is uniform flow, the acoustic pressure field is found by solving the convected wave equation. In this region, the solution is simply

$$\widetilde{p}_n = \widetilde{\eta}_n \, \mathrm{J}_n(k_r \bar{r}) + \widetilde{\gamma}_n \, \mathrm{H}_n^{(2)}(k_r \bar{r}), \tag{5.1.9}$$

where $\widetilde{\eta}_n(k_z)$ and $\widetilde{\gamma}_n(k_z)$ are amplitude coefficients of the incident and scattered waves respectively. The dispersion relationship in the uniform flow is still

$$k_r^2 + k_z^2 = (k_0 + k_z M_\infty)^2 . \tag{5.1.10}$$

Inside the boundary layer region, the pressure field will satisfy the Pridmore-Brown equation; an inviscid compressible isentropic perfect gas flow is assumed. Additionally, the mean flow is assumed to be axisymmetric and parallel, with constant mean density and sound speed profiles inside the boundary layer. In this case, the non-dimensional

Pridmore-Brown equation is

$$\frac{\mathrm{D}_0}{\mathrm{D}t}\left(\frac{\mathrm{D}_0^2 p}{\mathrm{D}t^2}-\nabla^2 p\right)-2M'\,\frac{\partial^2 p}{\partial\bar{r}\partial\bar{z}}=0\,, \tag{5.1.11}$$

where $M'=\mathrm{d}M/\mathrm{d}\bar{r}$. Inside the boundary layer, the total pressure field satisfies the Pridmore-Brown equation. Therefore, in the boundary layer the scattering effect of the cylinder is also included in the model. Inside the boundary layer the dispersion relationship is

$$k_r^2+k_z^2=\left(k_0+k_zM\right)^2. \tag{5.1.12}$$

The Pridmore-Brown equation is a third order PDE, to solve it we choose to use Fourier methods. On Fourier transforming in axial and azimuthal direction and time (Equation (3.1.10), page 29), the Pridmore-Brown equation reduces to

$$\left[\frac{\mathrm{d}^2}{\mathrm{d}\bar{r}^2}+\left(\frac{1}{\bar{r}}-\frac{2k_zM'}{k_0+k_zM}\right)\frac{\mathrm{d}}{\mathrm{d}\bar{r}}+\left(k_r^2-\frac{n^2}{\bar{r}^2}\right)\right]\widetilde{p}_n=0\,. \tag{5.1.13}$$

Equation (5.1.13) has a regular singularity at $k_0+k_zM(\bar{r}_c)=0$ on the real k_z axis, for a real valued k_0. Where this occurs, referred to as the critical layer, the phase speed equals the local flow velocity. Equation (5.1.13) can be solved by numerical integration across the boundary layer. However, special treatment must be given to the solution in the critical layer region.

Following the previous literature (Hanson and Magliozzi (1985), Lu (1990) and Brambley *et al.* (2012)), a Frobenius solution is used to bridge the singularity at $\bar{r}=\bar{r}_c$. Introducing the critical layer coordinate

$$\varsigma=\bar{r}-\bar{r}_c\,, \tag{5.1.14}$$

two independent solutions of the transformed Pridmore-Brown Equation (5.1.13) in the critical layer are given, up to $\mathrm{O}(\varsigma^3)$, by

$$\widetilde{p}_{n,F1}=\alpha_{F1}\varsigma^3 \quad \text{and} \quad \widetilde{p}_{n,F2}=\alpha_{F2}\left(1-\frac{1}{2}\left(k_z^2+\frac{n^2}{\bar{r}^2}\right)\varsigma^2+\Omega\alpha_{F1}\varsigma^3\ln\varsigma\right), \tag{5.1.15}$$

where α_{F1} and α_{F1} are constants, and

$$\Omega=-\frac{1}{3}\left(\frac{M''(\bar{r}_c)}{M'(\bar{r}_c)}-\frac{1}{\bar{r}_c}\right)\left(k_z^2+\frac{n^2}{\bar{r}_c^2}\right)-\frac{2n^2}{3\bar{r}_c^3}\,. \tag{5.1.16}$$

Note that these results are for a general boundary-layer profile close to $\bar{r}_c$. On taking a linear profile this result is found to be in agreement with Brambley *et al.* (2012) and Belyaev (2012). The derivation for this result is in the next section.

There is no known analytical solution to the Pridmore-Brown equation, therefore

a numerical integration routine (Runge–Kutta) is used. The pressure in the boundary layer, $\widetilde{p}_{n,bl}$, is normalised, i.e.

$$\widetilde{p}_{n,bl}(\bar{r}, k_z) = \widetilde{\alpha}_n(k_z)\widetilde{f}_n(\bar{r}, k_z)\,, \tag{5.1.17}$$

where $\widetilde{f}_n$ is the normalised pressure, which is scaled by $\widetilde{\alpha}_n(k_z)$. The integration, starting from the surface of the cylinder at $\bar{r} = 1$, is calculated by expressing the Pridmore-Brown equation as two first-order differential equations

$$\begin{bmatrix} x_2' \\ x_1' \end{bmatrix} = \begin{bmatrix} -\left(\frac{1}{\bar{r}} - \frac{2k_z M'}{k_0 + k_z M}\right) & -(k_r^2 - \frac{n^2}{\bar{r}^2}) \\ 1 & 0 \end{bmatrix} \begin{bmatrix} x_2 \\ x_1 \end{bmatrix}\,, \tag{5.1.18}$$

where $x_1 = \widetilde{f}_n$ and $x_2 = \mathrm{d}\widetilde{f}_n/\mathrm{d}\bar{r} = \widetilde{f}_n'$. With nondimensional specific acoustic admittance, A, and slip velocity is permitted at the wall, the impedance boundary condition is

$$\widetilde{p}_{n,bl}'(1, k_z) - jk_0 A\left(1 + j\frac{M_\infty k_z}{k}\right)\widetilde{p}_{n,bl}(1, k_z) = 0\,. \tag{5.1.19}$$

However, published acoustical impedance values for a metal cylinder are not available, therefore in this thesis the cylinder will be rigid and no slip is assumed. The rigid boundary condition is a valid assumption as a metal cylinder is almost rigid. Therefore, without loss of generality, on the surface of the rigid cylinder, the normalised pressure is set as $\widetilde{f}_n(1, k_z) = 1$, and the derivative $\widetilde{f}_n'(1, k_z) = 0$. Accordingly, the boundary conditions on the cylinder are

$$\widetilde{p}_{n,bl}(1, k_z) = \widetilde{\alpha}_n \quad \text{and} \quad \widetilde{p}_{n,bl}'(1, k_z) = 0\,. \tag{5.1.20}$$

The value of $\widetilde{\alpha}_n$ must be proportional to the incoming wave. The pressure and its derivative at the edge of the boundary layer can be used to formulate $\widetilde{\alpha}_n$ in terms of the incident wave amplitude. Applying continuity of pressure and the pressure gradient at the edge of the boundary layer gives

$$\widetilde{\alpha}_n \widetilde{f}_n\Big|_{1+\delta} = \widetilde{p}_{i,n}|_{1+\delta} + \widetilde{p}_{s,n}|_{1+\delta} = \widetilde{\eta}_n \mathrm{J}_n(k_r[1+\delta]) + \widetilde{\gamma}_n\, \mathrm{H}_n^{(2)}(k_r[1+\delta])\,, \tag{5.1.21a}$$

$$\widetilde{\alpha}_n \widetilde{f}_n'\Big|_{1+\delta} = \widetilde{p}_{i,n}'\big|_{1+\delta} + \widetilde{p}_{s,n}'\big|_{1+\delta} = \widetilde{\eta}_n k_r \mathrm{J}_n'(k_r[1+\delta]) + \widetilde{\gamma}_n k_r\, \mathrm{H}_n^{(2)\prime}(k_r[1+\delta])\,, \tag{5.1.21b}$$

where $\widetilde{\eta}_n(k_z)$ and $\widetilde{\gamma}_n(k_z)$ are amplitude coefficients of the incident and scattered waves respectively. This was why the incident field is formulated to be $\propto \widetilde{\eta}_i$. The pressure in the boundary layer is scaled to match the amplitude of the incoming wave, i.e.

$$\widetilde{\alpha}_n(k_z) = -\left(\frac{2j}{\pi[1+\delta]}\right)\left(\frac{\widetilde{\eta}_n}{\widetilde{f}_n\Big|_{1+\delta} k_r \mathrm{H}_n^{(2)\prime}(k_r[1+\delta]) - \widetilde{f}_n'\Big|_{1+\delta} \mathrm{H}_n^{(2)}(k_r[1+\delta])}\right), \tag{5.1.22}$$

for any source in the form of $\widetilde{\eta}_i f(\bar{r})$. The installation effect is

$$BL = -\left(\frac{2j}{\pi[1+\delta]}\right)\left(\frac{1}{\widetilde{f}_n\Big|_{1+\delta} k_r \mathrm{H}_n^{(2)\prime}(k_r[1+\delta]) - \widetilde{f}_n'\Big|_{1+\delta} \mathrm{H}_n^{(2)}(k_r[1+\delta])}\right), \tag{5.1.23}$$

which is $\widetilde{\alpha}$ without the incident field.

Inserting Equation (5.1.22) into (5.1.17), and then taking the inverse Fourier transform given by Equation (3.1.11) (on page 29), on the surface of the cylinder, the pressure can be calculated via

$$p_t(a_0, \bar{\phi}, \bar{z}) = \frac{1}{(2\pi)^2} \sum_{n=-\infty}^{\infty} \left(\int_{-\infty}^{\infty} \widetilde{\alpha}_n(k_z)\, \mathrm{e}^{-jk_z\bar{z}} \mathrm{d}k_z\right) \mathrm{e}^{-jn\bar{\phi}}\,. \tag{5.1.24}$$

5.1.3 Critical layer

In the previous section the Pridmore-Brown equation was added to the model to include the refraction effect of the boundary layer running down the fuselage. Pridmore-Brown (1958) was one of the first to model sound propagation in sheared flow. In the Fourier domain the Pridmore-Brown equation contains a singularity. The transformed Pridmore-Brown Equation (Equation (5.1.13)) is singular when $k_0 + k_z M(\bar{r}) = 0$, this occurs at the critical layer $\bar{r}_c$. The value of $\bar{r}_c$ is unique to the profile and frequency. To implement this solution as it is, the ODE would lose accuracy at this point. Therefore, special treatment is required to solve the equation at the critical layer. To bridge the singularity a Frobenius solution is derived for any monotonically increasing, axisymmetric boundary layer profile of constant thickness. Initially the transformed Pridmore-Brown equation needs to be rearranged into a form suitable to derive a Frobenius series solution (Kreyszig, 2011). Namely, this requires the Pridmore-Brown equation

$$\left[\frac{\mathrm{d}^2}{\mathrm{d}\bar{r}^2} + \left(\frac{1}{\bar{r}} - \frac{2k_z M'}{k_0 + k_z M}\right)\frac{\mathrm{d}}{\mathrm{d}\bar{r}} + \left(k_r^2 - \frac{n^2}{\bar{r}^2}\right)\right]\widetilde{p}_n = 0\,, \tag{5.1.25}$$

to be expressed in the form

$$\varsigma^2 P(\varsigma)\widetilde{p}'' + \varsigma Q(\varsigma)\widetilde{p}' + R(\varsigma)\widetilde{p} = 0. \tag{5.1.26}$$

In this section, the Pridmore-Brown equation is transformed into a PDE of this form, where the prime denotes ordinary differentiation w.r.t to ς. In order to obtain Equation (5.1.25) into this form the Binomial theorem is applied. Consequently care is taken over the order of the error of the approximations.

The equation is simplified by shifting the singularity to the origin by the change of variable

$$\varsigma = \bar{r} - \bar{r}_c, \tag{5.1.27}$$

so that the critical layer occurs at $\varsigma = 0$.

The derivatives transform to

$$\frac{\mathrm{d}}{\mathrm{d}\bar{r}} = \frac{\mathrm{d}}{\mathrm{d}\varsigma} \Rightarrow \frac{\mathrm{d}^2}{\mathrm{d}\bar{r}^2} = \frac{\mathrm{d}^2}{\mathrm{d}\varsigma^2}. \tag{5.1.28}$$

The Taylor's series expansion of the Mach profile is

$$M(\bar{r}_c + \varsigma) = M(\bar{r}_c) + \varsigma M'(\bar{r}_c) + \frac{\varsigma^2}{2!}M''(\bar{r}_c) + \frac{\varsigma^3}{3!}M'''(\bar{r}_c)..., \tag{5.1.29}$$

and the derivative

$$M'(\bar{r}_c + \varsigma) = M'(\bar{r}_c) + \varsigma M''(\bar{r}_c) + \frac{\varsigma^2}{2!}M'''(\bar{r}_c) + \frac{\varsigma^3}{3!}M''''(\bar{r}_c)... \,. \tag{5.1.30}$$

Substituting these expansions and employing the Binomial expansion, the important term involving M' in Equation (5.1.24) is

$$\frac{2k_z M'}{k + k_z M} = \frac{2k_z M'(\bar{r}_c)}{k_z \varsigma M'(\bar{r}_c)} \left(1 + \varsigma \frac{M''(\bar{r}_c)}{M'(\bar{r}_c)} + O(\varsigma^2)\right) \left(1 - \frac{\varsigma}{2!}\frac{M''(\bar{r}_c)}{M'(\bar{r}_c} + O(\varsigma^2)\right), \tag{5.1.31}$$

$$= \frac{2}{\varsigma}\left(1 + \frac{\varsigma}{2}\frac{M''(\bar{r}_c)}{M'(\bar{r}_c)}\right) + O\left(\varsigma^2\right). \tag{5.1.32}$$

The last term in Equation (5.1.25) also reduces

$$(k + k_z M)^2 = \left(k + k_z \left(M(\bar{r}_c) + \varsigma M'(\bar{r}_c) + O(\varsigma^2)\right)\right)^2. \tag{5.1.33}$$

Also, the final part of the equation to the second order leads to

$$(k + k_z M)^2 - k_z^2 - \frac{n^2}{\bar{r}^2} = -k_z^2 - \frac{n^2}{\bar{r}_c^2}\left(1 - 2\frac{\varsigma}{\bar{r}_c}\right) + O(\varsigma^2). \tag{5.1.34}$$

Using the same method

$$\frac{1}{\bar{r}^2} = \frac{1}{(\varsigma + \bar{r}_c)^2} = \frac{1}{\bar{r}_c^2}\frac{1}{\left(1 + \frac{\varsigma}{\bar{r}_c}\right)^2} = \frac{1}{\bar{r}_c^2}\left(1 - 2\frac{\varsigma}{\bar{r}_c}\right) + O\left(\varsigma^2\right). \tag{5.1.35}$$

Substituting these results into Equation (5.1.25) gives

$$\widetilde{p}'' + \left(\frac{1}{\bar{r}_c}\left(1 - \frac{\varsigma}{\bar{r}_c}\right) - \frac{2}{\varsigma}\left(1 + \frac{\varsigma}{2}\frac{M''(\bar{r}_c)}{M'(\bar{r}_c)}\right)\right)\widetilde{p}' + \left(-k_z^2 - \frac{n^2}{\bar{r}_c^2}\left(1 - 2\frac{\varsigma}{\bar{r}_c}\right)\right)\widetilde{p} + O(\varsigma^2) = 0. \tag{5.1.36}$$

The last step is to multiply by ς^2

$$\varsigma^2\widetilde{p}'' + \varsigma\left(-2 + \varsigma\left(\frac{1}{\bar{r}_c} - \frac{\varsigma}{\bar{r}_c^2} - \frac{M''(\bar{r}_c)}{M'(\bar{r}_c)}\right)\right)\widetilde{p}' + \varsigma^2\left(-k_z^2 - \frac{n^2}{\bar{r}_c^2}\left(1 - 2\frac{\varsigma}{\bar{r}_c}\right)\right)\widetilde{p} + O(\varsigma^4) = 0. \tag{5.1.37}$$

Equation (5.1.25) now in the form of Equation (5.1.26), where

$$P(\varsigma) = 1, \tag{5.1.38a}$$

$$Q(\varsigma) = -2 + \varsigma\left(\frac{1}{\bar{r}_c} - \frac{\varsigma}{\bar{r}_c^2} - \frac{M''(\bar{r}_c)}{M'(\bar{r}_c)}\right), \tag{5.1.38b}$$

$$R(\varsigma) = \varsigma^2\left(-k_z^2 - \frac{n^2}{\bar{r}_c^2}\left(1 - 2\frac{\varsigma}{\bar{r}_c}\right)\right). \tag{5.1.38c}$$

and is equivalent when $\varsigma^4 << 1$.

The singularity is now when $\varsigma = 0$ and this is a regular singularity because

$$\lim_{\varsigma\to 0}\left\{\varsigma\left[\frac{1}{\bar{r}_c}\left(1 - \frac{\varsigma}{\bar{r}_c}\right) + \frac{2}{\varsigma}\left(1 + \frac{\varsigma}{2}\frac{M''(\bar{r}_c)}{M'(\bar{r}_c)}\right)\right]\right\} = 2, \tag{5.1.39}$$

which is finite and infinitely differentiable. Where Equation (5.1.25) contains a regular singularity, the Frobenius solution may now be derived.

Frobenius Method

The critical layer singularity has been shifted to the origin and is in a suitable form for a Frobenius solution to be derived. This method has been chosen for consistency with installation effects literature: Hanson (1984), McAninch (1983), Hanson and Magliozzi (1985), Lu (1990) and Belyaev (2012). Another method, for example, of negating the critical layer would be to let ς or $\bar{r}$ (as in Smith (2004)) have a small imaginary component.

The equation we seek a solution for is

$$\varsigma^2\widetilde{p}'' + \varsigma\left(-2 + \varsigma\left(\frac{1}{\bar{r}_c} - \frac{\varsigma}{\bar{r}_c^2} - \frac{M''(\bar{r}_c)}{M'(\bar{r}_c)}\right)\right)\widetilde{p}' + \varsigma^2\left(-k_z^2 - \frac{n^2}{\bar{r}_c^2}\left(1 - 2\frac{\varsigma}{\bar{r}_c}\right)\right)\widetilde{p} = 0, \tag{5.1.40}$$

where terms of order ς^4 have been omitted.

For brevity let

$$\lambda = \frac{1}{\bar{r}_c} - \frac{M''(\bar{r}_c)}{M'(\bar{r}_c)} \text{ and } \gamma^2 = -k_z^2 - \frac{n^2}{\bar{r}_c^2}, \tag{5.1.41}$$

which simplifies to

$$\varsigma^2\frac{\mathrm{d}^2\widetilde{p}}{\mathrm{d}\varsigma^2} + \varsigma\left(\varsigma\left(\lambda - \frac{\varsigma}{\bar{r}_c^2}\right) - 2\right)\frac{\mathrm{d}\widetilde{p}}{\mathrm{d}\varsigma} + \varsigma^2\left(\gamma + 2\frac{n^2}{\bar{r}_c^3}\varsigma\right)\widetilde{p} = 0. \tag{5.1.42}$$

The solution is expressed in terms of a power solution of the form

$$\widetilde{p} = \sum_{\psi=0}^{\infty} a_\psi \varsigma^{\psi+\kappa}, \tag{5.1.43}$$

where for this section only a_ψ is the coefficient of order ψ – not radius of the source. Note a different form of solution is required at a turning point. A profile with a turning point would correspond to a separated boundary layer which is unlikely (in normal operating conditions) along the fuselage, and not considered in this thesis. The derivatives are given by

$$\widetilde{p}' = \sum_{\psi=0}^{\infty} (\psi+\kappa) a_\psi \varsigma^{\psi+\kappa-1}, \tag{5.1.44}$$

$$\widetilde{p}'' = \sum_{\psi=0}^{\infty} (\psi+\kappa)(\psi+\kappa-1) a_\psi \varsigma^{\psi+\kappa-2}. \tag{5.1.45}$$

Substitute Equations (5.1.43), (5.1.44) and (5.1.45) into Equation (5.1.42) to obtain

$$\sum_{\psi=0}^{\infty} (\psi+\kappa)(\psi+\kappa-1) a_\psi \varsigma^{\psi+\kappa} + \left(\varsigma\left(\lambda - \frac{\varsigma}{\bar{r}_c^2}\right) - 2\right) \sum_{\psi=0}^{\infty} (\psi+\kappa) a_\psi \varsigma^{\psi+\kappa} + \left(\gamma + 2\frac{n^2}{\bar{r}_c^3}\varsigma\right) \sum_{\psi=0}^{\infty} a_\psi \varsigma^{\psi+\kappa+2} = 0. \tag{5.1.46}$$

Next shift the indices and factorise the $\varsigma^{\psi+\kappa}$ term to obtain

$$\sum_{\psi=0}^{\infty} \left\{ \left[(\psi+\kappa)(\psi+\kappa-1) - 2(\psi+\kappa)\right] a_\psi + \lambda(\psi+\kappa-1) a_{\psi-1} + \left(\gamma - \frac{\psi+\kappa-2}{\bar{r}_c^2}\right) a_{\psi-2} + 2\frac{n^2}{\bar{r}_c^3} a_{\psi-3} \right\} \varsigma^{\psi+\kappa} = 0, \tag{5.1.47}$$

as the negative coefficients of a_ψ are identically zero by definition.

Taking the lowest term of $\psi = 0$ and since $a_0 \neq 0$, the indicial equation is

$$\kappa\,(\kappa - 3) = 0. \tag{5.1.48}$$

Two solutions with integer difference of this quadratic equation, $\kappa = 0$ and 3, and therefore leads to two linearly independent solutions (Kreyszig, 2011) of the form

$$\widetilde{p}_{F1} = \sum_{\psi=0}^{\infty} a_\psi \varsigma^{\psi+3} \text{ and } \widetilde{p}_{F2} = \Omega \widetilde{p}_1 \ln \varsigma + \sum_{\psi=0}^{\infty} b_\psi \varsigma^{\psi}, \tag{5.1.49}$$

where F stands for a Frobenius solution.

The first solution is simply

$$\widetilde{p}_{F1} = \varsigma^3 + O(\varsigma^4), \tag{5.1.50}$$

where $a_0 = 1$. For simple profiles a full solution may be derived (Brambley *et al.* (2012) Campos and Serrao (1998) , Campos *et al.* (1999), Lu (1990)) but our solution is valid for any profile so long as ς is sufficiently small.

The second solution is derived from the first solution. Taking the derivatives

$$\widetilde{p}_{F2} = \Omega \widetilde{p}_{F1} \ln \varsigma + \sum_{\psi=0}^{\infty} b_\psi \varsigma^\psi, \tag{5.1.51}$$

$$\widetilde{p}'_{F2} = \Omega \left(\ln \varsigma \widetilde{p}'_{f1} + \frac{\widetilde{p}_{f1}}{\varsigma} \right) + \sum_{\psi=0}^{\infty} b_\psi \psi \varsigma^{\psi-1}, \tag{5.1.52}$$

and

$$\widetilde{p}''_{F2} = \Omega \left(\ln \varsigma \widetilde{p}''_{F1} + 2\frac{\widetilde{p}'_{F1}}{\varsigma} - \frac{\widetilde{p}_{F1}}{\varsigma^2} \right) + \sum_{\psi=0}^{\infty} b_\psi \psi(\psi-1) \varsigma^{\psi-2}. \tag{5.1.53}$$

Substituting into Equation (5.1.42) the logarithm terms cancel, and subtracting the $\widetilde{p}_{F1}$ terms and shifting the indices leads to

$$\sum_{\psi=0}^{\infty} \left(\psi(\psi-3)b_\psi + (\psi-1)\lambda b_{\psi-1} + \left[\frac{2-\psi}{\bar{r}_c^2} + \gamma \right] b_{\psi-2} + 2\frac{n^2}{\bar{r}_c^3} b_{\psi-3} \right) \varsigma^\psi = \Omega \sum_{\psi=3}^{\infty} \left(-(2\psi-3)a_{\psi-3} - \lambda a_{\psi-4} + \frac{1}{\bar{r}_c^2} a_{\psi-5} \right) \varsigma^\psi. \tag{5.1.54}$$

By comparing coefficients of ς, b_ψ may be obtained

ψ	b_ψ
0	0 (this allows $b_0 = 1$),
1	0,
2	$\frac{\gamma}{2} = -\frac{1}{2}\left(k_z^2 + \frac{n^2}{\bar{r}_c^2}\right)$,
3	$-\lambda\gamma + 2\frac{n^2}{\bar{r}_c^3} = -3\Omega$,

therefore,

$$\Omega = -\frac{1}{3}\left(\frac{M''(\bar{r}_c)}{M'(\bar{r}_c)} - \frac{1}{\bar{r}_c} \right) \left(k_z^2 + \frac{n^2}{\bar{r}_c^2} \right) - \frac{2n^2}{3\bar{r}_c^3}. \tag{5.1.55}$$

To conclude, for $\varsigma^4 << 1$, the solutions at the critical layer are

$$\widetilde{p}_{F1} = \alpha_{F1} \varsigma^3 + O\left(\varsigma^4\right), \tag{5.1.56a}$$

and

$$\widetilde{p}_{F2} = \alpha_{F2} \left(1 - \frac{1}{2}\left(k_z^2 + \frac{n^2}{\bar{r}_c^2} \right) \varsigma^2 + \Omega \widetilde{p}_{F1} \ln \varsigma \right) + O\left(\varsigma^4\right), \tag{5.1.56b}$$

where $\alpha_{F1,F2}$ are constants. In full, the pressure is expressed as

$$\widetilde{p}_F(\bar{r}) = \alpha_{F1}\left(\bar{r}-\bar{r}_c\right)^3 + \alpha_{F2}\left(1-\frac{1}{2}\left(k_z^2+\frac{n^2}{\bar{r}_c^2}\right)\left(\bar{r}-\bar{r}_c\right)^2 + \Omega\alpha_{F1}\left(\bar{r}-\bar{r}_c\right)^3\ln\left(\bar{r}-\bar{r}_c\right)\right) + O\left(\left(\bar{r}-\bar{r}_c\right)^4\right). \quad (5.1.57)$$

This solution is consistent with Brambley *et al.* (2012), Belyaev (2012) and Campos and Serrao (1998).

The log singularity is finite at $\varsigma = 0$ by L'Hopital's rule i.e.

$$\lim_{\varsigma\to 0}\varsigma^3\ln\varsigma = \lim_{\varsigma\to 0}\frac{(\ln\varsigma)'}{(1/\varsigma^3)'} = \lim_{\varsigma\to 0}\frac{1/\varsigma}{-3/\varsigma^4} = 0, \quad (5.1.58)$$

as expected.

For negative ς the log is defined as

$$\ln(|\bar{r}-\bar{r}_c|) + j\pi, \qquad \bar{r} < \bar{r}_c. \quad (5.1.59)$$

5.1.4 $\delta = 0$: Scattering Case

The scattering effect of the cylinder and the refraction effect of the boundary layer were added to the model simultaneously. If the boundary layer is set equal to a thickness of zero then the total field may be separated into the incident and scattered field.

Mathematically, this is expressed by the familiar Fourier series of inverse Fourier transforms where under these conditions $\widetilde{\alpha}(1,k_z) = \widetilde{p}_i + \widetilde{p}_s$

$$p_t = \frac{1}{(2\pi)^2}\sum_{n=-\infty}^{\infty}\left(\int_{-\infty}^{\infty}\left(\widetilde{p}_i+\widetilde{p}_s\right)\mathrm{e}^{-jk_z\bar{z}}\,\mathrm{d}k_z\right)\,\mathrm{e}^{-jn\bar{\phi}}. \quad (5.1.60)$$

The result can be derived from the incident field as in McAlpine, Gaffney and Kingan (2015) or from the solution presented here.

The transformed pressure of the surface of the cylinder is given by

$$\widetilde{\alpha}(1,k_z) = -\left(\frac{2j}{\pi[1+\delta]}\right)\left(\frac{\widetilde{\eta}_n}{\widetilde{f}_n\Big|_{1+\delta}k_r\mathrm{H}_n^{(2)\prime}(k_r[1+\delta]) - \widetilde{f}_n'\Big|_{1+\delta}\mathrm{H}_n^{(2)}(k_r[1+\delta])}\right), \quad (5.1.61)$$

so if the boundary layer is of infinitesimal thickness, $\delta = 0$, $\widetilde{\alpha}$ reduces to

$$\lim_{\delta\to 0}\widetilde{\alpha}_n(1,k_z) = -j\frac{2}{\pi}\,\frac{\widetilde{\eta}_n}{k_r\mathrm{H}_n^{(2)\prime}(k_r)}, \quad (5.1.62)$$

on the surface of the rigid cylinder because $\widetilde{f}(1) = 1$ and $\widetilde{f}'(1) = 0$. With the aid of the

Wronskian identity

$$\mathrm{J}_\ell(\square)\mathrm{H}_\ell^{(2)\prime}(\square) - \mathrm{J}_\ell'(\square)\mathrm{H}_\ell^{(2)}(\square) = -\jmath\frac{2}{\pi\square}, \tag{5.1.63}$$

the function $\widetilde{\alpha}$ can be expressed as

$$\widetilde{\alpha}_n(1,k_z) = \widetilde{\eta}_{i,n}\frac{\mathrm{J}_n(k_r)\mathrm{H}_n^{(2)\prime}(k_r) - \mathrm{J}_n'(k_r)\mathrm{H}_n^{(2)}(k_r)}{\mathrm{H}_n^{(2)\prime}(k_r)}, \tag{5.1.64}$$

which, when separated leads to

$$\widetilde{\alpha}_n(1,k_z) = \widetilde{\eta}_{i,n}\mathrm{J}_n(k_r) - \widetilde{\eta}_{i,n}\frac{\mathrm{J}_n'(k_r)\mathrm{H}_n^{(2)}(k_r)}{\mathrm{H}_n^{(2)\prime}(k_r)}. \tag{5.1.65}$$

If we note that the first part of Equation (5.1.65) is the incident field as defined in Equation (5.1.6), we can infer that the remainder must be the transformed scattered field:

$$\widetilde{p}_s = -\widetilde{\eta}_{i,n}\frac{\mathrm{J}_n'(k_r)}{\mathrm{H}_n^{(2)\prime}(k_r)}\mathrm{H}_n^{(2)}(k_r), \tag{5.1.66}$$

where $\mathrm{H}_n^{(2)}(k_r)$ can be interpreted as an outgoing cylindrical wave on the surface of the cylinder and the Bessel function derivatives occur owing to the rigid boundary conditions, which requires the pressure derivative to equal zero.

5.2 Installed Method and Validation

With the installation model now complete, the matter at hand is implementing the resulting equations. The model is implemented by MATLAB, from henceforth the numerical implementation will be referred to as either the method or code. The aim of this section is to validate the method. To achieve this end, initially the method is described with attention paid to mathematical characteristics that are exploited. The various components in the code that need validating are then done so: Fourier sum, ODE solver, critical layer and optimisation by interpolation. Under certain conditions the new solution is compared to existing predictions to validate the method.

The Wiener–Hopf method is different so discussed separately.

5.2.1 Description of Method

This section describes the method to implement the pressure on the surface of the cylinder from a spinning mode. The discussion in Section 3.2.1 on the decay of the Bessel functions as k_z goes large and the behaviour at $k_z^{\pm}$ is still valid and need not be reproduced. The solution for the wave on the surface of the cylinder immersed in a

boundary layer is given by the Fourier series

$$p_t(a_0, \bar{\phi}, \bar{z}) = \frac{1}{(2\pi)^2} \sum_{n=-\infty}^{\infty} \left(\int_{-\infty}^{\infty} \widetilde{\alpha}_n(k_z)\, \mathrm{e}^{-jk_z\bar{z}} \mathrm{d}k_z \right) \mathrm{e}^{-jn\bar{\phi}} \,. \tag{5.2.1}$$

The incoming wave may be any source, so long as it is in the appropriate form. For this discussion the spinning mode (l, q), i.e.

$$\widetilde{\eta}_{lq,n}(k_z) = \pi^2 \xi_{lq} P_{lq} (-1)^{l+n} \mathrm{e}^{-j(l-n)\beta} \left(k_0 + k_z M_\infty\right) \Psi_{lq} \mathrm{H}^{(2)}_{l-n}(k_r b) \,, \tag{5.2.2}$$

is chosen.

Figure (5.3) shows the process to calculate $\widetilde{\alpha}_n(k_z)$. Equation (5.1.18) is integrated using a standard Ordinary Differential Equation solver, starting from the surface of the cylinder at $\bar{r} = 1$, up to the edge of the boundary layer $\bar{r} = 1 + \delta$. If, for the prescribed value of k_z, there is a critical layer, the ODE solver integrates to near the critical layer at $\bar{r} = \bar{r}_c - \varepsilon$. Then the Frobenius solution is used to the bridge the layer, and the ODE solver is restarted on the other side of the critical layer at $\bar{r} = \bar{r}_c + \varepsilon$. The integration continues until the edge of the boundary layer at $\bar{r} = 1 + \delta$. At this point the boundary-layer solution is matched to the solution for uniform flow, which determines $\widetilde{\alpha}_n(k_z)$. The total pressure on the surface of the cylinder is then evaluated by integrating $\widetilde{\alpha}_n$ over k_z, in order to calculate the Fourier harmonics in the Fourier series solution (5.1.24). An appropriate number of harmonics are needed to ensure that the series has converged.

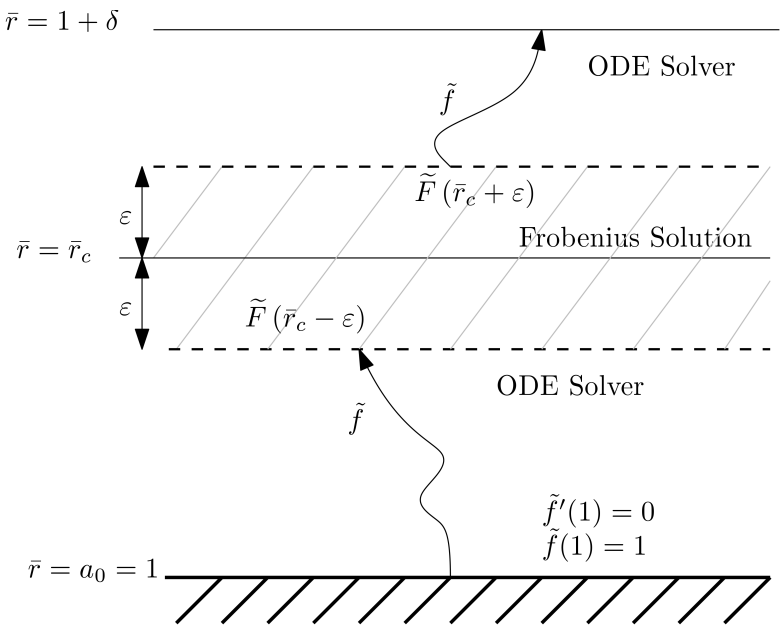

Figure 5.3: Illustration showing the method to solve the Pridmore-Brown equation in the boundary layer for a given harmonic n. The numerical solution obtained using a standard ODE solver is matched to the Frobenius solution either side of the critical layer, in order to bridge the critical point $\bar{r}_c$.

5.2.2 Validation

The new mode source code is verified in the section by inspecting the convergence of the Fourier sum and comparing against: established results of Fuller (1989), an existing method and against published refraction predictions. This code is compared against the mode source code for verification.

Fourier Series

To save time, the infinite Fourier series is truncated at a finite order. This is possible because the transformed incident wave amplitude decreases with increasing harmonic order. This is proved by the large order asymptote for the complex amplitude for the radiating mode

$$\lim_{n\to\infty} |\widetilde{\eta}_{n,lq}| \sim \lim_{n\to\infty} \left|\mathrm{H}^{(2)}_{n-l}(k_r b)\right| \propto \lim_{n\to\infty} j\sqrt{\frac{2}{\pi(n-l)}}\left(\frac{ek_r b}{2(n-l)}\right)^{l-n} = 0. \tag{5.2.3}$$

It is more difficult to explain why the denominator in Equation (5.1.22) either grows or at least remains finite because it depends on the result of the ODE solver.

A numerical example of convergence is presented. The Fourier series (5.1.24) is truncated at the $n = N$th term, once it has been verified that inclusion of further terms add a negligibly small contribution to the result. The value of N is not fixed, because it will depend on the parameters of each specific calculation (see the asymptotic approximation above, the ratio of k_r and b is clearly important). To verify the convergence of the Fourier series, the average root-mean-square (rms) relative error, ϵ_t, which is defined by

$$\epsilon_t(N') = \sqrt{\frac{1}{\mathrm{M}^\sharp}\sum^{\mathrm{M}^\sharp}\left|\frac{p_{tN'} - p_{tN}}{p_{tN}}\right|^2}, \tag{5.2.4}$$

is computed, where the subscript N' denotes the pressure field calculated by truncating at the $n = N'$th term. The squared relative error is then averaged over all the grid points on the surface of the cylinder (total number of points equals $\mathrm{M}^\sharp$). A typical example of the relative error is plotted in Figure (5.4). As N' increases, the error ϵ_t decreases until it is very small. In this example convergence is not achieved until the number of terms in the Fourier series has exceeded thirty.

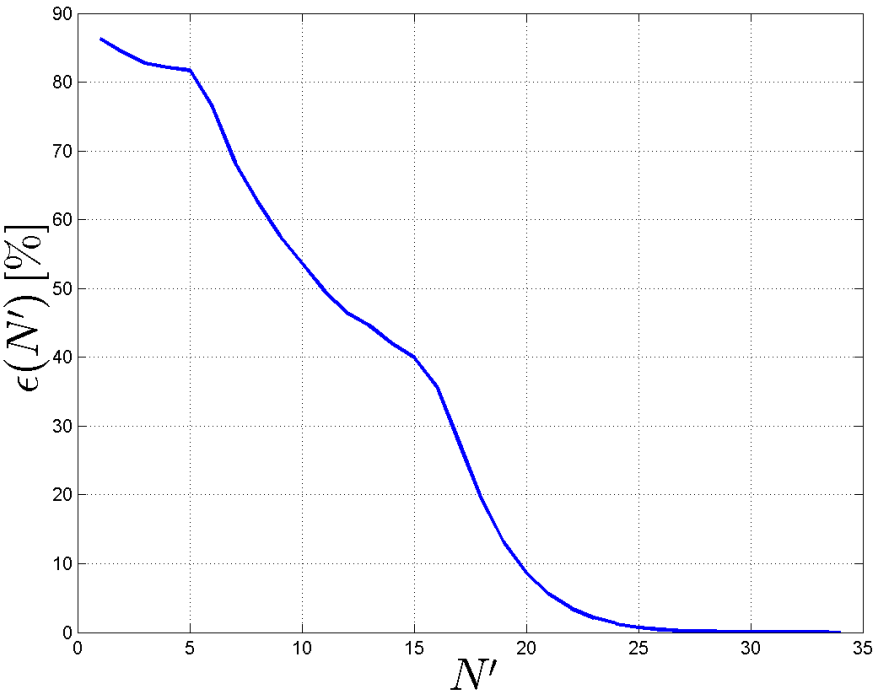

Figure 5.4: Example of convergence for the boundary-layer refraction cylinder scattering code as the number of harmonics in the Fourier series are increased to the final solution. The relevant parameters in this example are: $k_0 a = 10$, $a = 0.5$, $(l, q) = (4, 1)$, $b = 3$, $\delta = 0.1$ and $M_\infty = 0.75$.

Comparison to Fuller (1989)

The best way to validate the theory and method is to reproduce and compare against similar, published results. As the spinning mode source has not been formulated in previous work of this type of installation problem, it is difficult to find an exact comparison. A good paper would be Dierke *et al.* (2013) but the thickness of the boundary layer is not constant and never explicitly stated. Therefore the monopole approximation discussed in the previous chapter is used (Equation (3.2.2), page 38). Fuller (1989) published a solution for a monopole impinging on a rigid, infinite cylinder. He defined a coefficient

$$\alpha_c \,[\mathrm{dB}] = 20 \log_{10} \left(\frac{p_t}{p_i} \right), \tag{5.2.5}$$

and is plotted around half a rigid cylinder.

Figure (5.5) is the plane wave mode α_c predictions of radius $a = 0.01$, as discussed in the previous chapter, with no flow at several low values of wavenumbers. Under these conditions the two models may be compared. Figure (5.5) shows good agreement between the two methods and thus validates the new method under the limiting conditions described.

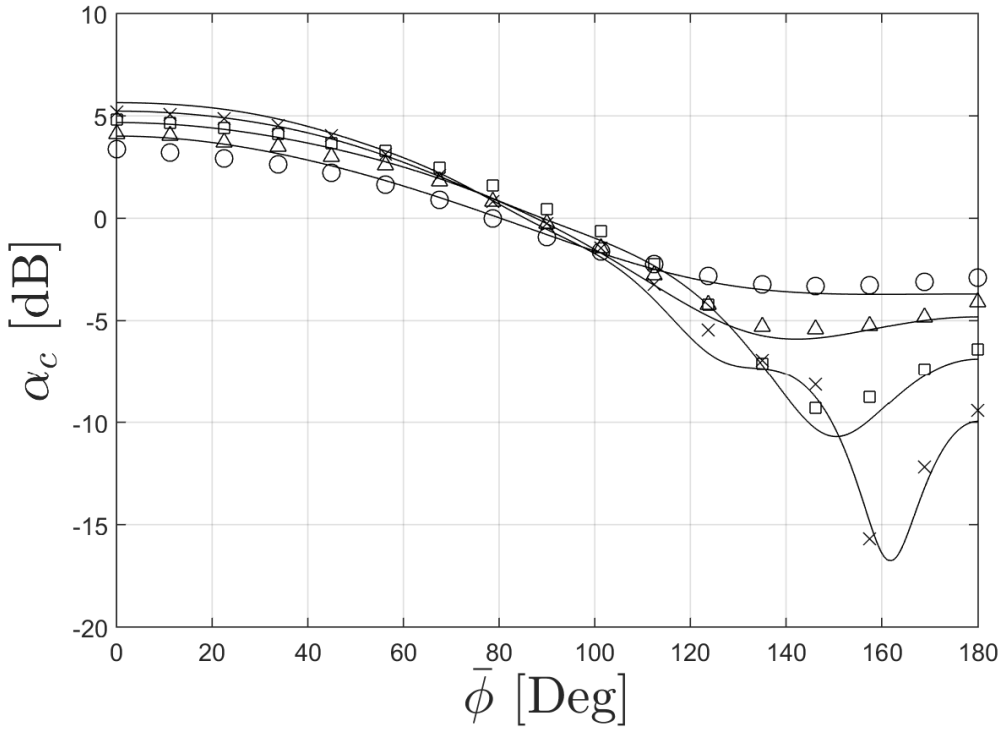

Figure 5.5: A reproduction of the scattering case in quiescent flow and the same variables given in Fuller (1989). The new code (solid lines) and; $k_0a_0 = 0.5$ ($\circ$), $k_0a_0 = 1$ ($\triangle$), $k_0a_0 = 2$ ($\square$) and $k_0a_0 = 4$ ($\times$). The other variables are: $a = 0.01$, $(l, q) = (0, 1)$, $b = 3$ and $M_\infty = 0$.

These results were chosen as a validation example because at the low frequencies the majority of the inverse Fourier transform is in the evanescent part of the spectrum. The critical layer is in this part of the spectrum (I_1). The agreement between Fuller and the new method shows that the modified Bessel functions are implemented correctly.

Comparison to Uniform Flow Solutions

A standard Runge–Kutta numerical integration routine is used to solve the Pridmore-Brown equation in the boundary-layer region. The solver can be checked by comparison with an analytic solution for the special case $M(\bar{r}) = M_\infty$. In this case, the Pridmore-Brown equation (Eq (5.1.13)), reduces to Bessel's differential equation. Hence, the normalised pressure can be expressed in terms of Bessel functions, in the form

$$\widetilde{f_n} = A_n(k_z)\mathrm{J}_n(k_r\bar{r}) + B_n(k_z)\mathrm{Y}_n(k_r\bar{r})\,. \tag{5.2.6}$$

The amplitude coefficients are determined by the boundary conditions:

$$\begin{Bmatrix} A_n(k_z) \\ B_n(k_z) \end{Bmatrix} = \begin{Bmatrix} 1 \\ 0 \end{Bmatrix} \begin{bmatrix} \mathrm{J}_n(k_r a_0) & \mathrm{Y}_n(k_r a_0) \\ k_r\mathrm{J}'_n(k_r a_0) & k_r\mathrm{Y}'_n(k_r a_0) \end{bmatrix}^{-1}. \tag{5.2.7}$$

These results are shown in Figure (5.6). The ODE solver gives extremely similar results, so close they are practically identical. This demonstrates that the ODE solver is implemented correctly.

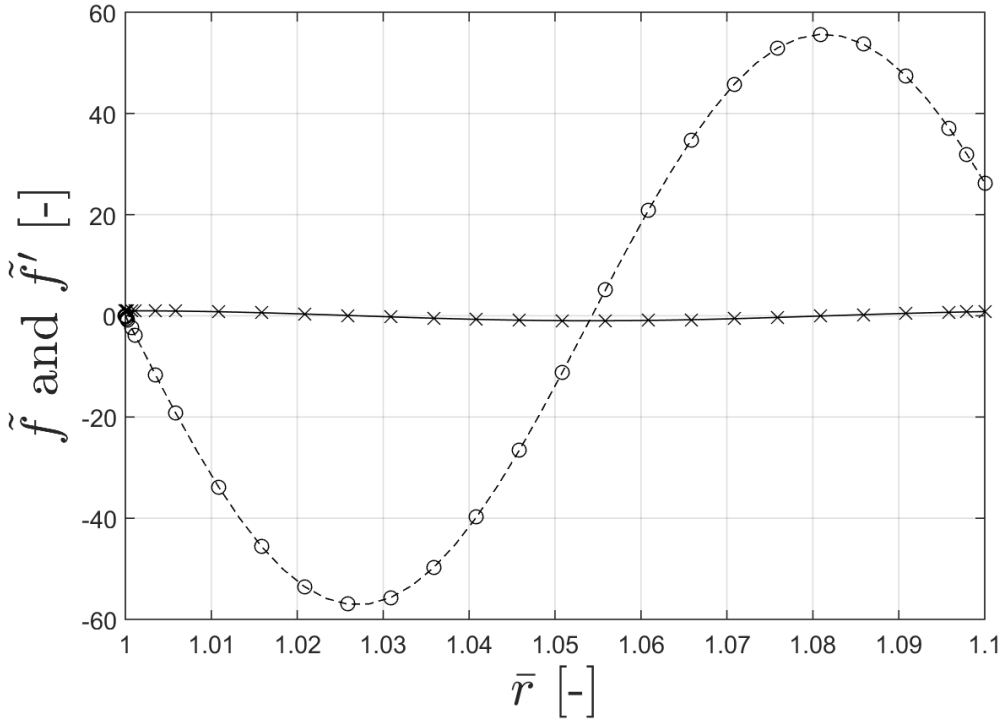

Figure 5.6: Solutions for $\widetilde{f}$ ODE solver (solid line) and theoretical ($\times$) and $\widetilde{f}'$ ODE solver (dashes) and theoretical ($\circ$). Parameters are: $k_0 a = 20$, $a = 0.5$, $(l, q) = (16, 1)$, $k_z = 95$, $b = 3$, $M_\infty = 0.75$ and $n = 0$.

Comparison to SYMPHONY methods

Having verified the accuracy of the numerical integration solver, the new method is compared against an in-house code. A code developed for the SYMPHONY project (McAlpine, 2013) includes the distributed source with a cylinder in uniform flow. By comparing the refraction with an infinitesimal boundary layer ($\delta = 0$) or of a finite boundary layer but on setting $M(\bar{r}) = M_\infty$, the two codes can be compared.

The SYMPHONY code is for uniform flow only. Verification of this code is published in McAlpine, Gaffney and Kingan McAlpine *et al.* (2015). Accordingly, all the verification results have been obtained by setting $M(\bar{r}) = M_\infty$, i.e. a finite thickness boundary-layer region is specified, but in this region, the flow velocity is set equal to the free stream velocity outside the boundary layer. This means that the term involving M' in Equation (5.1.18) is zero; otherwise, implementation of the boundary-layer refraction cylinder scattering code is identical to simulations when $M(\bar{r})$ is not set equal to a constant.

Figure (5.7) shows the normalised total pressure on the unfurled cylinder (in Sound

Pressure Level), calculated using the boundary-layer refraction cylinder scattering code. The SYMPHONY code was used as the reference result to calculate the relative error shown in Figures (5.8.a) and (5.8.b). The pressure field has been calculated in the axial region from $\bar{z} = 0$ (source plane) to $\bar{z} = 5$. Numerical results from the two methods show excellent agreement. For either of the boundary-layer thicknesses the relative error is significantly less than 1 % over the whole domain.

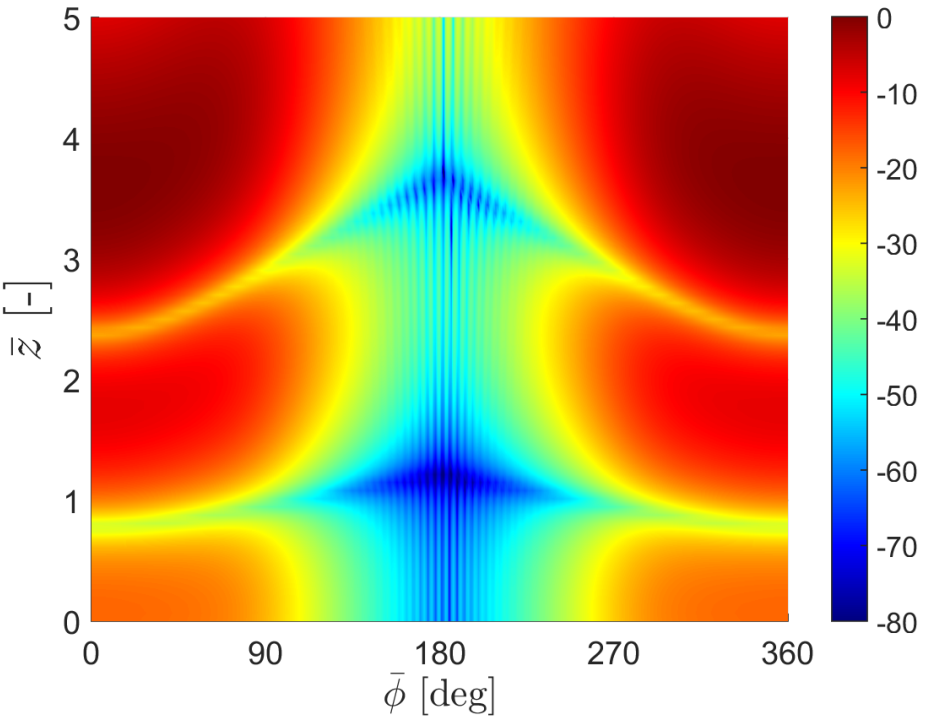

Figure 5.7: Normalised SPL using the uniform scattering code. The relevant parameters in this example are: $k_0 a = 20$, $a = 0.6$, $(l, q) = (16, 1)$, $b = 6$ and $M_\infty = 0.7$.

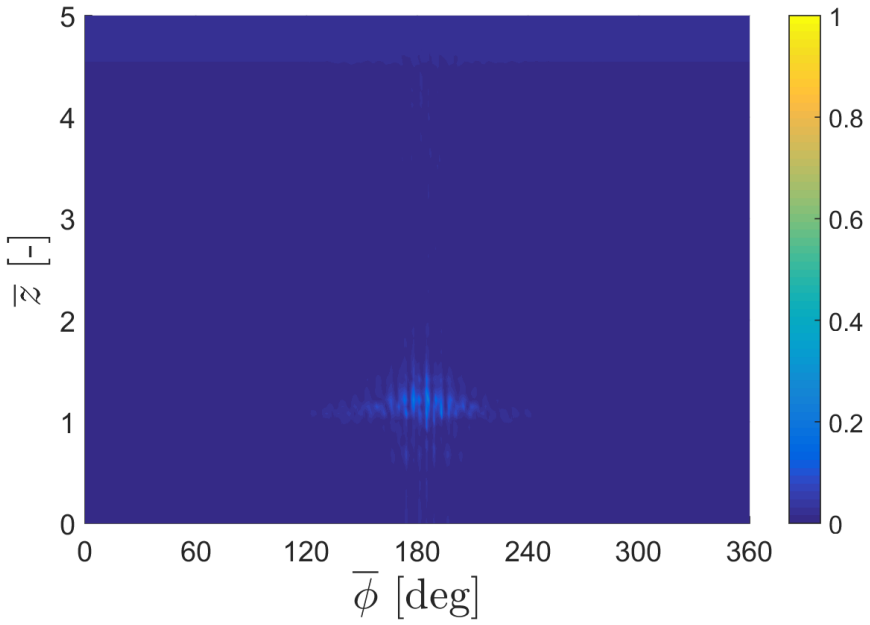

(a) Relative error (%) of the total pressure field calculated using the boundary-layer refraction cylinder scattering code with $\delta = 0.01$.

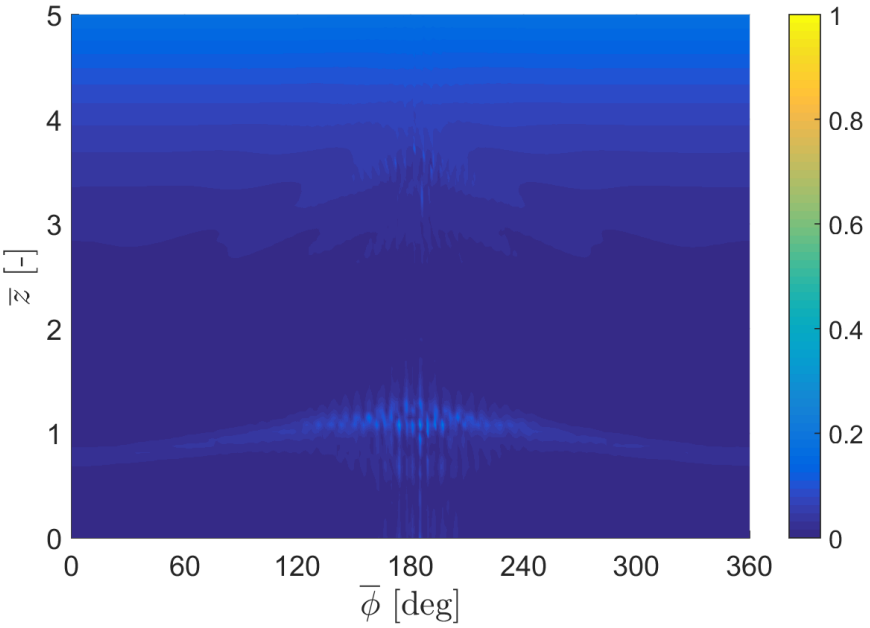

(b) Relative error (%) of the total pressure field calculated using the boundary-layer refraction cylinder scattering code with $\delta = 0.1$.

Figure 5.8: Comparison of the boundary-layer refraction and uniform flow cylinder scattering codes (SPL shown in Figure (5.7)). The relevant parameters in this example are: $k_0 a = 20$, $a = 0.6$, $(l, q) = (16, 1)$, $b = 6$ and $M_\infty = 0.7$.

Comparison to Lu (1990)

Lu (1990) examined a point monopole source located adjacent to a rigid cylinder, and calculated the pressure on the cylinder including the effect of boundary-layer refraction. In Lu (1990), Figure (6), he plots predictions of the difference between the SPL on the cylindrical fuselage at $\bar{\phi} = 0$ and the corresponding value of the SPL in the free field (in the absence of the cylinder). Negative values indicate shielding.

The comparison is shown here in Figure (5.9). The two predictions show similar agreement downstream of the source. However, upstream of the source, the two predictions do not compare well. Slightly upstream of the source, the prediction by Lu has an extremely rapid roll off, indicating extremely high shielding upstream. The prediction for the compact disc source has a lesser roll off rate, indicating less shielding. However, the shielding is still substantial with increasing axial distance upstream of the source. Lu's predictions for shielding decrease with increasing positive $\bar{z}$, this is physically unrealistic. It is difficult to draw a definitive conclusion from this result because there is only one example to compare against.

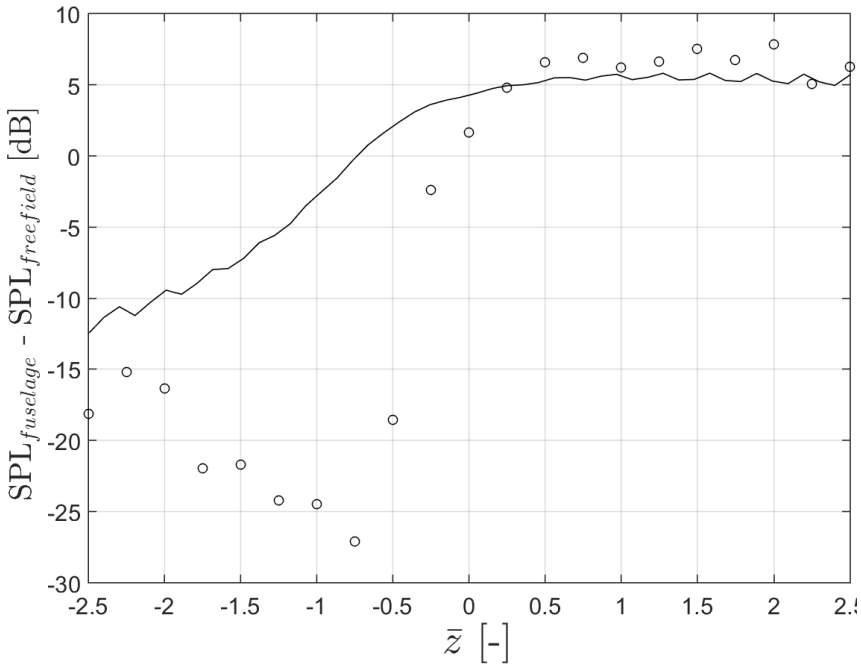

Figure 5.9: Difference in the predicted SPL between the installed fuselage pressure and the incident field pressure at $\bar{\phi} = 0$. Boundary-layer refraction cylinder scattering code (solid line) and prediction by Lu (1990) ($\circ$). The relevant parameters are: $k_0 a = 0.0523$, $(l, q) = (0, 1)$, $a = 0.01$, $b = 1.5$, $\delta = 0.125$ and $M_\infty = 0.7$.

Critical layer and Interpolation

The last part of the code to validate is the special attention paid to the critical layer; a Frobenius series is required when integrating along the real line. The implementation is

tested by varying the width of the series and inspecting the effect on the results. The correct value is taken when in a region where ϵ does not affect the results. To decrease computational time the integrand can be reused for each axial location. The following part discusses the optimisation by interpolation.

Figures (5.10) and (5.11) show the effect of evaluating integral I_1 while taking different widths of the critical layer Frobenius solution – the series is used in place of the numerical integration. The critical layer, where $k_0 + k_z M(\bar{r}_c) = 0$, will occur at $k_z < -M/k_0$, which lies in the region $k_z \in (-\infty, k_z^-]$. Thus, the critical layer will only affect integral I_1. As well as altering the width of the critical layer, the number of interpolation points used to evaluate $\widetilde{\alpha}_n$ also will affect the evaluation of I_1 (page 30).

The Frobenius series solution has been truncated at $\mathrm{O}(\varsigma^3)$, Equation (5.1.57) on page 77. Although it is required that the width of the critical layer is small, if ε is too small the ODE solver will lose accuracy. To establish an appropriate value for ε, the width of the Frobenius solution was varied whilst calculating the value of the integral I_1 for the zero-th Fourier harmonic. In Figure (5.10) it is seen that at a low frequency, the width of the critical layer series solution has little effect on the value of I_1. The results for $\varepsilon = 0.001$ and 0.002 are almost exactly the same. Therefore the value used for the reference solution was selected as $\varepsilon = 0.002$.

At a higher frequency, as shown in Figure (5.11), it is seen that the width of the critical layer does not change the value of I_1 significantly. This is because the contribution of the critical layer decreases as the frequency increases (Brambley *et al.*, 2012). Also, this is further compounded by the increased rate of decay of $\widetilde{\alpha}_n(k_z)$ outside the region $k_z \in (k_z^-, k_z^+)$ at higher frequencies.

The convergence results show that the ideal width of the critical layer, where the Frobenius series solution is applied, is between $\varepsilon = 0.001$ to 0.00". The reference value for all the results selected was $\varepsilon = 0.0015$.

The inverse Fourier transform integral Equation (5.1.24) is computationally expensive, and has to be evaluated at each axial position. However, the function $\widetilde{\alpha}_n(k_z)$ does not depend on $\bar{z}$, therefore $\widetilde{\alpha}_n$ may be pre-calculated for each harmonic order n. A spline interpolation routine is implemented to evaluate $\widetilde{\alpha}_n(k_z)$ at any value of k_z required by the adaptive numerical integration solver.

Since the function $\widetilde{\alpha}_n(k_z)$ can be highly oscillatory, the number of interpolation points must be sufficient to ensure accurate interpolation, and thus accurate evaluation of the inverse Fourier transform. Figures (5.10) and (5.11) show convergence results for two different frequencies. As the number of interpolation points of $\widetilde{\alpha}_n(k_z)$ is increased, convergence is achieved reasonably quickly. In an effort to normalise the number of interpolation points (N) of the function $\widetilde{\alpha}_n(k_z)$ by the axial wavenumber, we divide N by $k_z^+ - k_z^-$ (denoted by k_z^Δ). It is seen that convergence is achieved at a higher rate for the higher frequency, compare Figure (5.11) with Figure (5.10). The two frequencies

have a similar integration range, due to the slower decay rate of $\widetilde{\alpha}(k_z)$ as $k_z \to \pm\infty$ for the lower frequency case. Yet, because there are fewer interpolation points, thanks to the reference value k_z^{Δ}, convergence is achieved at a slower rate for the lower frequency.

These results show that the integral has converged by $N \approx 10\, k_z^{\Delta}$. This reference value was selected for all the results in the thesis.

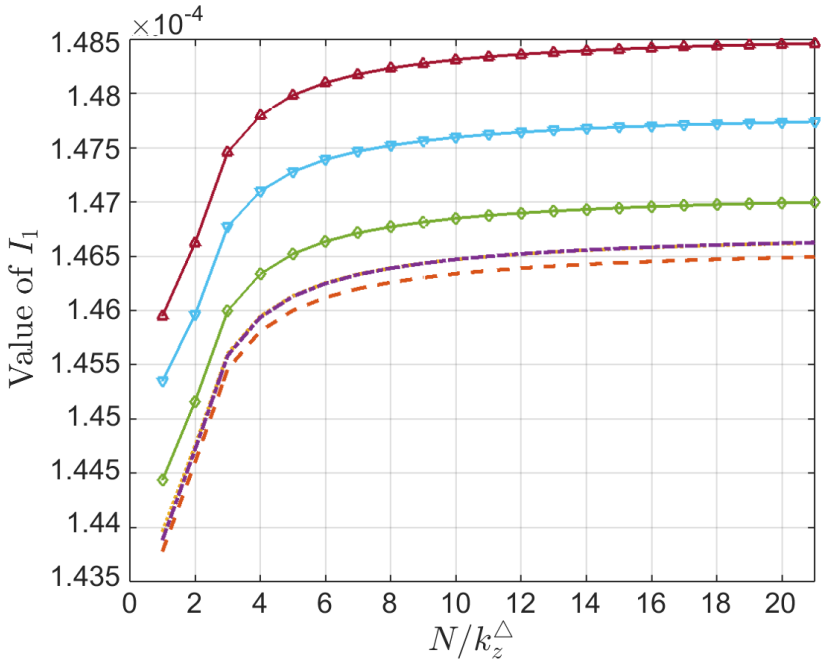

(a) Value of I_1.

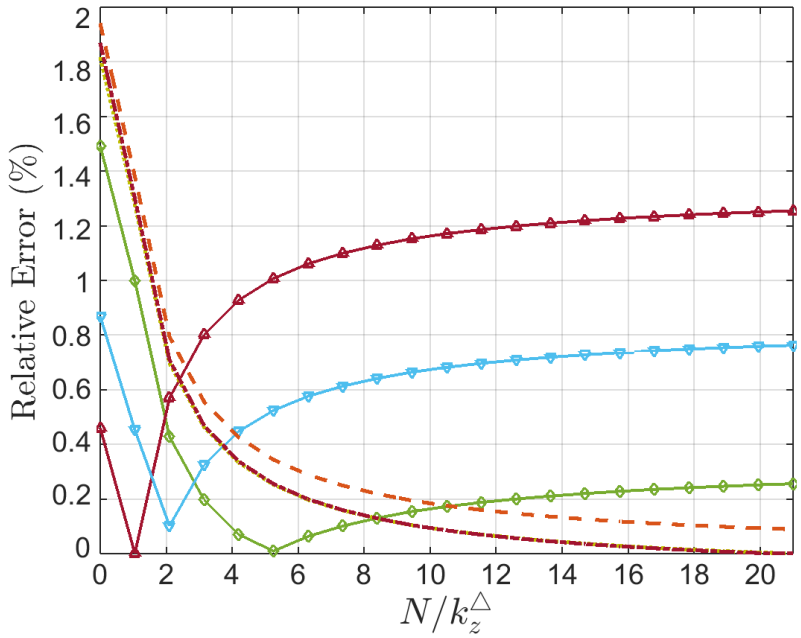

(b) Relative error of I_1.

Figure 5.10: Effect of width of the critical layer (Frobenius solution) and number of interpolation points used to evaluate I_1. Key: $\varepsilon = 0.0002$ (orange dashes), 0.001 (yellow dots), 0.002 (purple dash dots), 0.003 (green, $\diamond$), 0.005 (cyan, ∇) and 0.01 (maroon, $\triangle$). The relevant parameters in this example are: $k_0 a = 0.0524$, $(l, q) = (0, 1)$, $a = 0.01$, $b = 1.5$, $\delta = 0.125$ and $M_\infty = 0.7$.

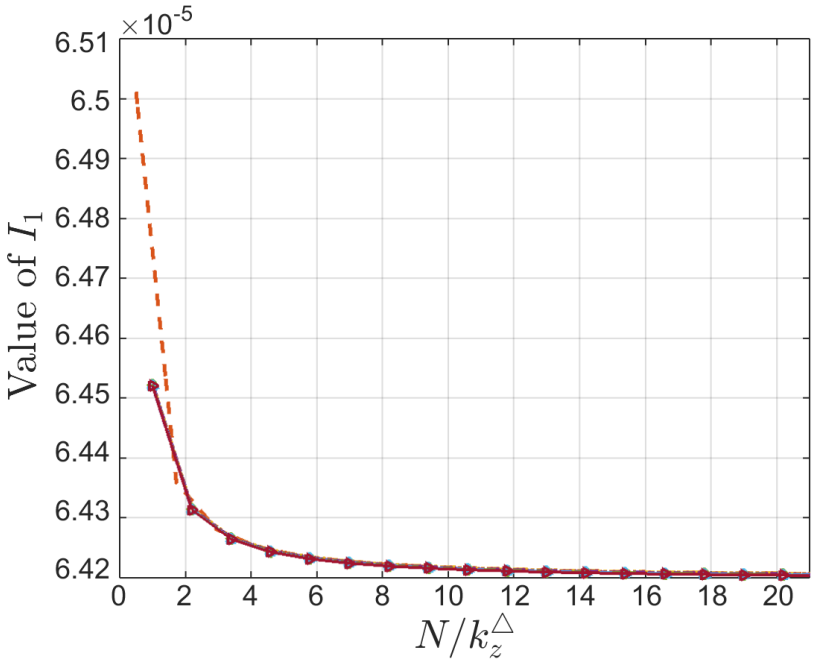

(a) Value of I_1.

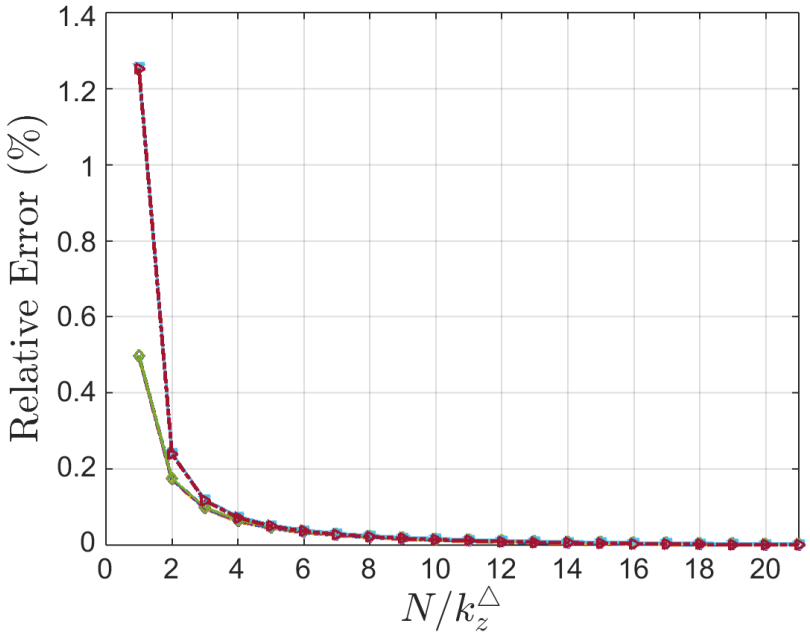

(b) Relative error of I_1.

Figure 5.11: Effect of width of the critical layer (Frobenius solution) and number of interpolation points used to evaluate I_1. Key: $\epsilon = 0.0002$ (orange dashes), 0.001 (yellow dots), 0.002 (purple dash dots), 0.003 (green, $\diamond$), 0.005 (cyan, ∇) and 0.01 (maroon, $\triangle$). The relevant parameters in this example are: $k_0 a = 10$, $a = 0.5$, $(l, q) = (0, 1)$, $b = 3$, $\delta = 0.1$ and $M_\infty = 0.75$.

A common test for numerical solvers is to integrate in one direction, then, using the end results as initial conditions, reverse the direction of integration back to the initial point. If the ODE solver is working correctly, the initial conditions of $\widetilde{f}(1) = 1$ and

$\widetilde{f}'(1) = 0$ should be recovered. This test is shown in Figure (5.12). The integration follows the same path and the end result of $\widetilde{f}(1) = 1$ and $\widetilde{f}'(1) = -1.3536 \times 10^{-4} + j1.4654^{-19}$. This is excellent considering the solution range is very large. It also shows that the Frobenius solution is implemented correctly.

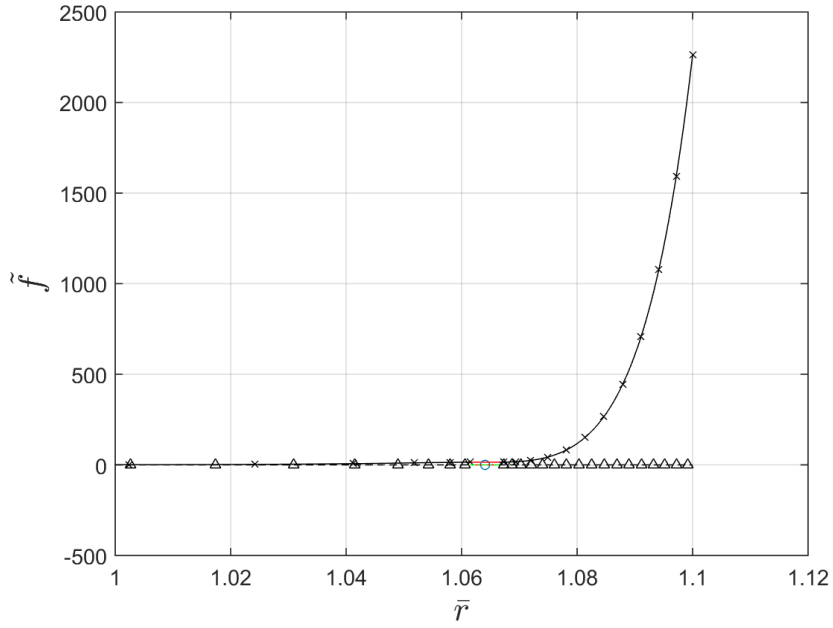

(a) $\widetilde{f}$.

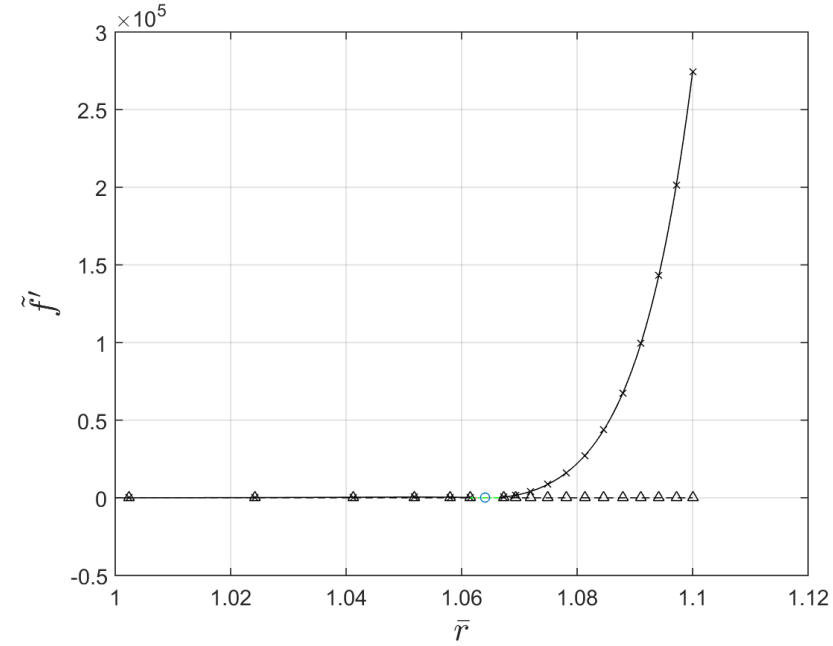

(b) $\widetilde{f}'$.

Figure 5.12: The ODE solver results for a quarter-sine boundary-layer profile of thickness 0.1. The outwards results are shown in the solid (real) and dashed (imaginary) lines, the inwards results are shown with added symbols of $\times$ (real) and $\triangle$ (imaginary). The relevant parameters are $k_0 a = 20$, $a = 0.5$, $(l, q) = (16, 1)$, $b = 3$ and $M_\infty = 0.75$.

Validation of Wiener–Hopf Code

In the last section of this chapter, the installed Wiener–Hopf method is validated. This must be validated separately because the installation method (Graf's Addition theorem, cylinder and the ODE solver) is added to an established incident field method (GXMunt).

The Wiener–Hopf solution for the mode radiating from a cylindrical duct in the free-field has been implemented in a code called GXMunt. To implement the installation method for the Wiener–Hopf incident field the GXMunt code is modified. This is done because it calculates the numerically complicated F_+ function – it is easier to adapt the existing method than calculate this function from scratch. The installed Wiener–Hopf method is compared to the disc source method with uniform flow in order to validate it. To validate the boundary layer component, the Wiener–Hopf source is compared against uniform flow predictions to those with a boundary layer of constant velocity. Lastly, to validate the whole code, refraction predictions for the disc and Wiener–Hopf are compared. These successful comparisons demonstrate that the installed Wiener–Hopf theory is implemented correctly.

The incident field model includes diffraction and is thus too complex for the simple monopole comparison of the previous section.

The incident code is different to the disc method in several ways;

- the non-dimensional geometry is referenced to the duct radius,
- the axial wavenumbers are complex and normalised and the integration contour is deformed from the real axis
- and the time dependency is opposite to the disc method.

The most significant change is the complex wavenumbers and the deformed integration contour. The ODE solver is unchanged by the complex frequency. Serendipitously, the deformed contour avoids the branch cut due to the radial wavenumber and the branch cut along the real axis associated to the critical layer. This means the Frobenius series is largely unneeded. By integrating along a contour displaced from the real axis the singularities at $k_z^{\pm}$ are avoided. Therefore a quicker, less computationally expensive, but ultimately simpler, integration routine may be used to calculate the inverse Fourier transform. This means that the vastly more complex installed Wiener–Hopf code based on GXMunt is significantly quicker than the simpler installed disc source. This is mainly due to abandoning *quadgk*.

The rest of the section demonstrates for some cases the installed Wiener–Hopf field is working correctly.

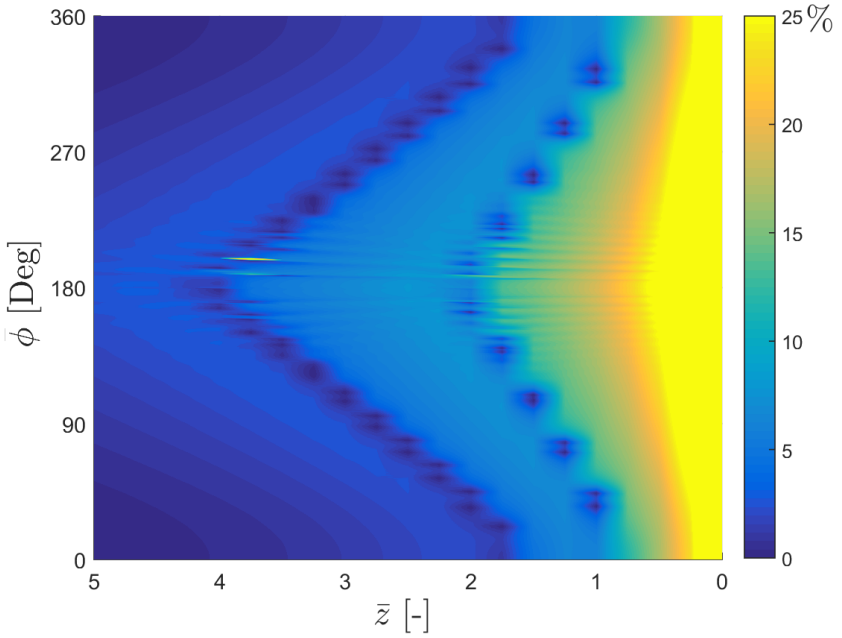

(a) Relative error.

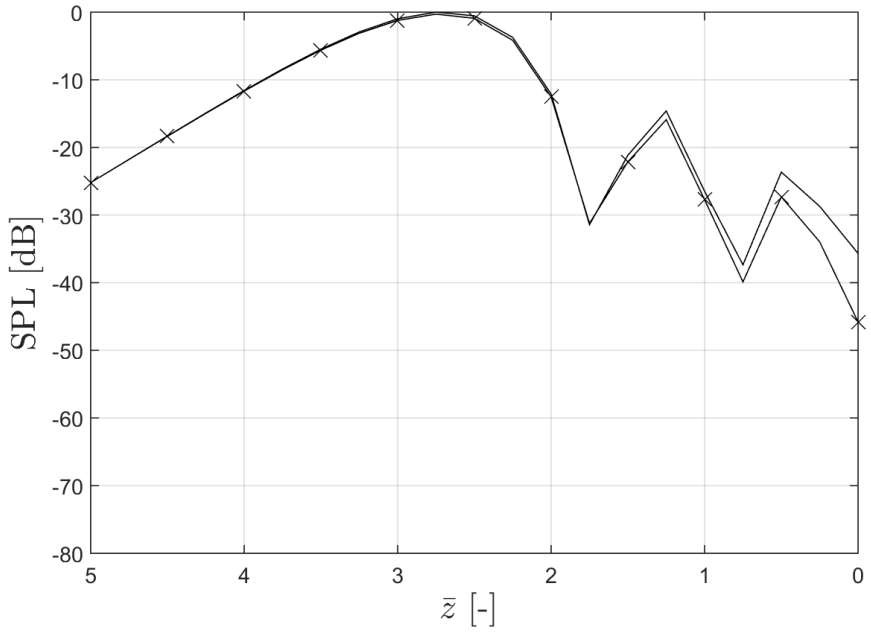

(b) SPL down cylinder at $\bar{\phi} = 0$. Disc source (solid line) and Wiener–Hopf (solid line, $\times$).

Figure 5.13: Relative error for the thick boundary layer for the installed radiating mode. The variables are: $k_0 a = 10$, $a = 0.4$, $(l, q) = (4, 1)$, $\delta = 0.1$, $b = 3$ and $M_\infty = 0.75$.

To ensure that the method (apart from the boundary layer) is implemented correctly, the predictions in uniform flow are compared between the Wiener–Hopf source and the disc source. By evaluating the relative error, shown in Figure (5.13.a), the codes agree well for axial positions greater than about –3.5 cylinder radii. The error is relative, so

on the far-side the reference values are very small which leads to an increase in error. These errors are small enough to have no effect on an SPL scale, Figure (5.13.b), and are therefore negligible.

The magnitude of error increases for axial distances less than –3.5. This is not error. At these small axial values the diffraction effect becomes significant and differences between the models is expected. Note that 3.5 corresponds to a polar angle of approximately 65°, above this polar angle the previous chapter demonstrated that the diffraction becomes significant. The differences between the models are approximately twice the differences in the incident field.

Following is the implementation of the boundary layer. Note that no critical layer is present for this case so this section does not validate any special treatment to the critical layer.

Figure (5.14.a) shows the relative error for the high frequency case for uniform flow and constant shear layer ($M_z = M_\infty$) to the uniform flow for the very cut-on mode of $(l, q) = (4, 1)$. The thickness of the boundary layer is 0.1, which led to marginally more error in the disc source validation.

The relative error of complex pressure shown in Figure (5.14.a) shows that the error is negligible apart from at the extreme end of the cylinder on the far-side. The relatively small errors do not affect the SPL values shown in Figure (5.14.b).

The same process is repeated for the barely cut-on case of $(l, q) = (24, 1)$ shown in Figure (5.15). In this case significantly more error occurs. So much so that the predictions on the logarithmic scale are very different at large axial positions. However, as very little sound radiates to the far end of the cylinder, for this high mode orders this error is not significant. The scale on Figure (5.15.b) descends to –400 dB. The noise floor for the Wiener–Hopf code is 10^{-9} but the numerical noise for the disc source is higher.

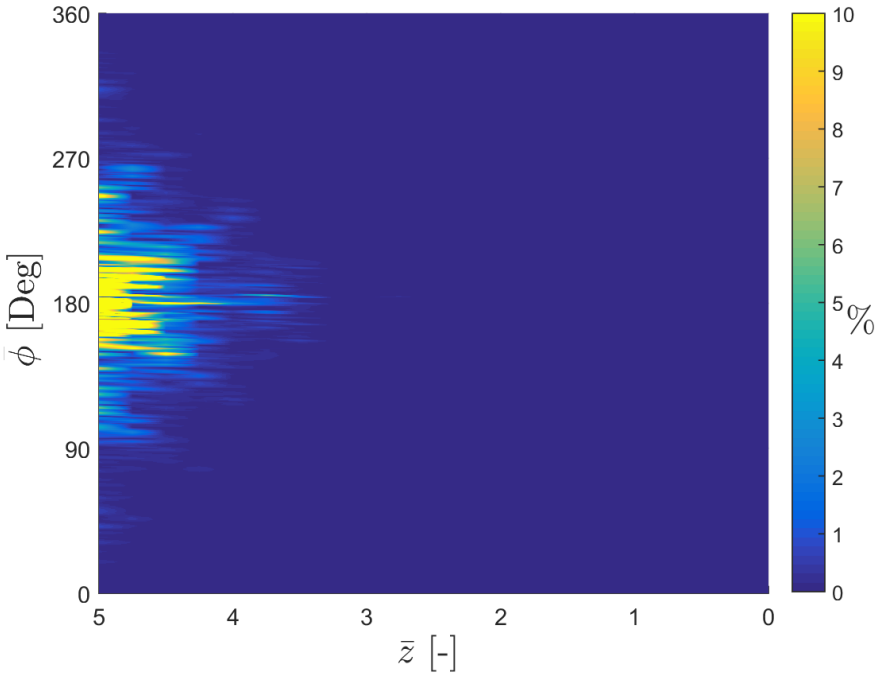

(a) Relative error.

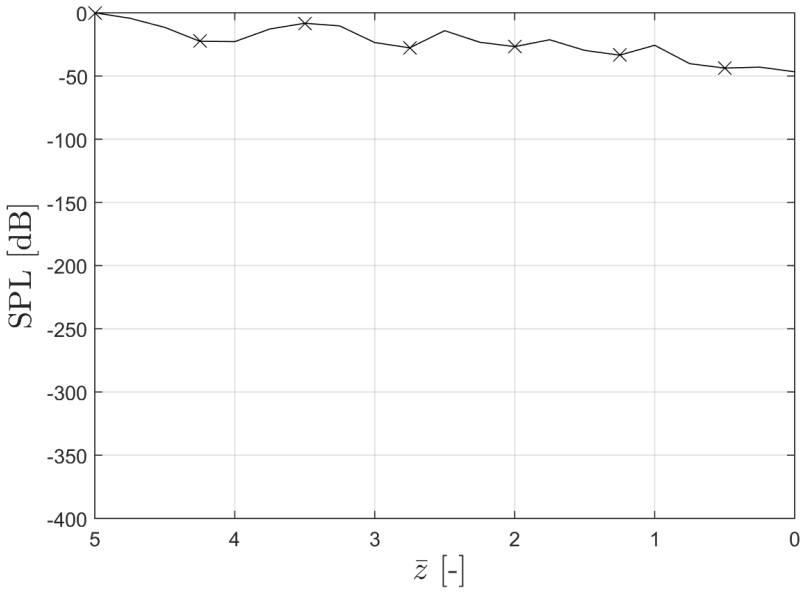

(b) SPL down cylinder at $\bar{\phi} = 0$. Both lines are shown, $\delta = 0$ (solid line) and $\delta = 0.1$ (dashes, $\times$).

Figure 5.14: Relative error for the thick boundary layer for the installed radiating mode. The variables are: $k_0 a = 20$, $a = 0.5$, $(l, q) = (4, 1)$, $\delta = 0.1$, $b = 3$ and $M_\infty = 0.75$.

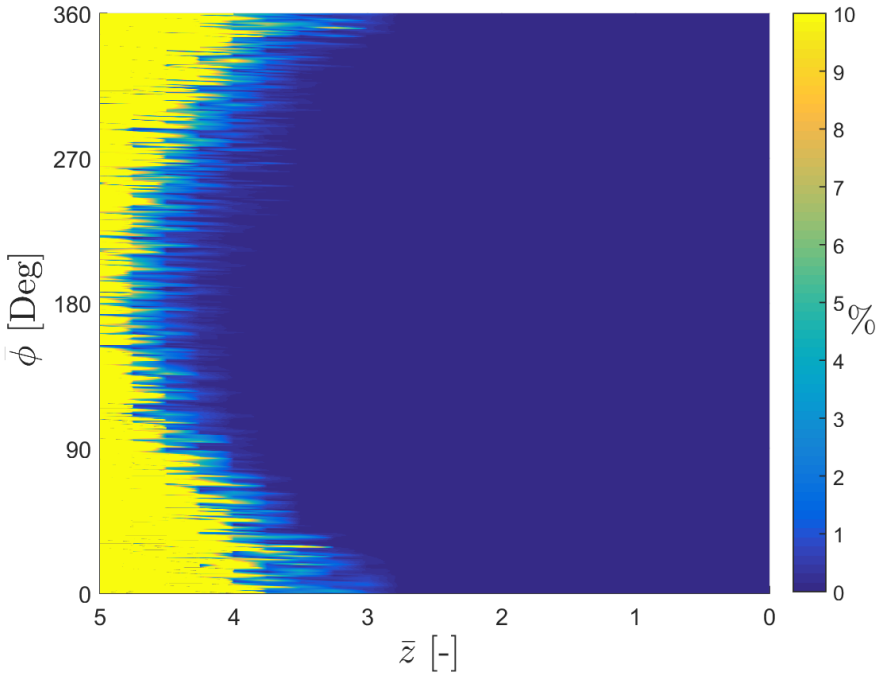

(a) Relative error.

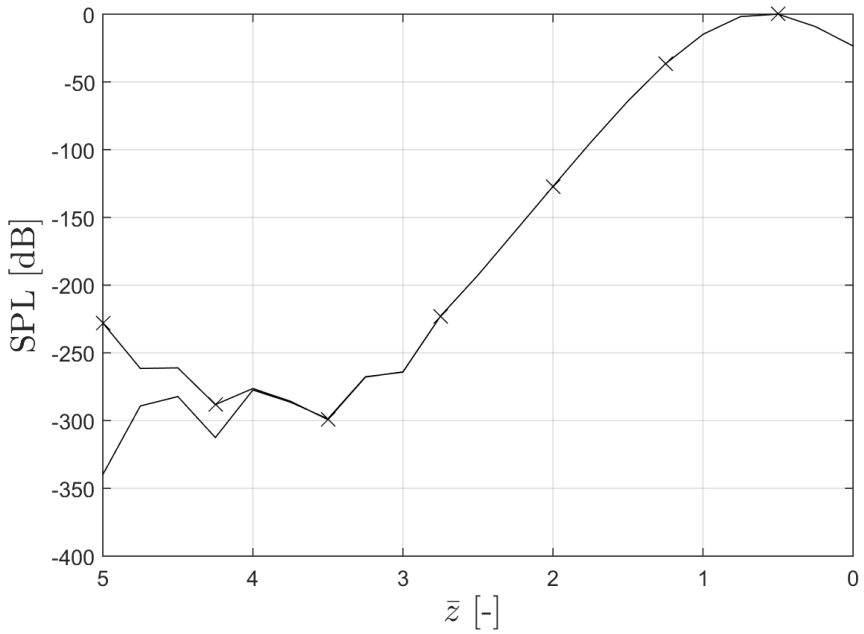

(b) SPL along cylinder at $\bar{\phi} = 0$. Uniform flow (solid line) and Wiener–hopf (solid line, $\times$).

Figure 5.15: Relative error and SPL on the cylinder for the uniform flow case and the thick boundary layer. Note the $y-$axis scale. The variables are: $k_0 a = 20$, $a = 0.5$, $(l, q) = (24, 1)$, $\delta = 0.1$, $b = 3$ and $M_\infty = 0.75$.

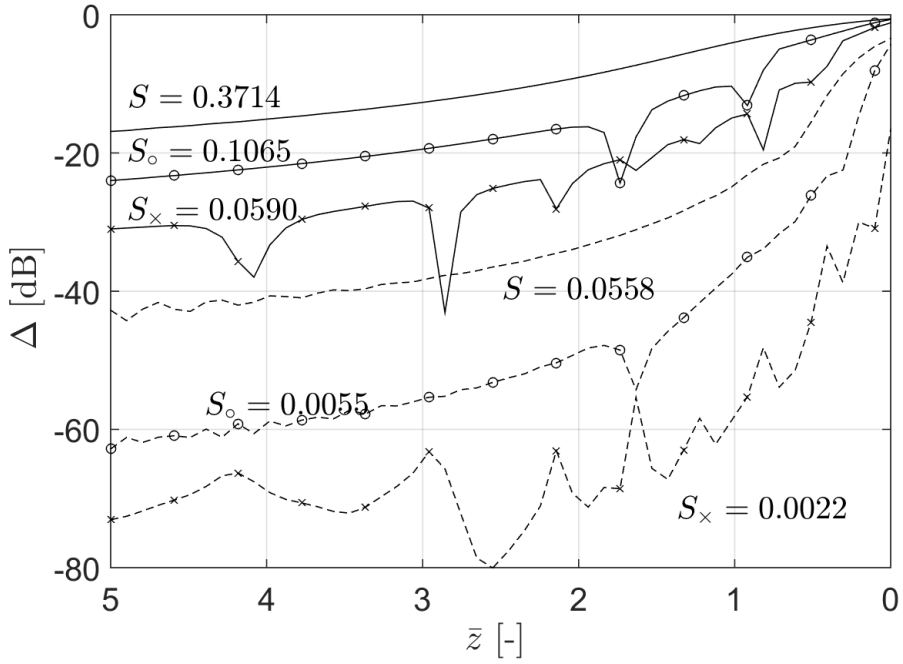

(a) Disc source. Reproduced from Gaffney *et al.* (2016) with S's added to the graph.

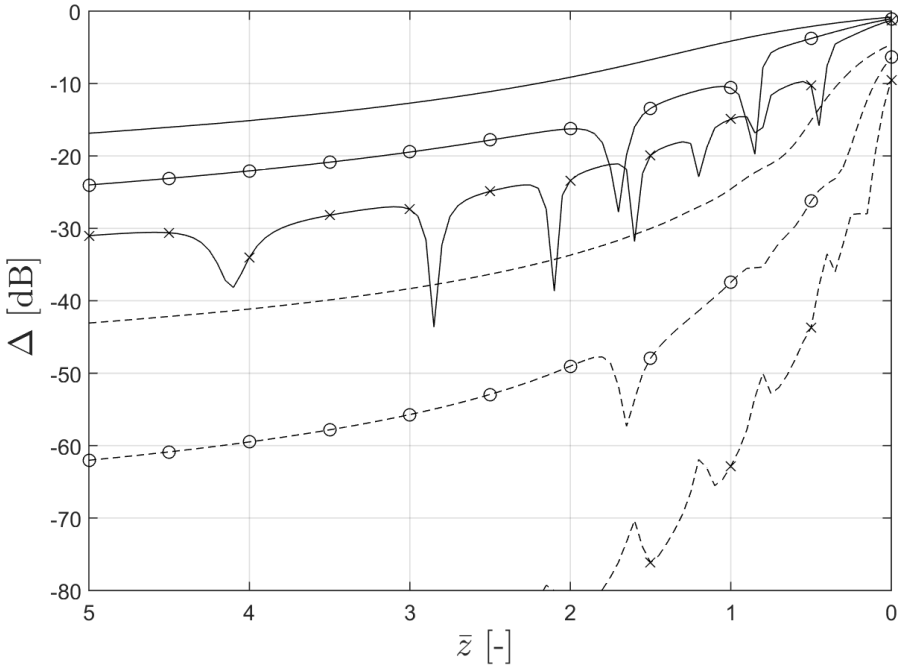

(b) Wiener–Hopf solution.

Figure 5.16: Δ along the cylinder at $\bar{\phi} = 0$ for the disc source (a) and the Wiener–Hopf solution (b) for three frequencies of $k_0 a = 5$ (solid line), 10 (solid line, $\circ$) and 20 (solid line. $\times$). The quarter-sine profile was $\delta = 0.01$ or 0.1. The other variables are: $a = 0.5$, $(l, q) = (4, 1)$, $b = 3$ and $M_\infty = 0.75$.

The last step is to compare simulations of the difference between predictions with and without the boundary layer (Δ) for the two different source methods. Comparing this difference is apt for validation because it is largely a measure of the boundary layer

effect. Figure (5.16) shows the Δ predictions of the disc and the Wiener–Hopf source. Figure (5.16.a) is taken from Gaffney et al (2016).

The figure shows that the difference is the same for either sources; except for $k_0 a = 20$ and $\delta = 0.1$. This is because the disc source method has a larger numerical floor value than the Wiener–Hopf method. The excellent agreement between the differences implies that the installed Wiener–Hopf method is implemented correctly, or at least as correctly as the disc source. The method was interrogated for the disc source, as the results have been recreated with the Wiener–Hopf method, this is deemed sufficient.

This validation has shown that, by comparing the new Wiener–Hopf source to the validated disc source method, in uniform flow, the method gives accurate predictions. By including the boundary layer code for a boundary layer of constant gradient the method was demonstrated to be implemented correctly. Furthermore, with shear the disc and Wiener–Hopf methods give very similar predictions.

5.3 Chapter Summary

Prior to this chapter, the new disc source for the radiating mode from a circular duct and a mode exciting a circular duct had been defined. This chapter included in the theoretical model an infinitely long cylinder to model the scattering effect of a fuselage. The refraction effect of an constant thickness boundary layer was included by solving the Pridmore-Brown equation. To do this the following steps were undertaken;

- the source coordinates were translated via Graf's addition theorem,
- new coordinates were introduced at the centre of an infinitely long cylinder,
- the sound propagation through a monotonically increasing, constant thickness boundary layer was modelled using the Pridmore-Brown equation,
- the scattering effect of a cylinder, with slip and impedance boundary conditions, was included in the model,
- the boundary conditions were then simplified to rigid and no slip,
- the singularity that occurs in the Pridmore-Brown equation was bridged using a Frobenius solution,
- the Frobenius solution was derived for a general (monotonically increasing) function,
- with a boundary layer of infinitesimal thickness the scattered field in uniform flow was recovered from the total field.

Type of Source	Subscript, $i =$	Complex amplitude, $\widetilde{\eta}_i$
Single monopole	σ	$(\pi/2)\,(k_0 + k_z M_z)\,Q_\sigma(-1)^n$ $\mathrm{H}^{(2)}_{l-n}(k_r b)$
Ring (order l)	l	$\pi^2 \xi_l (-1)^{l+n}\,(k_0 + k_z M_z)$ $\mathrm{J}_l(k_r\eta)\mathrm{J}_l(\kappa_l\eta)\mathrm{H}^{(2)}_{l-n}(k_r b)$
Mode (l,q)	lq	$\pi^2 \xi_{lq} (-1)^{l+n}\,(k_0 + k_z M_z)\,\Psi_{lq}$ $\mathrm{H}^{(2)}_{l-n}(k_r b)$
Diffracted (l,q)	d, lq	$\xi_{lq}(-1)^{l+n}(k_0 + k_z M_z)\frac{F_+}{k_r \mathrm{H}_l^{(2)\prime}(k_r a)}$ $\mathrm{H}^{(2)}_{l-n}(k_r b)$

Table 5.2: Abridged version of Table (5.1) with $\beta = 0$ and P's $= 1$.

The solution to the Pridmore-Brown equation must be solved by numerical integration of the ODE in Fourier space. The final solution is of the form

$$p_t(a_0, \bar{\phi}, \bar{z}) = \frac{1}{(2\pi)^2} \sum_{n=-\infty}^{\infty} \left(\int_{-\infty}^{\infty} \widetilde{\alpha}_n(k_z)\, \mathrm{e}^{-jk_z\bar{z}} \mathrm{d}k_z \right) \mathrm{e}^{-jn\bar{\phi}}\,, \tag{5.3.1}$$

with

$$\widetilde{\alpha}_n(k_z) = -\left(\frac{2j}{\pi[1+\delta]} \right) \left(\frac{\widetilde{\eta}_n}{\widetilde{f}_n\Big|_{1+\delta} k_r \mathrm{H}_n^{(2)\prime}(k_r[1+\delta]) - \widetilde{f}'_n\Big|_{1+\delta} \mathrm{H}_n^{(2)}(k_r[1+\delta])} \right), \tag{5.3.2}$$

where the source complex amplitudes $\widetilde{\eta}_n$ are given in Table (5.2). This new model completes Objective 6.

The new theory was implemented in a MATLAB code. The second part of this chapter discussed the implementation and validated the code. This aim was achieved by

- demonstrating convergence of the Fourier sum with increasing harmonic orders,
- recreating Fuller's (1989) results for a monopole adjacent to a rigid cylinder in still flow,
- comparing the distributed source against the scattering case,
- the interpolation used in the method was shown to be implemented correctly,
- the critical layer was shown to be implemented correctly by successful integration through the boundary layer in both directions.

The Wiener–Hopf method differs to the other source methods. Therefore, the Wiener–Hopf source was validated separately by recreating the shielding due to the boundary layer for the different sources.

Chapter 6

Near-Field Installed Results

The SPL on the surface of the fuselage has a direct effect on the levels of cabin noise. To reduce the amplitude of the cabin noise acoustic lagging is installed in the fuselage. The SPL on the surface of the fuselage has implications on the distribution and quantity of acoustic lagging. This, in turn, can have an effect on the weight of the aeroplane and, over an operation, a very significant effect on fuel consumption. For cost and emission considerations, reduction of weight is very important. To avoid placing lagging in unnecessary places accurate SPL predictions are required (Wilby and Scharton, 1973).

This chapter presents accurate predictions for the SPL on the surface of a cylinder for sound radiating from the inlet of a turbofan. Initially in uniform flow, the effect of changing source characteristics on the surface SPL are quantified. The SPL is then investigated with a boundary layer.

The boundary layer effect on the surface SPL is quantified by evaluating the difference in SPL with and without the boundary layer, and the average area mean square pressure. The following variables are changed; frequency, azimuthal order, ambient flow velocity, boundary layer profile and thickness. The boundary layer is a function of these variables, except azimuthal mode; the effect of the azimuthal mode is investigated because it can be engineered by altering the number of blades and stators. This chapter aims to consider practical applications, therefore discussion focuses on the physical reasons for the acoustic effects; the following chapter discusses the mathematics behind the acoustics.

The majority of the chapter presents the installed predictions for the Wiener–Hopf source. Therefore all results are new. The installed disc source results be found in Gaffney *et al.* (2016).

6.1 Geometry and Parameters

The dimensions of the geometry used throughout the results section are shown in Table (6.1). The dimensions were chosen to approximately resemble a twin engined aircraft used for medium haul flights. The diagram for this is shown in Figure (5.2), page 69. All results are for a single source on the right-hand-side of the cylinder.

Variable	Value/Range
a	0.5
$\bar{z}$	[–5,5]
b	3
β	0^o

Table 6.1: Dimensions for the parametric study presented in the chapter. The length values are non-dimensional with reference to the fuselage radius, a_0

The locations that SPL is evaluated are shown in Figure (6.1). The points $II.a - e$ are at $\bar{\phi} = 0^o$ and $\bar{z} = \{5, 2.5, 0, -2.5 \text{ and } -5\}$ respectively.

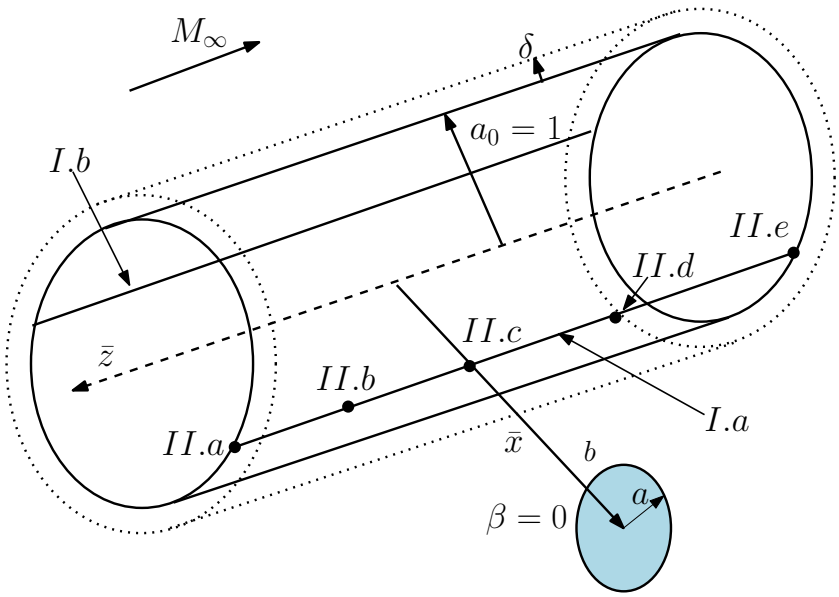

Figure 6.1: Schematic showing the locations where SPL is evaluated.

For each result, SPL is evaluated at 361 points in the azimuthal direction and 1001 points in the axial direction. The high frequency result took approximately 3 hours on a desktop, the lower frequency cases took much less time. The calculation of f and f', Equation (5.1.18), were parallelised over 4 cores.

6.2 Uniform Flow Results

Initially, the simple case of uniform flow is considered. This work can be found in McAlpine *et al.* (2015) and Gaffney *et al.* (2016) in full. The main conclusions are quoted in Table 6.2. The table succinctly details what effect changing a given variable has on the axial location of the maximum SPL on the cylinder. For a reasonably cut-on mode, the maximum SPL on the cylinder roughly occurs where the principal lobe intersects with the cylinder – proof of this can be found in Gaffney *et al.* (2016). Therefore to identify broad trends, the far-field angle of the principal lobe (ψ_{lq} – measured from the engine axis) can be useful in roughly predicting the location of largest SPL (the 'hot spot').

Variable		$\bar{z}_{max}$	Comment
k_0	Increase	Increase	The mode becomes increasingly cut-on, ψ_{lq} decreases.
	Decrease	Decrease	The mode becomes decreasingly cut-on such that ψ_{lq} increases.
a	Increase	Increase	As a increases the mode becomes increasingly cut-on, therefore ψ_{lq} decreases.
	Decrease	Decrease	The mode becomes increasingly cut-off, therefore ψ_{lq} increases.
l	Increase	Decrease	As l increases the mode becomes decreasingly cut-on up to cut-off. ψ_{lq} changes accordingly.
	Decrease	Increase	The principal lobe for $l = 0$ radiates on axis so does not intersect with cylinder.
b	Increase	Decrease	This is simply due to geometry of the problem.
	Decrease	Increase	Again, this is due to geometry of the problem.
M_∞	Increase	Increase	The directivity changes as the velocity increases, the effective wavelengths decreases which corresponds to a effective increase in k_0a.
	Decrease	Decrease	The same as above but with a decrease in effective k_0a.

Table 6.2: The effect of changing variables on the axial position of maximum SPL, called $\bar{z}_{max}$, on the cylinder in uniform flow.

To briefly take an example: if a were to increase, k_0a increases, so the principal

lobe angle decreases because the mode is more cut-on. Due to the decrease in ψ_{lq}, the maximum SPL would be pushed up the cylinder.

The new Wiener–Hopf source adjacent to a rigid cylinder is new. The more complex source extends the range to the rear arc. Therefore, some example cases SPL on the cylinder are shown in Figures (6.2) and (6.3).

The first set of results show the effect of frequency by plotting $ka = \{5, 10 \text{ and } 20\}$. The mode is $(l, q) = (4, 1)$. For the low frequency case $k_0 a$ is only slightly larger than the azimuthal order, l. Therefore the mode is barely cut-on which results in only a single lobe. The 'hot spot' occurs at an axial location of about one cylinder radius. Downstream of the source the SPL value is slightly lower and is evenly distributed.

Figure (6.2.c) shows a very cut-on mode for a frequency of $k_0 a = 20$. Upstream of the source the directivity leads to bands of high amplitude sound pressure. These correspond to the side lobes of the source directivity. The principal lobe is not in the range computed; unlike $k_0 a = 10$ where it is in the middle of the domain, see Figure (6.2.b). Engineering the principal lobe out the front of the fuselage is ideal for cabin noise purposes. Downstream of the source, the amplitude decreases at a quicker rate than the lower frequency cases.

Figure (6.3) shows the effect of changing the azimuthal order for the high frequency $k_0 a = 20$ with three different mode orders; $(l, q) = \{(4, 1),\ (16, 1) \text{ and } (24, 1)\}$. This frequency corresponds to roughly BPF. The very cut-on mode (Figure (6.3.a)) is the same figure as (6.2.c) so the same observations hold.

In future state-of-the-art turbofan engines the number of fan blades will be reduced. This would lead to a reduced rotor-locked mode order such as $(l, q) = (16, 1)$, shown in Figure (6.3.b). For this mode the principal lobe intersects the cylinder at roughly $\bar{z} = 2$. At $\bar{z} = 5$, on the near-side the pressure is less than 90 dB than compared to the maximum value. Downstream the sound is more localised than the very cut-on mode.

For the barely cut-on mode $(l, q) = (24, 1)$ the sound is very localised. The levels at approximately $\bar{z} = \pm 2.5$ along the cylinder are less than 100 dB than at the maximum. The maximum is located at 0.5 in front of the source plane. For this mode at this frequency it would be unnecessary to place lots of acoustic lagging at the tips of the fuselage.

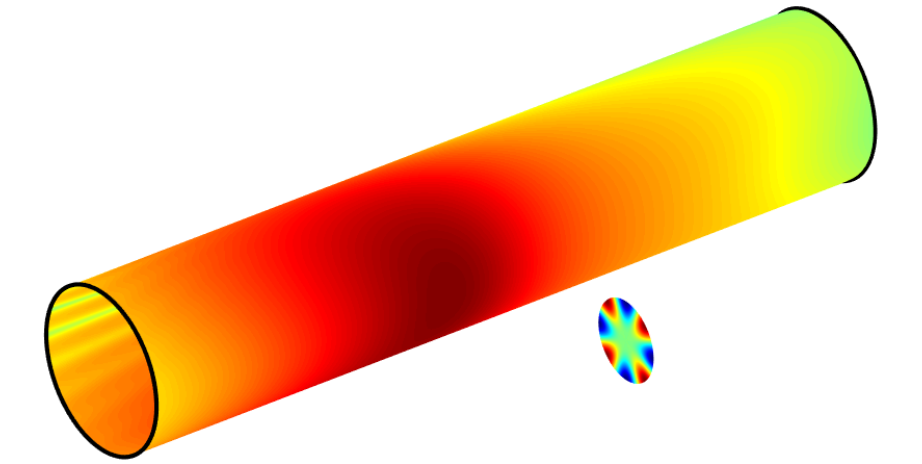

(a) $k_0 a = 5$.

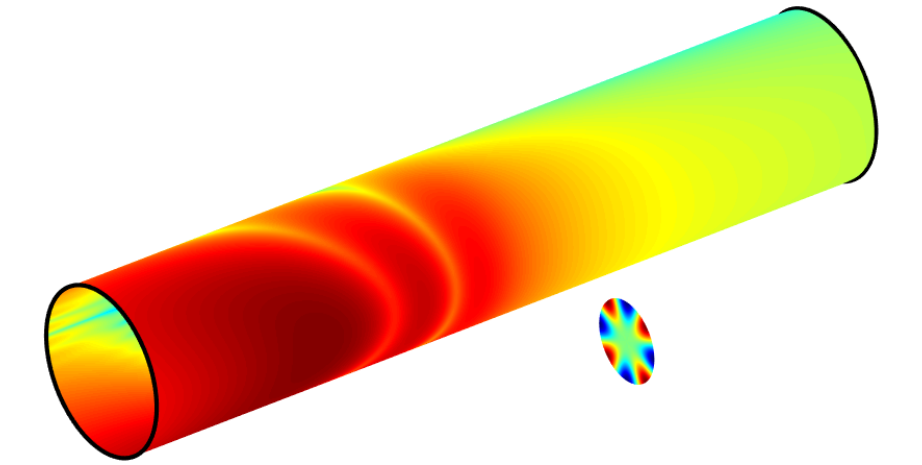

(b) $k_0 a = 10$.

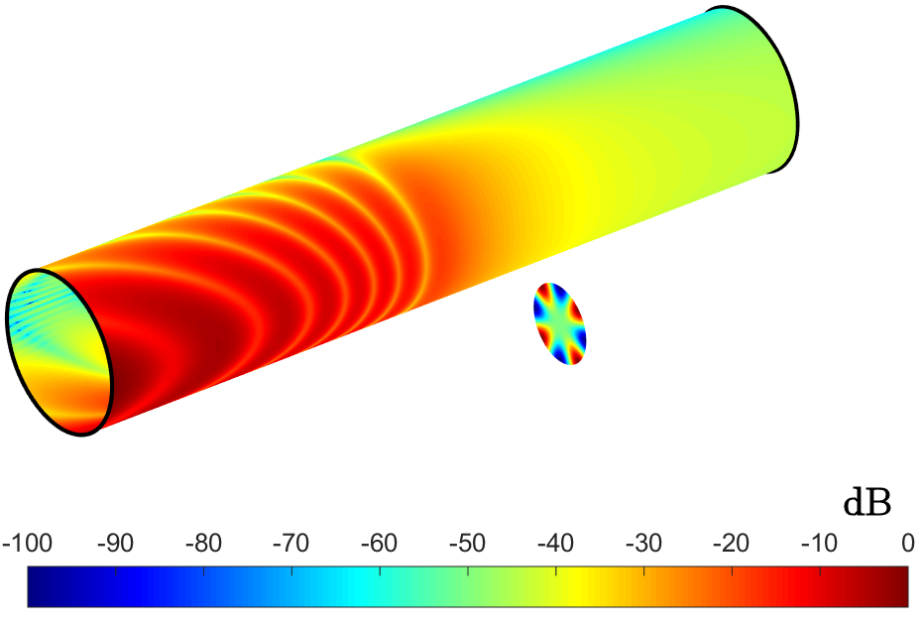

(c) $k_0 a = 20$.

Figure 6.2: SPL on the cylinder in uniform flow for three frequencies. The other parameters are: $(l, q) = (4, 1)$, $a = 0.5$, $b = 3$ and $M_\infty = 0.75$. All cylinder plots may be found unfurled in the appendix.

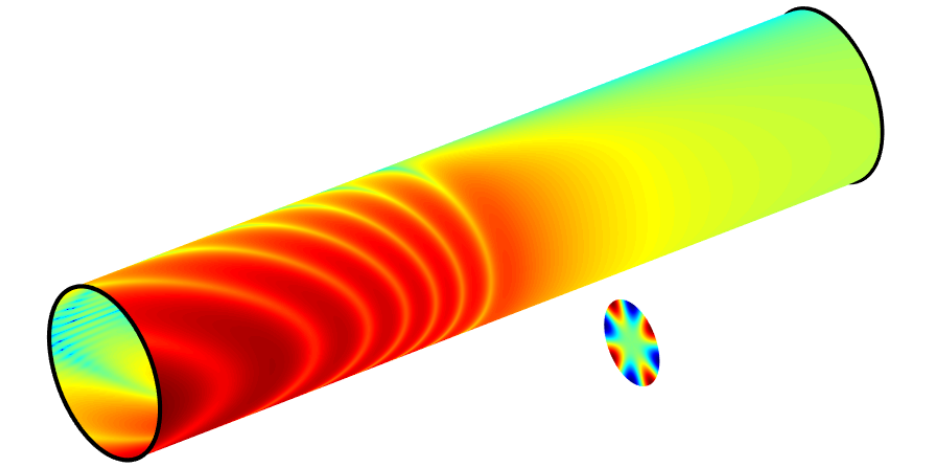

(a) $(l, q) = (4, 1)$.

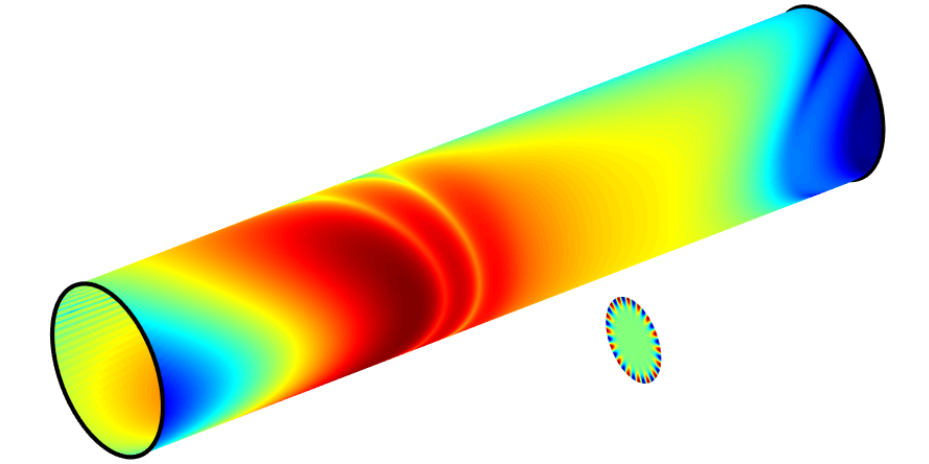

(b) $(l, q) = (16, 1)$.

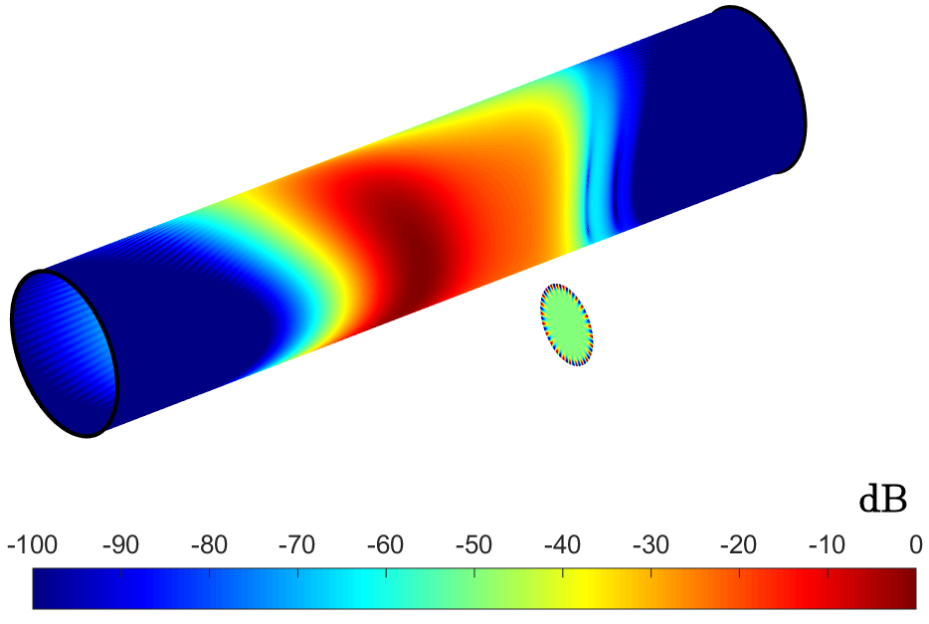

(c) $(l, q) = (24, 1)$.

Figure 6.3: SPL on the cylinder in uniform flow for three modes. The other parameters are: $k_0 a = 20$, $a = 0.5$, $b = 3$ and $M_\infty = 0.75$.

Lastly for the uniform flow section, the levels for the very cut-on mode at the high frequency are evaluated along the cylinder at $\bar{\phi} = 0^{\text{o}}, 90^{\text{o}}$ and 180^{o}. For this relevant frequency it is clear that the shielding effect of the cylinder is very significant. On the far side, the physical presence of the cylinder reduces the amplitude by up to 70 dB. Downstream the shielding is less effective, around 50 dB, because the convective effects of the flow increases the wavelengths. With longer acoustic wavelengths the ratio between the wavelengths and the radius of the cylinder decreases.

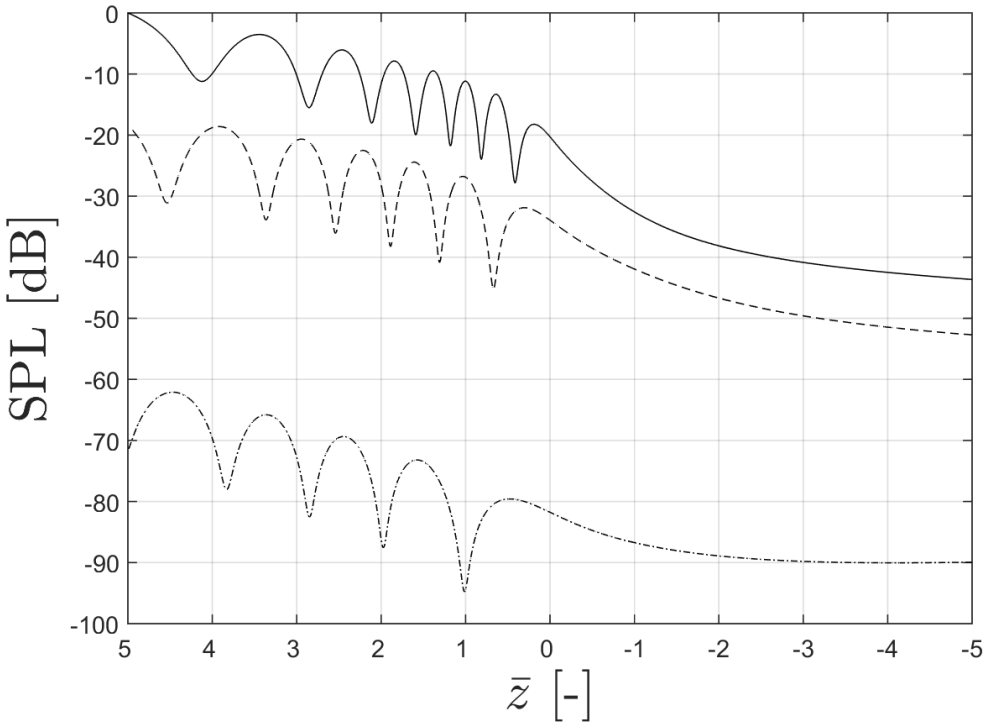

Figure 6.4: SPL along the cylinder at $\bar{\phi} = 0^{\text{o}}$ (solid line, contour $I.a$), $\bar{\phi} = 90^{\text{o}}$ (dashed line) and $\bar{\phi} = 180^{\text{o}}$ (dot-dashed line, contour $I.b$). The parameters are: $k_0 a = 20$, $(l, q) = (4, 1)$, $b = 3$, $a = 0.5$ and $M_\infty = 0.75$.

Although not shown here, Gaffney *et al.* (2016) demonstrated that the free-field directivity of the source cannot be used to predict the maximum SPL on the cylinder. The idea was that the principal lobe would correspond to location of the maximum SPL on the cylinder. However this simple model does not work, the geometric reduction is stronger than the level difference between side and principal lobes. To obtain accurate installed results the total field must be calculated.

This section has presented new results for the SPL on a cylinder in uniform flow due to a mode exiting a duct. As $k_0 a$ increases, the axial location of the maximum SPL on the cylinder increases. As $k_0 a$ becomes much larger than l, more and more side lobes are present, these are clearly visible in the SPL predictions on the cylinder. For a given frequency, as mode order increases the sound becomes more localised both upstream and downstream of the source. It was demonstrated that the cylinder has a significant

shielding effect on the far side. However these predictions do not include the refraction effect of the boundary layer. The boundary layer effect is examined in the subsequent sections in the chapter.

6.3 Boundary Layer Effect

The effect of the boundary layer is quantified in this section. The effect is quantified by two metrics, one of which was introduced in Gaffney *et al.* (2016).

Again, the installed Wiener–Hopf source is prioritised in this discussion so the downstream effects are also considered. Consequentially all the results are new. For reference, the disc source effects on the SPL on the cylinder results can be found in Gaffney *et al.* (2016).

6.3.1 Δ_{bl} and S

Two metrics are used to evaluate the effect of the boundary layer on the levels on the cylinder. First, we examine the difference in the predicted SPL on the cylinder with and without the boundary layer, i.e.

$$\Delta_{bl}\,[\mathrm{dB}] = \mathrm{SPL}_{bl} - \mathrm{SPL}. \tag{6.3.1}$$

The difference Δ_{bl} is useful for predicting the reduction in levels at the 'hot spot' (region where the SPL is a maximum). However, examining Δ_{bl} in isolation can be misleading. For example, a large difference predicted on the far side of the cylinder will not be significant because, as shown in Figure (6.4), in uniform flow, i.e. with no boundary-layer shielding, the levels on the far-side of the cylinder are less than 100 dB compared to the maximum on the near side. A large reduction in these levels is not important to cabin noise.

Next, to obtain a more overall view of the boundary-layer effect we introduce a simple 'shielding' coefficient denoted by S. This ratio is the spatially averaged mean-square pressure on the cylinder with and without the boundary layer. This, in turn, is roughly proportional to the amount of energy of the incident wave refracted away by the cylinder. Accordingly, we define S by

$$S = \frac{(1/A)\int_A \overline{p_{bl}^2}\mathrm{d}A}{(1/A)\int_A \overline{p^2}\mathrm{d}A} \approx \frac{\sum^{\mathrm{M}^\sharp} \overline{p_{bl}^2}}{\sum^{\mathrm{M}^\sharp} \overline{p^2}}, \tag{6.3.2}$$

where, for equal areas, in practice it is sufficient to evaluate S via a sum of the predicted mean-square pressures over the $\mathrm{M}^\sharp$ grid points distributed over the cylinder's surface.

To examine the effects of flow upstream and downstream the shielding ratio will be

split where

$$S_- = \left.\frac{\sum^{\mathrm{M}_-^\sharp} \overline{p_{bl}^2}}{\sum^{\mathrm{M}_-^\sharp} \overline{p^2}}\right|_{\bar{z}<0} \text{ and } S_+ = \left.\frac{\sum^{\mathrm{M}_+^\sharp} \overline{p_{bl}^2}}{\sum^{\mathrm{M}_+^\sharp} \overline{p^2}}\right|_{\bar{z}>0}. \tag{6.3.3}$$

An S value of unity represents no shielding, zero corresponds to total shielding and above one would lead to waves refracting towards the cylinder.

The relevant equation governing the effect of the boundary layer is

$$BL(k_0, k_z, M_z, \delta) = -\left(\frac{2j}{\pi[1+\delta]}\right)\left(\frac{1}{\left.\widetilde{f}_n\right|_{1+\delta} k_r \mathrm{H}_n^{(2)\prime}(k_r[1+\delta]) - \left.\widetilde{f}_n'\right|_{1+\delta} \mathrm{H}_n^{(2)}(k_r[1+\delta])}\right). \tag{6.3.4}$$

The parameters affecting the function BL are: the forcing frequency, the flow velocity, the boundary-layer thickness and its profile. The profile effect is manifest by the results of the ODE solver. The forcing frequency is a source characteristic, however, the other parameters are flow characteristics. The subsequent analysis is split between source and flow characteristics.

Note the radial mode number and the radial distance to the source, b, are omitted from the analysis. The likely application of the method is fan tones. In this context, the radial mode is less important. Moving the source away from the cylinder has a trivial effect on the predictions.

6.3.2 Source Characteristics

In this section the effect of the boundary layer is quantified as the source variables are changed. Initially the frequency, $k_0 a$, is varied, followed by the mode order. The boundary layer is a quarter-sine profile

$$M = M_\infty \sin\left(\frac{\pi}{2\delta}\bar{r}\right). \tag{6.3.5}$$

of thin ($\delta = 0.01$) and thick ($\delta = 0.1$) thickness (Dierke *et al.*, 2013). The thicker value is approximately the actual value of the boundary layer thickness in the plane of the source. The thinner boundary value was chosen arbitrarily.

Frequency $-\, k_0 a$

While the mode of the source is kept constant at $(l, q) = (4, 1)$, the frequency is varied; $k_0 a = \{5,\ 10 \text{ and } 20\}$, and the metrics are evaluated. The ratio of the boundary-layer thicknesses to wavelengths are shown in Table (6.3). For all frequencies the thickness of the boundary layer is significantly less than the acoustic wavelength.

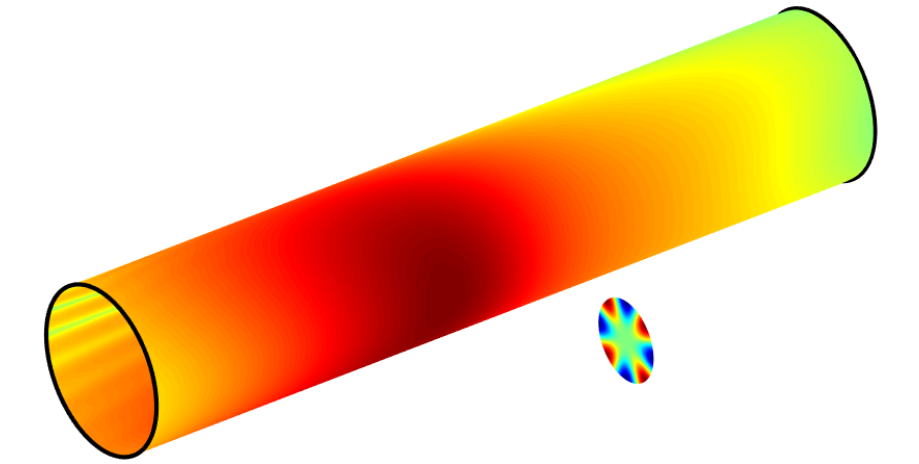

(a) $\delta = 0$.

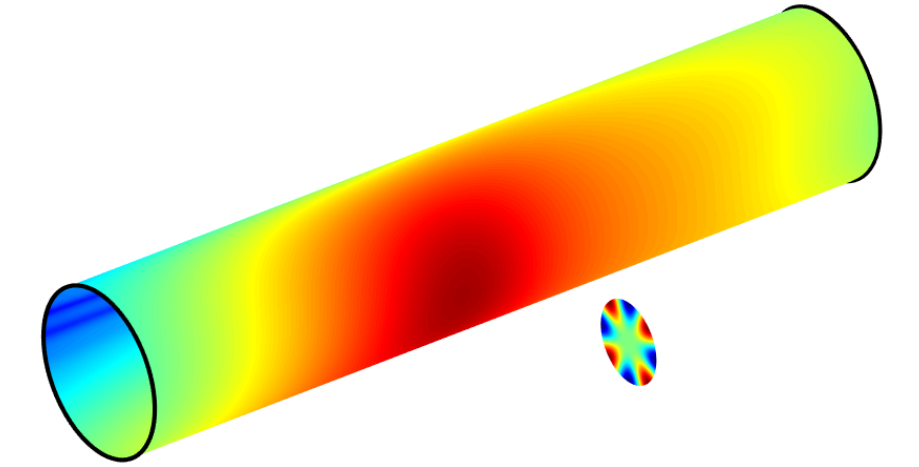

(b) $\delta = 0.01$.

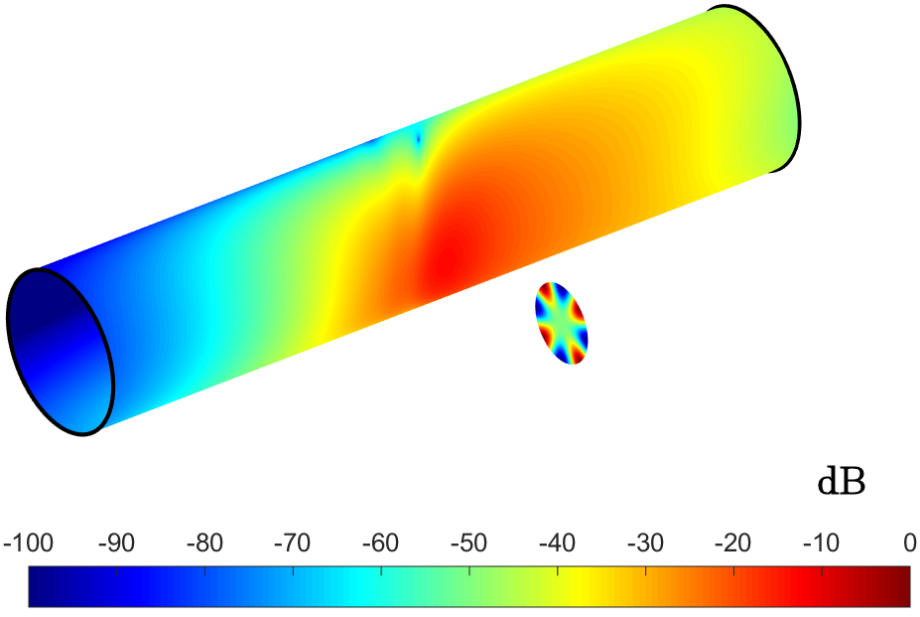

(c) $\delta = 0.1$.

Figure 6.5: SPL on the cylinder in uniform flow for three boundary-layer thicknesses. The other parameters are: $k_0 a = 5$, $(l, q) = (4, 1)$, $a = 0.5$, $b = 3$ and $M_\infty = 0.75$.

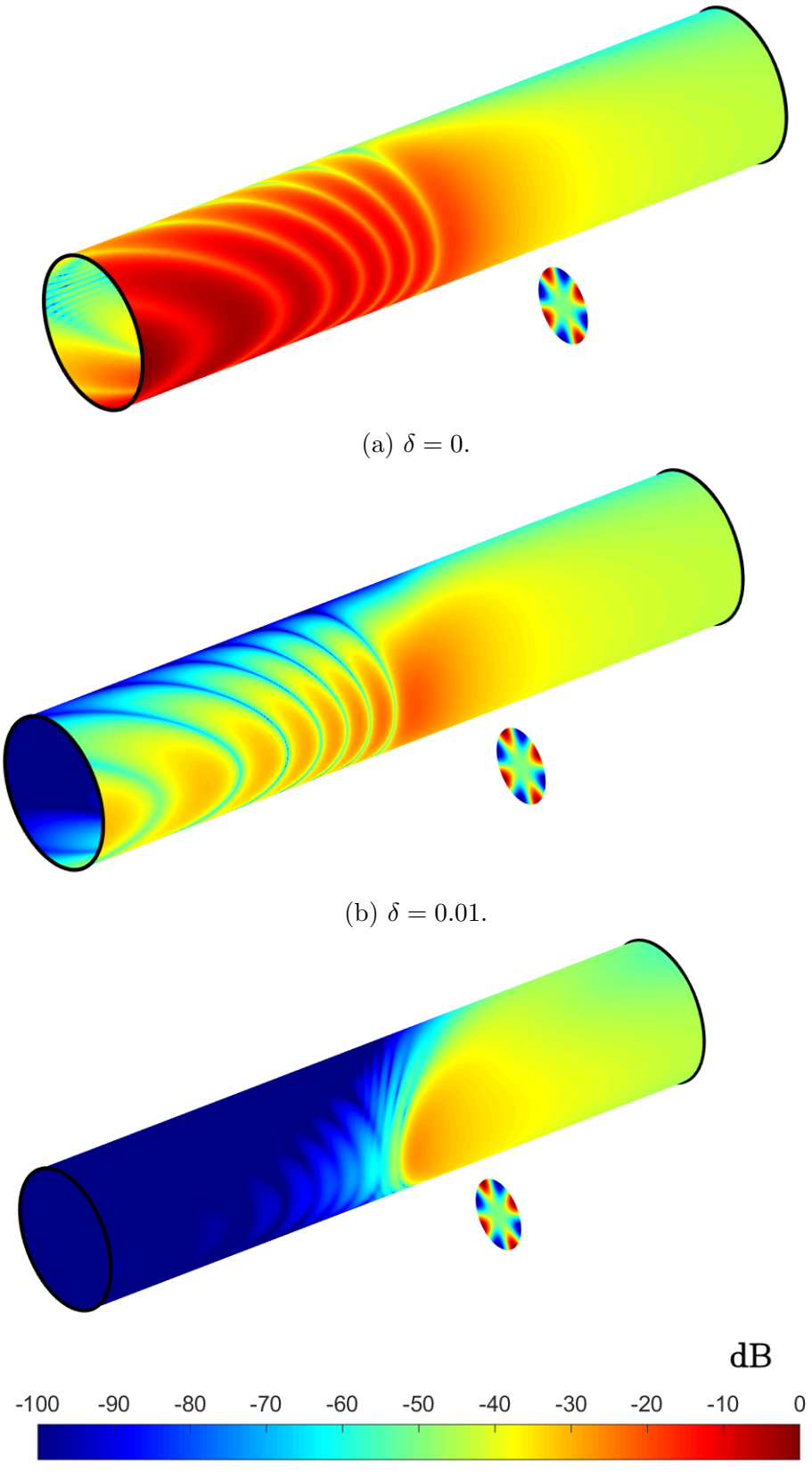

(a) $\delta = 0$.

(b) $\delta = 0.01$.

(c) $\delta = 0.1$.

Figure 6.6: SPL on the cylinder in uniform flow for three boundary-layer thicknesses. The other parameters are: $k_0 a = 20$, $(l, q) = (4, 1)$, $a = 0.5$, $b = 3$ and $M_\infty = 0.75$.

Some examples of the SPL on the cylinder are shown in Figures (6.5) and (6.6), with $k_0a = 5$ and $k_0a = 20$ respectively, in: uniform flow, and then with a thin and thick boundary layer. The uniform flow results are the same as those shown in Figure (6.2.a) and (6.2.c). The figures show that upstream of the source the boundary layer causes the sound to be refracted away from the cylinder. For the thin boundary layer, the directivity of the source is still clearly visible. However, for the thick boundary-layer causes a reduction in amplitude of more than 100 dB. Downstream of the source the uniform flow predictions are not significantly affected by the boundary layer. On the far-side of the cylinder, the amplitude of the destructive interference pattern is significantly reduced.

Let us step back from the problem for a moment. For all wave problems, the ratio of the wavelength to the characteristic length of the object is important. For example, for a radiation problem the ratio k_0a (where a is the characteristic length of the source) gives an indication to the directivity; for scattering problems the Helmholtz ratio k_0a_0 (a_0 is the characteristic length of the scattering object) is relevant. The refraction problem is no different. Here, the ratio of the thickness of the boundary layer (δ) to the acoustic wavelength (λ) is pertinent.

δ	k_0a		
	5	10	20
0.01	0.0159	0.0318	0.0637
0.1	0.1592	0.3183	0.6366

Table 6.3: Ratio of δ/λ_0 for the two boundary layer thickensses for the three frequencies. The variables are: $a = 0.5$, $(l, q) = (4, 1)$, $b = 3$ and $M_\infty = 0.75$

This ratio of the source wavelength (λ_0) is given in Table (6.3). However, when flow is present the wavelengths are affected. Downstream of the source the wavelengths are extended, and upstream the wavelengths are shortened. As a very rough approximation, assuming plane waves, at cylinder point $II.e$ the wavelength extends from $\lambda_0 = 0.1571$ to $\lambda_{II.e} = 0.2665$. The wavelengths were calculated via $\lambda = k_0/1 \pm M_\infty \cos\Theta$, where Θ is the angle between the plane-wave front and the flow at 0.75 M. Therefore at the downstream point ($II.e$) of the cylinder $\delta/\lambda_{II.e} = 0.3752$. At the upstream point ($II.a$) this ratio is $\delta/\lambda_{II.a} = 2.094$. This means that the boundary layer depth is twice the length of the acoustic wavelength upstream and the boundary layer thickness is much shorter than the acoustic wavelength downstream. The significance of these ratios is that we would expect the boundary layer to have little effect downstream of the source and will have a large effect upstream.

The discussion now focuses on the Δ_{bl} predictions shown in Figure (6.7). It is clear

that upstream of the source the boundary layer changes the levels significantly from the uniform flow predictions. Downstream of the source the boundary layer will refract the wave towards the cylinder. For the thick boundary layer there is a very slight increase in amplitude in downstream axial locations of -1 to -4. Conversely upstream, the high frequency shielding at $II.a$ is approximately 100 dB for the thick boundary layer and downstream the effect is negligibly ($\Delta_{bl} \approx 0$), this supports the δ/λ argument of the previous paragraph.

At the plane of the engine, at $\bar{z} = 0$, Δ_{bl} is slightly negative for the thin boundary layer and between -5 and -8 dB for the thick boundary layer. This result is interesting because the sound wave does not propagate into or with the flow. The reduction is due to the shear in the azimuthal direction. This would not be present at this location for a shear layer over a flat plate. Again, the shear is larger for the high frequency waves than the longer wavelengths of low frequencies.

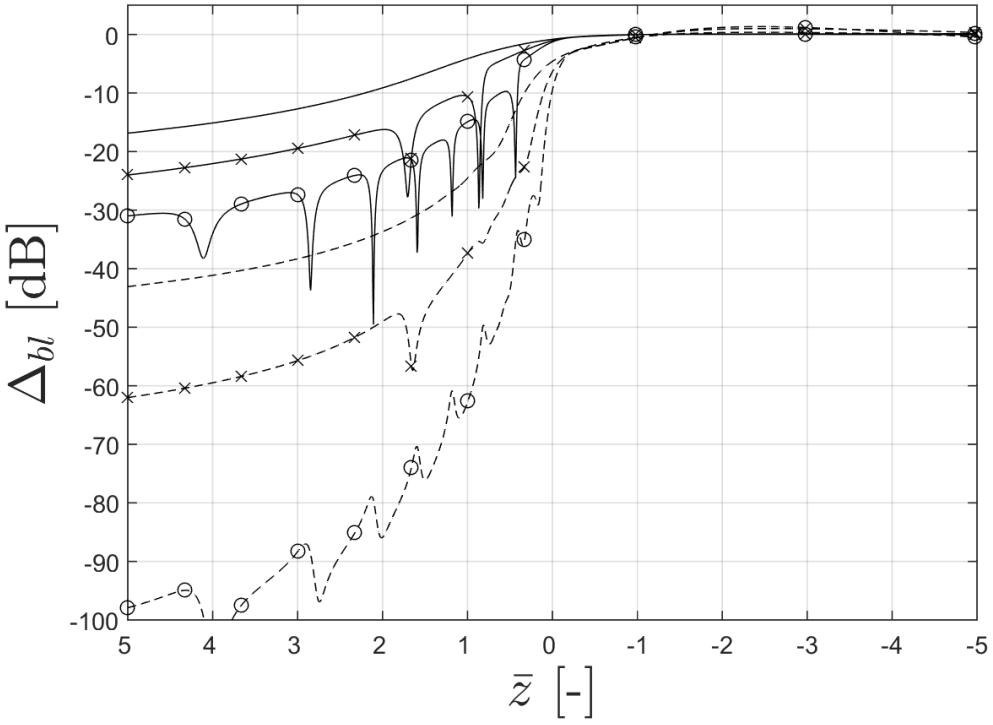

Figure 6.7: Δ_{bl} along the cylinder at $\bar{\phi} = 0^{\circ}$ for three frequencies. The variables are $k_0 a = 5$ (no symbols), $k_0 a = 10$ ($\times$) and $k_0 a = 20$ ($\circ$) for a boundary layer thickness of $\delta = 0.01$ (solid lines) and $\delta = 0.1$ (dashed lines). The other parameters are: $(l, q) = (4, 1)$, $a = 0.5$, $b = 3$ and $M_{\infty} = 0.75$ (the same as Table (6.3.2).

Upstream of the source the boundary layer leads to significant amounts of shielding. Even for the relatively low frequency and thin thickness the shielding at the tip of the cylinder is around 18 dB. For the thick boundary layer and high frequency the shielding is predicted to be 100 dB. When the sound propagates into the flow the wavelengths are effectively shortened, as discussed previously.

The value of Δ_{bl} becomes more negative as $\bar{z}$ increases, the rate of increase is nonlinear and the rate of change is at a maximum between zero and $\bar{z} = 3$. At $\bar{z} > 3$ the shielding begins to flatten out. If the location of the principal lobe can be increased from $\bar{z} = 1$ to 2, a large reduction would be measured. Whereas if it were to increase from $\bar{z} = 3$ to 4, the reduction would not be so great.

The middle and high frequencies show notches in the Δ_{bl}. All the sound is refracted including the location of the nulls. These notches are showing the location of the nulls have changed slightly.

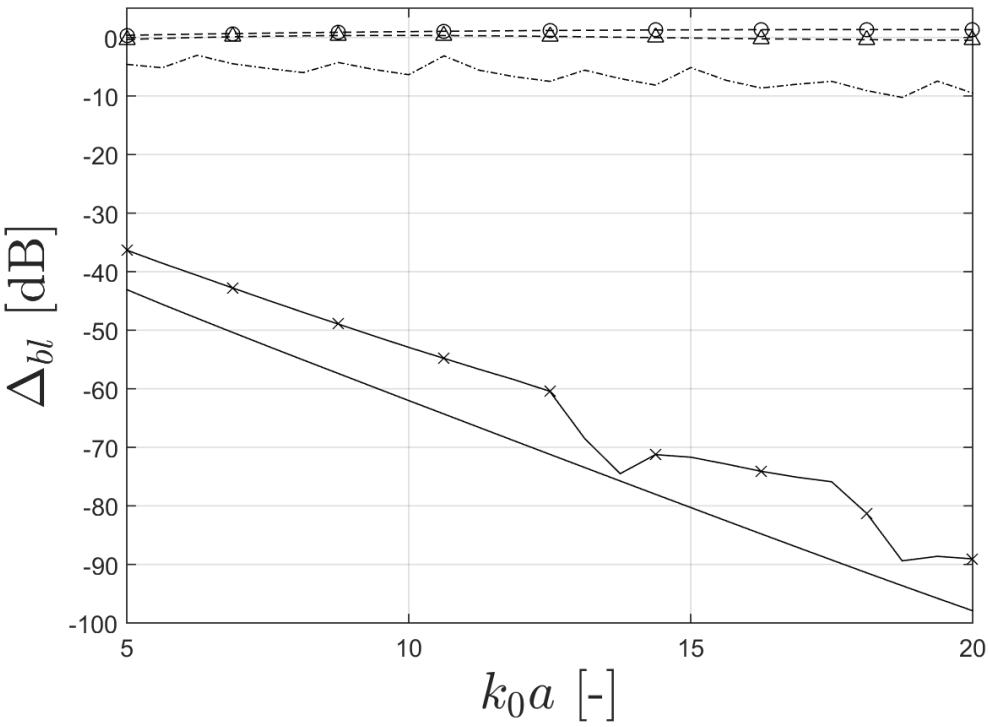

Figure 6.8: Δ_{bl} at the points for increasing $k_0 a$ for a boundary-layer thickness of 0.1. Point $II.a$ (solid line, no symbols), $II.b$ (solid line, $\times$), $II.c$ (dot-dashed line, no symbols), $II.d$ (dashed line, $\triangle$) and $II.e$ (dashed line, $\circ$). The other parameters are: $(l, q) = (4, 1)$, $a = 0.5$, $b = 3$ and $M_\infty = 0.75$.

As $\bar{z}$ increases, the angle of incidence to the boundary layer of the incident wave decreases. The angle of incidence to the boundary layer is important because the refraction problem is, in essence, an extended application of Snell's Law[1]. Furthermore, the wave spends longer in the shear layer than near the source. Therefore the wave is subject to more shear and thus more refraction.

The difference between the uniform flow and the thick boundary layer predictions at various positions are shown in Figure (6.8). The figure shows that the shielding does not significantly change with frequency at locations in the plane of the source and

[1]In 2D Cartesian coordinates Snell's law is $u_{01} + c_{01}/\cos\alpha = u_{02} + c_{01}/\cos\theta$ where θ is the incident angle and α is the transmitted angle. This is implemented in Section 7.4.

downstream of the source. In the plane of the source the shielding slightly increases from –5 dB to –10 dB.

Upstream of the source, the shielding is very dependent on frequency. At the tip of the cylinder ($II.a$) the shielding increases from about –43 dB to nearly –100 dB. The increase between these two frequencies is roughly linear. Halfway up the cylinder the shielding increases linearly from $k_0a = 5$ to 13, at a slightly lesser rate than at the tip of the cylinder. Above $k_0a = 13$ notches are present. This is because two side lobes pass through.

Now attention is paid to the spatially averaged mean-square pressure ratio, Figure (6.9). Over the whole domain, S, the ratio inversely drops with increasing frequency, Figure (6.9.a). For the thick boundary the shielding ratio for $k_0a = 5$ is approximately 0.01. This means that roughly 99% of the energy is refracted away from the cylinder by the boundary layer. For the thin boundary layer, $S = 0.005$ for the high frequency of $k_0a = 20$. This means that the boundary-layer effect averaged over the cylinder is approximately equivalent for the two values just stated. The associated δ/λ ratio is 0.0063 and 0.0007.

Figure (6.9.b) demonstrates that the shielding ratio downstream of the engine S_- does not change massively with increasing frequency. The values are around 0.75 and 0.5 for the thin and thick profiles. These values are less than unity which indicates shielding. Shielding also occurs on the far-side of the cylinder at axial values of $\bar{z} = -1$ to -3, not shown.

Upstream, the shielding ratio (S_+) follows the same trend as S. At frequencies above $k_0a = 6.5$ approximately 99% of the energy of the incident wave will be refracted away from the cylinder for a quarter-sine profile of thickness 0.01. For the thick boudnary layer the value of S_+ is barely above zero for the whole range.

In summary, the boundary layer leads to significant shielding upstream of the source. The convective effect of the flow alters the effective acoustic wavelength which changes the ratio of δ/λ. The boundary layer has a modest effect downstream of the source on the acoustic levels measured in decibels. However, the shielding coefficient showed that the boundary layer does have a shielding effect downstream, but it was not significantly affected by changes in the frequency. Even for low frequencies significant shielding is predicted upstream. This is due to a combination of shorten wavelengths and a shallow angle of incidence to the boundary layer.

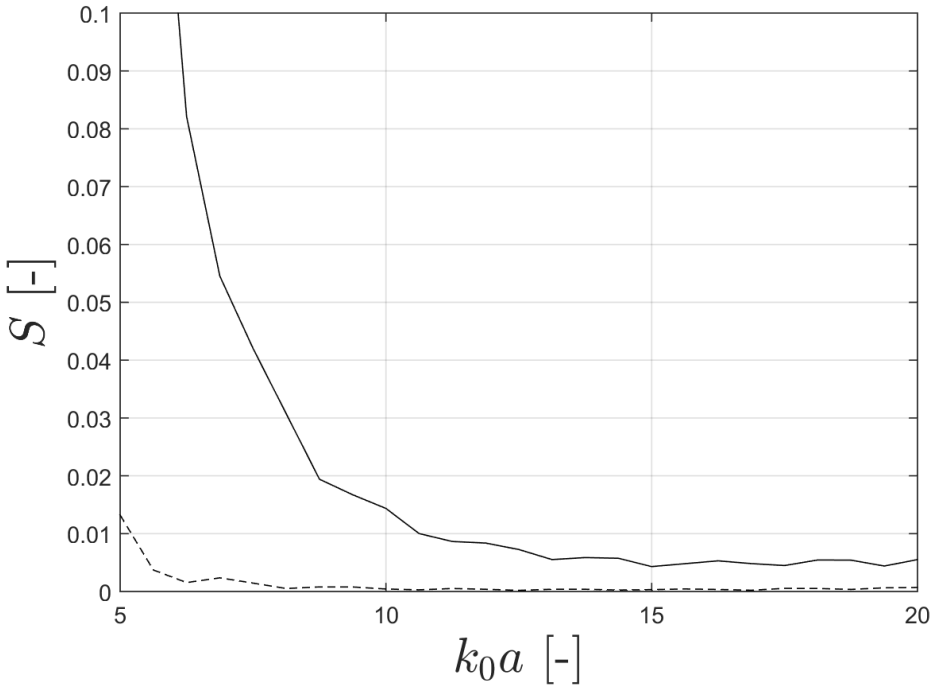

(a) $S-$ note the $y-$axis scale.

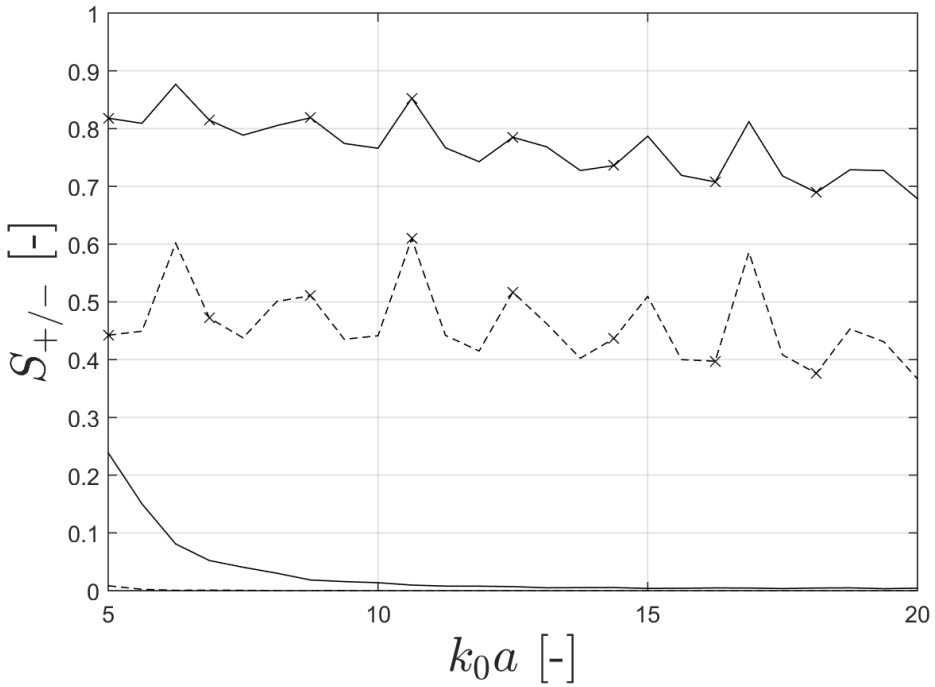

(b) S_+ (no symbols) and S_- ($\times$). Note the $y-$axis scale.

Figure 6.9: The three S's for increasing k_0a with $\delta = 0.01$ (solid line) and $\delta = 0.1$ (dashed line). The other parameters are: $(l, q) = (4, 1)$, $a = 0.5$, $b = 3$ and $M_\infty = 0.75$. The y–axis scales are different on (a) and (b).

Azimuthal Order $-l$

Now attention is shifted to the effect of azimuthal order on boundary layer shielding. The azimuthal mode is increased from the plane wave mode to the 24th (the highest cut-on mode) while keeping the source frequency constant at $k_0 a = 20$. As previously stated; in theory the boundary layer transfer function does not depend on the azimuthal order. However, it is shown that the difference in pressure does change with azimuthal order.

Figure (6.10) shows Δ_{bl} along the cylinder. For most of the axial positions for the thin boundary layer Δ_{bl} values are similar. For the $(l, q) = (4, 1)$ mode the notches are due to side-lobe refraction. The maximum shielding is about -30 dB and -100 dB for $(l, q) = (4, 1)$ and $(24, 1)$ at the tip of the cylinder $(II.a)$ respectively

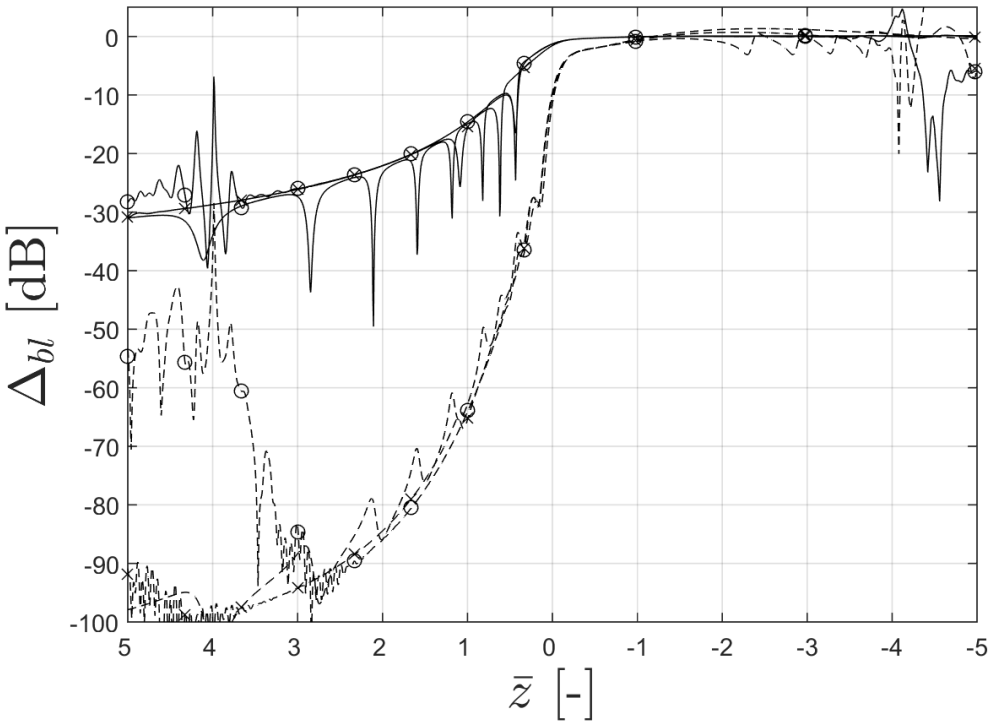

Figure 6.10: Δ_{bl} down the cylinder at $\bar{\phi} = 0^{\circ}$ for three azimuthal modes; $(l, q) = (4, 1)$ (no symbol) $(l, q) = (16, 1)(\times)$ $(l, q) = (24, 1)(\circ)$. Shown with two boundary layer thickenesses; $\delta = 0.01$ (solid lines) and $\delta = 0.1$ (dashed lines). The other parameters are: $k_0 a = 20$, $a = 0.5$, $b = 3$ and $M_{\infty} = 0.75$.

The predictions for Δ_{bl} for a barely cut-on mode are significantly different, especially for the thick boundary layer at large axial positions. This discrepancy is because the metric is a difference, not absolute values. For this mode, the amplitude predicted with uniform flow at the end of the cylinder is very small. Figure (6.3.c) shows that the ends are more than 100 dB less than the maximum. Once the boundary layer is introduced these very low amplitudes are then further reduced by the presence of the boundary

layer. These values are sufficiently low that the reductions (of up to 100 dB) are in the computational noise floor. Once this happens, the difference between the uniform flow and boundary layer decreases.

This is also shown in Figure (6.11). The azimuthal order does not change the difference much – except from at $\bar{z} = 5$. The difference increases to above 100 dB at $l = 8$ and reduces for modes higher than $l = 15$. This is because at the tip of the cylinder for $l = 8$ to 15 the principal lobe is present. For azimuthal orders below eight, the principal lobe is in front of the cylinder. Above sixteen the principal lobe intersection is slightly in front of the source plane.

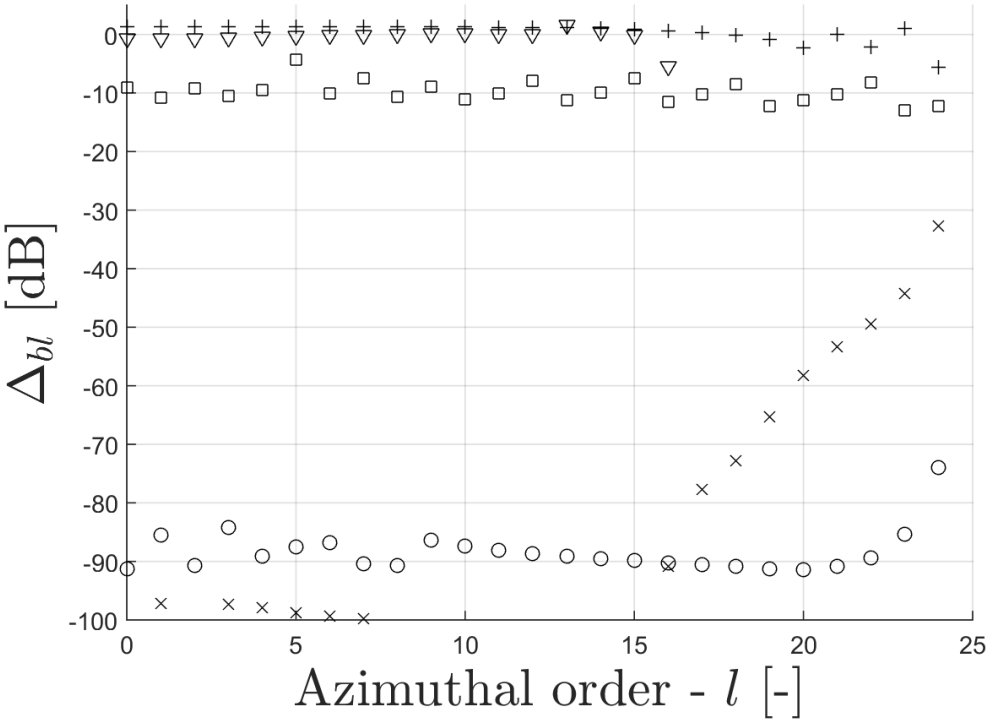

Figure 6.11: Δ_{bl} at the points for increasing azimuthal order. Key: $II.a$ ($\times$), $II.b$ ($\circ$), $II.c$ ($\square$), $II.d$ ($\triangle$) and $II.e$ ($+$). The other parameters are: $k_0 a = 20$, $a = 0.5$, $b = 3$, $\delta = 0.1$ and $M_\infty = 0.75$.

The overall amplitude ratio, S, is very small over all modes, shown in Figure (6.12). As before, for small azimuthal orders the principal lobe does not intersect with the cylinder. As the azimuthal order increases to 5 the principal mode enters the domain and this reduces S from 0.0075 to 0.002. For the thinner boundary layer, S increases as the mode approaches cut-off, this corresponds to less shielding. As the mode approaches cut-off the angle of incidence to the boundary layer increases. As alluded to before, a steeper grazing angle corresponds to less shielding. Overall, the values of S are very low, which suggests the boundary layer refracts most of the energy away from the cylinder. The principal lobe seems to dominate S predictions.

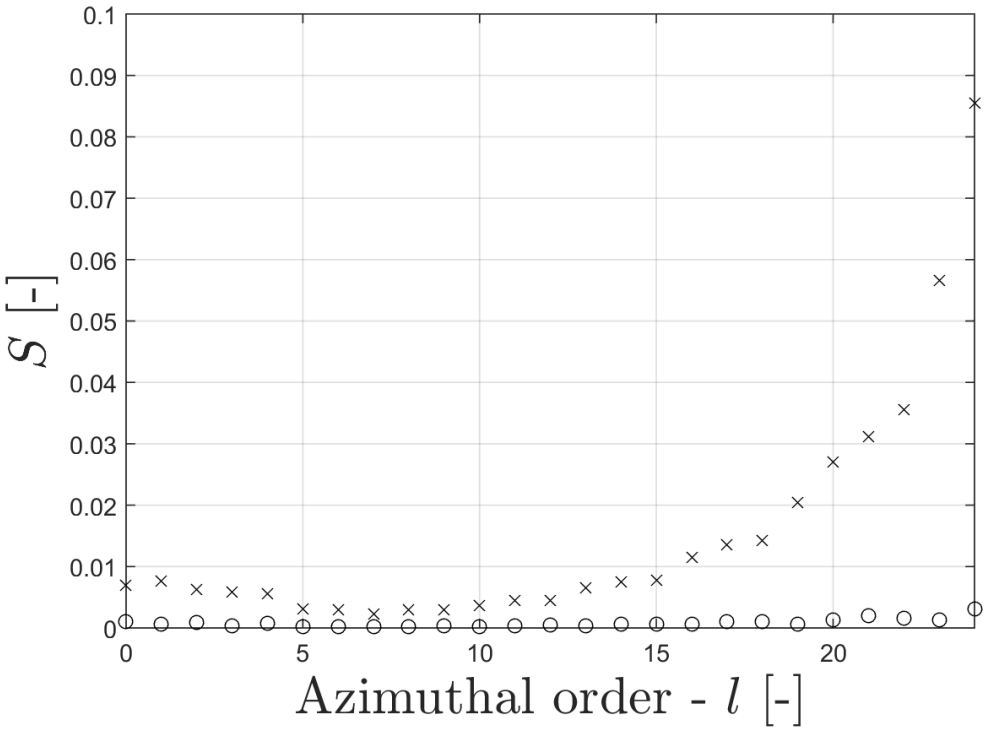

Figure 6.12: S for increasing azimuthal mode for the thin ($\delta = 0.01 - \times$) and thick ($\delta = 0.1 - \circ$) boundary layer thicknesses. The other parameters are: $k_0 a = 20$, $a = 0.5$, $b = 3$ and $M_\infty = 0.75$.

The ratio evaluated downstream of the source shows a similar trend when plotted against $k_0 a$. A slight decrease is observed in Figure (6.13.a). However Figure (6.13.b) shows that upstream the trend for S_+ follows that of S.

This section has shown that although the boundary layer effect does not directly depend on the azimuthal order of the source, the azimuthal order does affect the total amount of shielding. It has been demonstrated that the most reduction occurs when the principal lobe grazes the boundary layer at a shallow angle. The maximum reduction due to the boundary layer could be engineered by reducing the azimuthal mode. The Δ_{bl} is affected by computational noise and S moderately affected by the larger amplitudes of the principal lobe.

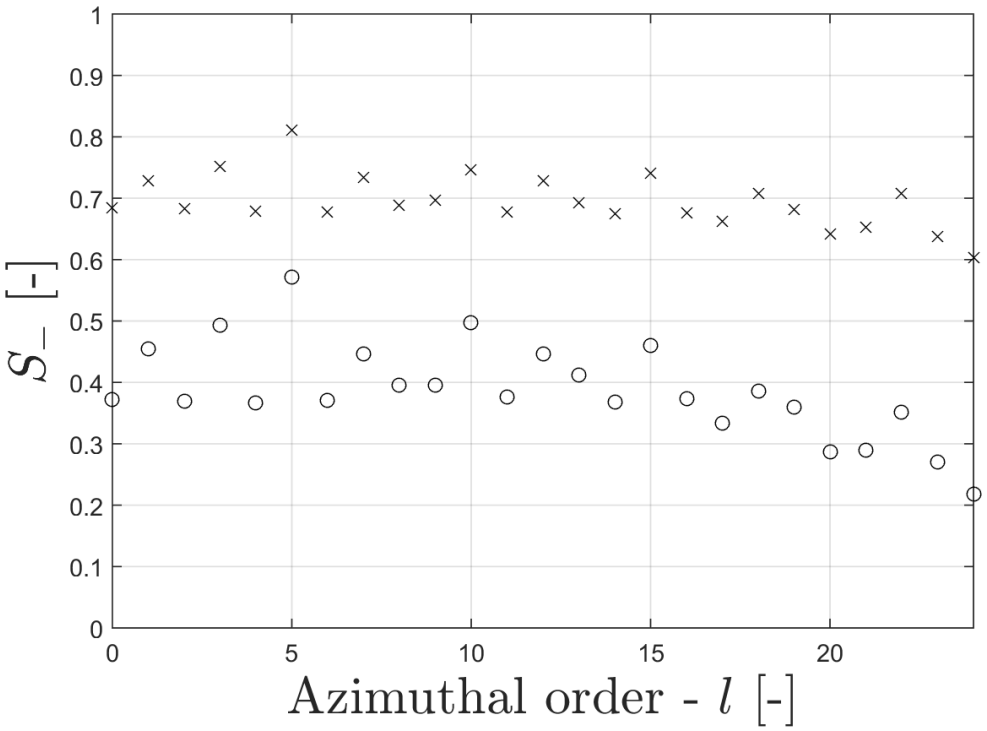

(a) S_- – note the $y-$axis scale.

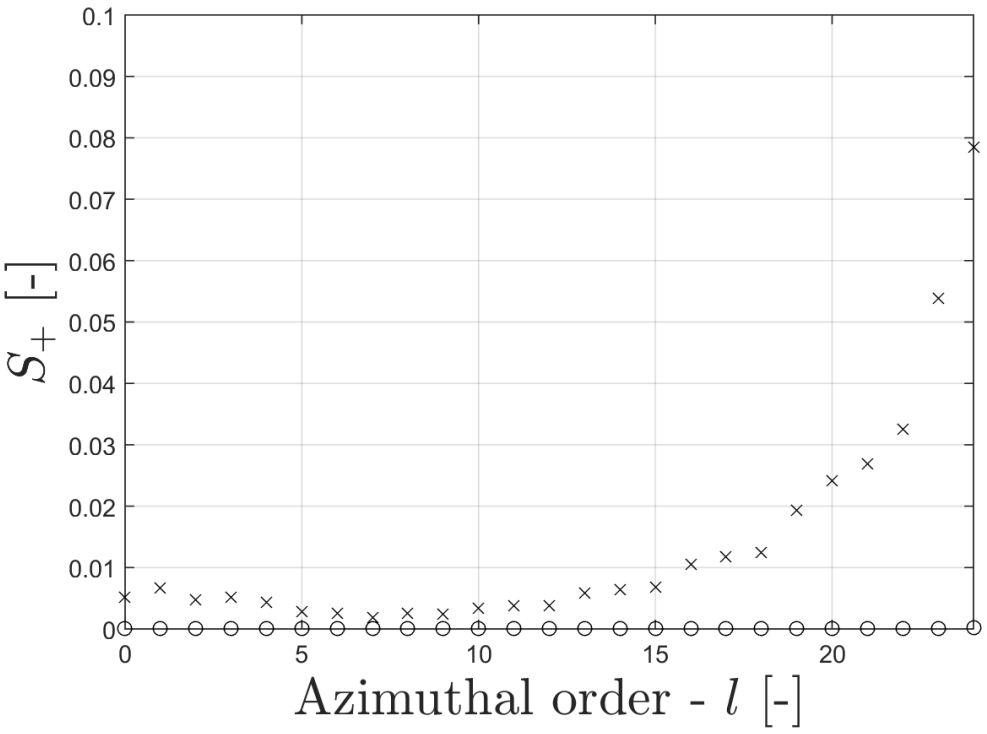

(b) S_+ note the $y-$axis scale.

Figure 6.13: $S_{+/-}$ for increasing azimuthal mode for the thin ($\delta = 0.01 - \times$) and thick ($\delta = 0.1 - \circ$) boundary layer thicknesses. The other parameters are: $k_0 a = 20$, $a = 0.5$, $b = 3$ and $M_\infty = 0.75$.

6.3.3 Flow Characteristics

In this section the flow characteristics effects on the surface acoustic pressure are quantified. This is achieved by changing the ambient flow velocity, boundary layer profile and boundary layer thickness. While these are changed the source characteristics are kept at $k_0 a = 20$ and $(l, q) = (4, 1)$. The frequency is realistic for BPF whereas the mode is low. This low order could be an interaction tone. This mode was chosen because in uniform flow the SPL is well distributed over the whole cylinder.

Bear in mind that the ambient flow velocity changes the directivity of the source. Initially the effect of the ambient flow is quantified, this is followed by examining the boundary layer thickness and then the profile shape.

Ambient Flow Velocity $- M_\infty$

As the ambient flow velocity is increased the profile is kept constant as the quarter-sine. The velocity is increased from 0 to 0.75 M and, as in the previous section, two thicknesses are evaluated, thin – $\delta = 0.01$, and thick – $\delta = 0.1$.

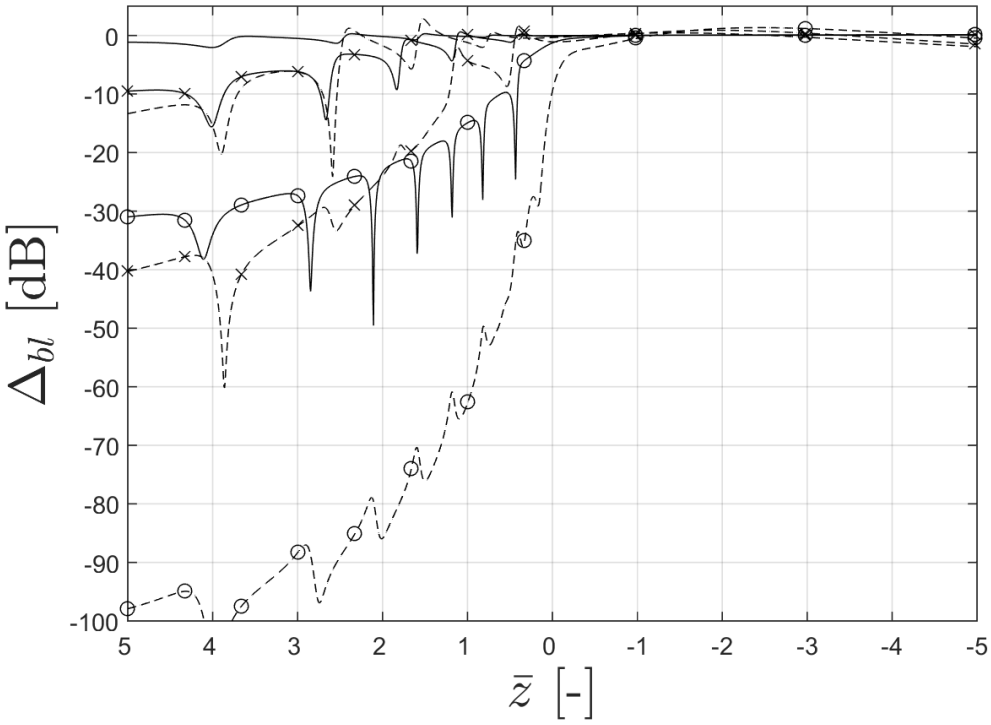

Figure 6.14: Δ_{bl} down the cylinder at $\bar{\phi} = 0^o$ for the three ambient flow velocities. The variables are: $M_\infty = 0.25$ (no symbols), $M_\infty = 0.5$ ($\times$) and $M_\infty = 0.75$ ($\circ$) for a boundary layer thickness of $\delta = 0.01$ (solid lines) and $\delta = 0.1$ (dashed lines). The other parameters are: $k_0 a = 20$, $(l, q) = (4, 1)$, $a = 0.5$ and $b = 3$.

The difference between the uniform and boundary layer (Δ_{bl}) is shown in Figure (6.14). The effect of the flow velocity is modest downstream of the source. Similarly,

upstream of the source the thin boundary layer leads to very little shielding (<2 dB) for flow values less than 0.25 M.

However, as the flow velocity is increased to 0.5 M shielding increases. Infact, the thick boundary layer at 0.25 M gives roughly equivalent shielding as the thin boundary layer at 0.5 M.

The notches in the shielding predictions change in position and quantity with flow velocity because the flow affects the source directivity. As the flow increases the effective wavelengths propagating upstream decrease which leads to more side-lobes to become present in the source directivity.

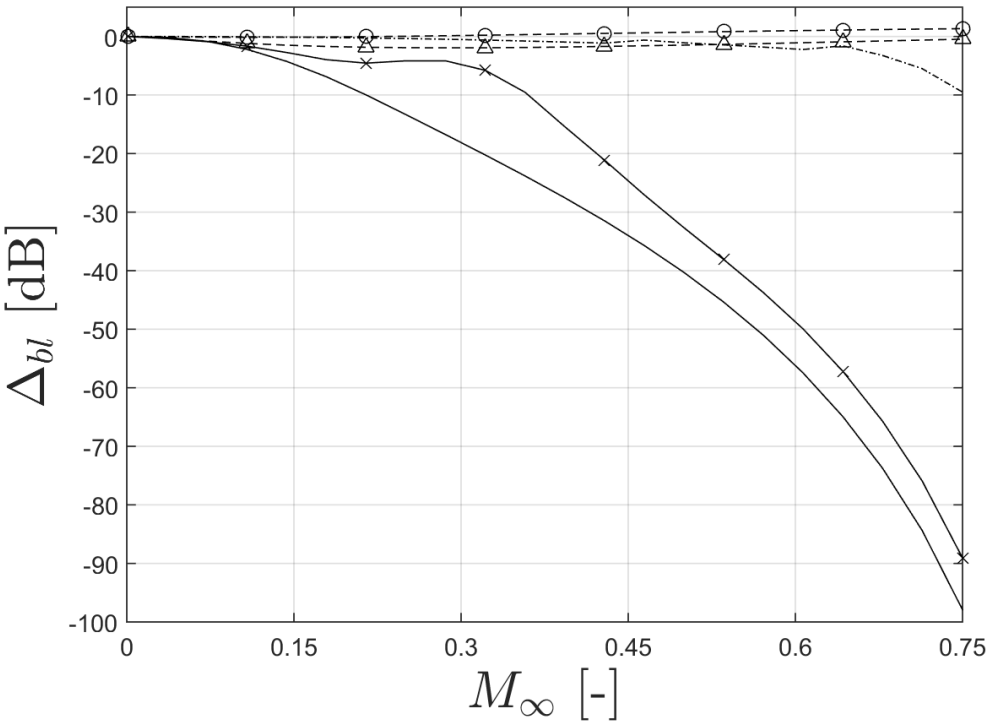

Figure 6.15: Δ_{bl} at the points for increasing M_∞. Point $II.a$ (solid line, no symbols), $II.b$ (solid line, $\times$), $II.c$ (dashed line, no symbols), $II.d$ (dashed line, $\triangle$) and $II.e$ (dashed line, $\circ$). The other parameters are: $k_0 a = 20$, $(l, q) = (4, 1)$, $a = 0.5$ and $b = 3$.

Figure (6.15) demonstrates that the relationship between the ambient flow and the shielding is nonlinear. For the thick boundary layer, as the velocity is increased from zero to 0.15 M, at the tip of the cylinder the shielding increases from zero to 5 dB. However, if the flow were to increase by the same amount, for example from 0.6 M to 0.75 M, the increase in shielding due to the flow would be in the region of 40 dB.

The shielding coefficient S shows a similar trend, see Figure (6.16.a). At low velocities, the large values of S indicates that little shielding occurs, however for the thick boundary layer the value of S is less than 0.01 for flow speeds above 0.5 M. For S_- at low ambient flow values, the ratio is greater than unity. This infers an increase in

the average amplitude downstream of the source at these velocities. However, at higher velocities S_- reduces to below unity.

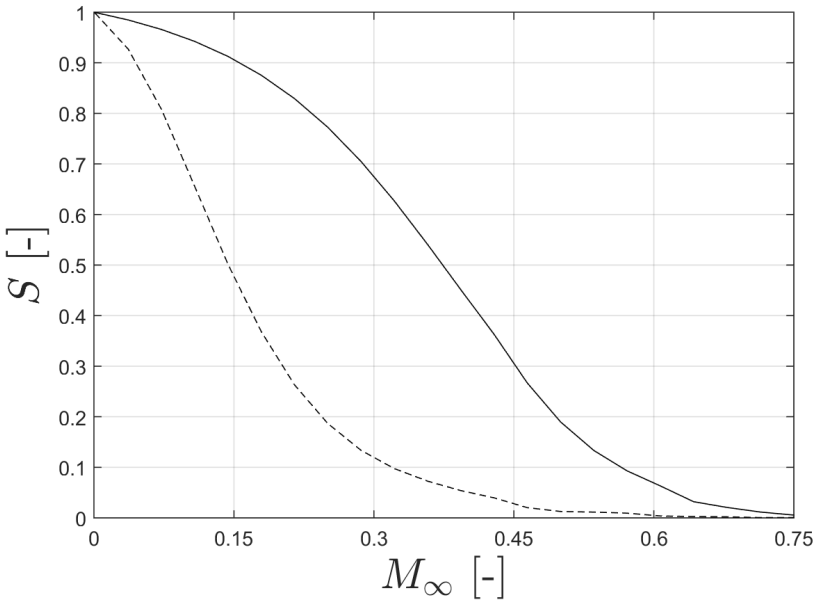

(a) S.

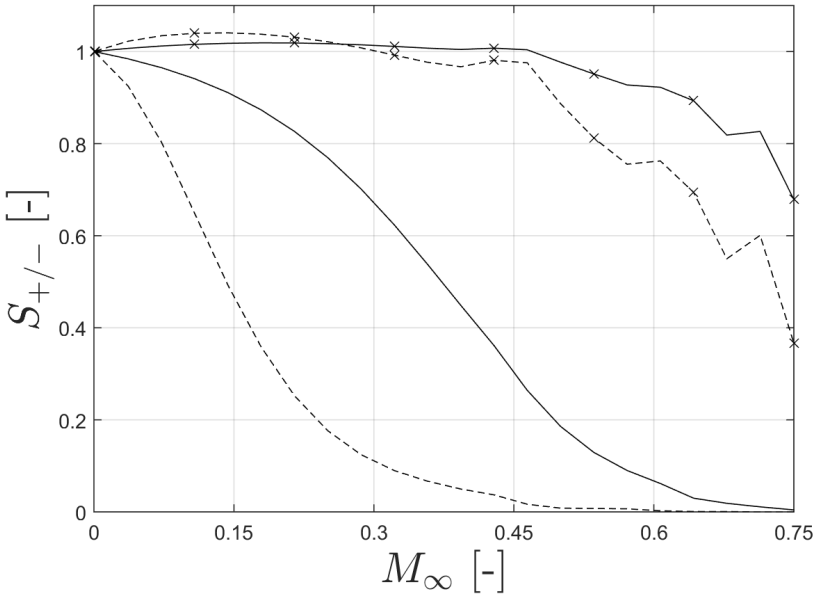

(b) S_+ (no symbols) and S_- (×). Note the y axis scale.

Figure 6.16: The three S's for increasing M_∞ with $\delta = 0.01$ (solid line) and $\delta = 0.1$ (dashed line). The other parameters are: $k_0 a = 20$, $(l, q) = (4, 1)$, $a = 0.5$ and $b = 3$.

To quickly summarise, at low velocities the boundary layer does not cause significant amounts of shielding. However, flow velocities above 0.5 M lead to very significant shielding upstream of the source and the rate increases with at higher velocities. Above 0.5 M also leads to a slight reduction in the spatial average mean-square pressure downstream of the source.

Thickness $-\delta$

The effect of varying the thickness of the boundary layer is examined in this section. By increasing the thickness from 0 to 0.1 the effect on the surface SPL is quantified. As before the source is unchanged, the flow velocity is 0.75 M and the boundary layer profile is the quarter-sine function.

Figure (6.17) shows Δ_{bl} at $\bar{\phi} = 0^{\text{o}}$ for six different thicknesses. The thinnest boundary layer is 0.0025 ($\delta/\lambda_0 = 0.0159$) which is very thin. Remarkably, even with this very thin boundary layer a significant amount of shielding is predicted. At the tip of the cylinder the boundary layer causes a reduction of 19 dB. The boundary layer thickness is approximately 1.5% of the wavelength.

The example just given has a similar δ/λ_0 ratio to the $k_0 a = 5$ and $\delta = 0.01$ case presented earlier in Section 6.3.2. The shielding values (excluding the notches in the high frequency case) are very similar down the cylinder. Both shielding values at the tip of the cylinder are about -18 dB. This result suggests that the important factor on the shielding is the ratio δ/λ_0.

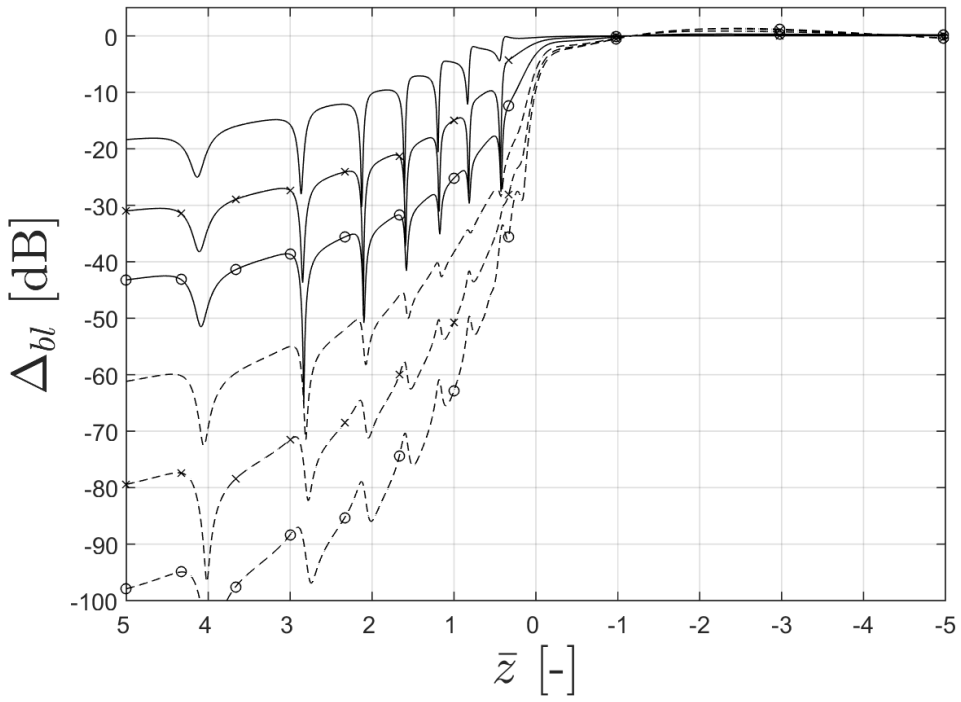

Figure 6.17: Δ_{bl} down the cylinder at $\bar{\phi} = 0^{\text{o}}$ for the six boundary layer thicknesses. The variables are $\delta = 0.0025$ (solid line, no symbols), $\delta = 0.01$ (solid line, $\times$), $\delta = 0.025$ (solid line, $\circ$), $\delta = 0.05$ (dashed line, no symbols), $\delta = 0.075$ (dashed line, $\times$), $\delta = 0.1$ (dashed line, $\circ$) The other parameters are: $k_0 a = 20$, $a = 0.5$, $(l, q) = (4, 1)$, $b = 3$ and $M_\infty = 0.75$.

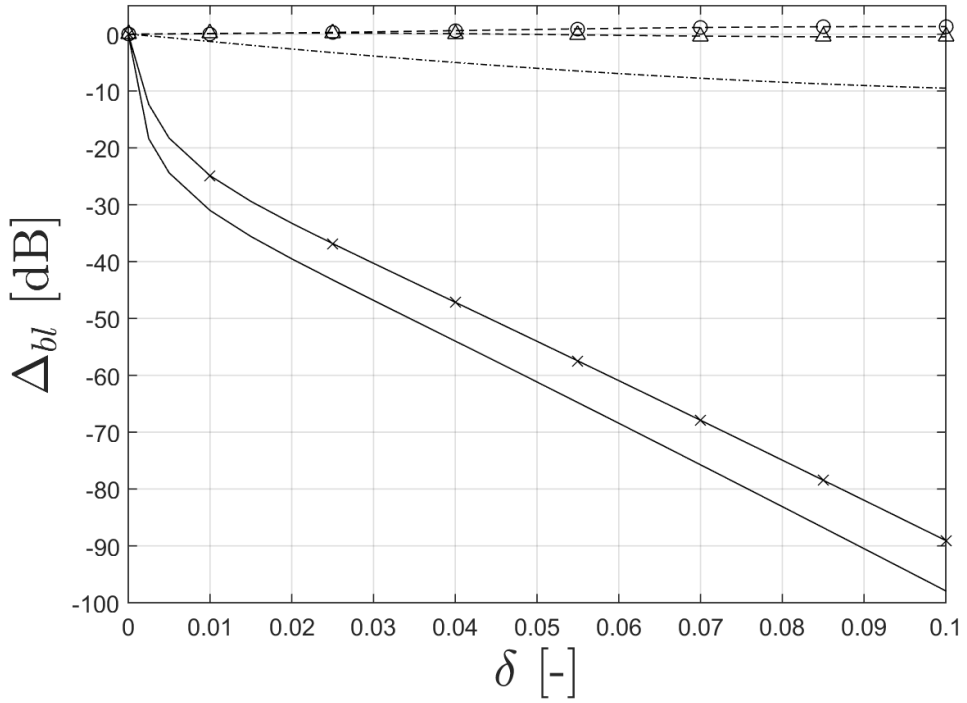

Figure 6.18: Δ_{bl} at the points for increasing δ. Point $II.a$ (solid line, no symbols), $II.b$ (solid line, $\times$), $II.c$ (dot-dashed line, no symbols), $II.d$ (dashed line, $\triangle$) and $II.e$ (dashed line, $\circ$). The other parameters are: $k_0 a = 20$, $a = 0.5$, $(l, q) = (4, 1)$, $b = 3$ and $M_\infty = 0.75$.

The shielding at the tip of the cylinder ($II.a$) as the boundary-layer thickness is increased is shown in Figure (6.18). For values of $\delta < 0.01$ the rate of increase is very sharp and nonlinear. For thicker boundary layers the increase is roughly linear. At the tip ($II.a$) the linear increase is at a slightly greater rate compared with half way down the cylinder ($II.b$). However, the main difference is observed with the very thin boundary layers.

The model is for a constant thickness boundary layer. This assumption is not realistic. This linear increase could be useful to compare predictions at different axial locations and will be exploited further in the next chapter.

The value of the shielding coefficient, S, is shown in Figure (6.19.a) as the boundary layer thickness is increased. The ratio quickly reduces to below 0.1 at around $\delta = 0.0075$. At thicker values the line flattens out to less than 0.02.

The downstream value of the shielding ratio is much larger. Above about $\delta = 0.03$ S_+ decreases linearly.

The main result of this section is that a linear increase in boundary-layer thickness leads to a linear increase in shielding. The linear increase is for a reasonably thick boundary layer. These results are based on the quarter-sine profile. This discussion is continued in Chapter 7, Sections 7.5 and 7.6.

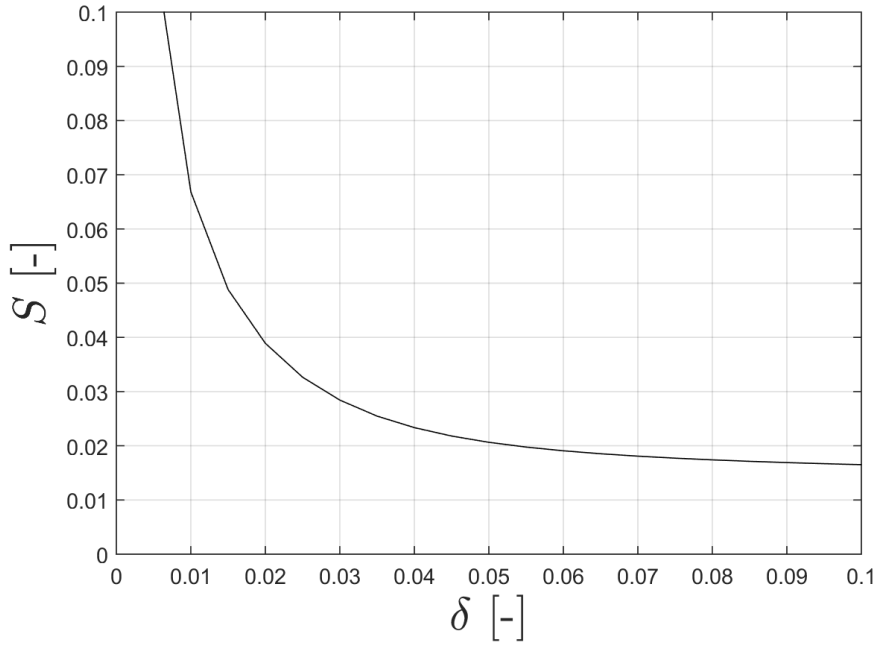

(a) $S-$ note the $y-$axis scale.

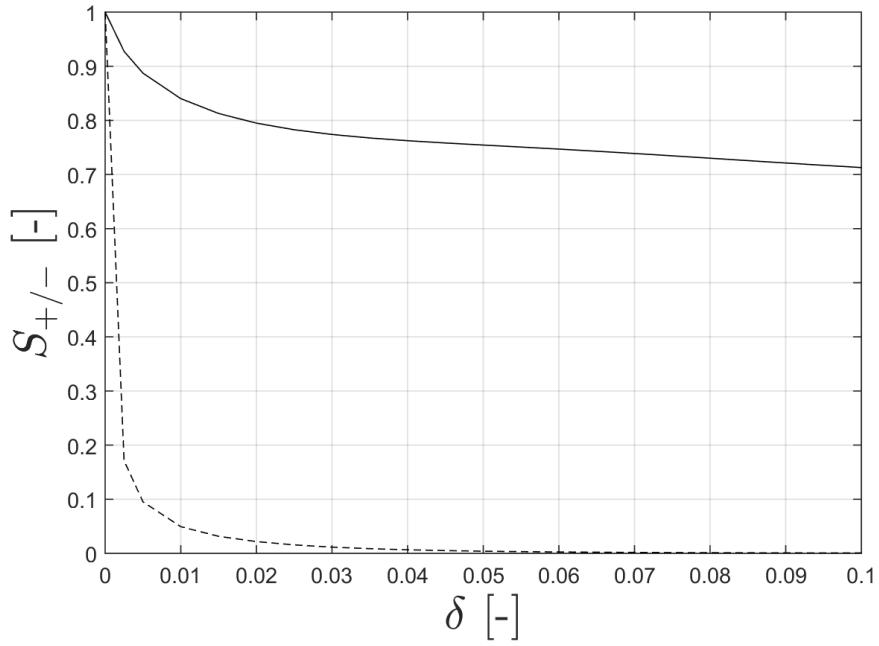

(b) S_+ (dashed line) and S_- (solid line). Note the $y-$axis scale.

Figure 6.19: The three S's for increasing δ. The other parameters are: $k_0 a = 20$, $a = 0.5$, $(l, q) = (4, 1)$ and $b = 3$

Profiles – M_z

Throughout the analysis the boundary-layer profile has been a quarter-sine boundary layer. The effect of different boundary layers are briefly quantified in this section. Also

examined, are the linear and power-law profiles:

$$M_L = \frac{M_\infty}{\delta_L}\bar{r} \quad \text{and} \quad M_{PL} = M_\infty \left(\frac{\bar{r}}{\delta_t}\right)^{\frac{1}{7}} . \tag{6.3.6}$$

The power-law profile has a linear sub-layer of thickness $\delta_{PL}/5000$. The linear profile is simple to implement and the power-law resembles a turbulent boundary layer. For all three profiles the location of the critical layer may be found analytically. Any analytic function describing the profile may be used, however it is more time intensive to locate the critical layer numerically. As before, the profiles are evaluated at a thin and thick thickness ($\delta = 0.01$ and 0.1) for the same source.

Figure (6.20) shows the shielding along the cylinder. Upstream of the source the turbulent boundary layer gives significantly less shielding compared with the other two profiles. For the thin boundary layer the difference between the power-law and quarter-sine profile at the tip of the cylinder is more than 15 dB. And for the thick boundary layer the difference is nearly 40 dB.

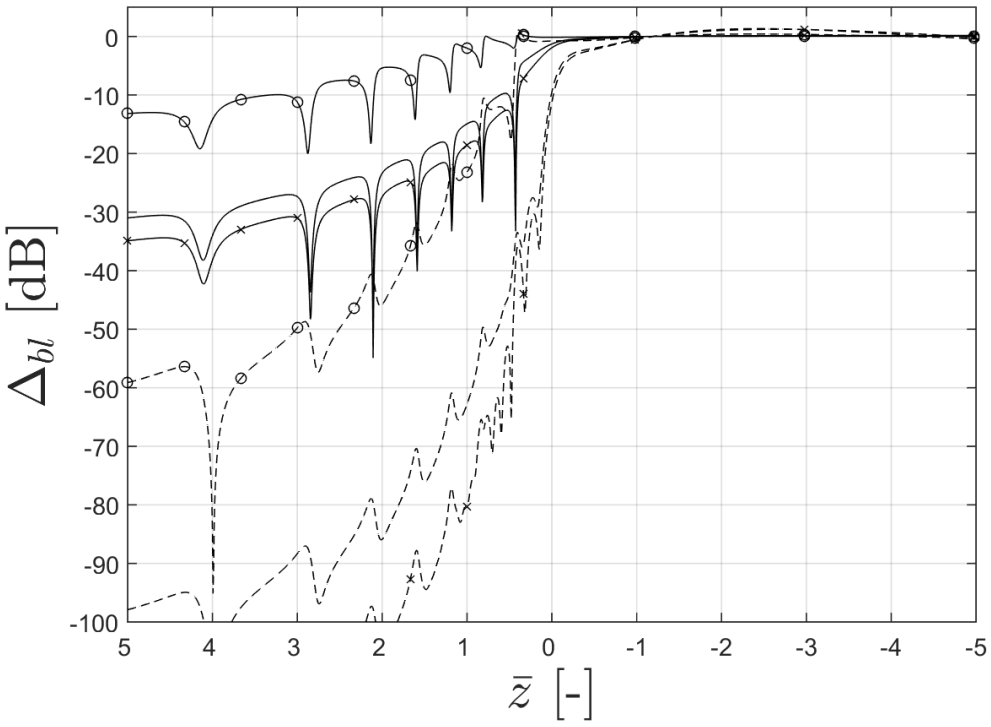

b

Figure 6.20: Δ_{bl} down the cylinder at $\bar{\phi} = 0^o$ for the quarter-sine (no symbol), linear ($\times$) and power-law ($\circ$) profiles for a boundary layer thickness of $\delta = 0.01$ (solid lines) and $\delta = 0.1$ (dashed lines). The other parameters are: $k_0 a = 20$, $a = 0.5$, $(l, q) = (4, 1)$, $b = 3$ and $M_\infty = 0.75$.

It is clear that the shielding due to the linear and quarter-sine profiles are similar. The thin boundary-layer predictions at the tip of the cylinder are only approximately 5 dB different. The overall shape of Δ_{bl} is very similar i.e. the curve is scaled and the

notches in Δ_{bl} are at roughly the same position. A similar result can be found for the boundary-layer attenuation inside ducts in Nayfeh *et al.* (1974).

The shielding ratio in Table (6.4) for the various profiles show similar results to the previous graph. They show that the power-law profile gives significantly less shielding compared with the linear and quarter-sine profiles.

Profile	S	
	0.01	0.1
Quarter-sine	0.0668	0.0165
Linear	0.0506	0.0157
Power Law	0.2885	0.0364

Table 6.4: The value of S for the three profiles for the two different thicknesses. The variables are the same as in Figure (6.20).

The profile effect is further discussed in Section 7.14 (on page 153).

6.4 Chapter Summary

In this chapter the fuselage installation effects on a spinning mode radiating from the inlet of a circular duct have been quantified. Initially the results with uniform flow were presented. It was demonstrated that the presence of the cylinder causes a reduction of more than 70 dB in the SPL on the far-side surface of the cylinder.

Then the effect of the boundary layer on the SPL on the surface of the cylinder was quantified. The relevant equation is

$$BL(k_0, k_z, M_z, \delta) = -\left(\frac{2j}{\pi[1+\delta]}\right)\left(\frac{1}{\widetilde{f}_n\Big|_{1+\delta} k_r \mathrm{H}_n^{(2)\prime}(k_r[1+\delta]) - \widetilde{f}_n'\Big|_{1+\delta} \mathrm{H}_n^{(2)}(k_r[1+\delta])}\right). \tag{6.4.1}$$

The effects can be split into source frequency (k_0) and azimuthal order (l) and the flow characteristics (δ and profile shape) and also the ambient flow velocity which affects both.

The following conclusions were found:

- Due to refraction towards the cylinder and an unfavourable δ/λ ratio, the shielding effect was not strong downstream of the source. At the furthest upstream position evaluated a minimum of 20 dB reduction is predicted.

- The azimuthal order of the mode does not affect Δ_{bl} at a practical level, however S was slightly affected by l.

- A linear relationship between the thickness of the boundary layer and Δ_{bl} was observed for $\delta > 0.01$.
- Furthermore, the turbulent boundary-layer profile had a significantly less effect on the surface SPL compared with the quarter-sine and linear profile.

From the evidence presented in this chapter, the best way of reducing noise on the surface of the cylinder is to increase the forcing frequency and decrease the azimuthal mode in the duct.

In presenting these results Objective 7 has been met.

Chapter 7

Near-Field Installed Discussion

The previous chapter examined the effect of changing the source and the boundary layer characteristics. The effects were discussed in terms of physical acoustics. This chapter probes the mathematics underpinning the physical acoustics. Initially the model itself is critiqued by examining the pros and cons and the scope of the model. Then an alternative way of modelling the refraction inspired by the results is presented. The critical layer is then analysed in the context of installation acoustics. A relationship between the asymmetry and the direction of spin of the mode is then mathematically proved. Lastly, the boundary layer thickness for different profiles is investigated. The purpose of these investigations is two fold; to glean insight but also explore ways to radically optimise the method.

This chapter fulfils Objective 7.

7.1 The Model

Before the main discussion, a critique of the model is necessary in order to establish the accuracy of the predictions. This section will briefly remind the reader what the model does and the method to implement it. The advantages are outlined, then, the important aspects of scope and limitations of the model, and method, are discussed with limiting cases given where appropriate.

The model is a simple mathematical model to predict radiating inlet engine fan tones adjacent to a cylindrical fuselage with a boundary layer. The disc source is a canonical model, however the Wiener–Hopf source is too complex for this label. The geometry is simplified in order that the problem may be solved using Fourier methods. To model the refraction effect, due to the shear layer running down the cylinder, the Pridmore-Brown equation was solved in this region. This can be solved using an ODE solver in the Fourier domain.

The major advantage of formulating the method analytically is computational effi-

ciency. The computational cost is small compared to an equivalent finite element code. The method is fully 3 dimensional, a CAA code implementing diffraction from an inlet of a duct over a large 3D domain including a large scattering object and refraction would take many cores a very long time to compute. For example Dierke *et al.* (2013) calculated an installation problem using 4 CPU and took a full week to calculate. Parallelised over four cores, the method implemented in this thesis takes only about 2/3 hours on a desktop. Furthermore, the method lends itself to parallelisation; the total computational time is roughly inversely proportional to the number of cores available.

The decrease in computational time is traded against simplifications in geometry. The fuselage is approximated as an infinitely long cylinder. Initially this seems ludicrous, however Figure (7.1) shows the surface SPL of the dominant rotor locked tone at $k_0 a = 20$ with 16 blades (typical for a state-of-the-art engine) in uniform flow. The figure shows the principal lobe intersects at approximately $\bar{z} = 2$, i.e. two cylinder radii, in front of the source plane. Less than ∼100 dB (relative to the maximum value on the cylinder) is radiated to $\bar{z} = 5$, equivalent to the nose of the fuselage, due to the source directivity alone. Furthermore, the previous chapter showed that at these high frequencies the thin turbulent boundary layer profile causes around 20 dB of shielding. If any significant noise were radiating to the tip of the cylinder it would be refracted away by the boundary layer. Therefore, the cylinder approximation does not curtail the validity of the model.

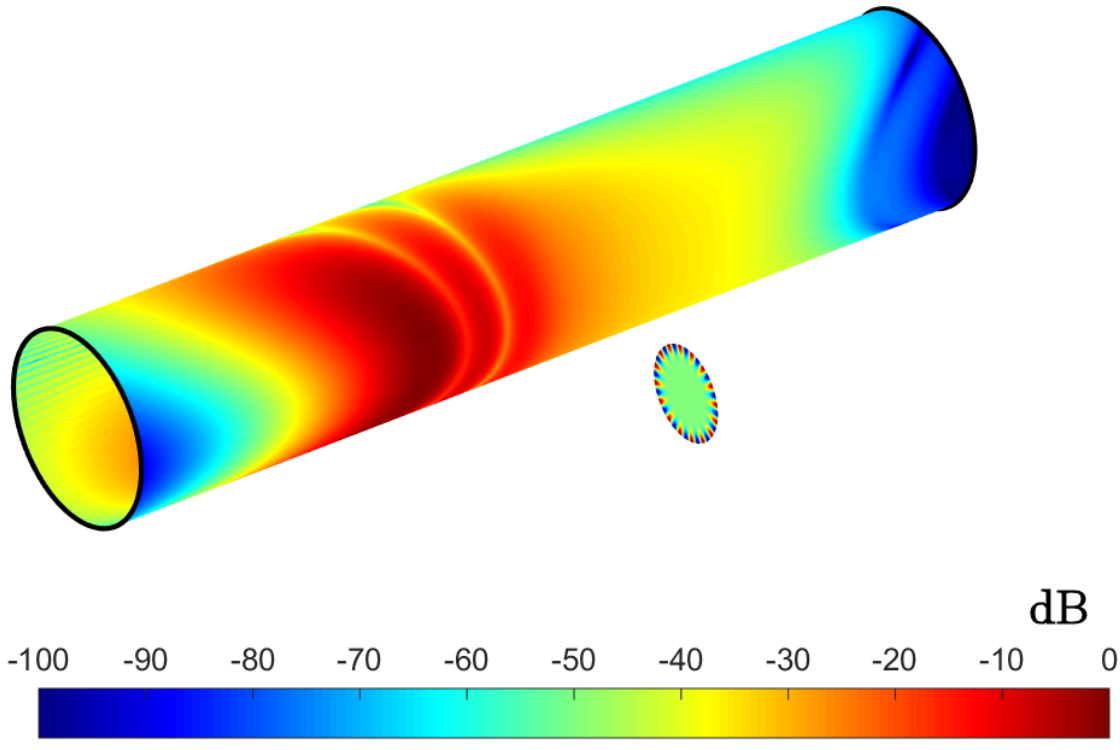

Figure 7.1: SPL on cylinder for $k_0 a = 20$ and $(l, q) = (16, 1)$. This source is reasonably realstic of future generations of turbofan engines. With no boundary layer, very little sound reaches the tip of the cylinder at $\bar{z} = 5$ in this simulation.

An infinite cylinder does neglect the diffraction of any noise reaching the nose of the fuselage. Of what little noise that does reach the tip of the cylinder (perhaps a low frequency and flow velocity) nose diffraction could be added in the scattering model. Bowman and Uslenghi (1969) lists analytic expressions for scattering due to a cone. It was neglected here under the assumption that the gradual change in shape has little effect on the relatively short wavelengths and does not affect the results. Including the boundary layer over this shape is beyond the scope of analytical modelling.

The geometry of the engine inlet is simplified to a semi-infinite circular duct. This was allowed to let the mode shapes be integrated analytically when forming the disc source (the important part of McAlpine, Gaffney and Kingan, 2015). Real engine inlets are not perfectly circular, a squashed circle changes the directivity slightly. In Tyler and Sofrin (1962), the rectangular duct had a directivity which was remarkably similar to the circular duct. The circular duct approximation allows for analytic formulation for a modest drop in accuracy of the directivity predictions.

Furthermore, the infinitesimal engine duct wall thickness is unavoidable in theoretical models. The effect of walls with finite thickness may be significant, especially for short wavelengths. Including finite wall thickness is well beyond the theoretical method's scope and thin walls are a good approximation at low frequencies.

Another issue with the source is the uniform flow assumption. In recent years the effect of inlet flow distortion on radiation has been modelled, see Daroukh *et al.* (2016). The effect on the blade passing frequency was affected by around 8 dB. Changes in the flow velocity must be computed with a CAA method and is thus beyond the scope of this project.

For aerodynamic reasons the highlight of the engine is normal to the flow. The engine is slightly off axis, this means the duct termination is at an angle to the duct axis. In quiescent flow, this angular offset has been analytically modelled in the free-field and far-field by McAlpine *et al.* (2012). Adapting this and including it to the model would be possible but the mathematics is very complex. This angular displacement can be simulated, to a first approximation, by changing the frequency and altering the boundary-layer thickness such that λ_0/δ is constant.

Reflections between the fuselage and the engine cylinder are not modelled. Including these reflections is unnecessary because they are both cylindrical diffusers and would lead to negligible amplitudes of the reflected waves. No aeroacoustic references are readily available to support this. However, cylindrical diffusers are commonly installed in auditoria to induce a diffuse field. The benefits of convex surfaces are detailed in Barron (2010).

The previous paragraphs have demonstrated that the geometry simplifications have been shown to have little effect on the model. However the flow assumptions; parallel flow and constant boundary layer thickness are more significant.

The flow was modelled such that the time-average mean velocity was taken. This assumption is appropriate in the uniform flow regime. In the boundary layer the turbulence effect is explicitly neglected. For example, Powles *et al.* (2011) demonstrated that turbulence cannot be neglected when modelling tones propagating through a shear layer. Haystacking could result in a modest reduction in the amplitude of the tone on the surface of the cylinder and leakage into other frequencies. That being said, the boundary layer is thinner than the mixing region of a jet so the effects may not be so strong.

In the model, the boundary layer has a constant thickness all along the cylinder. This assumption is wrong; the boundary layer is zero at the nose and grows along the fuselage. This omission is one of the weakest parts of the model because the refraction changes with boundary layer thickness. The model starts by taking a Fourier transform in the axial direction, this would not be appropriate for a growing boundary layer. However, Rienstra (2003) has analytically modelled a duct with a cross section that slowly changes. This analysis could be modified to boundary layer growth and included in the model.

However, boundary layers grow slowly; this could be exploited when estimating shielding at axial locations near to one another. However the calculation would have to be repeated with different thicknesses to compare the shielding at axial positions far apart from each other.

Lastly, the usual assumptions on the fluid were assumed; inviscid, compressible, isentropic perfect gas. Inviscid flow in the boundary layer is an unavoidable contradiction. These assumptions are common for all theoretical models (Rienstra and Hirschberg, 2013).

To sum up, as the model is theoretical, the method is very quick and computationally cheap relative to an equivalent CAA method. This speed was traded off through simplifications in geometry and flow characteristics e.g. a semi-infinite circular duct is not a realistic approximation of an inlet. Further improvements correspond to a serious increase in complexity for a relatively modest increase in accuracy. Upstream, the infinite cylinder approximation of a fuselage was also shown to be a fair approximation owing to the directivity of the source and the refraction effect of the boundary layer. The Wiener–Hopf solution assumes infinitesimal duct walls, this trade–off in simplicity extends the solution to the rear arc. Finally, the flow simplifications are more significant and may affect the accuracy of the predictions. The constant boundary layer thickness is the main drawback with the model. The intended purpose of the method is for parametric studies to refine the design parameters. This would lead to a rough idea of shielding, once the desired variables have been chosen, a detailed CAA method could be used.

7.2 Spectra Inspection

The previous chapter presented many results via the parametric study. The reason for differing amounts of shielding was described in terms of physical acoustics. In this section, the effect of varying different variables on the mathematics is discussed. The analysis is conducted in the Fourier domain, initially on the isolated 'installation' function BL, then the complex directivity for the Wiener–Hopf source is then included in the analysis. Finally some simple observations lead to a wavenumber filter that simulates refraction based on the uniform flow method.

7.2.1 The Installation Effect

As isolated before (page 72), the scattering effect of a rigid, infinitely long cylinder and the refraction effect of the boundary layer running down the cylinder can be modelled via the function

$$BL(k_0, k_z, M_z, \delta) = -\left(\frac{2j}{\pi[1+\delta]}\right)\left(\frac{1}{\widetilde{f}_n\Big|_{1+\delta} k_r \mathrm{H}_n^{(2)\prime}(k_r[1+\delta]) - \widetilde{f}_n'\Big|_{1+\delta} \mathrm{H}_n^{(2)}(k_r[1+\delta])}\right). \tag{7.2.1}$$

The function is dependent on frequency and flow velocity (manifest in k_r), the boundary-layer profile (shown in the result of the ODE solver, $\widetilde{f}$ and$\widetilde{f}'$, and k_r) and the boundary-layer thickness in all terms.

The flow is in the negative axial direction and for the following analysis is a reasonably high Mach number of 0.75. Therefore, positive wavenumbers propagate against the flow and negative wavenumbers propagate with the flow.

The function BL acts like a transfer function at each wavenumber. When dealing with transfer functions the amplitude effect on the incident field is most pertinent. The amplitude of BL in the Fourier domain is plotted in Figure (7.2.a). It is shown for uniform flow (the rigid cylinder effect) and for the thick and thin quarter-sine boundary-layer profile.

The uniform flow case shows the cylinder effect in isolation. The cylinder suppresses wavenumbers in the middle of the spectrum and amplifies near the Doppler shifted frequencies of $k_z^{\pm}$. The pattern is symmetrical about the mid-value between the Doppler shifted frequencies of about –11 and 80.

Once a thin boundary layer (of 0.01) is introduced, the high positive wavenumber content is massively suppressed. However, the low valued positve wavenumbers of less than 30 and the wavenumbers travelling with the flow are unaffected.

A thick boundary layer leads to almost total reduction of the wavenumbers travelling against the flow, above about 40 and below 20 a reduction is observed. Contrary to the other cases, downstream the negative wavenumbers are slightly amplified.

At slightly above $k_z = 20$ all three transfer functions converge. The reason for this is unknown but it occurs very close to $k_z = k_0$.

Not shown, but the rate of roll-off for high positive wavenumbers increases in a similar manner (for a given boundary layer thickness). The most important factor for a transfer function is not k_0 nor δ but rather the ratio of λ_0/δ.

The total effect of the boundary layer including the Wiener–Hopf source characteristics, $\widetilde{\eta}_{d,lq}$, are shown in Figure (7.2.b) by plotting $\widetilde{\alpha}$ over the relevant domain. It shows that the uniform flow case is dominated by large wavenumbers travelling with the flow.

With the addition of the thin boundary layer, the high frequency content is significantly reduced to the same order of magnitude of the negative wavenumbers. However, the thick boundary layer reduces the amplitude of $\widetilde{\alpha}$ at large positive values to zero. This means that the integrand is now dominated by negative wavenumbers. The pressure is now constituted by low valued wavenumbers propagating against the flow and the full range of those travelling in the direction of the flow.

It is also worth noting that $\widetilde{\alpha}$ corresponds to the spectra of the pressure at $\bar{z} = 0$. The additional effect of the axial location is plotted on Figure (7.3). It shows that the axial location does affect the amplitude of the integrand, bare in mind k_z is complex. However, the reduction in amplitude alone cannot be the cause for the reduction of 100 dB in the SPL at either end of the cylinder.

Instead, the phase must also be a culprit. The inverse transform can be simplified to the relevant parts and the exponent can be split

$$p \propto \int \widetilde{\alpha}\, e^{-jk_z\bar{z}}\, \mathrm{d}k_z = \int \widetilde{\alpha}\, \left(\cos\left(k_z\bar{z}\right) - j\sin\left(k_z\bar{z}\right)\right)\, \mathrm{d}k_z. \tag{7.2.2}$$

The change in axial location is manifest only in the sine term. Therefore, the integral can be written upstream as

$$p^{+} = \int \widetilde{\alpha}\, \left(\cos\left(k_z\bar{z}\right) - j\sin\left(k_z\bar{z}\right)\right)\, \mathrm{d}k_z, \qquad \bar{z} > 0, \tag{7.2.3}$$

and downstream

$$p^{-} = \int \widetilde{\alpha}\, \left(\cos\left(k_z\bar{z}\right) + j\sin\left(k_z|\bar{z}|\right)\right)\, \mathrm{d}k_z, \qquad \bar{z} < 0. \tag{7.2.4}$$

Upstream of the source the shielding is very strong. Therefore, the value of the inverse transform must be much less than downstream. The only possible way in which this can happen is

$$\int \widetilde{\alpha}\, \cos\left(k_z\bar{z}\right)\, \mathrm{d}k_z \approx j\int \widetilde{\alpha}\sin\left(k_z\bar{z}\right)\, \mathrm{d}k_z. \tag{7.2.5}$$

The composing functions of $\widetilde{\alpha}$ are too complex to be taken further analytically. However a numerical example supports this theory. Downstream the absolute value of p^{-}

$= 0.0013$ whereas upstream $p^+ = 2.3 \times 10^{-6}$. So amplitude and phase are important for the axial change. This, in part, causes the reductions in pressure that signify shielding.

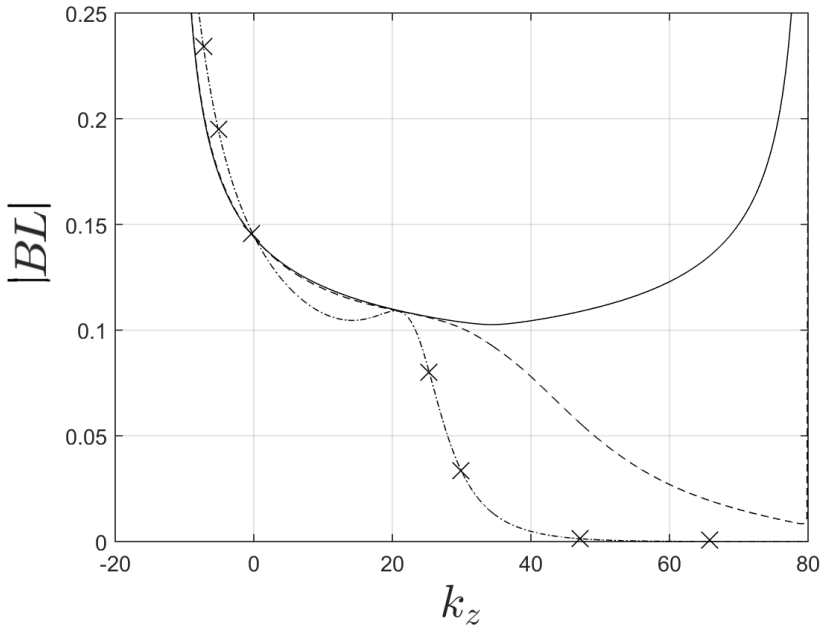

(a) BL for the three boundary-layer thicknesses.

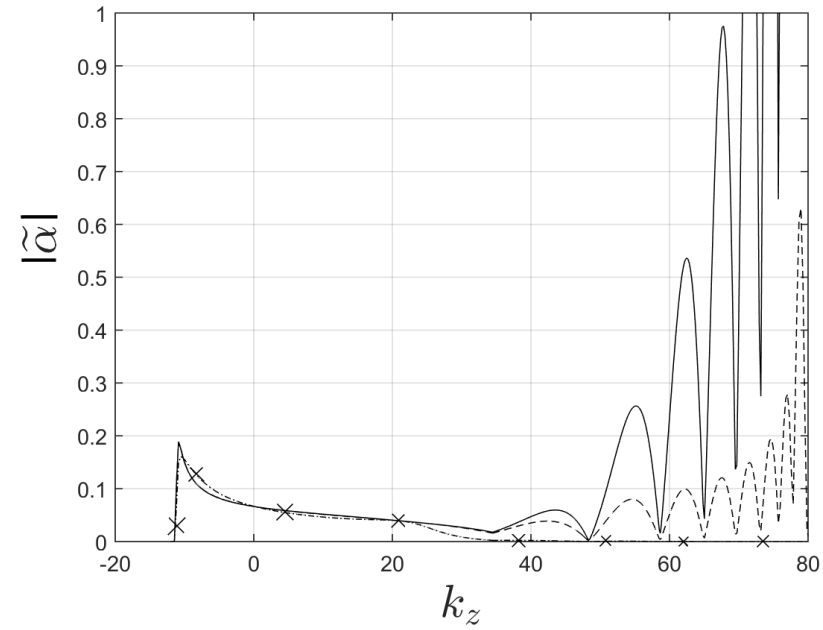

(b) $\widetilde{\alpha}$ for the boundary-layer thicknesses.

Figure 7.2: BL and $\widetilde{\alpha}$ (for the WH source) with $\delta = 0$ (solid line), 0.01 (dashed line) and 0.1 (dot-dashed line, $\times$) for $n = 0$. The other parameters are: $k_0 a = 20$, $a = 0.5$, $b = 3$, $(l, q) = (4, 1)$ and $M_\infty = 0.75$.

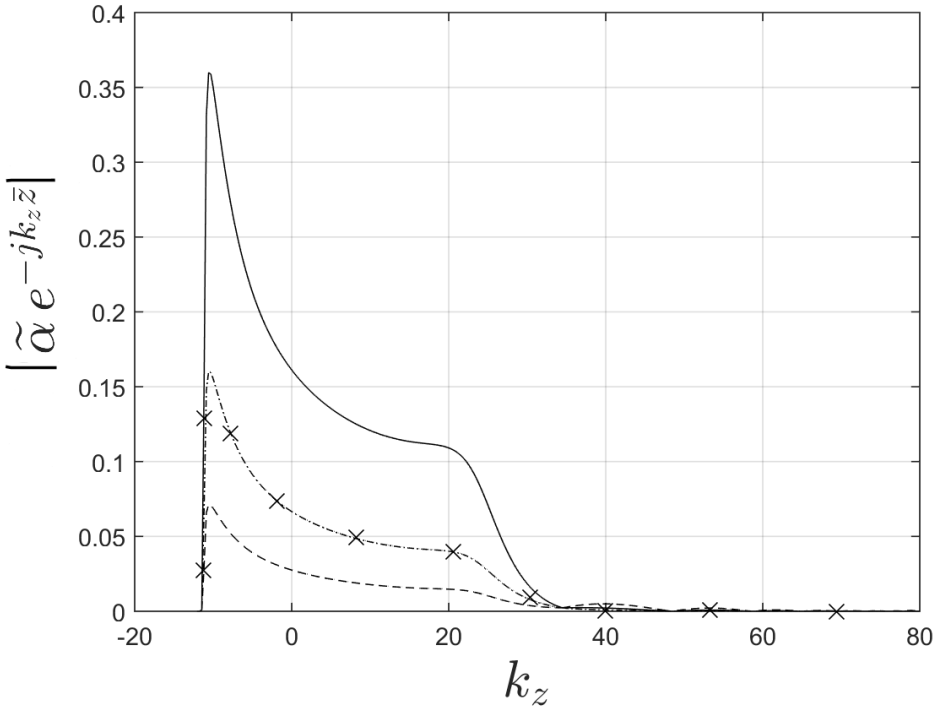

Figure 7.3: $|\widetilde{\alpha}\,\mathrm{e}^{-jk_z\bar{z}}|$ for $\bar{z}=-5$ (solid line), 0 (dashed line) and 5 (dot-dashed line, $\times$) for $n=0$. The other parameters are: $k_0a=20$, $a=0.5$, $b=3$, $l=4$, $M_\infty=0.75$. Bare in mind k_z is complex.

7.2.2 Spectra Manipulation

The reduction of the wavenumbers is exploited in this section. As ascertained, the boundary layer acts like a wavenumber filter, where the high valued wavenumbers propagating into the flow are suppressed and the rest are unchanged. Therefore, as an alternative to the relatively time intensive process of integrating through the boundary layer with the ODE solver, a filter is applied to the uniform flow method. The most simple of filters to crudely recreate the effect of BL is defined as

$$W\left(k_z\right)=\begin{cases}1, & k_z\leqslant 0,\\ 1-k_z/k_z^+, & 0<k_z\leqslant k_z^+,\\ 0, & k_z>k_z^+.\end{cases} \tag{7.2.6}$$

This filter leaves negative wavenumbers unchanged and linearly reduces high valued wavenmubers to zero at the upper shifted wavenumber. This filter alters the uniform flow expression for pressure to

$$p_t(a_0,\bar{\phi},\bar{z})=\frac{1}{(2\pi)^2}\sum_{n=-\infty}^{\infty}\left(\int_{-\infty}^{\infty}\widetilde{\alpha}_n(k_z)\,W\left(k_z\right)\mathrm{e}^{-jk_z\bar{z}}\mathrm{d}k_z\right)\mathrm{e}^{-jn\bar{\phi}}\,, \tag{7.2.7}$$

where $\widetilde{\alpha}$ is defined as before with $\delta = 0$. An example of the integrand is shown in Figure (7.4).

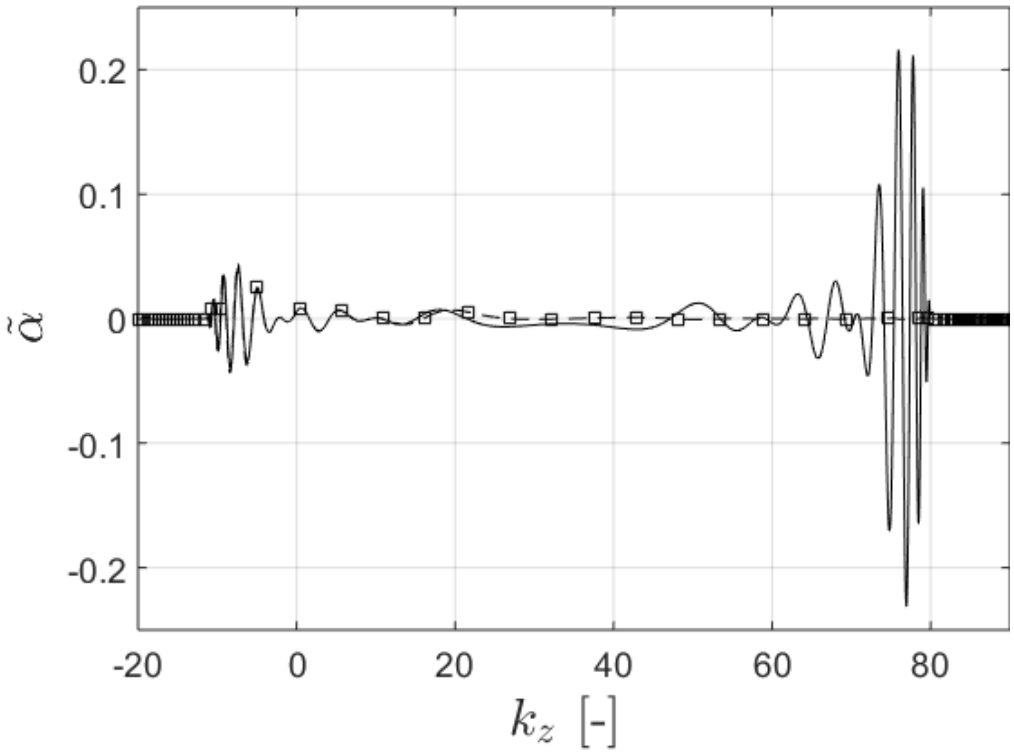

Figure 7.4: The function $\widetilde{\alpha}_n$ for the zeroth azimuthal mode with (dashed line, □) and without W (solid line). The parameters are: $k_0 a = 10$, $a = 0.5$, $(l, q) = (4, 1)$, $b = 3$ and $M_\infty = 0.75$.

Since shielding is pertinent upstream the simpler disc source is used in this analysis. An example of the uniform flow case and the uniform flow with the filter is shown in Figure (7.5). The result with the window applied does seem to simulate the refraction effect reasonably closely to that of implementing the full solution (including BL).

The difference between the two methods (Δ_W) on the near side of the cylinder is shown in Figure (7.6). The difference is similar to the Δ_{bl} for $k_0 a = 20$ and $\delta = 0.01$, Figure (6.7), however this is serendipitous. At the tip of the cylinder the window method over predicts by approximately 2 dB. The method does not predict the shielding accurately at low axial values. At the source plane the model with W over predicts by about 5 dB. This difference in shielding is small, but problematically, the shape of the curve in Δ_W is not identical to the full model.

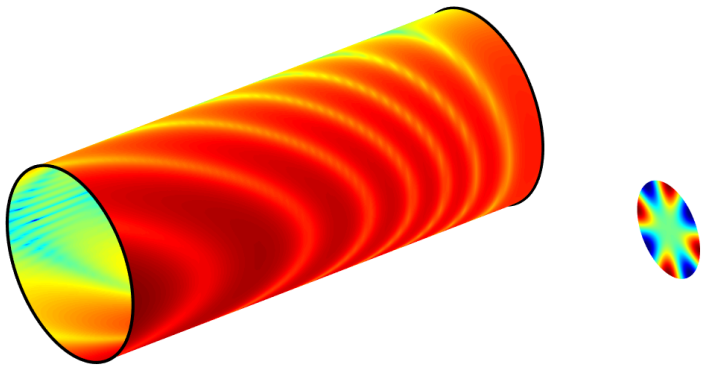

(a) Uniform flow.

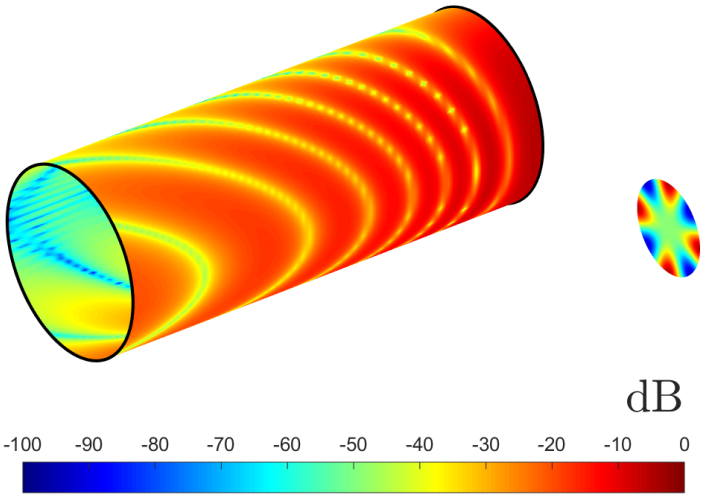

(b) With filter W.

Figure 7.5: Uniform flow and simulated shielding with W. The relevant parameters are: $k_0 a = 20$, $a = 0.5$, $(l, q) = (4, 1)$, $b = 3$ and $M_\infty = 0.75$.

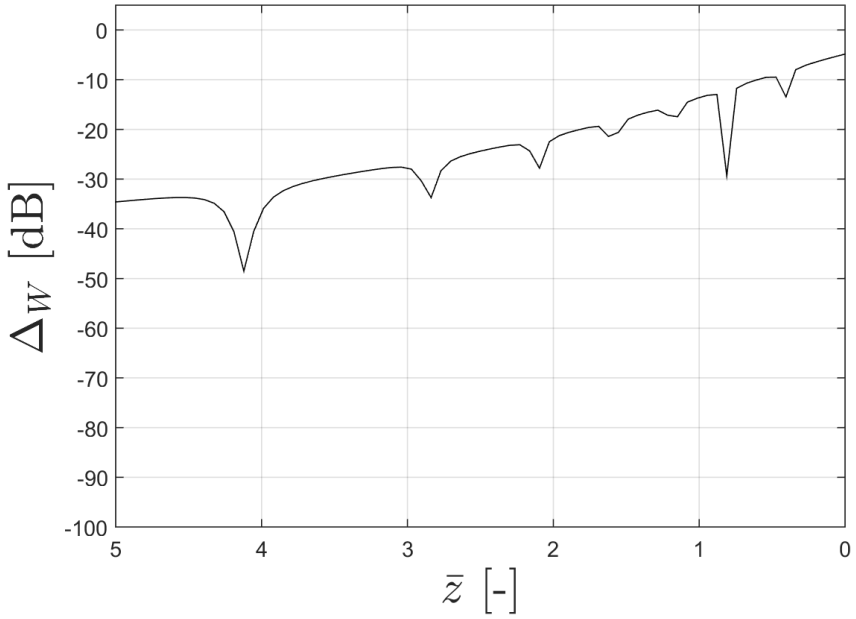

Figure 7.6: Difference between the two models in Figure (7.5) at $\bar{\phi} = 0$.

In summary, shielding has been simulated by approximating the function BL as a very simple window on the uniform flow wavenumbers. The shielding was roughly similar to that due to a quarter-sine profile boundary layer of wavelength ratio $\lambda_0/\delta = 0.637$. The method is very quick, however it is too crude to give accurate values of shielding for a given parameter. After refinements (exponential or polynomial decay and change the of rate of roll-off) it may be accurate but this has not been pursued because the full method (that implements BL) is relatively quick anyway.

7.3 (Not so) Critical layer

Previously, authors modelling sound propagation through a shear layer have devoted significant amounts of time to the critical layer. This section will discuss the critical layer specifically in installation acoustics.

The textbook definition of the critical layer is a point where the ambient flow velocity equals the phase velocity of the wave. Physically this means that the perturbation in pressure travels at the same velocity as the flow and is, in effect, hydrodynamic. This leads to the often quoted full hydrodynamic spectrum.

Mathematically, this occurs as a regular singularity in the transformed Pridmore-Brown equation, given the full treatment in Section 5.1.3 (page 72). The singularity occurs thanks to the transform of the material derivative. Therefore the critical layer occurs when

$$k_z = -\frac{k_0}{M_z(\bar{r}_c)}, \tag{7.3.1}$$

for

$$k_z \leqslant -\frac{k_0}{M_\infty}. \tag{7.3.2}$$

These wavenumbers occur in the evanescent part of the wavenumber spectrum for waves travelling with the flow.

If the forcing frequency and profile function are real then the critical layer is always at a real wavenumber. This becomes an issue in assembling the inverse Fourier transform integrand. For a given frequency and profile the ODE solver must cross the singularity. The singularity can either be bridged by the Frobenius series (favoured in installation acoustics) or avoided all together by letting the axial wavenumber be complex.

The critical layer is a regular singularity. Therefore a finite valued solution to the Pridmore-Brown equation is found by the Frobenius series, see for example Figure (5.12). This form of the Frobenius series is only valid away from turning points. This limits the profile choice such that no flow separation can be modelled along a cylinder – this would occur at stall, so noise propagation is not a priority.

Brambley *et al.* (2012) reports that the critical layer caused accuracy issues when calculating duct modes as long ago as Swinbanks (1975). Brambley shows that the Froebnius series leads to much more accurate mode predictions for the numerical calculation of sound fields in a duct. However, the fuselage installation problem is an exterior problem and there are no modes.

He also demonstrates that the critical layer must be included when the source is located inside the shear region. Again, for the problem at hand, the source is always in the uniform flow, well away from the boundary layer.

Brambley reports that the critical layer does contribute to the total solution in the duct when the source is in uniform flow. The method in this thesis calculated the limits of the inverse Fourier transform integration by converging from very large values of k_z. If the critical layer had contributed significantly to the integral this process would have ensured that it would be included in the solution. As it was, for the forcing frequencies considered in this thesis, the limits of integration were often inside the cut-on region (I_2).

Therefore, for installation problems, it would seem the critical layer does not significantly contribute to the overall solution. This conclusion is evidence based and not watertight. A point mass for the convected wave euquation was the starting position, and not the Green's function for the Pridmore-Brown equation. Therefore hyrodynamic perturbations, such as vortices from monopoles in the shear layer, are not included in the method. Furthermore, if haystacking were to be included in the problem, then the interaction between the hydrodynamic and acoustic fields may cause the critical layer to be important.

An alternative to the Frobenius solution is to let the axial wavenumbers be complex.

This method was suggested by Kopiev *et al.* (1992). By using complex wavenumbers the critical layer is avoided. This is a benefit because no special treatment is required, no restrictions on the profile are imposed, and the method is quicker because it does not require switching to the series solution. It also avoids the singularities at $k_z^{\pm}$.

It is worth noting, of course, that including viscosity in the shear layer would render this discussion void.

7.4 Ray Approximation to Predict Trapped Sound

It was noted in the previous chapter that downstream of the source, the boundary layer is responsible for a slight increase in amplitude with increasing axial distance, see Figure (6.7). Due to the high forcing frequency, a possible cause for the pressure increase could be 'trapped' sound. The sound enters the boundary layer and after a reflection, cannot leave due the shear refracting the ray back to the rigid boundary. To test this theory, an in-house code used to implement ray equations in Pierce (1981) (page 375) was adapted to include the rigid reflections at the boundary. The code is in 2D Cartesian coordinates but the characteristics of the boundary layer are similar.

As Figure (7.7) shows, upstream of the source the rays are strongly refracted away from the rigid boundary and downstream they refract towards the plate. In the relevant axial range none of the rays are refracted back into the boundary layer. Therefore it is unlikely that channelling is the mechanism for the increase in amplitude.

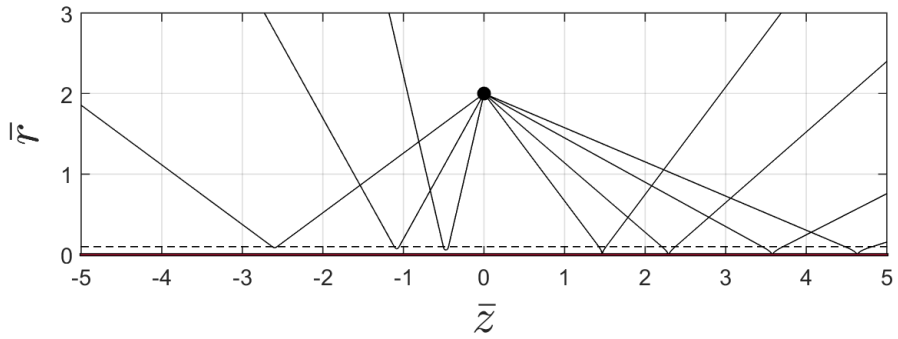

Figure 7.7: The ray tracing code with the quarter-sine profile of $\delta = 0.1$ and $M_\infty = 0.75$.

Upstream, the high frequency of the source and the convective effect of the flow is high enough enough for the ray approximation, downstream the results may be specious. The flow elongates the wavelengths, as discussed previously the ratio between wavelength and boundary layer thickness is comparable. The results have been included in the analysis because it helps the conclusion: if high frequencies are not channelled then the realistic lower frequencies will certainly not be.

A possible alternative mechanism could be creeping waves spiralling around the cylinder back to the near-side. This would be more difficult to test.

7.5 Instantaneous Pressure on the Cylinder

Cabin noise is prioritised in this thesis. Panel resonance is forced by the incident pressure field (Sas *et al.*, 1993). It is sound transmitted through the panel in the sidewall of the aircraft that is largely responsible for cabin noise. This means for cabin noise applications the instantaneous pressure is very important.

Figure (7.8) shows examples of the real (a) and imaginary (b) components of the normalised pressure on the cylinder for the low frequency example ($k_0 a_0 = 5$) with a thin quarter-sine boundary-layer profile. They show that upstream of the source the flow effects cause the wavelengths to decrease. Downstream of the source the flow stretches the waves such that they have very long wavelengths. Examples of the unfurled pressure in still flow can be found in Figure (7.10.a) on page 149.

These predictions may not match fuselage measurements; in reality the panel has some flexibility (which is not accounted for on the rigid cylinder) and this will couple, to some extent, to the pressure field.

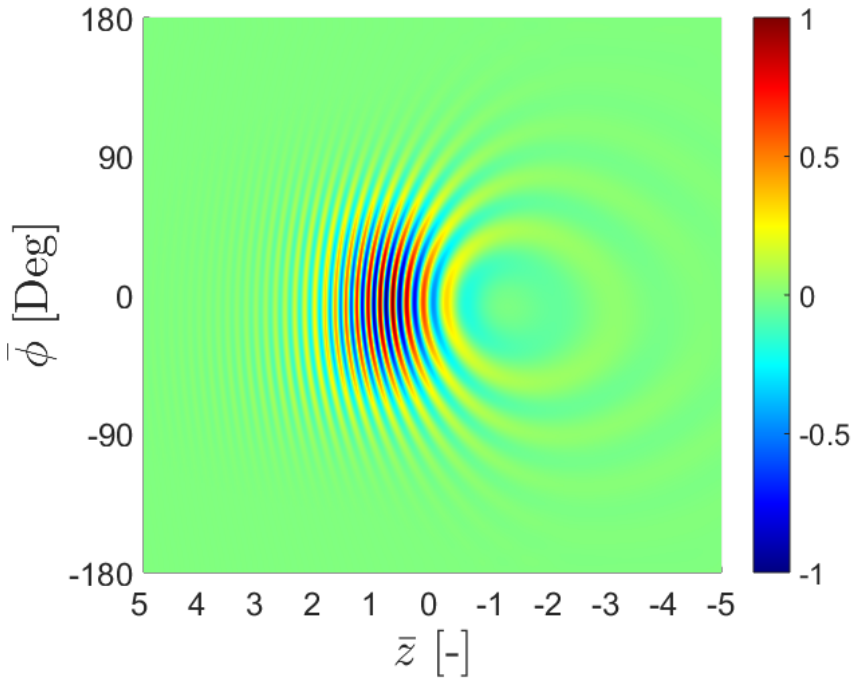

(a) Real.

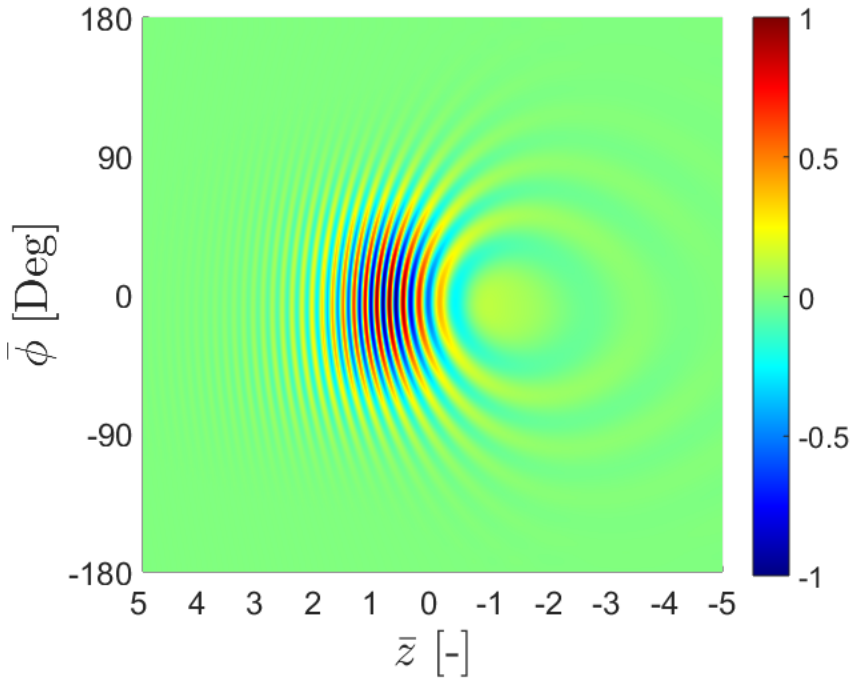

(b) Imaginary

Figure 7.8: Normalised instantaneous pressures (real (a) and imaginary (b)) on the unfurled cylinder. The relevant parameters are: $k_0 a = 5$, $(l, q) = (4, 1)$, $a = 0.5$, $b = 3$, $\delta = 0.01$ and $M_\infty = 0.75$.

7.6 Asymmetry on the Cylinder

Measured in decibels, the incident field is axisymmetric because it has an $e^{jl\phi}$ dependency. However, the SPL on the surface of the cylinder is slightly asymmetric. This was observed when analysing the results. The difference between the SPL is shown to be dependent on the direction of the mode. The difference is also frequency and mode dependent and is shown to behave in the opposite manner to a propeller type source.

The analysis is conducted on the uniform flow model to avoid requiring the numerical solutions gained via the ODE solver.

7.6.1 Direction of Spin

The difference between the SPL on one side of the cylinder to the other is defined by

$$\Delta_{\bar{\phi}} = \text{SPL}|_{\bar{\phi}} - \text{SPL}|_{-\bar{\phi}}. \tag{7.6.1}$$

This difference is shown in Figure (7.9). The figure shows the difference for a low frequency of $k_0 a = 5$ and for the same mode spinning in both directions. This leads to a reflection in SPL in the $\bar{x}$-axis, or SPL $(-l, \bar{\phi})$ = SPL $(l, -\bar{\phi})$. This result is consistent with propeller type sources, where the direction of spin of the source changes.

This relationship can be proved mathematically. If the direction of spin is reversed the pressure on the cylinder is reflected about $\bar{\phi} = 0$. This is expressed as

$$\left|p_t(-l, \bar{\phi})\right| = \left|p_t(l, -\bar{\phi})\right|. \tag{7.6.2}$$

However, the mathematics reveals more to this relationship.

First, for brevity extract the parts of the total equation which concern l and ϕ

$$p_t(l, \bar{\phi}) \sim \sum_n (-1)^{l+n} \int \frac{\mathrm{H}^{(2)}_{l-n}(k_r b)}{\mathrm{H}^{(2)}_n(k_r)} \mathrm{e}^{-jk\bar{z}} \,\mathrm{d}k_z \, \mathrm{e}^{-jn\bar{\phi}}. \tag{7.6.3}$$

Splitting the azimuthal Fourier term gives

$$p_t(l, \bar{\phi}) \sim \sum_n (-1)^{l+n} \int \frac{\mathrm{H}^{(2)}_{l-n}(k_r b)}{\mathrm{H}^{(2)}_n(k_r)} \mathrm{e}^{-jk_z\bar{z}} \,\mathrm{d}k_z \, \left(\cos(n\bar{\phi}) - j\sin(n\bar{\phi})\right), \tag{7.6.4}$$

and for negative $\bar{\phi}$

$$p_t(l, -\bar{\phi}) \sim \sum_n (-1)^{l+n} \int \frac{\mathrm{H}^{(2)}_{l-n}(k_r b)}{\mathrm{H}^{(2)}_n(k_r)} \mathrm{e}^{-jk_z\bar{z}} \,\mathrm{d}k_z \, \left(\cos(n|\bar{\phi}|) + j\sin(n|\bar{\phi}|)\right). \tag{7.6.5}$$

It is clear that for positive and negative $\bar{\phi}$ the pressures will not necessarily be equal due

to the $\pm j\sin(n|\bar{\phi}|)$ term.

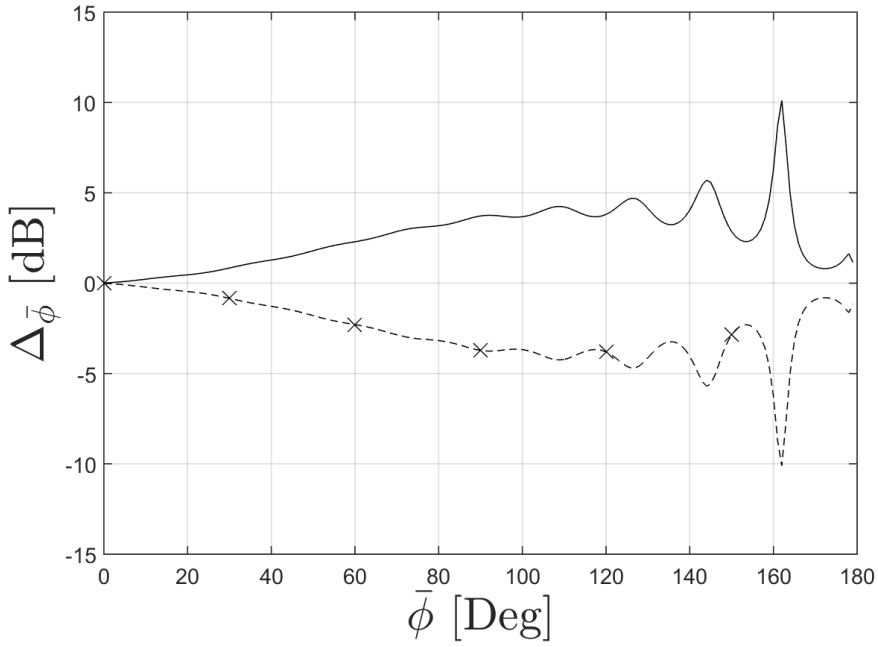

Figure 7.9: The difference, $\Delta_{\bar{\phi}}$ at $\bar{z} = 4$. The top line is for mode order $(l, q) = (4, 1)$ and the bottom line (with $\times$) is for $(l, q) = (-4, 1)$. The other variables are: $k_0 a = 5$, $a = 0.5$, $b = 3$ and $M_\infty = 0.75$.

Now the analysis is repeated but the source azimuthal order is changed from l to $-l$

$$p_t(-l, \bar{\phi}) \sim \sum_n (-1)^{-l+n} \int \frac{\mathrm{H}^{(2)}_{-l-n}(k_r b)}{\mathrm{H}^{(2)}_n(k_r)} \mathrm{e}^{-jk_z\bar{z}}\, \mathrm{d}k_z\, \mathrm{e}^{-jn\bar{\phi}}, \tag{7.6.6}$$

using $\mathcal{B}_{-\ell} = (-1)^\ell \mathcal{B}_\ell$, the Hankel function on the numerator can be written

$$p_t(-l, \bar{\phi}) \sim \sum_n (-1)^{2n} \int \frac{\mathrm{H}^{(2)}_{l+n}(k_r b)}{\mathrm{H}^{(2)}_n(k_r)} \mathrm{e}^{-jk_z\bar{z}}\, \mathrm{d}k_z\, \mathrm{e}^{-jn\bar{\phi}}. \tag{7.6.7}$$

Lastly, replace n for $-n$

$$p_t(-l, \bar{\phi}) \sim \sum_n (-1)^{n} \int \frac{\mathrm{H}^{(2)}_{l-n}(k_r b)}{\mathrm{H}^{(2)}_n(k_r)} \mathrm{e}^{-jk_z\bar{z}}\, \mathrm{d}k_z\, \mathrm{e}^{jn\bar{\phi}}. \tag{7.6.8}$$

The expression for negative order is similar to positive l, to make them identical multiply by $(-1)^l$

$$p_t(l, -\bar{\phi}) = (-1)^l\, p_t(-l, \bar{\phi}), \tag{7.6.9}$$

for even orders the pressure is identical[1]. Evidence of this phase change is shown in

[1]Note that this is very similar to the result as the in-duct relationship in Equation (3.1.9) on page 28.

Figure (7.10) for a low frequency and flow velocity values which gives long wavelengths and clearly visible wavefronts. When comparing SPL the pressure is squared so all orders are identical

$$20\log_{10}\left|p_t(l,-\bar{\phi})\right| = 20\log_{10}\left|p_t(-l,\bar{\phi})\right|. \tag{7.6.10}$$

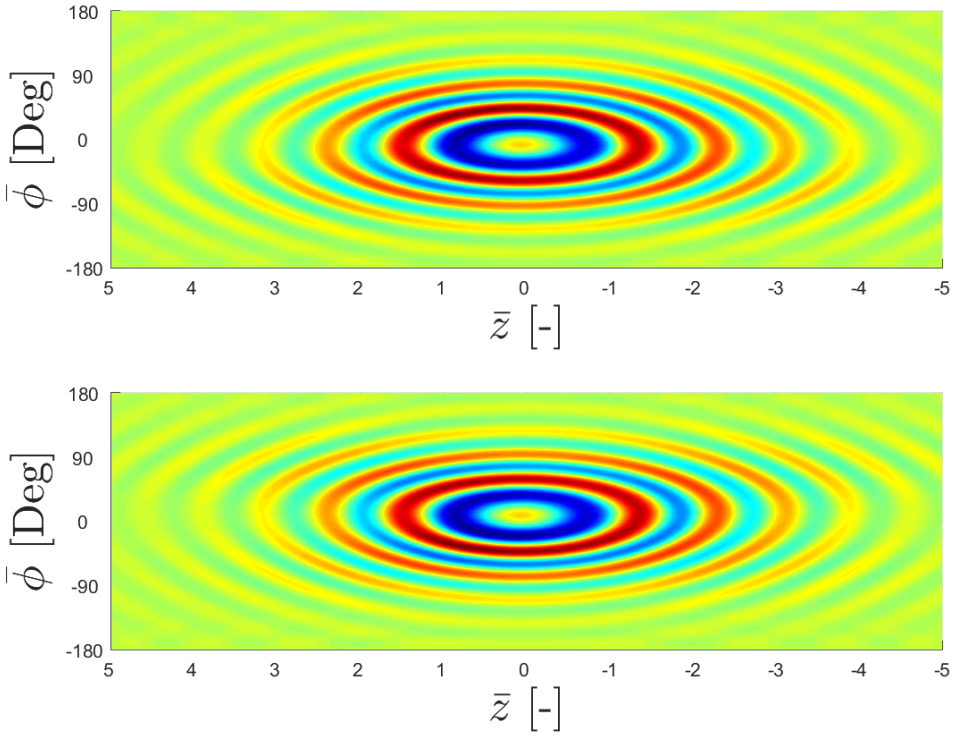

(a) Even l; upper $l = 4$ and lower $l = -4$.

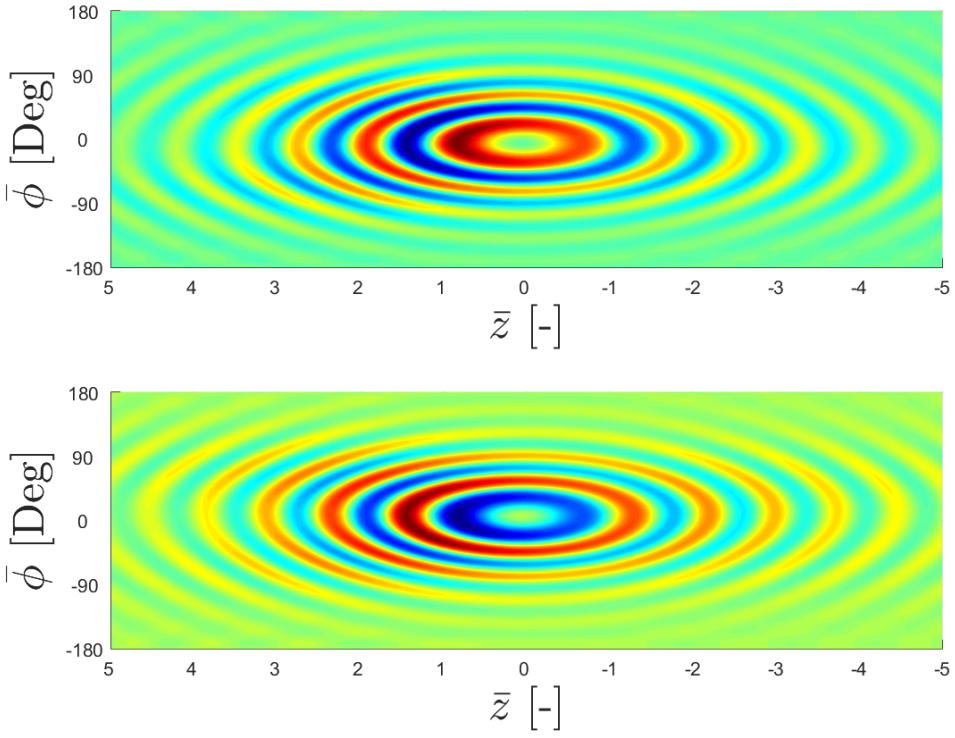

(b) Odd l; upper $l = 3$ and lower $l = -3$.

Figure 7.10: Normalised pressure on the unfurled cylinder for even and odd source modes in opposite spin directions. The relevant parameters are: $k_0 a = 5$, $a = 0.5$, $b = 3$ and $M_\infty = 0$.

7.6.2 Propeller Analogy

As suggested in the previous section, if the spinning mode were indeed spinning, then an increase in frequency would lead to a faster rate of 'spin' and thus more convective amplification. One way to increase the circumferential phase velocity is to increase the frequency, k_0. The other way is to decrease the source azimuthal mode, l. By changing these and inspecting the differences between the upper and lower side of the cylinder it is shown the source behaves in the opposite manner to that of a moving source.

The pressure on either side of the cylinder is shown in Figure (7.11.a) for the three frequencies and mode $(l, q) = (4, 1)$ at the axial location $\bar{z} = 4$. This figure shows that the difference is greatest for the low frequency. The difference between the lines is plotted in Figure (7.11.b). This figure shows clearly that the asymmetry effect is least effective for highest frequencies than lower ones. This behaviour is directly contrary to the way in which a moving source would behave.

In Figure (7.12) the mode is changed for the frequency $k_0 a = 20$. The axial location is changed to 0.1, because for $l = 24$ the mode is barely cut-on. The mode $(l, q) = (4, 1)$ spins five times faster than $(24, 1)$. Yet, as before, the difference $\Delta_{\bar{\phi}}$ behaves in the opposite manner to a moving source; with increasing mode order the difference between the two sides increases.

The results shown in this section demonstrate that the spinning modes cannot be thought of as analogous to a rotating source. Perhaps they should be renamed, arotational spinning modes. For inlet turbofan applications, the asymmetry result can be treated as spurious. The inlet of a turbofan is not perfectly circular and as such the modes of a slightly elliptical cylinder cannot be interpreted as spinning modes.

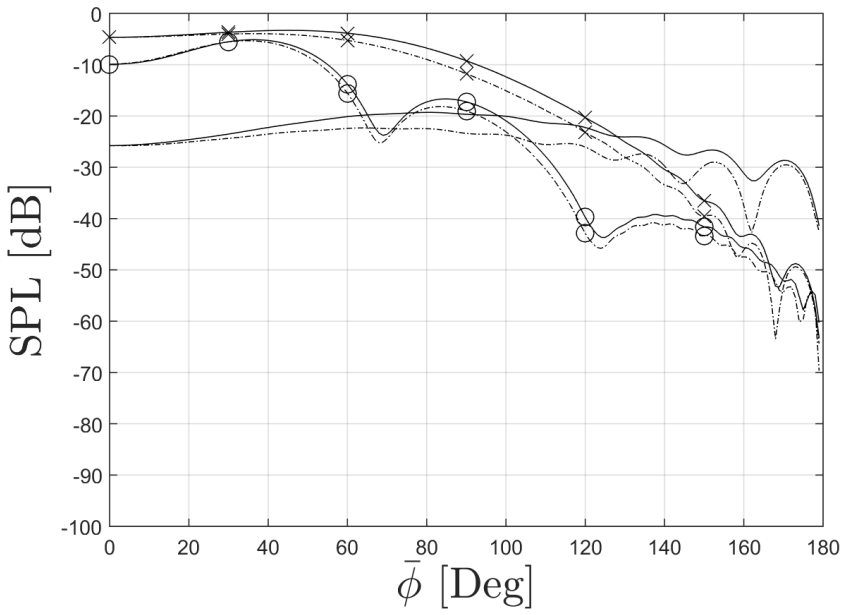

(a) Solid line $0 \to 180^{\text{o}}$ and dashed line $0 \to -180^{\text{o}}$.

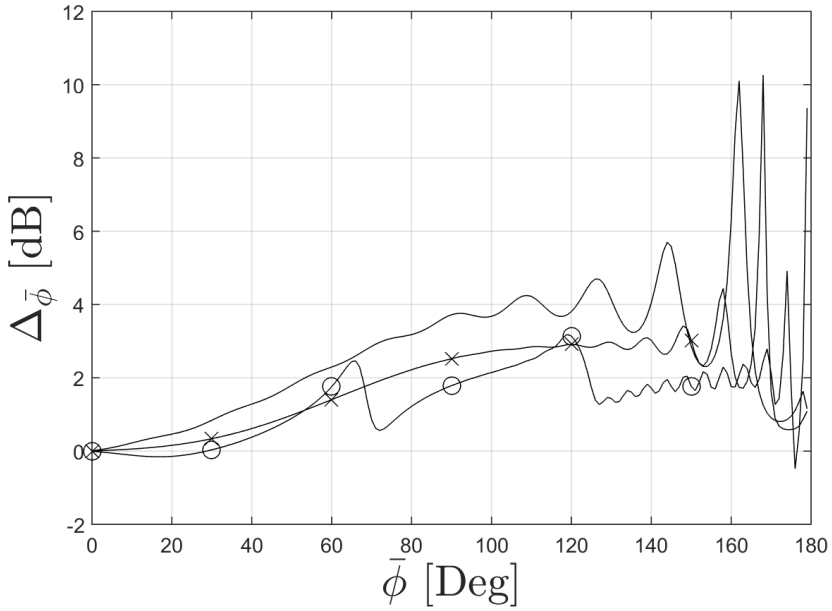

(b) $\Delta_{\bar{\phi}}$.

Figure 7.11: The SPL on the cylinder (a) and $\Delta_{\bar{\phi}}$ (b) at $\bar{z} = 4$ for $k_0 a = 5$ (no symbol), 10 ($\times$) and 20 ($\circ$). The other parameters are: $a = 0.5$, $b = 3$, $(l, q) = (4, 1)$ and $M_\infty = 0.75$.

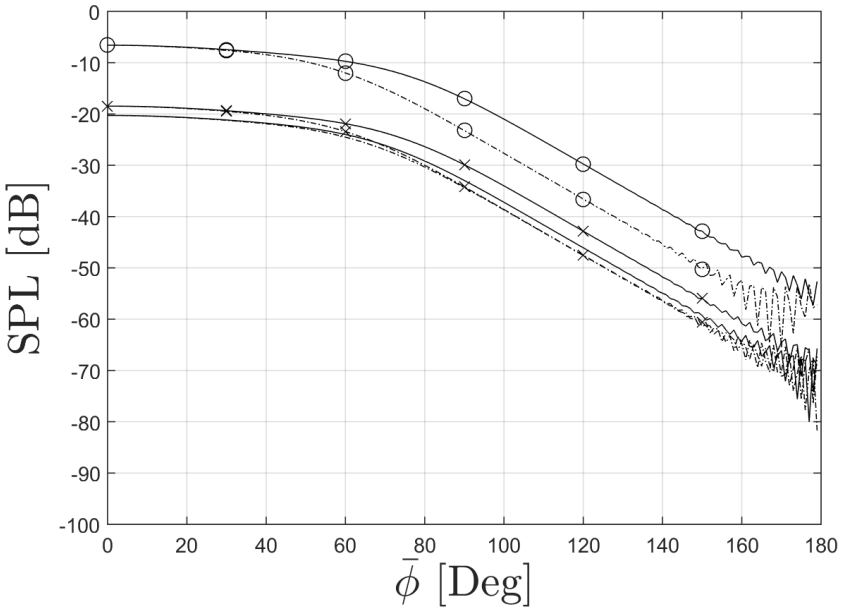

(a) SPL on either side of the duct for the three modes.

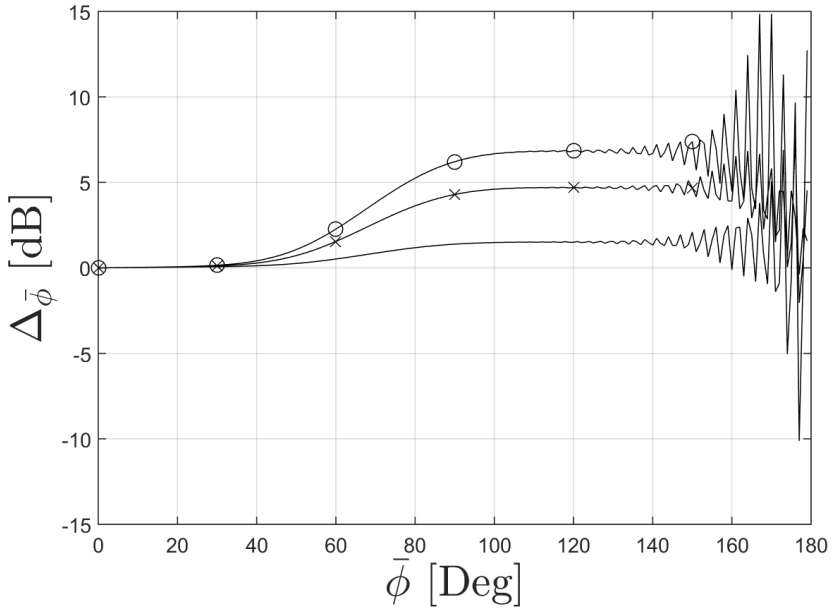

(b) $\Delta_{\bar{\phi}}$ for the three modes.

Figure 7.12: The SPL (a) and $\Delta_{\bar{\phi}}$ (b) at $\bar{z} = 0.1$ for modes $(l, q) = (4, 1)$ (no symbol), (16,1) ($\times$) and (24,1) ($\circ$). The other parameters are: $k_0 a = 20$, $a = 0.5$, $b = 3$ and $M_\infty = 0.75$.

7.7 Further Boundary Layer Discussion

In the previous chapter (Section 6.3.3) the effect of boundary-layer thickness and profile on shielding was quantified. It was noted that as the boundary layer thickness increased there was a nonlinear increase at small δ values, at higher values the increase was linear. This is further investigated, but initially the effect of the profile is examined for the

purposes of method optimisation.

7.7.1 Displacement Thickness Normalisation

The parametric study in the previous chapter showed that two different boundary-layer profiles of the same thickness lead to very different amounts of shielding, Figure (6.20) Section 6.3.3 on page 128. This result is not surprising because the power-law profile has a very different distribution of shear compared to a linear profile. However, of the profiles tested, it was noted that the overall shape of the shielding was similar. The previous chapter also demonstrated a linear relationship between Δ_{bl} and increasing boundary layer thickness. This, and the profile observation, suggests that the different profiles can be made equivalent by altering the thicknesses. This section shows that three profiles of identical displacement thickness lead to similar shielding in two of the cases. The displacement thickness of a profile is given by

$$\delta^* = \int_0^{\delta} \left(1 - \frac{M_z(\bar{r})}{M_\infty}\right) \mathrm{d}\bar{r}. \tag{7.7.1}$$

The displacement thicknesses are referenced to the power-law profile by changing the thickness of the laminar and quarter-sine profiles.

Using a linear or quarter-sine profile is of benefit because the power-law profile has a switch to implement the viscous sub layer. This switch means that the predictions take longer to compute than the other profiles. Furthermore, the linear and quarter-sine profiles have a smaller δ for the same displacement thickness. It takes less time to integrate a thin boundary than a thick one. Therefore, for two reasons it is significantly quicker to implement a scaled quarter-sine or linear boundary for turbulent boundary layer predictions.

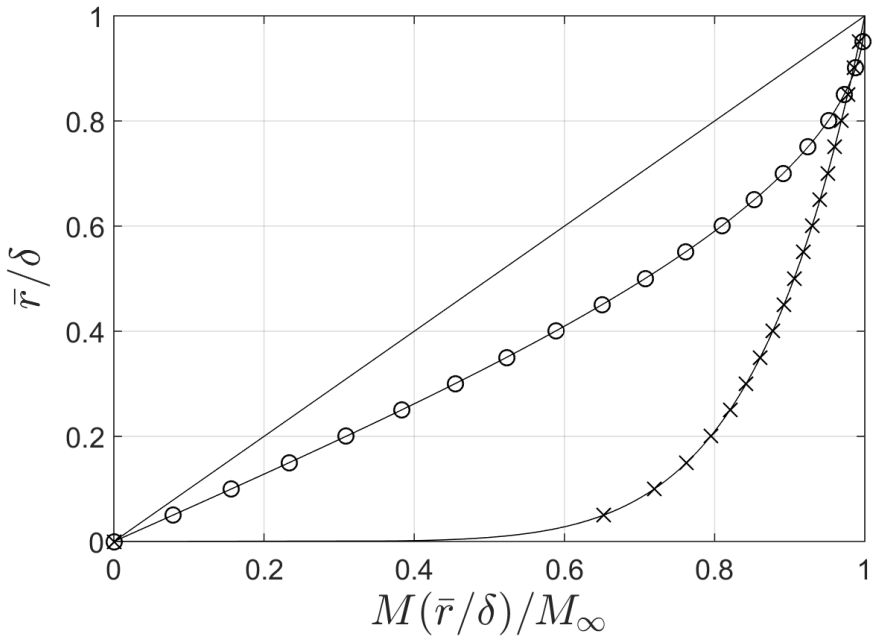

Figure 7.13: The linear (solid line), quarter-sine (solid line, ∘) and seventh-power-law (solid line, ×) profiles. The Polhousen profile was used in the validation.

The profiles are shown in Figure (7.13) and the displacement thickness of the tested profiles are shown in Table (7.1).

Profile	δ^*
Linear	$\delta_L/2$
Quarter Sine	$(1-2/\pi)\,\delta_{QS}$
Seventh-Power Law	$\delta_{PL}/8$

Table 7.1: Displacement thicknesses for linear, quarter-sine and power-law profiles.

The quarter-sine and linear profile thicknesses (δ) are changed as such. The displacement thicknesses are all equal $\delta^*_{PL} = \delta^*_{QS} = \delta^*_L$. The quarter-sine and linear profile thickness are thus adjusted to

$$\delta_{QS} = \frac{1}{1-2/\pi}\frac{\delta_{PL}}{8} \qquad \text{and} \qquad \delta_L = 2\frac{\delta_{PL}}{8}, \tag{7.7.2}$$

where δ_{PL} will be varied from 0 to 0.1.

Nayfeh *et al.* (1974) showed that for ducted flow, for all but one of the profiles the attenuation predictions 'collapsed' to the same values when displacement thicknesses were used. The only profile that did not conform was the power-law profile. This was confirmed for flow over a plate with an impedance boundary condition (Gabard, 2013) for incident plane waves.

The singular profile is the power-law profile and cannot be scaled to match the other boundary layers. The scaling cannot be done because the nonlinear increase, at very small values of δ, is less than the gradient of the linear regime. No simple scaling will fix this. The key to the success is the shape of the shielding curve is similar for the quarter-sine and linear profiles and different to the power-law profile.

Figure (7.14) shows that the result of Nayfeh *et al.* (1974) is applicable to the *exterior* problem; where the boundary layer running down a cylinder shields sound waves from the surface.

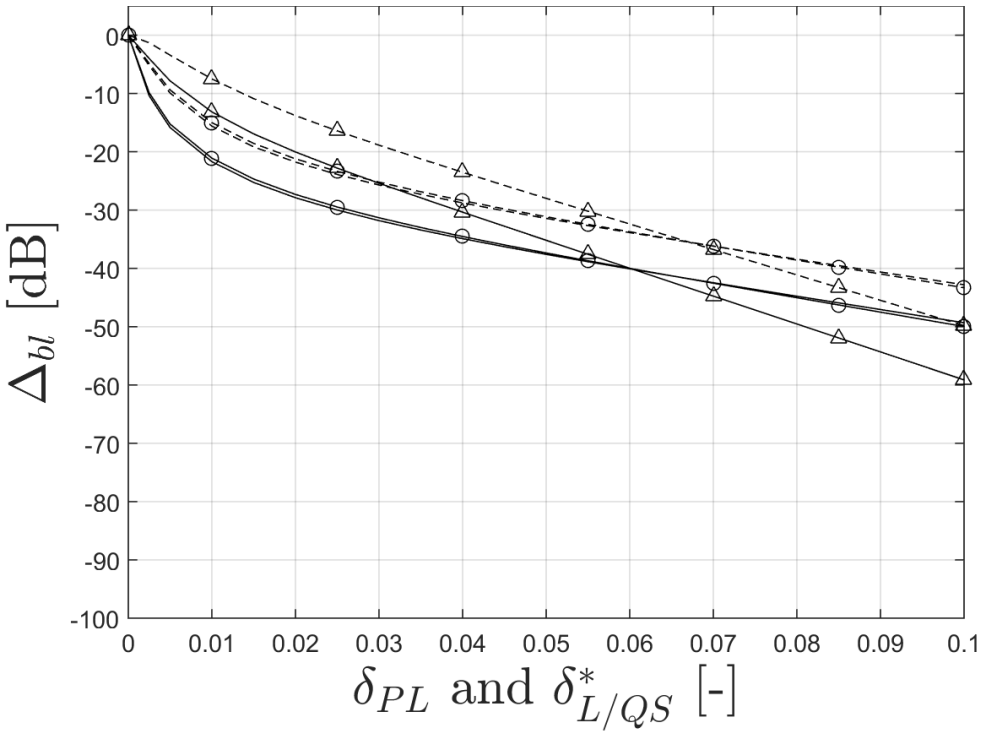

Figure 7.14: Δ_{bl} of the power-law ($\triangle$), scaled linear (no symbols) and quarter-sine ($\circ$) profiles, all with identical displacement thicknesses. The other parameters are: $k_0 a = 20$, $a = 0.5$, $b = 3$ and $M_\infty = 0.75$.

7.7.2 Step Profile

The previous section demonstrated that different profiles of different thicknesses can lead to similar shielding. If profile is unimportant, the logical step is to try and normalise the simplest of boundary layers, the step profile, to the physically realistic profiles. The reason this is a good idea is that the step change boundary layer can be implemented using the wave equation and the convected wave equation only. Thus no numerical integration of the Pridmore-Brown equation is required. This can lead to a very significant reduction in computation time since only the analytic solutions of the wave equation are required. In doing this, the method would take only slightly longer than the uniform flow method – a few minutes on a desktop.

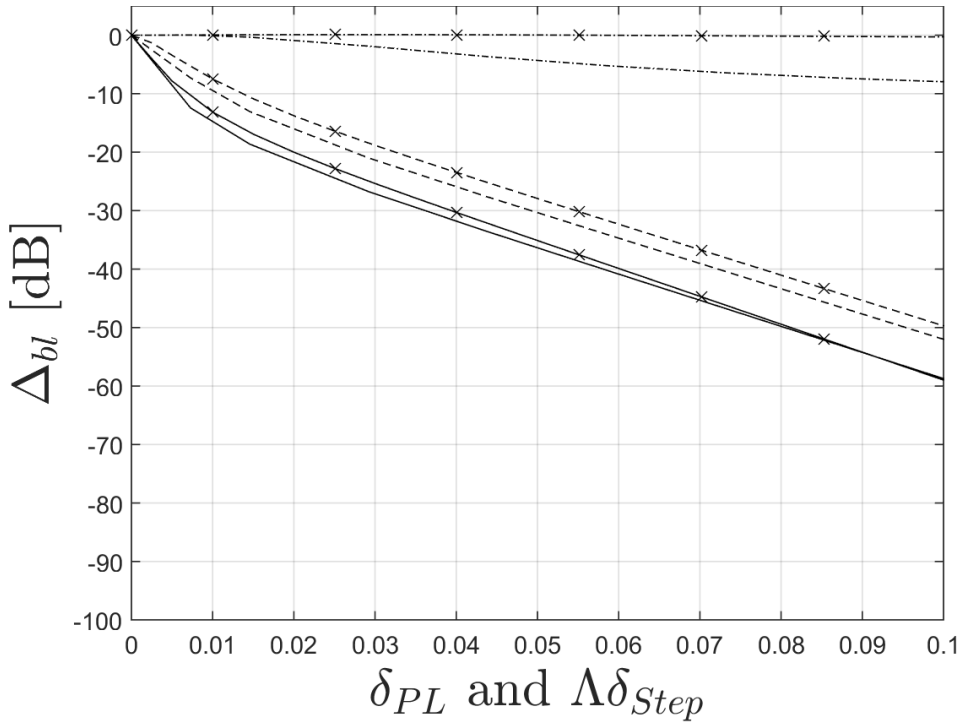

Figure 7.15: Power-law (×) and the step-change (no symbol) profiles shielding at point $I.a$ (solid lines), $I.c$ (dashed lines) and $I.e$ (dot-dashed lines). The value of $\Lambda = 1/3$. The other parameters are: $k_0 a = 20$, $a = 0.5$, $b = 3$ and $M_\infty = 0.75$.

Not shown, but when the displacement thicknesses were identical the shielding was not similar. However the overall shape of the curve Δ_{bl} was similar when plotted against δ. To equivalent the two an empirical method was used to obtain a scaling factor.

The shielding due to the different profiles, one of which is scaled, is equivalent when

$$\delta_{PL} = \Lambda\delta_{step}, \tag{7.7.3}$$

where Λ is to be found empirically from the results.

Using this method leads to similar shielding when $\Lambda \approx 1/3$. With this value, the shielding is shown in Figure (7.15).

Considering the simplicity of the method, the scaled step-change profile gives extremely good predictions upstream of the source. Downstream of the source the power-law profile leads to a very slight increase in amplitude. Downstream of the source the step-change leads to significant shielding. Therefore it is accurate only in the forward arc. This is fine because the power-law profile has no significant effect on the downstream predictions.

7.7.3 Δ_{bl} against δ/λ_0

The nonlinear to linear increase in shielding with increasing δ was shown in Section 6.3.3. This relationship was demonstrated for non-dimensional units, however the relevant length scale is the acoustic wavelength. For the forcing frequency $\lambda_0 = 0.157$.

Figure (7.16) shows the shielding at point $II.a$ for increasing δ for the four boundary layer examined in this thesis. The thickness of the boundary layer is shown as a percent of the acoustic wave (λ_0). For all the profiles it shows that the nonlinear regime is for $\delta < 10\%$ of λ_0. Above this values all the profiles have a linear relationship.

If the linear relationship were to be applied to predictions, care would need to be taken to ensure that $\delta > \lambda_0/10$.

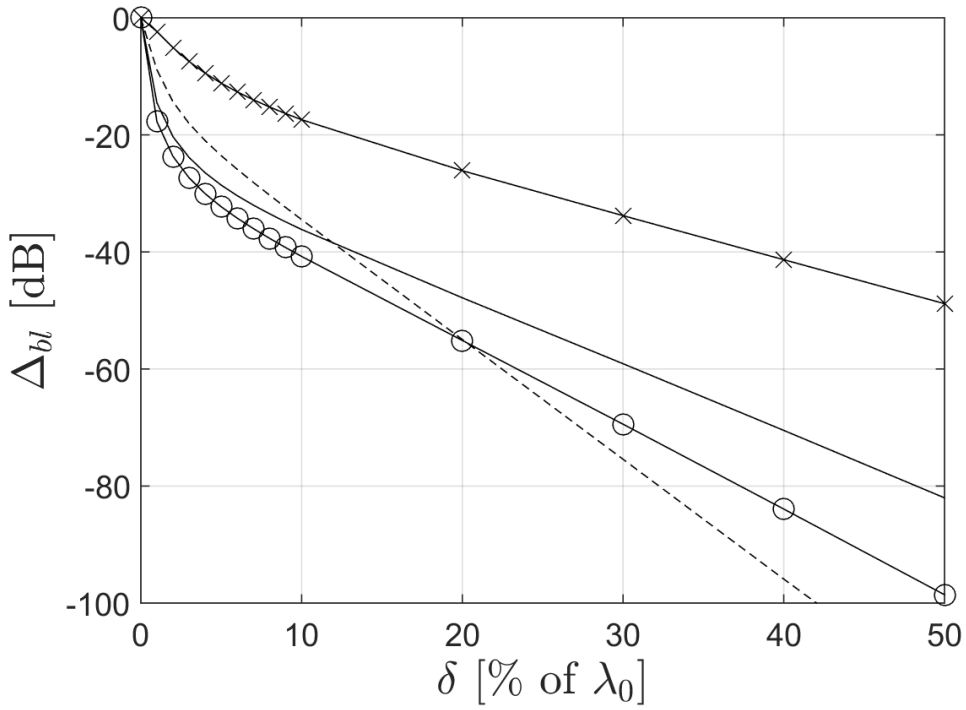

Figure 7.16: Δ_{bl} for the quarter-sine (solid line), linear (solid line, $\circ$), power-law (solid line, $\times$) and step-change (dashed line) profiles against percent of wavelength at location $II.a$. The parameters are: $k_0 a = 20$, $a = 0.5$, $(l, q) = (4, 1)$, $b = 3$ and $M_\infty = 0.75$.

7.8 Multimode Source

The results presented so far are for a single mode. This, of course, is unrealistic of any noise field in a duct, never-mind a turbofan engine. Thankfully, the boundary layer effects function BL (Equation (7.2.1)) is dependent on; source frequency, boundary-layer thickness and boundary-layer profile. However it does not depend on the azimuthal mode order. Therefore, the multimode simulations can be computed relatively quickly.

Obtaining the correct amplitudes for each mode is notoriously difficult since information about the source is required. The analysis presented here is intentionally over simplified.

An example result is shown in Figure (7.17). The results are for $k_0 a = 20$ which has cut-on modes $(l, q) = (\{-24, -23, \ldots, -2, -1, \quad 0, 1, 2, \ldots, 23, 24\}, 1)$. The three cases are; equal amplitude, equal amplitude with mode protrusion of 20 dB and 45 dB. The mode is with the protrusion is $(l, q) = (-16, 1)$. This corresponds to a realistic rotor-locked mode for a future state-of-the-art engine with and without an optimised inlet liner (which reduces the tone amplitude).

Although the function BL can be recycled for each mode, the incident field is computed for each azimuthal order l. The pressure for each mode is summed incoherently.

For a single mode, the SPL on the cylinder is very clearly the source directivity extended over the surface. However, as Figure (7.17.a) demonstrates, for multimode predictions the lobes and nulls definition is lost. The pressure is fairly equally distributed over the near-side of the cylinder. The far-side of the cylinder has also lost the clear destructive interference pattern of a single mode.

The 20 dB protrusion shown in Figure (7.17.b) leads to slightly higher SPL levels near the cylinder, however the difference is not massive. The 45 dB amplitude protrusion is significantly large enough to dominate the prediction. On the near-side the cylinder the directivity of the source at this mode is clearly seen. For compariseon, this single mode prediction can be seen in Figure (6.3.b), on page 107.

This short section was included to demonstrate that multimode results can be calculated quickly; this example with 49 modes only took 1 hour more (on a single core) than the single mode result.

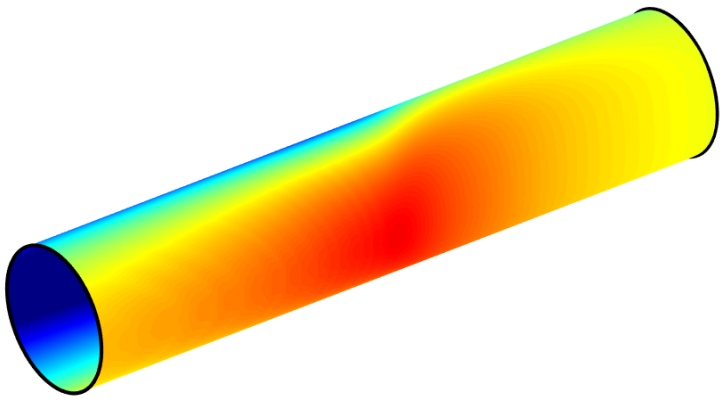

(a) Equal amplitude modes.

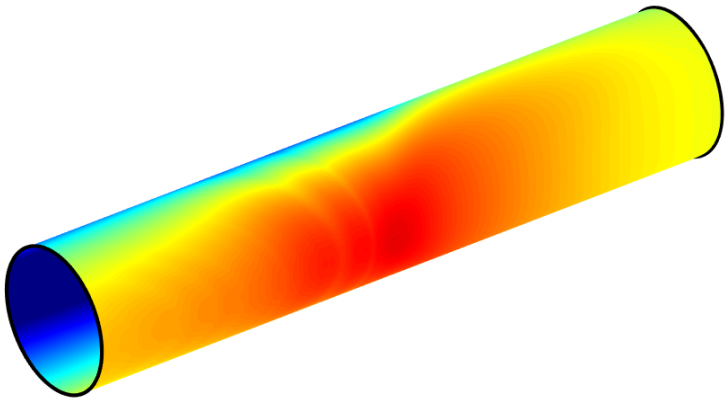

(b) Equal amplitude modes with a 20 dB protrusion.

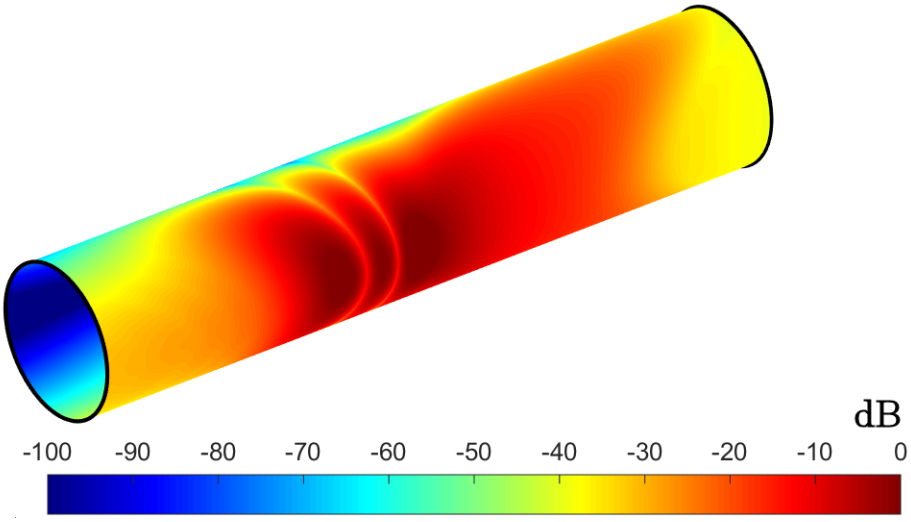

(c) Equal amplitude modes with a 45 dB protrusion.

Figure 7.17: Multimode SPL on the cylinder for modes; $(l, q) = (-24 : 24, 1)$; with a quarter-sine profile of thickness $\delta = 0.01$. The other parameters are: $k_0 a = 20$, $a = 0.5$, $b = 3$ and $M_\infty = 0.75$.

7.9 Chapter Summary

The aim of this chapter was to obtain more insight into the problem. To achieve this, a discussion of the model highlighted its scope. It was reasoned that the predictions are good at a point, but due to the constant boundary-layer thickness, predictions at large axial distances cannot be trusted without recalculating the boundary-layer thickness.

The rest of the chapter showed:

- Investigations into the characteristics of the boundary layer in Fourier space led to a method of manipulating the amplitudes of the inverse Fourier transform integrand to simulate refraction for the uniform flow model. The benefit is this modification can significantly increase the computational run-time of the method.
- The critical layer was demonstrated to be of limited importance to the installation problem at relevant parameters considered here.
- A simple model based on ray theory showed that no channelling occurs in the boundary layer downstream of the source.
- The symmetric incident field gave rise to asymmetric results on the cylinder surface. The mathematics predicts this and a phase change for odd azimuthal orders radiated from the inlet duct.
- Boundary layer characteristics reported in the literature for interior duct problems was shown to be consistent for exterior refraction along a cylinder.
- Upstream of the source, for well chosen thicknesses, the step-change profile was shown to give similar shielding as the power law. By using this approach the method can be greatly optimised for a modest decrease in accuracy.

Chapter 8

Conclusions and Future Work

8.1 Conclusions

The aim of the thesis was to present the development of a theoretical model to predict the fuselage installation effects of engine fan tones. The aim was achieved by combining the most sophisticated free-field analytical model for modes radiating from a duct and theoretical models for fuselage installation effects.

A simplified inlet duct model using the Wiener–Hopf method was derived in Chapter 4. The following chapter demonstrated how to install the source. The scattering effect of the cylinder and the refraction effect of the boundary layer was included in the model and solutions were found by using Fourier methods.

The model predicts very large amounts of boundary-layer shielding upstream of the source. The noise radiating with the flow was not significantly affected to the extent that uniform flow predictions are sufficient. A shielding coefficient was introduced to give an overall measure of the shielding.

In the discussion in Chapter 7 the wavenumber spectrum was inspected. By isolating the installation effects in the mathematics, the effect was examined in terms of a transfer function. It was shown that refraction can be simulated by altering the wavenumber content in the Fourier domain. Furthermore, it was demonstrated that the axisymmetric source (in SPL) leads to slight asymmetry in SPL once installed. Yet, the SPL trends were the opposite of how a rotating source would typically behave. An appropriately scaled step-change boundary layer profile gave very similar shielding values as the physically relevant power-law profile. This observation could lead to an optimised method requiring only the analytic wave and convected wave equation solutions. Fast computational times is one of the principal benefits of this range of theoretical methods.

This model contains a realistic source; it is unlikely that the source model can be improved significantly using theoretical methods. The limiting factor is the boundary layer. The boundary layer is modelled with a constant thickness. This is appropriate

when comparing local axial values; however comparing two axial locations far apart would need to be calculated twice for different thicknesses.

Any numerical model must be carefully appraised when compared to measurements. Therefore, one of the intended uses of the method is to obtain a rough idea of shielding at the early design phase. Owing to the speed of the model, a parametric study can be done quickly (especially if parallelised, which scales inversely with the number of cores available) before a detailed CAA method would include the nuances of the geometry, turbulent flow and a growing boundary layer. This is the scope of the model.

The objectives listed in the introduction have been referred to in the text when completed; so will not be listed again. In summary, the main contribution to knowledge presented in this thesis is

- to have developed a source, representative of a radiating turbofan tone, adjacent to a rigid cylinder with a boundary layer running down its length. The model can be used to predict and reduce SPL on the surface of an aeroplane fuselage with a turbofan engine. Reducing SPL on the fuselage could lead to reductions in cabin noise and possibly reduce the amount of acoustic lagging required, hence reducing weight.

Furthermore, the following has been accomplished:

- The near-field behaviour of the diffracted field was quantified.
- The refraction effect of the boundary layer on acoustic pressure on the surface of the cylinder was quantified:
  - upstream of the source, the boundary layer refracts sound away from the cylinder and downstream causes refraction towards the cylinder,
  - even for a low frequency, roughly a quarter of blade-passing frequency, and a thin boundary layer leads to up to 20 dB of shielding at large axial values,
  - shielding increases linearly with increasing boundary layer thickness greater than approximately 10% of the acoustic wavelength,
  - the boundary-layer profile has a significant effect on shielding predictions,
  - reduction of the sound due to the principal lobe can be reduced by increasing frequency and reducing the azimuthal mode.
- The SPL directivity of the axisymmetric source leads to asymmetric SPL on the cylinder.
- Refraction can be simulated by altering the uniform flow wavenumber spectra.

- A step-change profile gives similar refraction predictions to that of the power-law profile.
- Interior duct attenuation refraction characteristics due to a boundary layer applies to the exterior problem presented here.

The simpler case of the disc source model has been published in uniform flow (McAlpine *et al.*, 2015), with a boundary layer (Gaffney *et al.*, 2016) and a journal paper on this model is currently under review. Furthermore, a journal paper is currently being written that is focusing on the installed Weiner–Hopf source presented and interrogated in this thesis. A further paper may be written to investigate the multimode source and far-field effects.

8.2 Future Work

The following are improvements that could be made to the model.

8.2.1 Far-Field Predictions

Generally the far-field solution is a simpler form than the near field. The approximate far-field solution is formed by converting to spherical polar coordinates and replacing the distance function, the Hankel function of the second kind, by its large argument asymptotic approximation. By doing this, the integral over axial wavenumber can be evaluated using the method of stationary phase. Then the predictions are very quick. This method can be used for community noise.

The full derivation can be found in Appendix C. Briefly, if

$$\Upsilon = \left(1 - M_\infty^2 \sin^2 \bar{\theta}\right)^{1/2}, \tag{8.2.1}$$

then we define

$$\Xi_{\sin} = \frac{\sigma \sin \bar{\theta}}{\Upsilon}, \tag{8.2.2}$$

and

$$\Xi_{\cos} = \frac{\cos \bar{\theta}}{\Upsilon}, \tag{8.2.3}$$

where

$$\sigma = \left(1 - M_\infty^2\right)^{1/2}. \tag{8.2.4}$$

The far-field approximation gives the total field as

$$p_t(\bar{R},\bar{\theta},\bar{\phi}) = \frac{1}{4\pi\bar{R}}\frac{2}{\sigma\pi\Upsilon\Xi_{\sin}^{1/2}}\mathrm{e}^{-j\bar{R}\frac{k_0}{\sigma^2}\left(M_\infty\cos\bar{\theta}+\Upsilon\right)}\sum_{n=-\infty}^{\infty}\widetilde{\eta}_n(\Xi_{\cos})\left(1+\Lambda_n(\Xi_{\cos})\right)\,\mathrm{e}^{-j(\frac{\pi}{2}+n\bar{\phi})}, \tag{8.2.5}$$

where Λ_n is

$$\Lambda_n = \frac{\widetilde{f}_n\Big|_{1+\delta}\widetilde{p}'_{i_n}\big|_{1+\delta} - \widetilde{f}'_n\Big|_{1+\delta}\widetilde{p}_{i_n}|_{1+\delta}}{\widetilde{f}_n\Big|_{1+\delta}\widetilde{p}'_{s_n}\big|_{1+\delta} - \widetilde{f}'_n\Big|_{1+\delta}\widetilde{p}_{s_n}|_{1+\delta}} = \frac{k_r\,\widetilde{f}_n\Big|_{1+\delta}\mathrm{J}'_n(k_r\left[1+\delta\right]) - \widetilde{f}'_n\Big|_{1+\delta}\mathrm{J}_n(k_r\left[1+\delta\right])}{k_r\,\widetilde{f}_n\Big|_{1+\delta}\mathrm{H}_n^{(2)\prime}(k_r\left[1+\delta\right]) - \widetilde{f}'_n\Big|_{1+\delta}\mathrm{H}_n^{(2)}(k_r\left[1+\delta\right])}, \tag{8.2.6}$$

and is found by eliminating α_n from Equations (5.1.21) on page 71.

8.2.2 Slowly Growing Boundary Layer

As discussed, the assumption of a constant thickness boundary layer is a weakness in the model. In Rienstra (1998), the sound propagation along a duct of varying radius was modelled analytically and subsequently in Rienstra (2003), a duct of changing arbitrary shape was modelled using the method of multiple scales.

A similar method could be used to model boundary layer growth. The Pridmore-Brown equation would need to be re-derived using the method of multiple scales: δ is replaced with $\delta(\epsilon\bar{z})$ (such that the thickness is a function of axial location) where ϵ is required to be small, but not as small as the acoustic perturbation. This would be ideal for modelling a growing boundary layer because the thickness increases at a relatively small rate. The increase in the solution complexity would be significant, but the solutions can be obtained without resorting to numerical methods.

8.2.3 Haystacking

Dierke *et al.* (2013) showed, using CAA methods, that haystacking affected the SPL on the surface of a fuselage due to an engine tone. Powles *et al.* (2011) produced an analytical model to predict spectral broadening. This model could be adapted to the boundary layer running down the outside of a cylindrical fuselage.

8.2.4 Wings

This is not a fuselage issue, and thus beyond the scope of this project, but the installation effects of the wings could be included in the model. Bowman and Uslenghi (1969) details the analytic solution for the scattered field due to a semi-infinite half plane. Kingan and Self (2012) analytically modelled half-plane scattering due to propeller type sources.

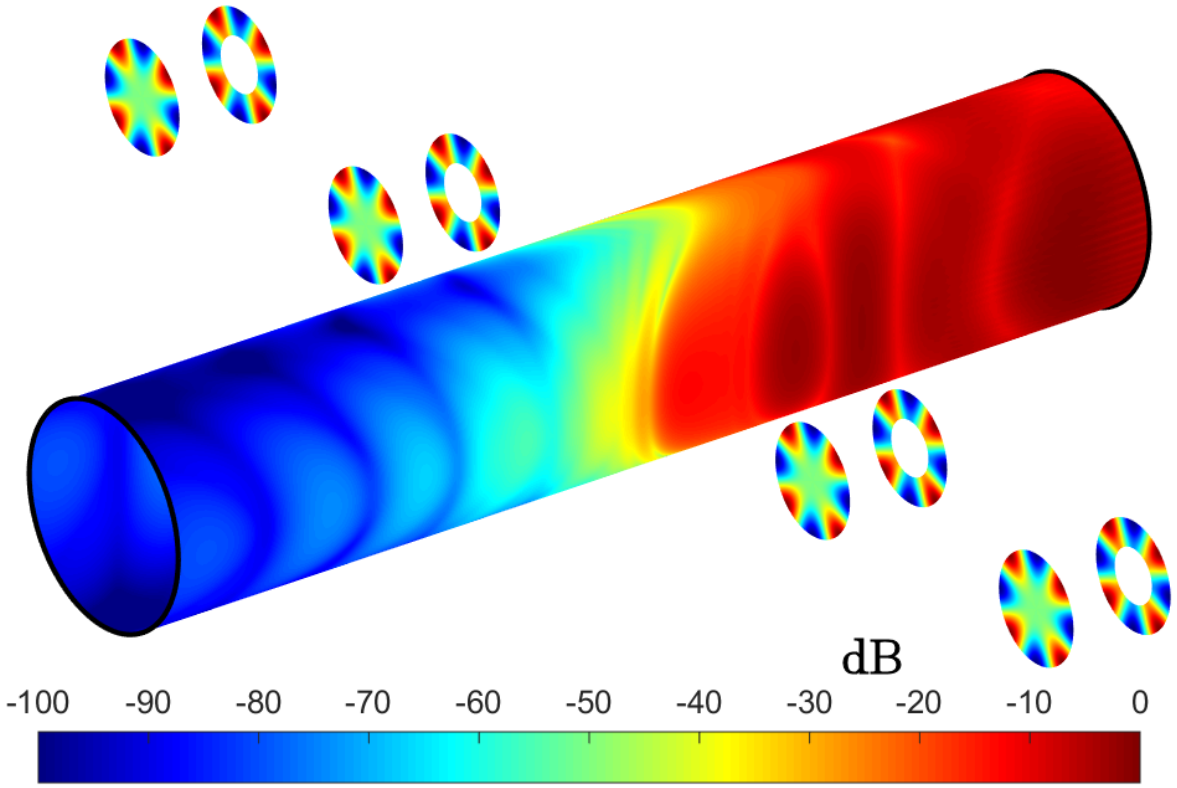

Figure 8.1: Four engines with outlet field and a quarter-sine boundary layer profile of $\delta = 0.1$. Parameters are: $k_0 a = 20$, $a = 0.5$, $a_{inner} = 0.5a$, $(l, q) = (4, 1)$, $b = 3$ and 6, $\beta = 0^o$ and 180^o and $M_\infty = 0.75$.

8.2.5 Outlet

In this thesis the results and discussion are limited to inlet noise, however, the model is easily adapted to include annular ducts (Section 4.1.1, page 55). GXMunt calculates the radiation from an annular duct with different flow in the annulus. And as laboured over previously, the boundary-layer model accepts any incident field of the appropriate form. Therefore the installation method can calculate both inlet and outlet radiation.

Academically this result is not significantly different to the hollow duct; the major difference being the first radiation lobe does not have the largest amplitude. However such a tool could be useful to industry.

For geometry based on a long haul aircraft, the SPL from the inlet and outlet of four engines are shown in Figure (8.1). All the solutions are added incoherently. The flow speed is 0.75 M all over and the inner radius of the outlet duct is $0.5a$. This prediction demonstrates that, under highly simplified circumstances, the noise radiating downstream of the engine leads to relatively large levels of noise.

Chapter 9

Appendices

9.1 Appendix A – Relevant Equations in Gabard and Astley (2006) Notation

The incident field is

$$p_i = \frac{\omega}{2j\pi} \sum_{v=-\infty}^{\infty} (-1)^{n+v} \int_\Gamma \frac{(1-uM_0)}{\lambda_0 \omega \, \mathrm{H}_v^{(2)\prime}(\lambda_0 \omega)} \mathrm{H}_{n-v}^{(2)}(\lambda_0 \omega b) \mathrm{J}_v(\lambda_0 \omega \bar{r}) \, \mathrm{e}^{j\omega u \bar{z}} \, \mathrm{d}u \, \mathrm{e}^{-jn\bar{\phi}}, \quad (9.1.1)$$

where v has been introduced and the total field on the surface of the cylinder is

$$p_t = \frac{\omega}{2j\pi} \sum_{v=-\infty}^{\infty} \int_\Gamma \widetilde{\alpha}_v(u) \, \mathrm{e}^{j\omega u \bar{z}} \, \mathrm{d}u \, \mathrm{e}^{-jv\bar{\phi}}, \quad (9.1.2)$$

where $\widetilde{\alpha}_v$ is essentially unchanged from $\widetilde{\alpha}_n$.

Pridmore-Brown for flow in the positive direction is

$$\frac{\mathrm{D}_0}{\mathrm{D}t} \left(\frac{\mathrm{D}_0^2 p}{\mathrm{D}t^2} - \nabla^2 p \right) + 2M' \frac{\partial^2 p}{\partial \bar{r} \partial \bar{z}} = 0 \, . \quad (9.1.3)$$

and using the Gabard notation the Pridmore-Brown equation transforms to

$$\left[\frac{\mathrm{d}^2}{\mathrm{d}\bar{r}^2} + \left(\frac{1}{\bar{r}} + \frac{2uM'}{1-uM} \right) \frac{\mathrm{d}}{\mathrm{d}\bar{r}} + \left((\omega \lambda(\bar{r}))^2 - \frac{v^2}{\bar{r}^2} \right) \right] \widetilde{p}_n = 0 \, . \quad (9.1.4)$$

The normalised dispersion relationship given as

$$\lambda^2(\bar{r}) = (1 - uM_z(\bar{r}))^2 - u^2. \quad (9.1.5)$$

9.2 Appendix B – Unfurled Cylinder Plots

The cylinder plots could perhaps be accused of being a little meretricious. So all cylinder plots in the thesis are shown here unfurled. This is in order so one can see the far-side of the cylinder. All the plots show normalised SPL between –100 and 0 dB.

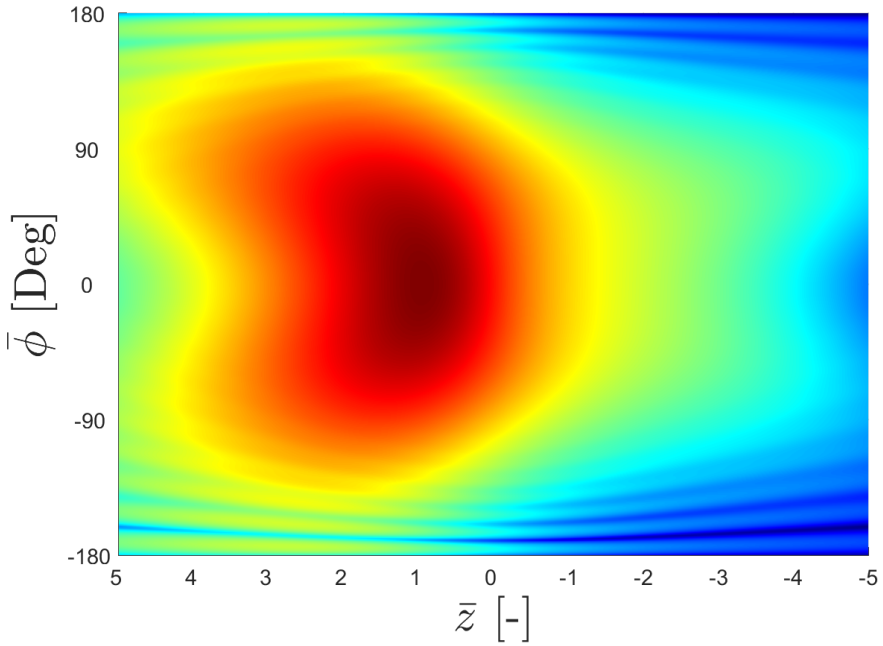

Figure 9.1: Figure (6.2.a), page 106

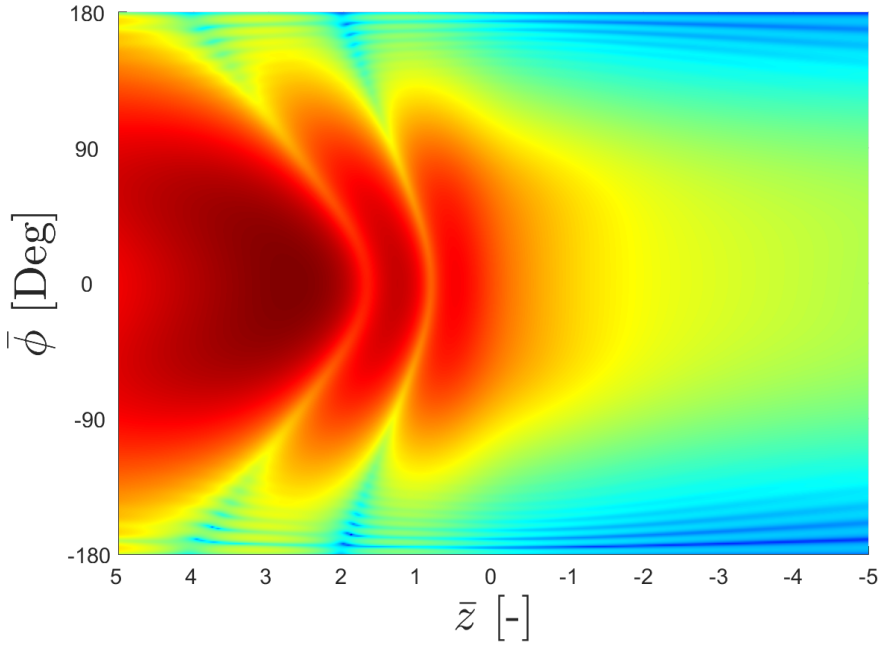

Figure 9.2: Figure (6.2.b), page 106

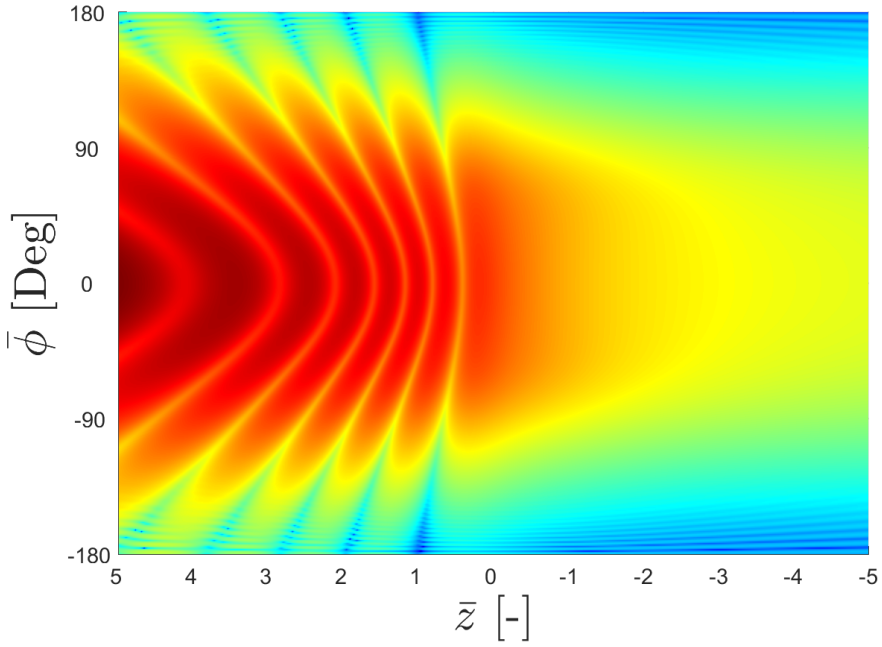

Figure 9.3: Figure (6.2.c) and (6.3.a), page 107

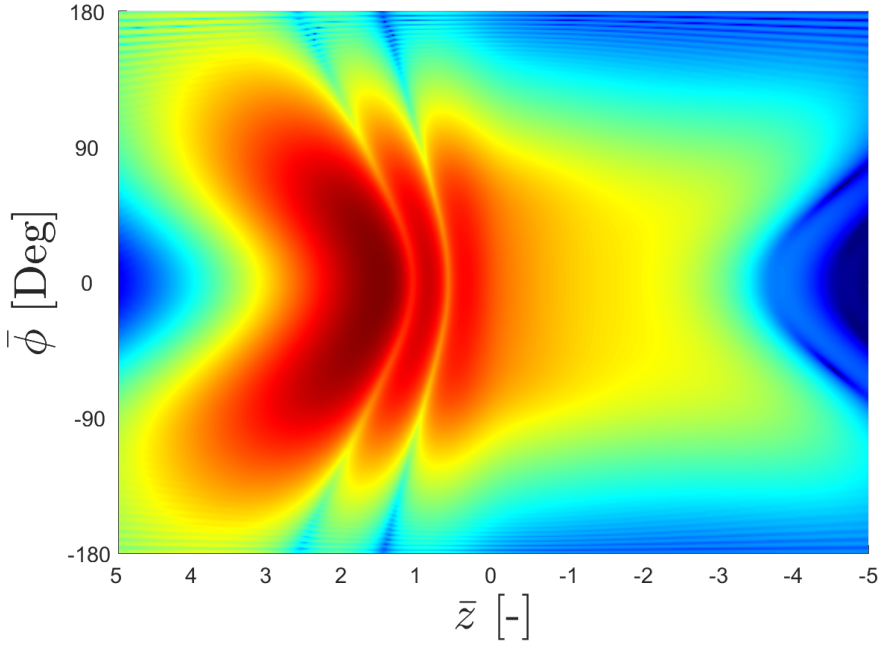

Figure 9.4: Figure (6.3.b), page 107

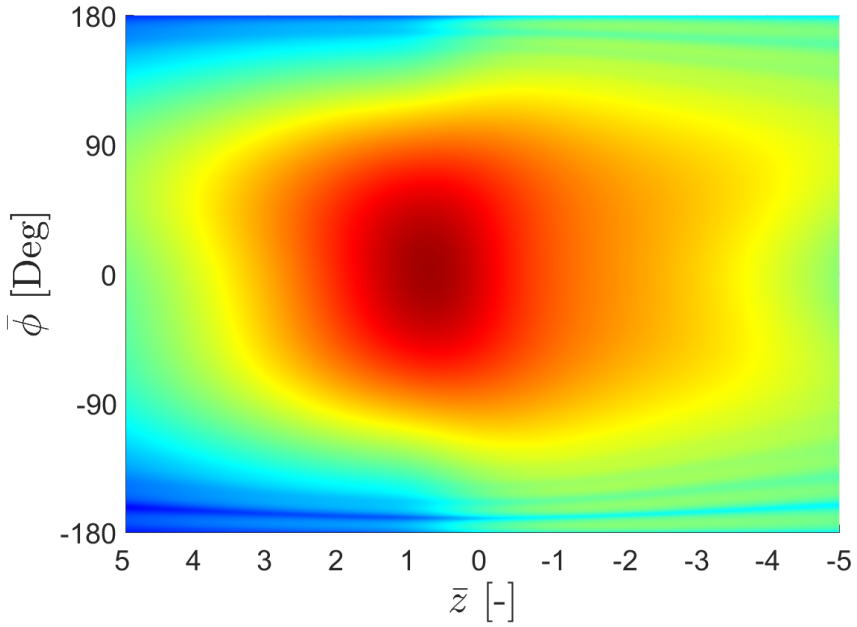

Figure 9.5: Figure (6.5.b), page 111

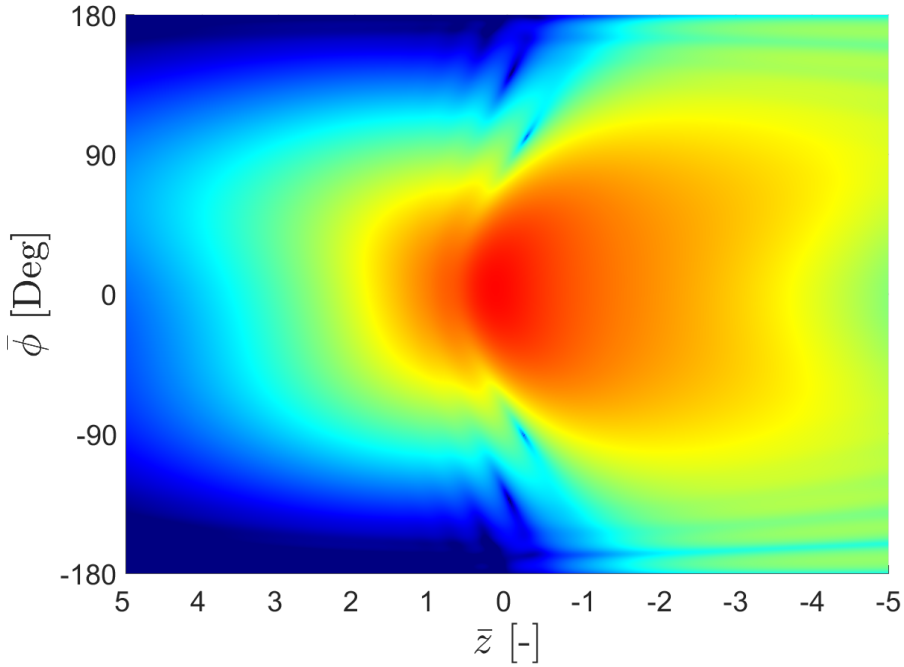

Figure 9.6: Figure (6.5.c), page 111

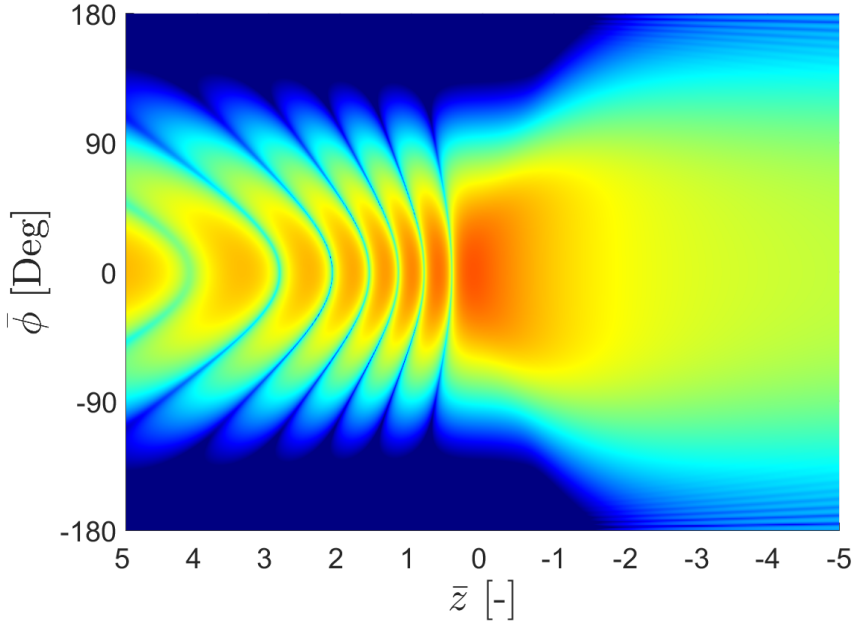

Figure 9.7: Figure (6.6.b), page 112

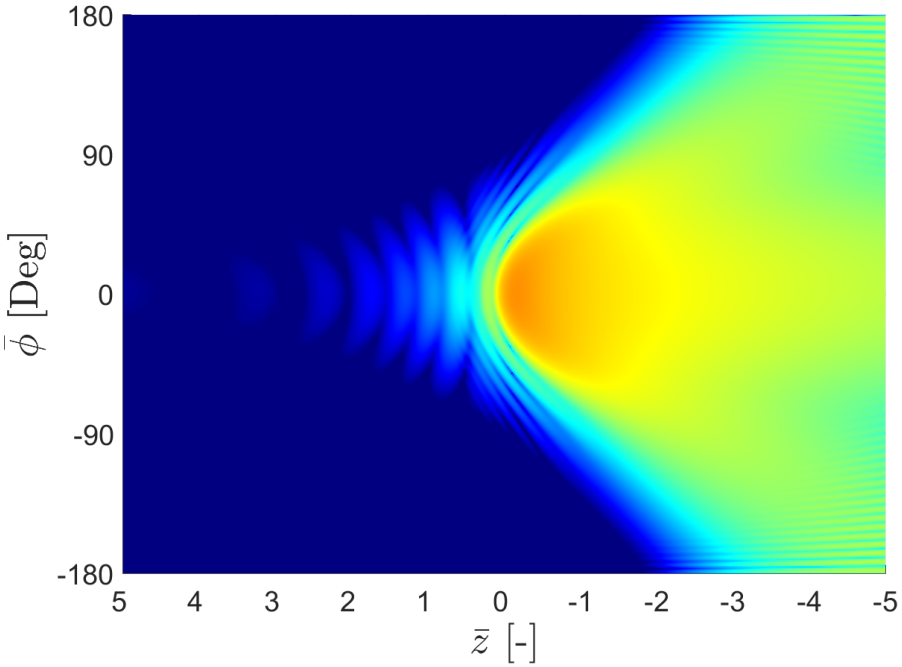

Figure 9.8: Figure (6.6.c), page 112

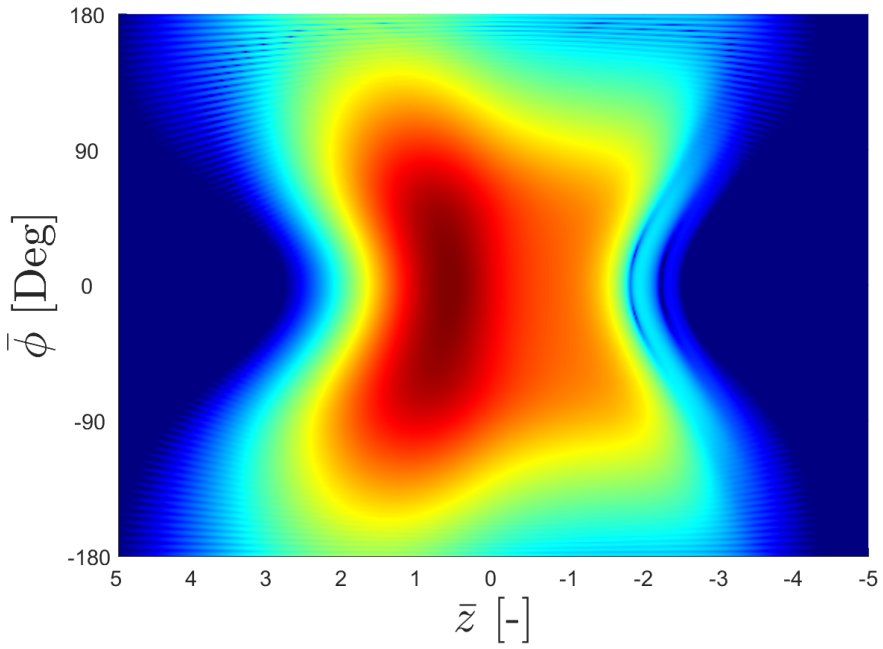

Figure 9.9: Figure (6.2.c), page 106

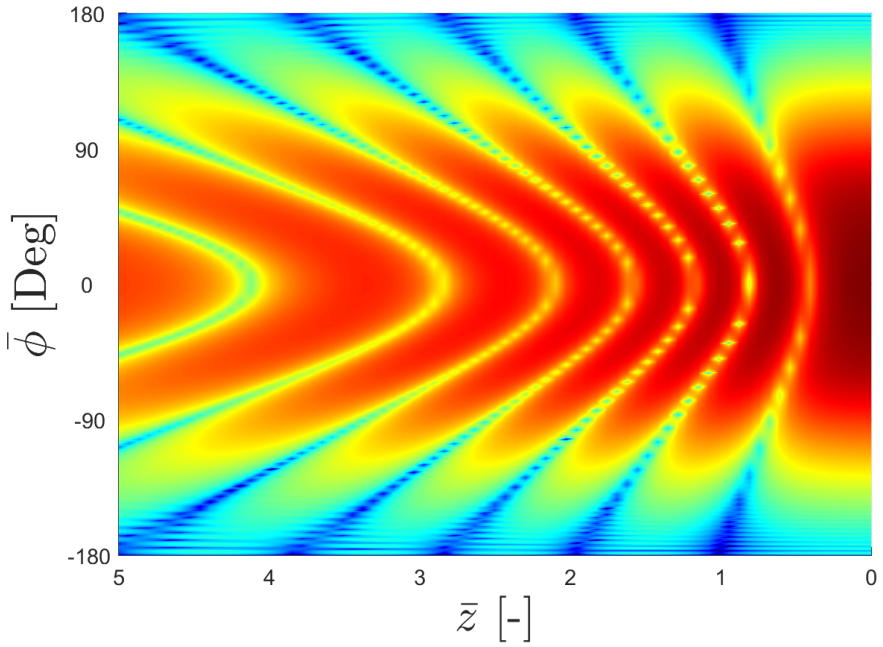

Figure 9.10: Figure (7.5.a), page 140

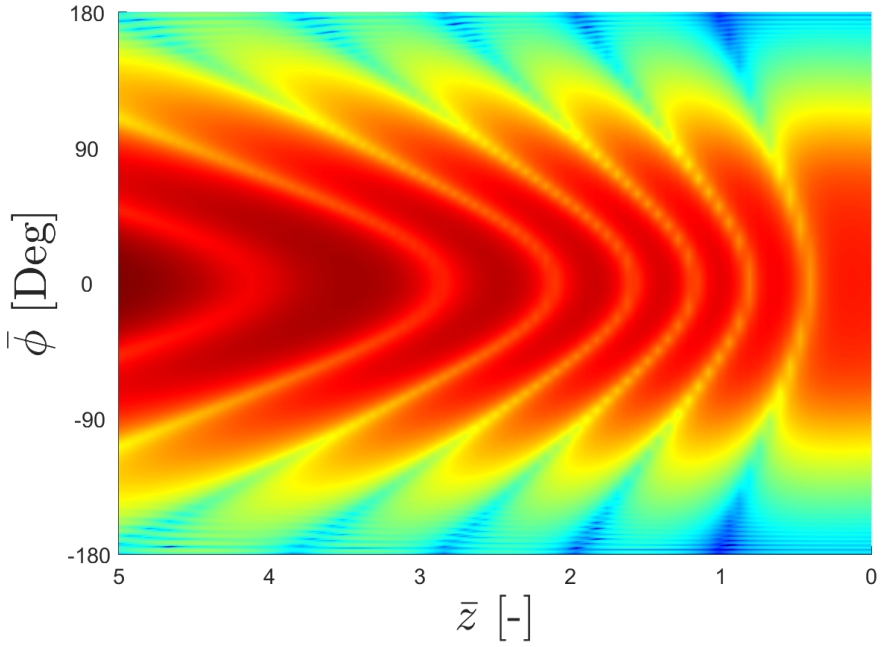

Figure 9.11: Figure (7.5.b), page 140

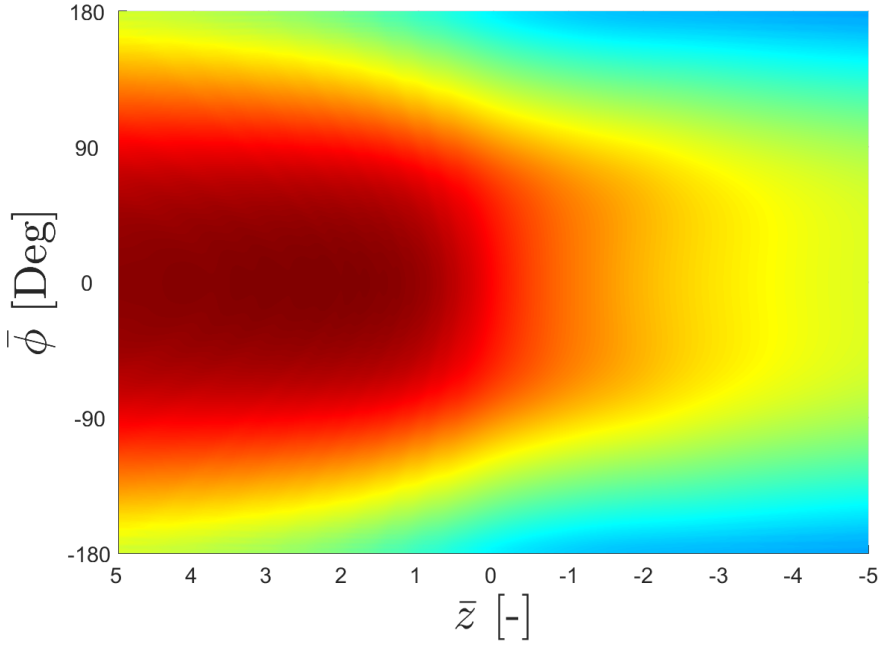

Figure 9.12: Figure (7.17.a), page 159

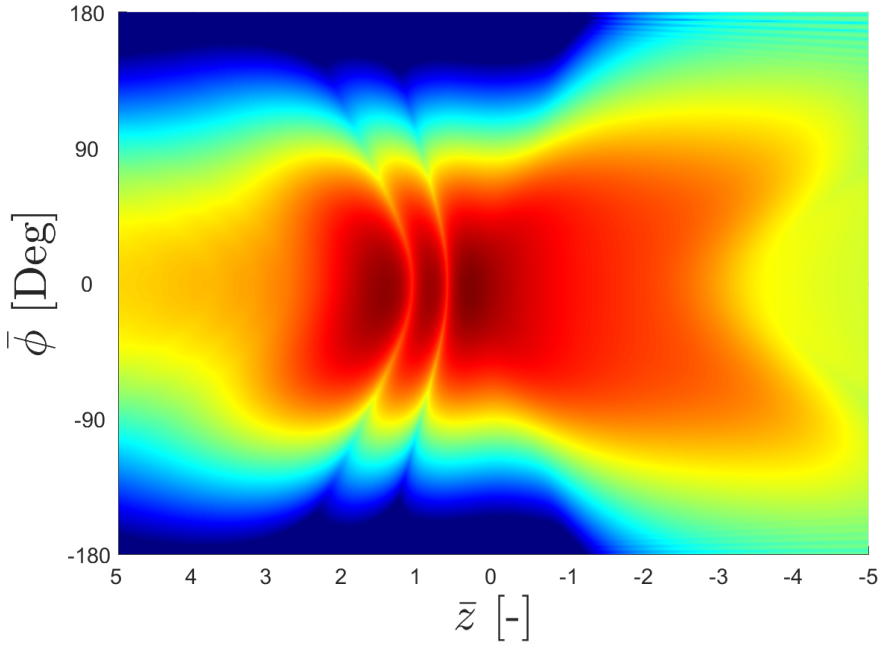

Figure 9.13: Figure (7.17.b), page 159

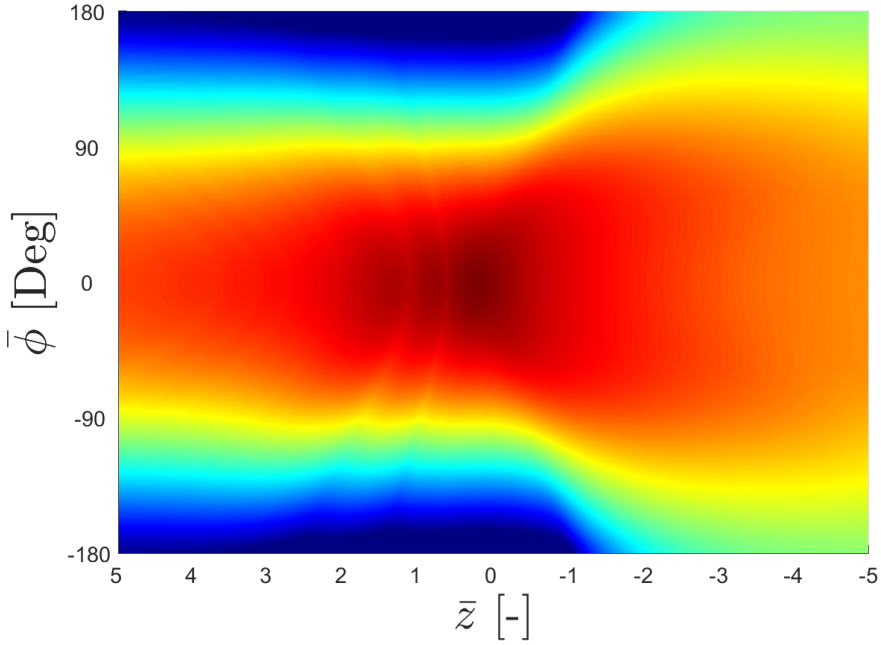

Figure 9.14: Figure (7.17.c), page 159

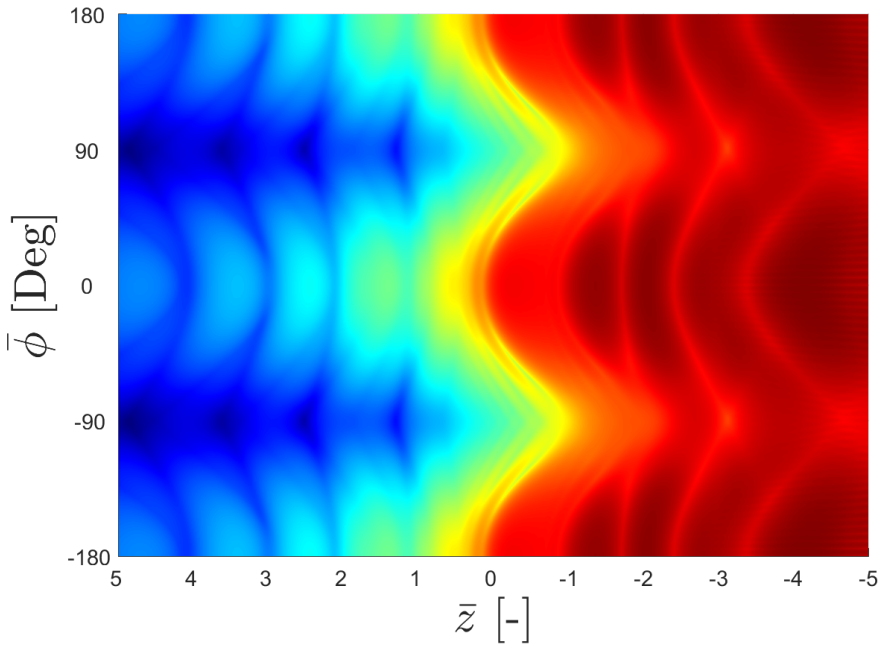

Figure 9.15: Figure (8.1), page 165

9.3 Appendix C – Far-Field Theory

Far-field effects are useful for community predictions. This section derives the far-field solutions using large argument asymptotic approximations.

The far-field version of Graf's Addition theory is

$$\mathrm{H}_l^{(2)}(k_r r)\,\mathrm{e}^{-jl\phi} = \sum_{n=-\infty}^{\infty} (-1)^{(l+n)} \mathrm{H}_{l-n}^{(2)}(k_r \bar{r}) \mathrm{J}_n(k_r b) \mathrm{e}^{-jn\bar{\phi}} \mathrm{e}^{-j(l-n)\beta}. \tag{9.3.1}$$

Therefore the incident field expressed in the cylinder coordinate system is

$$p_i(\bar{r}, \bar{\phi}, \bar{z}) = \frac{1}{(2\pi)^2} \sum_{n=-\infty}^{\infty} \int_{-\infty}^{\infty} \widetilde{p}_{i,n}\, \mathrm{e}^{-jk_z \bar{z}}\, \mathrm{d}k_z\, \mathrm{e}^{-jn\bar{\phi}}, \tag{9.3.2}$$

where the transformed pressure now takes the form

$$\widetilde{p}_{i,n} = \widetilde{\eta}_n\, \mathrm{H}_n^{(2)}(k_r \bar{r}). \tag{9.3.3}$$

The scattered field takes the form

$$\widetilde{p}_s = \widetilde{\gamma}_n(k_z) \mathrm{H}_n^{(2)}(k_r \bar{r}), \tag{9.3.4}$$

where the scattered field is proportional to the incident field and the effect of cylinder

and the effect of the boundary layer, represented by Λ_n

$$\widetilde{\gamma}_n = \widetilde{\eta}_n(k_z)\Lambda_n(k_z), \tag{9.3.5}$$

where Λ_n is found by eliminating $\widetilde{\alpha}_n$ from Equations (5.1.21), on page 71,

$$\Lambda_n = \frac{\widetilde{f}_n\Big|_{1+\delta}\,\widetilde{p}'_{i_n}\big|_{1+\delta} - \widetilde{f}'_n\Big|_{1+\delta}\,\widetilde{p}_{i_n}|_{1+\delta}}{\widetilde{f}_n\Big|_{1+\delta}\,\widetilde{p}'_{s_n}\big|_{1+\delta} - \widetilde{f}'_n\Big|_{1+\delta}\,\widetilde{p}_{s_n}|_{1+\delta}} = \frac{k_r\,\widetilde{f}_n\Big|_{1+\delta}\,\mathrm{J}'_n(k_r\,[1+\delta]) - \widetilde{f}'_n\Big|_{1+\delta}\,\mathrm{J}_n(k_r\,[1+\delta])}{k_r\,\widetilde{f}_n\Big|_{1+\delta}\,\mathrm{H}_n^{(2)\prime}(k_r\,[1+\delta]) - \widetilde{f}'_n\Big|_{1+\delta}\,\mathrm{H}_n^{(2)}(k_r\,[1+\delta])}. \tag{9.3.6}$$

Both incident and scattered are of the same form so factorise the Hankel function to form the transformed total field

$$\widetilde{p}_t = \widetilde{\eta}_n(k_z)\,(1+\Lambda_n(k_z))\,\mathrm{H}_n^{(2)}(k_r\bar{r}), \tag{9.3.7}$$

therefore the total field is given by

$$p_t(\bar{r},\bar{\phi},\bar{z}) = \frac{1}{(2\pi)^2}\sum_{n=-\infty}^{\infty}\int_{-\infty}^{\infty}\widetilde{\eta}_n(k_z)\,(1+\Lambda_n(k_z))\,\mathrm{H}_n^{(2)}(k_r\bar{r})\,\mathrm{e}^{-jk_z\bar{z}}\,\mathrm{d}k_z\,\mathrm{e}^{-jn\bar{\phi}}. \tag{9.3.8}$$

Before the large argument asymptotic are applied, the coordinate system is change to spherical polar coordinates. First, the radius is

$$\bar{R} = \left(\bar{z}^2+\bar{r}^2\right)^{1/2}, \tag{9.3.9}$$

where

$$\bar{r} = \bar{R}\sin\bar{\theta} \qquad \text{and} \qquad \bar{z} = \bar{R}\cos\bar{\theta}. \tag{9.3.10}$$

However, due to the flow, these need to be transformed by the method of Chapman (2000) in order to do a Lorenz type transform. This temporary variables are denoted by a hat and are related to the cylinder variables by

$$\hat{R} = \frac{\bar{R}}{\sigma}\left(1-M_\infty^2\sin^2\bar{\theta}\right)^{1/2}, \tag{9.3.11}$$

and

$$\cos\hat{\theta} = \frac{\cos\bar{\theta}}{\left(1-M_\infty^2\sin^2\bar{\theta}\right)^{1/2}} \qquad \text{and} \qquad \sin\hat{\theta} = \frac{\sigma\sin\bar{\theta}}{\left(1-M_\infty^2\sin^2\bar{\theta}\right)^{1/2}}, \tag{9.3.12}$$

where $\sigma^2 = 1-M_\infty^2$. These results lead to

$$\bar{R}\sin\bar{\theta} = \hat{R}\cos\hat{\theta} \qquad \text{and} \qquad \bar{R}\cos\bar{\theta} = \hat{R}\sigma\cos\hat{\theta}. \tag{9.3.13}$$

From Rienstra (1984), the integration is most easily performed with a change in variable

$$\tau = \sigma^2 \frac{k_z}{k_0} - M_\infty, \tag{9.3.14}$$

where

$$k_z = \frac{k_0}{\sigma^2}\left(\tau + M_\infty\right) \qquad \text{and} \qquad k_r = \frac{k_0}{\sigma}\left(1-\tau^2\right)^{1/2}, \tag{9.3.15}$$

which leads to

$$\mathrm{d}k_z = \frac{k_0}{\sigma^2}\mathrm{d}\tau. \tag{9.3.16}$$

Therefore in polar coordinates the total field is given by

$$p_t = \frac{1}{(2\pi)^2}\sum_{n=-\infty}^{\infty}\int_{-\infty}^{\infty}\frac{k_0}{\sigma^2}\widetilde{\eta}_n(\tau)\left(1+\Lambda_n\widetilde{\eta}_n(\tau)\right)\mathrm{H}_n^{(2)}\left(\frac{k_0}{\sigma}\left(1-\tau^2\right)^{1/2}\hat{R}\sin\hat{\theta}\right)\,\mathrm{e}^{-j\frac{k_0}{\sigma}(\tau+M_\infty)\hat{R}\cos\hat{\theta}}\,\mathrm{d}\tau\mathrm{e}^{-jn\bar{\phi}}. \tag{9.3.17}$$

As $\hat{R}$ is very large replace the Hankel function with

$$\mathrm{H}_\ell^{(2)}(\square) = \left(\frac{2}{\pi\square}\right)^{1/2}\,e^{-j\left(\square-\frac{1}{2}\ell\pi-\frac{1}{4}\pi\right)}, \tag{9.3.18}$$

Therefore the pressure in the far-field is

$$p_t = \frac{1}{(2\pi)^2}\sum_{n=-\infty}^{\infty}\frac{k_0}{\sigma^2}\mathrm{e}^{-j\left(\frac{1}{2}n\pi-\frac{1}{4}\pi\right)}\,\mathrm{e}^{-jn\bar{\phi}}$$
$$\int_{-\infty}^{\infty}\widetilde{\eta}_n(\tau)\left(1+\Lambda_n(\tau)\right)\left(\frac{2}{\pi\frac{k_0}{\sigma}\left(1-\tau^2\right)^{1/2}\hat{R}\sin\hat{\theta}}\right)^{1/2}\mathrm{e}^{-j\frac{k_0}{\sigma}\left(1-\tau^2\right)^{1/2}\hat{R}\sin\hat{\theta}}\,\mathrm{e}^{-j\frac{k_0}{\sigma}(\tau+M_\infty)\hat{R}\cos\hat{\theta}}\,\mathrm{d}\tau, \tag{9.3.19}$$

and rearranging gives

$$p_t = \frac{1}{(2\pi)^2}\sum_{n=-\infty}^{\infty}\frac{k_0}{\sigma^2}\mathrm{e}^{-j\left(\frac{1}{2}n\pi-\frac{1}{4}\pi\right)}\left(\frac{2}{\pi\frac{k_0}{\sigma}\hat{R}\sin\hat{\theta}}\right)^{1/2}$$
$$\int_{-\infty}^{\infty}\frac{\widetilde{\eta}_n(\tau)\left(1+\Lambda_n(\tau)\right)}{\left(1-\tau^2\right)^{1/2}}\,\mathrm{e}^{-j\hat{R}\frac{k_0}{\sigma}\left(\left(1-\tau^2\right)^{1/2}\sin\hat{\theta}+(\tau+M_\infty)\cos\hat{\theta}\right)}\,\mathrm{d}\tau\,\mathrm{e}^{-jn\bar{\phi}}. \tag{9.3.20}$$

Extracting the integrand and noting that the evanescent part of the spectrum does not propagate to the far-field, the integration limits change to

$$I_n = \int_{k_z^-}^{k_z^+}\frac{\widetilde{\eta}_n(\tau)\left(1+\Lambda_n(\tau)\right)}{\left(1-\tau^2\right)^{1/2}}\,\mathrm{e}^{j\hat{R}\frac{k_0}{\sigma}\left(-\left(1-\tau^2\right)^{1/2}\sin\hat{\theta}-(\tau+M_\infty)\cos\hat{\theta}\right)}\,\mathrm{d}\tau, \tag{9.3.21}$$

which can be evaluated using the method of stationary phase

$$I_n(\tau) = \frac{\widetilde{\eta}_n(\tau)\left(1+\Lambda_n(\tau)\right)}{\left(1-\tau^2\right)^{1/2}}\left(\frac{2\pi\sigma(1-\tau^2)^{3/2}}{k_0\hat{R}\sin\hat{\theta}}\right)^{1/2} \mathrm{e}^{j\hat{R}\frac{k_0}{\sigma}\left(-\left(1-\tau^2\right)^{1/2}\sin\hat{\theta}-(\tau+M_\infty)\cos\hat{\theta}\right)+j\frac{\pi}{4}}, \tag{9.3.22}$$

about the point $\tau = \cos\hat{\theta}$

$$I_n = \frac{\widetilde{\eta}_n(\cos\hat{\theta})\left(1+\Lambda_n(\cos\hat{\theta})\right)}{\left(1-\cos^2\hat{\theta}\right)^{1/2}}\left(\frac{2\pi\sigma(1-\cos^2\hat{\theta})^{3/2}}{k_0\hat{R}\sin\hat{\theta}}\right)^{1/2} \mathrm{e}^{j\hat{R}\frac{k_0}{\sigma}\left(-\left(1-\cos^2\hat{\theta}\right)^{1/2}\sin\hat{\theta}-\left(\cos\hat{\theta}+M_\infty\right)\cos\hat{\theta}\right)+j\frac{\pi}{4}}. \tag{9.3.23}$$

After evaluation this is

$$I_n = \widetilde{\eta}_n(\cos\hat{\theta})\left(1+\Lambda_n(\cos\hat{\theta})\right)\left(\frac{2\pi\sigma}{k_0\hat{R}}\right)^{1/2} \mathrm{e}^{-j\hat{R}\frac{k_0}{\sigma}\left(M_\infty\cos\hat{\theta}+1\right)+j\frac{\pi}{4}}, \tag{9.3.24}$$

which is substituted back in to Equation (9.3.21) to give

$$p_t = \frac{1}{(2\pi)^2}\frac{2}{\sigma\hat{R}\sin^{1/2}\hat{\theta}} \sum_{n=-\infty}^{\infty} \mathrm{e}^{-j\frac{1}{2}n\pi}\widetilde{\eta}_n(\cos\hat{\theta})\left(1+\Lambda_n(\cos\hat{\theta})\right) \mathrm{e}^{-j\hat{R}\frac{k_0}{\sigma}\left(M_\infty\cos\hat{\theta}+1\right)} \mathrm{e}^{-jn\bar{\phi}}, \tag{9.3.25}$$

which is equivalent to

$$p_t(\bar{R},\bar{\theta},\bar{\phi}) = \frac{1}{(2\pi)^2}\frac{2}{\bar{R}\left(1-M_\infty^2\sin^2\bar{\theta}\right)^{1/2}\left(\frac{\sigma\sin\bar{\theta}}{\left(1-M_\infty^2\sin^2\bar{\theta}\right)^{1/2}}\right)^{1/2}}\times \sum_{n=-\infty}^{\infty} \mathrm{e}^{-j\frac{1}{2}n\pi}\widetilde{\eta}_n\left(\frac{\cos\bar{\theta}}{\left(1-M_\infty^2\sin^2\bar{\theta}\right)^{1/2}}\right)\left(1+\Lambda_n\left(\frac{\cos\bar{\theta}}{\left(1-M_\infty^2\sin^2\bar{\theta}\right)^{1/2}}\right)\right)\times \mathrm{e}^{-j\frac{\bar{R}}{\sigma^2}k_0\left(M_\infty\cos\bar{\theta}+\left(1-M_\infty^2\sin^2\bar{\theta}\right)^{1/2}\right)}\times \mathrm{e}^{-jn\bar{\phi}}, \tag{9.3.26}$$

in the polar coordinates.

To simplify the expression let

$$\Upsilon = \left(1-M_\infty^2\sin^2\bar{\theta}\right)^{1/2}, \tag{9.3.27}$$

with

$$\Xi_{\sin} = \frac{\sigma\sin\bar{\theta}}{\Upsilon}, \tag{9.3.28}$$

and

$$\Xi_{\cos} = \frac{\cos\bar{\theta}}{\Upsilon}, \tag{9.3.29}$$

such that the final expression is given by

$$p_t(\bar{R},\bar{\theta},\bar{\phi}) = \frac{1}{4\pi\bar{R}}\frac{2}{\sigma\pi\Upsilon\Xi_{\sin}^{1/2}}\sum_{n=-\infty}^{\infty}\widetilde{\eta}_n(\Xi_{\cos})\left(1+\Lambda_n(\Xi_{\cos})\right)\,\mathrm{e}^{-j\bar{R}\frac{k_0}{\sigma^2}\left(M_\infty\cos\bar{\theta}+\Upsilon\right)}\mathrm{e}^{-j(\frac{\pi}{2}+n\bar{\phi})}. \tag{9.3.30}$$

Bibliography

Abramowitz, M. and Stegun, I. (1964). *Handbook of Mathematical Functions*. United States Department of Commerce.

ACARE (2001). European aeronautics: A vision for 2020.

Agarwal, A., Dowling, A. P., Shin, H., Graham, W., and Sefi, S. (2007). Ray-tracing approach to calulate acoustic shielding by a flying wing airframe. *American Institute of Aeronautics and Astronautics*, **45**(5), 1080 – 1090.

Astley, R. (2014). Can technology deliver acceptable levels of aircraft noise. *Internoise Melbourne, Australia*, pages 369 – 382.

Astley, R., Sugimoto, R., Achunche, I., Kewin, M., Mustafii, P., and Deane, E. (2010). A review CAA for fan duct propagation and radiation, with application to liner optimisation. *Procedia Engineering*, **6**, 143 – 152.

Atalla, N. and Glegg, S. (1991). Ray-acoustics approach to fuselage scattering of rotor noise. *American Helicopter Society, 47th Annual Forum Proceedings*, pages 841 – 853.

Barron, M. (2010). *Auditorium Acoustics and Architectural Design*. Spon Press.

Belyaev, I. V. (2012). The effect of an aircraft's boundary layer on propeller noise. *Acoustical Physics*, **58**, 425 – 433.

Bowman, J. J. Senior, T. B. A. and Uslenghi, P. L. E. (1969). *Electromagnetic and Acoustic Scattering by Simple Shapes*. Horth-Holland Publishing Co.

Brambley, E., Darau, M., and Rienstra, S. (2012). The critical layer in linear-shear boundary layers over acoustic linings. *Journal of Fluid Mechanics*, **710**, 545 – 568.

Brand, R. S. and Nagel, R. T. (1982). Reflection of sound by a boundary layer. *Journal of Sound and Vibration*, **85**(1), 31 – 38.

Brouwer, H. (2016). The scattering of open rotor tones by a cylindrical fuselage and its boundary layer. In *22nd AIAA/CEAS Aeroacoustics Conference, Lyon*, number AIAA-2016-2741.

Campos, L. M. B. C. and Serrao, P. G. T. A. (1998). On the acoustics of an exponential boundary layer. *Philisophical Transactions of the Royal Society of London*, **356**, 2335 – 2378.

Campos, L. M. B. C., Oliveira, J. M. G. S., and Kobayashi, M. H. (1999). On sound propagation in a linear shear flow. *Journal of Sound and Vibration*, **219**(5), 739 – 770.

Candel, S. M. (1972). *Etudes Theoriques et Experimental de la Propagation Acoustique en Milieu Inhomogene et en Mouvement*. Ph.D. thesis, Universite de Paris VI.

Candel, S. M. (1973). Acoustic radiation from the end of a two-dimensional duct - effects of uniform flow and duct lining. *Journal of Sound and Vibration*, **28**, 1 – 13.

Casalino, D., Diozzi, F., Sannino, R., and Paonessa, A. (2008). Aircraft noise reduction technologies: A bibliographic review. *Aerospace Science and Technology*, **12**, 1 – 17.

Chapman, C. (2000). Similarity variables for sound radiation in a uniform flow. *Journal of Sound and Vibration*, **233**, 157 – 164.

Crighton, D. and Leppington, F. (1970). Scattering of aerodynamic noise by a semi-infinite compliant plate. *Journal of Fluid Mechanics*, **43**(4), 721 – 736.

Crighton, D., Dowling, A., Ffowcs-Williams, J., Heckl, M., and Leppington, F. (1992). *Modern Methods in Analytical Acoustics*. Springer.

Daroukh, M., Moreau, S., Gourdain, N., Boussuge, J., and Sensiau, C. (2016). Influence of distortion on fan tonal noise. In *22th AIAA/CEAS Aeroacoustics Conference, Lyon, France*, number AIAA-2016-2818.

Davisdson, P. A. (2004). *Turbulence: An introduction for scientists and engineers*. Oxford Press.

Dierke, J., Ewert, R., Delfs, J., Stohr, C., and Rose, M. (2013). The effect of a boundary layer on engine noise propagating to the fuselage at flight conditions. In *19th AIAA Conference Proceedings*, number AIAA-2013-2006.

Dobrzynski, W. M., Chow, L. C., Guion, P., and Shiells, D. (2002). Research into landing gear airframe noise reduction. In *8th AIAA/CEAS Aeroacoustics Conference & Exhibit, Colorado*, number AIAA-2002-2409.

European Commission (2011). Flightpath 2050 - Europe's Vision for Aviation.

Ffowcs Williams, J. E. and Hawkings, D. L. (1969). Sound generation by turbulence and surfaces in arbitrary motion. *Philosophical Transactions of the Royal Society*, **246**(1151), 321 – 346.

Fuller, C. R. (1989). Free-field correction factor for spherical acoustic waves impinging on cylinders. *American Institute of Aeronautics and Astronautics*, **27**(12), 1722 – 1726.

Gabard, G. (2013). A comparison of impedance boundary condtitions for flow acoustics. *Journal of Sound and Vibration*.

Gabard, G. and Astley, R. J. (2006). Theoretical model for sound radiation from annular jet pipes: far- and near-field solutions. *Journal of Fluid Mechanics*, **549**, 315 – 341.

Gaffney, J., McAlpine, A., and Kingan, M. (2016). Sound radiation of fan tones from an installed turbofan aero-engine: fuselage boundary–layer refraction effects. In *22nd AIAA/CEAS Aeroacoustics Conference, Lyon, France*, number AIAA-2016-2878.

Goldstein, M. E. (2001). An exact form of Lilley's equation with a velocity quadrupole/termperature dipole source term. *Journal of Fluid Mechanics*, **443**, 231 – 236.

Hanson, D. B. (1984). Shielding of prop-fan cabin noise by the fuselage boundary layer. *Journal of Sound and Vibration*, **22**(1), 63 –70.

Hanson, D. B. (1985). Near-field frequency domain theory for propeller noise. *American Institute of Aeronautics and Astronautics*, **23**(4), 499 – 504.

Hanson, D. B. and Magliozzi, B. (1985). Propagation of propeller tone noise through a fuselage boundary layer. *Journal of Aircraft*, **22**(1), 63 – 70.

Hocter, S. (1999). Exact and approximate directivity patterns of the sound radiated from a cylindrical duct. *Journal of Sound and Vibration*, **222**(2), 397 – 407.

Homicz, G. F. and Lordi, J. A. (1975). A note on the radiative directivity patterns of duct acoustic modes. *Journal of Sound and Vibration*, **41**(3), 283 – 290.

ICAO (2008). Environmental protection - Volume 1 - Aircraft Noise.

ICAO (2011). Annual report of the council. International Civil Aviation Organization, 2011.

Joseph, P. and Morfey, C. L. (1999). Multimode radiation from an unflanged, semi-infinite circular duct. *Journal of the Acoustical Society of America*, **105**(5), 2590 – 2600.

Kingan, M. J. and Self, R. (2012). Open rotor tone scattering. *Journal of Sound and Vibration*, **331**, 1806 – 1828.

Kopiev, V., Maslov, A., and Chernyshov, S. (1992). Prop-fan sound shielding by the fuselage boundary layer. *DGLR/AIAA-92-08-068, DGLR/AIAA 14th Aeroacoustic Conference*.

Kreyszig, E. (2011). *Advanced Engineering Mathematics*. Wiley.

Lansing, D. L., Drischler, J. A., and Pudsey, C. G. (1970). Radiation of sound from an unflanged circular duct with flow. *Journal of the Acoustical Society of America*, **48**(75).

Lawrence, J. (2014). *Aeroacoustic Interactions of Installed Subsonic Round Jets*. Ph.D. thesis, University of Southampton.

Lee, K., Bae, J., Kong, B., and Lee, S. (2014). Effect of chevron tip count and shape on the subsonic jet mixing noise emitted from hot air lance. *Journal of Mechanical Science and Technology*, **28**(11), 4573 – 4581.

Lighthill, M. J. (1952). On sound generated aerodynamically: 1 General theory. *Proceedings of the Royal Society of London A: Mathematical, Physical and Engineering Sciences*, **A**, 564 – 578.

Lighthill, M. J. (1954). On sound generated aerodynamically: 2 Turbulence as a source of sound. *Proceedings of the Royal Society of London A: Mathematical, Physical and Engineering Sciences*, **37**(2), 145 – 153.

Lighthill, M. J. (1972). The propagation of sound through moving fluids. *Journal of Sound and Vibration*, **24**, 471.

Lilley, G. (1958). On the noise from air jets. *Aeronautical Research Council*.

Lilley, G. (2001). The prediction of airframe noise and comparison with experiment. *Journal of Sound and Vibration*, **239**(4), 849 – 859.

Lockard, D. and Lilley, G. (2004). The airframe noise reduction challenge. Technical report, NASA, TM-2004-213013,.

Lockard, D., Khorrami, M., and Li, F. (2004). High resolution calculation of a simplified landing gear. In *10th AIAA/CEAS Aeroacoustics Conference, Manchester*, number AIAA-2004-2887.

Lu, H. Y. (1990). Fuselage boundary-layer effects on sound propagation and scattering. *American Institute of Aeronautics and Astronautics*, **28**(7), 1180 – 1186.

Marretta, R. A., Davi, G., and Milazzo, A. (2001). A procedure for the evaluation of installed propeller noise. *Journal of Sound and Vibration*, **244**(4), 697 – 716.

McAlpine, A. (2013). Symphony: Near-field installation for fan tones. Unpublished technical report.

McAlpine, A. and Kingan, M. J. (2012). Far-field sound radiation due to an installed open rotor. *International Journal of Aeroacoustics*, **11**, 213 – 245.

McAlpine, A., Daymond-King., A, P., and Kempton., A. (2012). Sound radiation from a flanged inclined duct. *Journal of Acoustical Society of America*, **132**(6), 3637 – 3646.

McAlpine, A., Gaffney, J., and Kingan, M. J. (2015). Near-field sound radiation of fan tones from an installed turbofan aero-engine. *Journal of the Acoustical Society of America*, **138**, 1313 – 1324.

McAninch, G. L. (1983). A note on propagation through a realistic boundary layer. *Journal of Sound and Vibration*, **88**(2), 271 – 274.

McAninch, G. L. (1987). Effects of velocity profile on boundary layer shielding. *American Institute of Aeronautics and Astronautics*, **84**(2678), 1 – 11.

McAninch, G. L. and Rawls, G. L. (1984). Effects of boundary layer refraction and fuselage scattering on fuselage surface noise from advanced turboprop propellers. *American Institute of Aeronautics and Astronautics*, **84**, 0249.

Miles, J. W. (1957). On the reflection of sound at an interface of relative motion. *Journal of Sound and Vibration*, **29**, 226 – 228.

Morse, P. M. and Ingard, K. U. (1968). *Theoretical Acoustics*. McGraw-Hill Book Co.

Munt, R. (1977). The interaction of sound with a subsonic jet issueing from a semi-infinite cylindrical pipe. *Journal of Sound and Vibration*, **83**, 283 – 290.

Nayfeh, A., Kaiser, J., and Shaker, B. (1974). Effect of mean-velocity profile shapes on sound transmission through two-dimensional ducts. *Journal of Sound and Vibration*, **34**(3), 413 – 423.

Noble, B. (1958). *Methods Based on the Wiener–Hopf Technique*. Pergamon.

Pastouchenko, N. and Tam, C. (2007). Installation effects on the flow and noise of wing mounted jets. *American Institute of Aeronautics and Astronautics*, **45**(12), 2851 – 2860.

Phillips, O. (1960). On the generation of sound by supersonic turbulent shear layers. *Journal of Fluid Mechanics*, **9**(1), 1 – 28.

Pierce, A. (1981). *Acoustics - An Introduction to Its Physical Principles and Applications*. McGraw–Hill Book Company.

Powles, C., Tester, B., and McAlpine, A. (2011). A weak–scattering model for turbine-tone haystacking outside the cone of silence. *International Journal of Aeroacoustics*, **10**(1), 17 – 50.

Pridmore-Brown, D. (1958). Sound propagation in a fluid flow through an attenuating duct. *Journal of Fluid Mechanics*, **4**(4), 393 – 406.

Ribner, H. S. (1957). Reflection, transmission, and amplification of sound by a moving medium. *Journal of Sound and Vibration*, **29**, 435 – 441.

Rice, E. J., Heidmann, M. F., and Sofrin, T. G. (1979). Modal propagation angles in a cylindrical duct with flow and their relation to sound radiation. *NASA-TM-79030*.

Rienstra, S. (1984). Acoustic radiation from a semi-infinite annular duct in a uniform subsonic mean flow. *Journal of Sound and Vibration*, **94**, 267 – 288.

Rienstra, S. (1998). Sound transmission in slowly varying circular and annular lined ducts with flow. *Journal of Fluid Mechanics*, **380**, 279 – 296.

Rienstra, S. (2003). Sound propagation in slowly varying lined flow ducts of arbitrary cross-section. *Journal of Fluid Mechanics*, **495**, 157 – 173.

Rienstra, S. W. and Hirschberg, A. (2013). *An Introduction to Acoustics*. https://www.win.tue.nl/ sjoerdr/papers/boek.pdf.

Salikuddin, M., Tam, C. K. W., and Burrin, R. H. (1988). An experimental and theoretical investigation of the propagation of sound waves through a turbulent boundary layer. *Journal of Sound and Vibration*, **127**, 91 – 121.

Sas, P., Bao, C., Augusztinovicz, F., and Desmet, W. (1993). Active control of sound transmission through a double panel partition. *Journal of Sound and Vibration*, **180**(4), 609–625.

Siefert, M. and Delfs, J. (2011). Refraction and scattering in high mach number boundary layers. In *17th AIAA/CEAS Aeroacoustics Conference*, number AIAA-2011-2847.

Sinayoko, S., Joseph, P., and McAlpine, A. (2010). Multimode radiation from an unflanged, semi-infinite circular duct with uniform flow. *Journal of Acoustical Society of America*, **127**(4), 2159 – 2168.

Smith, M. (2004). *Sound Radiation from a Vibrating Surface Under a Boundary Layer*. Ph.D. thesis, University of Southampton.

Smith, M. J. T. (1989). *Aircraft noise*. Cambridge Press.

Spence, P. (1992). Effect of fuselage boundary layer on noise propagation from advanced propellers. *Journal of Aircraft*, **29**(6), 1005 – 1011.

Stanescu, D., Hussaini, M. Y., and Farrasat, F. (2003). Aircraft engine noise scattering by fuselage and wings: a compuational approach. *Journal of Sound and Vibration*, **263**, 319 – 333.

Stanton, T. K. (1988). Sound scattering by cylinders of finite length. i. fluid cylinders. *Journal of the Acoustical Society of America*, **83**(1), 55 – 63.

Stoker, R., Guo, Y., Streett, C., and Burnside, N. (2003). Airframe noise source locations of a 777 aircraft in flight and comparisons with past model-scale tests. In *9th AIAA/CEAS Aeroacoustics Conference and Exhibit*.

Stone, J. (2015). *Cones of Silence, Complex Rays & Catastrophes: Novel Sources of High-Frequency Noise in Jets*. Ph.D. thesis, University of Southampton.

Sulc, J., H. J. and Benda, L. (1982). Exterior noise on the fuselage of light propeller driven aircraft in flight. *Journal of Sound and Vibration*, **84**, 105 – 120.

Swinbanks, M. (1975). The sound field generated a source distribution in a long duct carrying shear flow. *Journal of Sound and Vibration*, **40**, 610 – 626.

Tam, C. K. W. and Morris, P. J. (1980). The radiation of sound by the instability waves of a compressible plane turbulent shear layer. *Journal of Fluid Mechanics*, **98**(2), 348 – 381.

Tyler, J. M. and Sofrin, T. G. (1962). Axial flow compressor noise studies. *SAE Technical Paper*.

Wang, T. Q. and Zhou, S. (1998). Investigation on sound field model of propeller aircraft – the effect of rigid fueslage boundary. *Journal of Sound and Vibration*, **209**(2), 317 – 328.

Whitham, G. B. (1974). *Linear and Nonlinear Waves*. Wiley.

Wilby, J. and Scharton, T. (1973). Acoustic transmission through a fuselage sidewall. Technical report, NASA.

Wright, M., editor (2001). *Lecture Notes on the Mathematics of Acoustics*. Imperial College Press.

Ye, Z. (1997). A novel approach to sound scattering by cylinders of finite length. *Journal of Acoustical Society of America*, **102**(2), 877 – 884.